AC MAGNETOTRANSPORT, MAGNETOCALORIC AND MULTIFERROIC STUDIES IN SELECTED OXIDES

VINAYAK BHARAT NAIK

NATIONAL UNIVERSITY OF SINGAPORE

2011

AC MAGNETOTRANSPORT, MAGNETOCALORIC AND MULTIFERROIC STUDIES IN SELECTED OXIDES

VINAYAK BHARAT NAIK

(*M. Sc., Mangalore University, India*)

A THESIS SUBMITTED

FOR THE DEGREE OF DOCTOR OF PHILOSOPHY IN SCIENCE

DEPARTMENT OF PHYSICS

NATIONAL UNIVERSITY OF SINGAPORE

2011

ACKNOWLEDGEMENTS

I would like to express my sincere gratitude to my supervisor, *Asst. Prof. Ramanathan Mahendiran* for his expert guidance and continuous support in completing this work successfully. I'm very grateful to him for his constant motivation, fruitful suggestions, kind support, guidance and continuous encouragement in all aspects that made my candidature a truly enriching experience at National University of Singapore.

I would like to express my wholehearted thanks to my colleagues in the lab comprising *Alwyn*, *Sujit*, *Suresh*, *Aparna*, *Mahesh*, *Mark*, *Zhuo Bin*, *Pawan*, *Dr. Raj Sankar*, *Dr. C. Krishnamoorthy*, *Dr. Rucha Desai* and *Dr. Kavitha* for their generous support, fruitful discussions, immense help provided throughout the period of my research work and more importantly, for creating a cheerful and cooperative working atmosphere in the lab.

My sincere thanks to *Prof. B. V. R Chowdari* for allowing me to use their lab facilities. I'm very thankful to *Prof. G. V. Subba Rao* and *Dr. M. V. V. Reddy* for their fruitful suggestions and kind help.

My heartfelt thanks to *Prof. H. L. Bhat* and *Dr. Suja Elizabeth* for giving me an opportunity to start my research career at IISc, Bangalore as a junior researcher. I'm very grateful to them for their kind support, motivation and continuous encouragement.

Special thanks to my close friends in NUS comprising *Bibin*, *Sujit*, *Suresh*, *Naresh*, *Raghu*, *Saran*, *Alwyn*, *Aparna*, *Christie*, *Venkatesh*, *Nitya*, *Venkatram*, *Nakul*, *Mahesh*, *Amar*, *Pradipto*, *Tanay*, *G. K.*, *Pawan*, *Suvankar*, *Abhinav*, *Arun*, *Rajendra*, *Rakesh*, *Sunil* and *Ankush* for making my days in NUS more enjoyable and refreshing. My heartfelt thanks to my close friends comprising *Ganesh*, *Jyothi*, *Ganesh Kamath*, *Dinesh*, *Ravish*, *Mohan*, *Babu*, *Venky*, *Sukesh*, *Damu* and Singapore Kannada Sangha friends for their motivation and continuous encouragement.

I would like to thank physics department workshop staff, especially *Mr. Tan* for his timely help, and office staff for their continuous help.

I would like to acknowledge Faculty of Science, National University of Singapore for providing financial support through graduate student fellowship.

Finally and most importantly, I feel a deep sense of gratitude to my father, *Bharat Channappa Naik* and my mother, *Chandrakala Bharat Naik* for their continuous support, advice and encouragement since from schooldays to till now. I am very happy to dedicate this thesis to them. My heartfelt special thanks to my loved fiancée, *Smita* and loved family members *Veena*, *Bavaji*, *Santhu*, my lovely niece, *Sanjana* and nephew, *Sumukh* and all my cousins for their encouragement and inspiration, and also the affection shown to me.

TABLE OF CONTENTS

SUMMARY

Oxide materials particularly, manganites (Mn-based) and ferrites (Fe-based) exhibiting fascinating properties and multiple functionalities have become very attractive for potential applications and hence, the subject of many experimental and theoretical studies. In this thesis, the intriguing properties of these materials such as *rf* magnetoabsorption, magnetoimpedance, magnetocaloric and multiferroic properties are investigated in detail.

Magnetoabsorption refers to a large change in electromagnetic absorption by a magnetic material under an external magnetic field that remains less explored. The *rf* magnetoabsorption in ferromagnetic systems, $La_{1-x}Ba_{x-y}Ca_yMnO_3$ and $Sm_{0.6-x}La_xSr_{0.4}MnO_3$ series, is investigated by a homebuilt LC resonant circuit powered by an integrated chip oscillator (ICO) resonating at $f \approx 1.5$ MHz by monitoring the changes in resonance frequency (f_r) and current (I) through ICO. It is demonstrated that a simple ICO circuit is a versatile contactless experimental tool to study magnetization dynamics as well as to investigate magnetic and structural phase transitions in manganites. A giant *rf* magnetoabsorption observed in $La_{0.67}Ba_{0.33}MnO_3$ ($\Delta f_r/f_r$ = 46% and $\Delta I/I = \Delta P/P$ = 23%) and also in $La_{0.6}Sr_{0.4}MnO_3$ ($\Delta f_r/f_r$ = 65% and $\Delta P/P$ = 7.5%) around the ferromagnetic transition (T_C) at H = 1 kG can be exploited for magnetic field sensor and other applications.

The exploitation of colossal magnetoresistance (MR) observed in manganites for practical device applications has been hindered by the need of high magnetic fields ($\mu_0 H > 2$ T) to induce more than 20% MR at room temperature. Hence, an alternative approach to obtain a considerable MR at low magnetic field is presented in this study. The ac magnetotransport in ferromagnetic systems, $La_{1-x}Ba_{x-y}Ca_yMnO_3$ and $Sm_{0.6-x}La_xSr_{0.4}MnO_3$ series, is investigated in detail by measuring the ac resistance (R) and reactance (X) using the impedance spectroscopy as a function of magnetic field (H) over a wide frequency (f) and temperature range. A giant magnetoimpedance effect is observed in $La_{0.67}Ba_{0.33}MnO_3$ around T_C, which showed fractional changes as much as -45% in ac magnetoresistance and -40% in magnetoreactance at f = 5 MHz under a low magnetic field of H = 1 kG. The results obtained

in this study reveal that ac magnetotransport is an alternative strategy to enhance ac magnetoresistance in manganites, and also a valuable tool to study magnetization dynamics, to detect magnetic and structural transitions. The ac magnetotransport studies in $Sm_{0.6-x}La_xSr_{0.4}MnO_3$ compounds showed unusual features and the possible origins of the observed effects are discussed.

Magnetic refrigeration (MR) based on magnetocaloric effect (MCE), wherein temperature of a magnetic material changes by applying magnetic field, is currently attracting much attention due to its potential impact on energy savings and environmental concerns compared to conventional gas-compression technology. While the extensive investigations of MCE have been done in ferromagnetic manganites which show normal MCE (change in magnetic entropy, ΔS_m is negative under H), antiferromagnets which show inverse MCE (ΔS_m is positive under H) are rarely studied due to the need of high magnetic field ($\mu_0 H$ > 5 T) to destroy the antiferromagnetic state. In this work, a comprehensive study of MCE is conducted in $Pr_{1-x}Sr_xMnO_3$ (x = 0.5 and 0.54) which revealed the coexistence of both normal and inverse MCEs due to ferromagnetic exchange-interaction between Mn spins and the destruction of antiferromagnetism under the magnetic field, respectively. A giant inverse MCE is observed in x = 0.54 (ΔS_m = +9 $Jkg^{-1}K^{-1}$ around T_N), and the coexistence of both normal (ΔS_m = -4.5 $Jkg^{-1}K^{-1}$ around T_C) and inverse (ΔS_m = +7 $Jkg^{-1}K^{-1}$ around T_N) MCEs observed in x = 0.5 for ΔH = 7 T makes $Pr_{1-x}Sr_xMnO_3$ system very attractive from the viewpoints of MR technology. A clear experimental evidence for both normal and inverse MCEs is obtained from home-built differential scanning calorimetry (DSC) and differential thermal analysis (DTA). A detailed investigation of magnetic and magnetocaloric properties has also been carried out in $Sm_{0.6-x}La_xSr_{0.4}MnO_3$ series which showed normal and unusual inverse MCEs. This is the first observation of inverse MCE in a ferromagnetic compound and the origin of which is attributed to the antiparallel coupling of 3*d* spins of Mn sublattice and 4*f* spins of Sm sublattice.

The magnetoelectric (ME) multiferroic materials, which show a strong coupling between ferromagnetic and ferroelectric order parameters, have recently attracted a surge of attention from the viewpoints of both fundamental research and practical device applications. In this context, perovskite $BiFeO_3$ has stimulated a great deal of interest in the past few years for its rare room temperature multiferroicity. In the present study, a detailed magnetic and ME properties of pure and cation doped $Bi_{1-x}A_xFeO_3$ (A = Sr, Ba and $Sr_{0.5}Ba_{0.5}$ and x = 0 and 0.3) has been investigated. It is observed that the divalent cation doping in antiferromagnetic $BiFeO_3$ enhances the magnetization with a well-developed hysteresis loop due to the effective suppression of spiral spin structure, and the magnitude of spontaneous magnetization increases with size of the cation dopants. The $A = Sr_{0.5}Ba_{0.5}$ compound showed maximum transverse ME coefficient T-α_{ME} = 2.1 mV/cmOe in the series, although it is not the compound with highest saturation magnetization hence, it is suggested that the compounds need not to have high saturation magnetization to show high ME coefficient.

LIST OF PUBLICATIONS

Articles

- V. B. Naik and R. Mahendiran, "*Normal and inverse magnetocaloric effects in ferromagnetic $Sm_{0.6-x}La_xSr_{0.4}MnO_3$*", **J. Appl. Phys**. **110**, 053915 (2011).

- V. B. Naik and R. Mahendiran, "*High frequency electrical transport in $La_{0.67}Ba_{0.33}MnO_3$*", **IEEE transactions on Magnetics**, **47**, 2712 (2011).

- V. B. Naik, S. K. Barik, and R. Mahendiran, and B. Raveau, "*Magnetic and calorimetric investigations of inverse magnetocaloric effect in $Pr_{0.46}Sr_{0.54}MnO_3$*", **Appl. Phys. Lett. 98**, 112506 (2011).

- V. B. Naik, A. Rebello, and R. Mahendiran, "*Dynamical magnetotransport in $Ln_{0.6}Sr_{0.4}MnO_3$ (Ln = La, Sm)*", **J. Appl. Phys**. **109**, 07C728 (2011).

- V. B. Naik, M. C. Lam, and R. Mahendiran, "*Detection of structural and magnetic transitions in $La_{0.67}Ba_{0.23}Ca_{0.1}MnO_3$ using rf resonance technique*", **J. Magn. Magn. Mater. 322**, 2754 (2010).

- V. B. Naik, M. C. Lam, and R. Mahendiran, "*Radio-frequency detection of structural anomaly and magnetoimpedance in $La_{0.67}Ba_{0.23}Ca_{0.1}MnO_3$*", **J. Appl. Phys**. **107**, 09D720 (2010).

- V. B. Naik and R. Mahendiran, "*Magnetically tunable rf wave absorption in polycrystalline $La_{0.67}Ba_{0.33}MnO_3$*", **Appl. Phys. Lett. 94**, 142505 (2009).

- V. B. Naik, A. Rebello, and R. Mahendiran, "*A large magneto-inductance effect in $La_{0.67}Ba_{0.33}MnO_3$*", **Appl. Phys. Lett. 95**, 082503 (2009).

- V. B. Naik and R. Mahendiran, "*Magnetic and magnetoelectric studies in pure and cation doped $BiFeO_3$*" **Solid. State. Commun. 149**, 754 (2009).

- A. Rebello, V. B. Naik, and R. Mahendiran, "*Huge ac magnetoresistance of $La_{0.7}Sr_{0.3}MnO_3$ in sub-kilo gauss magnetic fields*", **J. Appl. Phys**. **106**, 073905 (2009).

- V. B. Naik and R. Mahendiran, "*Electrical, magnetic, magnetodielectric and magnetoabsorption studies in multiferroic $GaFeO_3$*", **J. Appl. Phys**. **106**, 123910 (2009).

- V. B. Naik and R. Mahendiran, "*Magnetic and magnetoabsorption studies in multiferroic $Ga_{2-x}Fe_xO_3$ nanoparticles*", **IEEE transactions on Magnetics 47**, 3776 (2011).

- V. B. Naik and R. Mahendiran, "*Direct and indirect measurements of magnetocaloric effect in $Pr_{0.5}Sr_{0.5}MnO_3$*" (submitted to **Solid. State. Commun**.).

Conference Proceedings

- V. B. Naik, A. Rebello, and R. Mahendiran, "*Unusual Dielectric Response of $Sm_{1-x}Sr_xMnO_3$ (x = 0.3 and 0.4)"*, **ICMAT, Singapore (2011**).

- V. B. Naik, M. C. Lam, and R. Mahendiran, "*Detection of structural anomaly and magnetoimpedance in pure and Ca substituted $La_{0.67}Ba_{0.33}MnO_3$ using rf measurements*", **MRS-S Conference on Advanced Materials**, IMRE, Singapore (2010).

- V. B. Naik, M. C. Lam, and R. Mahendiran, "*Magnetoimpedance and structural anomaly in $La_{0.67}Ba_{0.23}Ca_{0.1}MnO_3$*", **MMM Conference**, USA (2010).

- A. Rebello, V. B. Naik, S. K. Barik, M. C. Lam, and R. Mahendiran, *Giant magnetoimpedance in oxides*", **MRS-Spring,** San Francisco (2010).

- V. B. Naik, and R. Mahendiran, "*Effect of cation substitution on magnetic and magnetoelectric properties of the $BiFeO_3$ perovskite*", **ICMAT, Singapore (2009**).

- V. B. Naik, and R. Mahendiran, "*Multifunctional properties of multiferroic oxides***",** **MPSGC**, Chulalonkarn University, Bangkok, Thailand, (2009).

- V. B. Naik, and R. Mahendiran, "*The Study of Magnetoelectric Effect, Magnetic and Electrical Properties of Doped $BiFeO_3$ Compounds*", **AsiaNano**, Singapore (2008).

- V. B. Naik, and R. Mahendiran, "*Nonresonant radio-frequency power absorption in colossal magneto-resistive material using IC oscillator*", **MRS-S Conference on Advanced Materials**, IMRE, Singapore (2008).

LIST OF TABLES

LIST OF FIGURES

LIST OF SYMBOLS

R	Resistance
ρ	Resistivity
σ	Conductivity
T	Temperature
T_S	Surface temperature
G	Effective thermal conductance
t	Time
V	Voltage
e	Electronic charge
E	Electric field
I	Current
P	Polarization
X	Reactance
L	Inductance
Z	Electrical impedance
M	Magnetization
H	Magnetic field
μ	Magnetic permeability
μ_0	Permeability of free space
μ_ϕ	Circumferential permeability
f	Frequency
k_B	Boltzmann constant
δ	Skin depth
ε	Dielectric permittivity

ω	Angular frequency
S	Magnetic entropy
C	Curie Weiss constant
P_{eff}	Effective magnetic moment
C_p	Heat capacity
m	Mass
Q	Heat
α_{ME}	Magnetoelectric coefficient
L-α_{ME}	Longitudinal magnetoelectric coefficient
T-α_{ME}	Transverse magnetoelectric coefficient

Chapter 1

Introduction

Oxide materials exhibiting fascinating properties and multiple functionalities have become very attractive for potential applications and also the subject of many experimental and theoretical studies. Particularly, Mn and Fe-based oxides in the ABO_3 perovskite family have attracted a lot of attention in the past few decades since they show various exotic properties such as ferroelectricity, multiferroicity, colossal magnetoresistance, metal-insulator transitions, giant piezoelectricity, charge, orbital and spin ordering, magnetoabsorption and magnetocaloric effect (MCE) etc. [1] Majority of these properties results from strongly correlated electronic behavior and turned out to be very sensitive to external parameters such as temperature, electric and magnetic fields, pressure and light irradiation etc. A traditional route to understand these kinds of emergent properties is to create them in new materials such that one can study the different states of matter with different characteristics. Currently, these oxides are under investigation in view of device applications in the ambitious field of oxide electronics which aims to develop new electronics based on oxides. Generally, searches for these emergent phenomena are often performed in bulk or thin-film materials, either crystalline or nanometer-scale in size.

In this chapter, a brief review about the interesting properties of manganese (Mn) based oxides (manganites), iron (Fe) based oxides (ferrites) and also overviews of research activities in these materials are presented. This chapter is organized as follows. We first give a brief introduction to manganites and several magnetic interactions involved in, and then we discuss few exotic phenomena exhibited by these materials such as charge ordering, orbital ordering, phase separation etc. Next we briefly discuss the four main phenomena, which occur in Mn and Fe-based oxides, investigated in this thesis work. First we present a brief description of alternating current magnetotransport properties of metallic ferromagnetic manganites or it is generally referred as giant magnetoimpedance effect. Next we give a short description on

magnetoabsorption properties of manganites. This is followed by a short review on MCE in manganites is presented along with the various techniques involved in the indirect and direct measurements of MCE. We then present a brief introduction to multiferroics and ME effect which occurs in few Mn and Fe-based oxides. Finally, we outline the scope and objectives of this thesis work along with a brief note on the organization of rest of the thesis. The issues related to various phenomena investigated in the present study in selected Mn and Fe-based oxides are emphasized in the introduction of the corresponding chapters.

1. 1 A brief introduction to manganites

In the past few years a lot of attention has been focused on the colossal magnetoresistance (CMR) properties of the hole-doped pseudocubic perovskite $RE_{1-x}AE_xMnO_3$, where *RE* – rare earth element (La, Nd, Pr, Dy…) and *AE* – alkaline-earth element (Sr, Ca, Ba, Pb…) and its relation to structural and magnetic properties. [1] Jonker and Van Santen [2, 3, 4] were the first to study the physical properties of manganites of $La_{1-x}Ca_xMnO_3$ dopant ranging from x = 0 to 1. The parent compound $LaMnO_3$ is antiferromagnetic insulator with a Neel temperature, $T_N \approx 150$ K. [2, 3, 4] By controlling the hole-doping level, x, a whole new set of interesting properties are observed and thus, the manganites have very rich and complex phase diagrams in terms of various physical phenomena. [1] Some of the important phases of manganites are: antiferromagnetic insulator, ferromagnetic insulator, ferromagnetic metal, charge and orbital ordered states. In addition, some manganites also show a series of structural transitions as a function of temperature and doping. All these properties are highly sensitive to external parameters such as temperature, magnetic field, electric field, pressure as well as electromagnetic radiation. There are some fundamental interactions operating in these hole-doped manganites which include double exchange interaction leading to ferromagnetic metallic state, antiferromagnetic superexchange interaction, crystal field and Jahn Teller (JT) effects. In this chapter, we have explained some of these interactions and effects briefly. Although the antiferromagnetic insulating, ferromagnetic insulating and ferromagnetic metallic phases were observed in the earlier years,

additional phases such as charge and orbital ordering were discovered only in the early 90`s. [1]

In 1993, renewed interest was generated in manganites because of the colossal magnetoresistance (CMR) exhibited by these systems. [1] The CMR effect refers to a large change in the dc electrical resistivity of manganites in the presence of external dc magnetic fields and it received a lot of attention due to possible device applications in magnetic sensors and profound fundamental physics involved. The basic physics of CMR effect comes from the fact that Mn ion in the parent compound $RE\mathrm{MnO_3}$ has a valency of 3+. Due to divalent doping of AE^{2+}, Mn^{4+} ions are created and this results in a vacancy of one electron in Mn^{4+} site. This is equivalent to the formation of a hole and this hole is mobile in nature and hops from Mn^{4+} to Mn^{3+} site mediated by core spins of both ions which will eventually lead to various electrical and magnetic properties of the system.

1. 1. 1 Crystallographic structure

The manganites with general formula $RE_{1-x}AE_x\mathrm{MnO_3}$ have a perovskite structure of the type $AB\mathrm{O_3}$, where *A* is the trivalent *RE* (rare-earth) or divalent *AE* (alkaline-earth) atom and *B* is the Mn atom. A schematic diagram of the cubic perovskite structure of $AB\mathrm{O_3}$ type with $B\mathrm{O_6}$ octahedra is shown in Fig. 1.1. In the basic perovskite structure, a set of $B\mathrm{O_6}$ octahedra are linked together by corner-shared oxygen atoms with *A* atoms occupying the space in between. Thus, the larger size *RE* trivalent ions and *AE* divalent ions occupy the *A*-site with 12-fold oxygen coordination and the smaller Mn ions in the mixed-valence state Mn^{3+}–Mn^{4+} located at the centre of an oxygen octahedron occupy the *B* site with 6-fold coordination. For a stoichiometric manganite system with formula $RE_{1-x}AE_x\mathrm{MnO_3}$, the proportions of Mn ions in the valence states of 3+ and 4+ are 1-x and x, respectively.

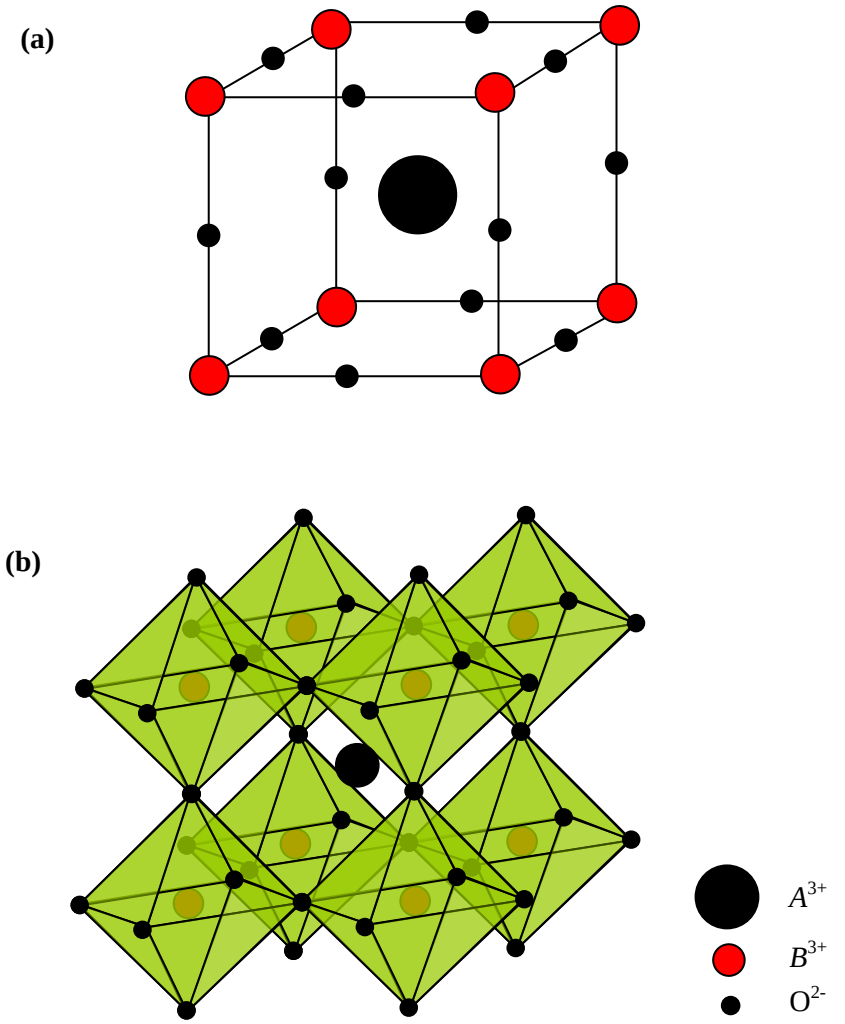

Fig. 1. 1 Schematic diagram of the (a) cubic perovskite (ABO_3) and (b) BO_6 octahedra

Due to the mismatch between the size of the *A* and *B* cations, the structural distortions takes place resulting in buckling of the MnO_6 octahedron. A similar type of distortion arises due to Jahn-Teller effect which will be discussed subsequently. This buckling and lattice distortion of MnO_6 octahedra result in lowering the symmetry of the perovskite structure in which the coordination number of *A* and *B* site ions are reduced for instance, the coordination number of *A* site ions decreases from 12 to as low as 8. This kind of lattice distortion is governed by Goldschmidt's tolerance factor (*t*) rule [5] and this factor is given by,

$$t = \frac{< r_A > + < r_B >}{\sqrt{2}(< r_B > + < r_O >)}$$

where, r_i (i = *A*, *B*, O) represents the (averaged) ionic size of each element. A cubic perovskite of ABO_3 type is stable only if the tolerance factor (t) is nearly equal to unity and thus, t measures the deviation from perfect cubic symmetry. As the value of t decreases, symmetry of the crystal structure also reduces, hence the structure transforms from cubic (t = 1) to rhombohedral ($0.96< t <1$) and to orthorhombic ($t < 0.96$). In addition, the Mn-O-Mn bond angle is sensitive to the size of the *A*-site ion and it deviate from 180˚. Fig. 1.2 illustrates the distortion of structure due to *A*-site cation size mismatch.

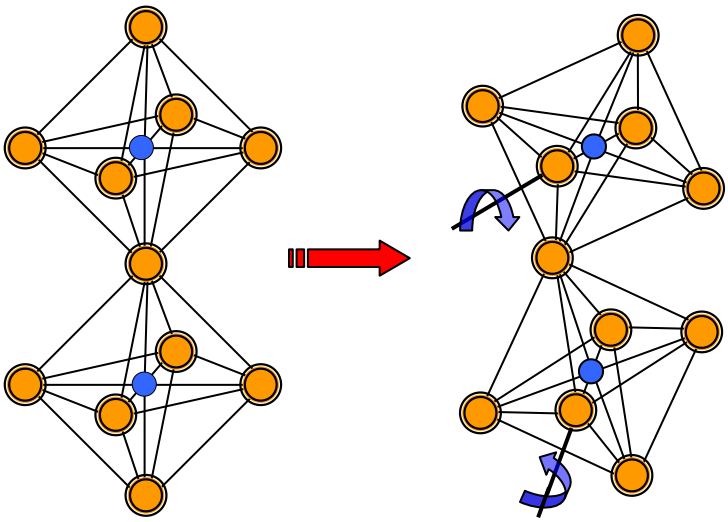

Fig. 1. 2 A schematic diagram of the MnO_6 distortion due to *A*-site cation size mismatch.

1. 2 Magnetic interactions

1. 2. 1 Crystal field effect

The crystal field effect at both *A*-site and Mn site cations in perovskite structure plays an important role on the electronic and magnetic properties of manganites. Although the ideal structure should have cubic symmetry, the distorted perovskite structure of manganites will have the reduced symmetry. The Mn^{3+} ion is surrounded by oxygen octahedra. The Mn^{3+} ion has four electrons in its outermost energy level and five degenerated orbital states are available to the 3*d* electrons with l = 2. The 3*d* orbitals of Mn are subjected to partial lifting of the degeneracy due to crystal field, which is an electric field derived from neighboring atoms

in the crystal. In crystal field theory, the size and nature of crystal field effects depend crucially on the symmetry of the local octahedral environment. [6] Fig. 1.3 illustrates the energy levels and orbitals of Mn^{4+} and Mn^{3+} ions in a crystal field of octahedral symmetry and with axial elongation. The electronic configuration of Mn^{3+} ion is $t_{2g}^3 e_g^1$ with $S = 2$, whereas of Mn^{4+} is t_{2g}^3 with $S = 3/2$. While the three low lying states are t_{2g}, the upper two states are the e_g. The low lying t_{2g} states are d_{xy}, d_{yz}, d_{xz} and the upper two e_g states are $d_{x^2-y^2}$ and $d_{3z^2-r^2}$. The energy involved in the crystal field splitting between t_{2g} and e_g states is of the order of 1 eV. This crystal field splitting of the energy levels of outermost electron occurs in all manganites with rare earth ion except La-based manganites where the crystal field effect is absent due to the fact that La has closed shell. The t_{2g} and e_g energy levels undergo further splitting due to Jahn-Teller effect, which are shown in Fig. 1.3 and we discuss next.

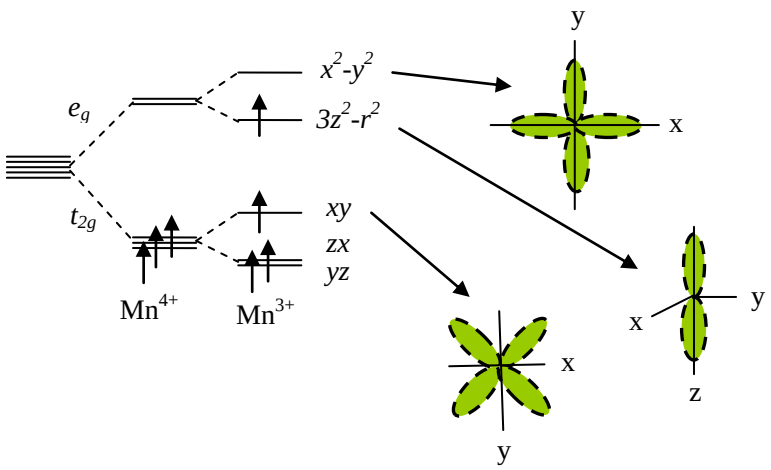

Fig. 1. 3 Two e_g and three t_{2g} energy levels and orbitals of Mn^{4+} and Mn^{3+} in a crystal field of octahedral symmetry. The splitting of e_g and t_{2g} energy levels due to Jahn-Teller distortion is also shown.

1. 2. 2 Jahn-Teller effect

The Jahn-Teller theorem by H. A. Jahn and E. Teller was published in 1937 which explains some of the distortions observed in transition metal complexes. [7] It states that “any non-linear molecular system in a degenerate electronic state will be unstable and will undergo distortion to form a system of lower symmetry and lower energy thereby removing the degeneracy". This distortion is called Jahn-Teller distortion or Jahn-Teller effect. There are

basically two types of Jahn-Teller effects: non-cooperative Jahn-Teller effect (NCJTE) and co-operative Jahn-Teller effect (CJTE) depending upon the presence of Jahn-Teller ion in the lattice system. While the NCJTE occurs in a system where there is an isolated Jahn-Teller distorted ion present in the host lattice as an impurity, CJTE takes place in a system where there are many Jahn-Teller ions present in the lattice. In Jahn-Teller effect, both electronic and lattice motions are coupled. In manganites, the orbital degeneracy of the e_g electrons are lifted because of the movement oxygen ions from their original positions. There are 21 modes of vibration for the movement of oxygen and Mn ions. [8] However, only two modes of vibrations are responsible for the splitting of the e_g doublet *i.e.*, for Jahn-Teller distortion. [9] These two modes of vibration are named as $Q2$ and $Q3$ and are shown in Fig. 1.4(a) and (b), respectively. The Q_3 mode is a tetragonal distortion which results in an elongation or contraction of the MnO_6 octahedron due to the movement of oxygen corresponding to the filled $3d_{3z^2-r^2}$ or $3d_{x^2-y^2}$ orbitals, respectively. Whereas the Q_2 mode is an orthorhombic distortion obtained by certain superposition of $3d_{3z^2-r^2}$ and $3d_{x^2-y^2}$ orbitals. In the case of Q_2 mode, a certain superposition of $3d_{x^2-y^2}$ and $3d_{3z^2-r^2}$ orbitals is obtained [10] which results in a rod-type or cross-type orbital ordering as shown in the Fig. 1.5. These Jahn-Teller distortions are not independent from one Mn^{3+} site to another and are CJTE. A long range ordering is established throughout the whole crystal which is also accompanied by a long range ordering of the orbital degree of freedom. [11, 10] In such a Jahn-Teller-distorted and orbital-ordered state, $LaMnO_3$ shows an *A*-type antiferromagnetic ordering below T = 120 K where the ferromagnetic *xy* planes are coupled antiferromagnetically along the *z*-axis. The Jahn-Teller distortion is rather effective in the lightly doped manganites. However, with increasing the doping level which increases the Mn^{4+} ions content, the Jahn–Teller distortions are reduced and the stabilization of the $3d_{3z^2-r^2}$ e_g orbital becomes less effective.

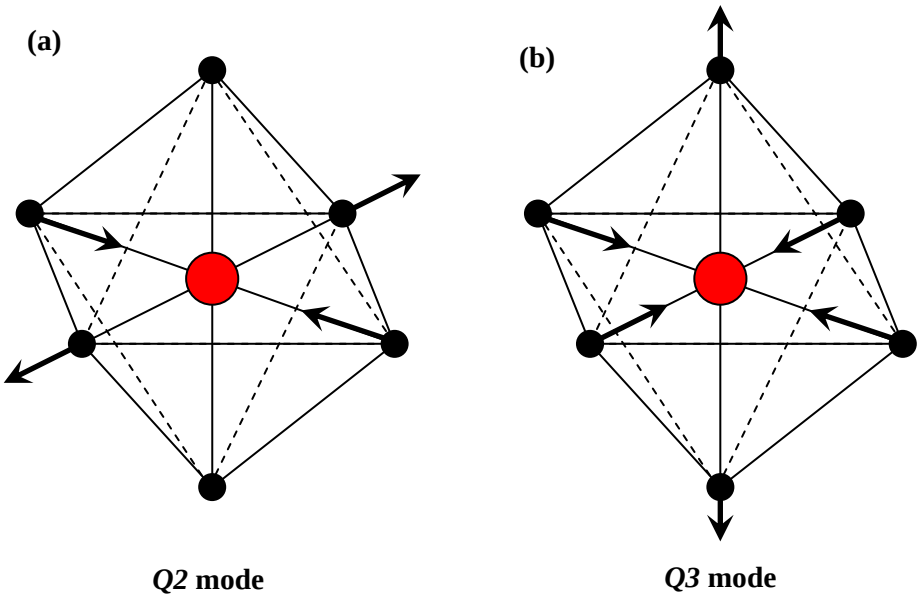

Fig. 1. 4 The two John-Teller modes: (a) *Q*2 and (b) *Q*3, which are responsible for the splitting of e_g doublet.

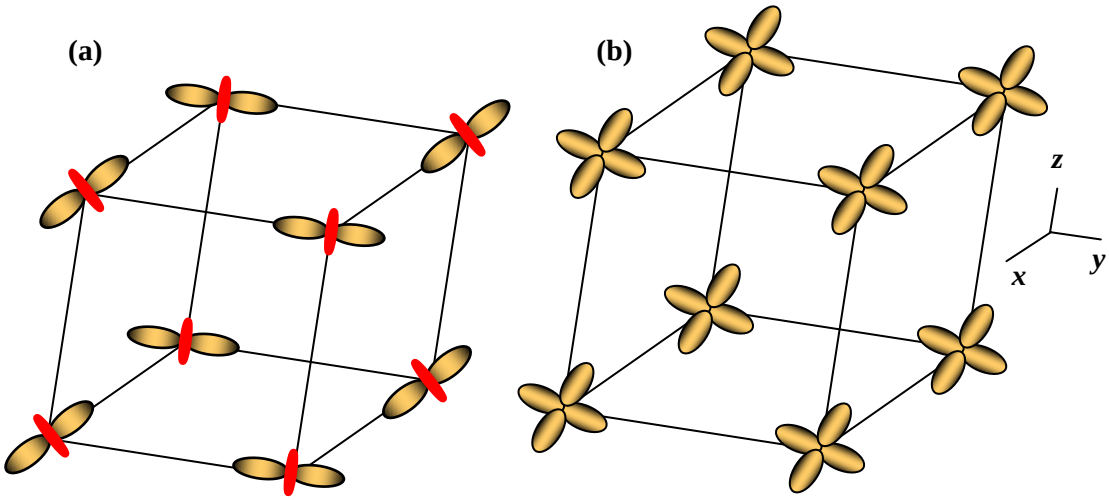

Fig. 1. 5 A schematic diagram of the (a) rod-type and (b) cross-type orbital ordering.

1. 2. 3 Double exchange interaction

Ferromagnetic order in the mixed-valence manganites is induced by the double-exchange mechanism proposed by Zener in 1951. [12] This mechanism is based on the assumption of a strong intra-atomic exchange interaction between a localized spin and a delocalized electron. According to this mechanism, ferromagnetic metallic phase is established by double exchange interaction supported by strong Hund's rule coupling (J_H)

between the different d electrons of Mn which causes the Mn^{3+} ion to have maximum possible spin of S = 2. As we have discussed earlier, in manganites, the degeneracy of the d shell is lifted due to the crystal field and hence, three electrons occupy the lower t_{2g} level forming localized magnetic moment of net spin S = 3/2 and fourth electron moves to the e_g level forming an itinerant band with spin parallel to the core spin by strong Hund's rule coupling present in the system. Further, the Jahn-Teller distortion causes e_g band to split into two bands with spins parallel and antiparallel to the core spins. Only the lower band corresponding to parallel spins is involved in the low energy properties of the system due to the fact that J_H is large. In the strong coupling limit where the Hund's-rule coupling energy or the exchange energy J_H exceeds the inter-site hopping interaction t^0_{ij} of the e_g electron between the neighboring sites, i and j *i.e.*, $J_H >> t_{ij}$, the effective hopping interaction of the conduction electron is expressed as, [13]

$$t_{ij} = t^0_{ij}\cos(\theta_{ij}/2).$$

Thus, the hopping magnitude of itinerant e_g electron depends on $\cos(\theta_{ij}/2)$ where θ_{ij} is the angle between neighboring core spins. This parallel alignment of neighboring core spins leads to ferromagnetism as well as metallicity in the system. In hole doped manganites, the hopping of e_g electron from Mn^{3+} ion to Mn^{4+} ion via oxygen ion is called double exchange and this exchange interaction leads to metallic ferromagnetism. Fig. 1.6 shows the schematic diagram of the double exchange mechanism.

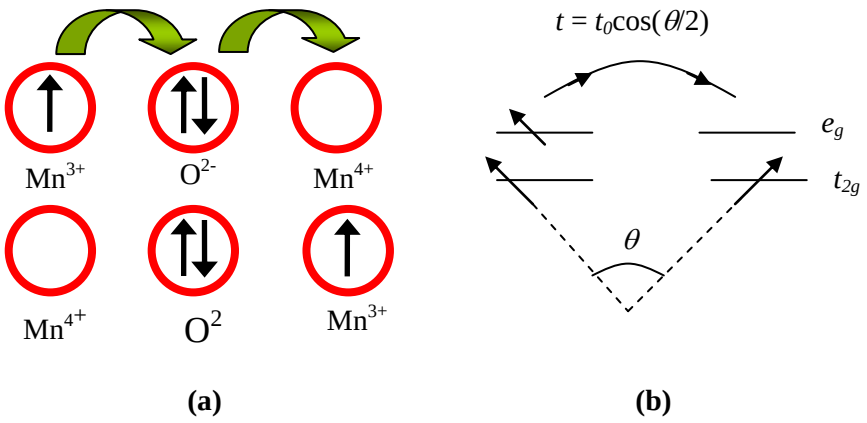

Fig. 1. 6 (a) A schematic diagram of the double exchange mechanism proposed by Zener and (b) relative configurations of the spin-canted states.

1. 2. 4 Superexchange interaction

The superexchange interaction mechanism was first proposed by Hendrik Kramers [14] in 1934 and was developed by Anderson in 1950. [15] This mechanism gives rise to antiferromagnetic interaction between cations which have half-filled or more-than-half filled *d*-shell and a ferromagnetic interaction between cations with less-than-half filled *d*-shell. Further, the interaction is antiferromagnetic when the half-filled *d*-orbitals (d_γ) of two cations overlap with a *p* orbital of O^{2-}. The angle between the orbitals is nearly 180^0 with respect to each other in the same plane for maximum overlap as can be seen in the Fig. 1.7. Whereas, the interaction is ferromagnetic if the *d* orbitals (d_γ) of the two cations overlapping with the anion p_σ orbital are such that one is half-filled and the other is empty. The Heisenberg Hamiltonian of the t_{2g} spins is given by

$$H_{SE} = J_{AF} \sum S_i . S_j$$

where, S_i represent the t_{2g} spin at site *i* and summation is over all the neighboring pairs <*ij*> and J_H is the antiferromagnetic interaction. In manganites of $RE_{1-x}AE_xMnO_3$ form, this J_H interaction is more dominant at and around x = 0 composition to stabilize antiferromagnetic phase. However, this interaction is negligible compared to Hund's rule coupling in ferromagnetic phase.

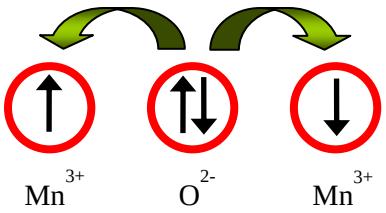

Fig. 1. 7 Schematic diagram of the superexchange interaction

1. 2. 5 Magnetic structure

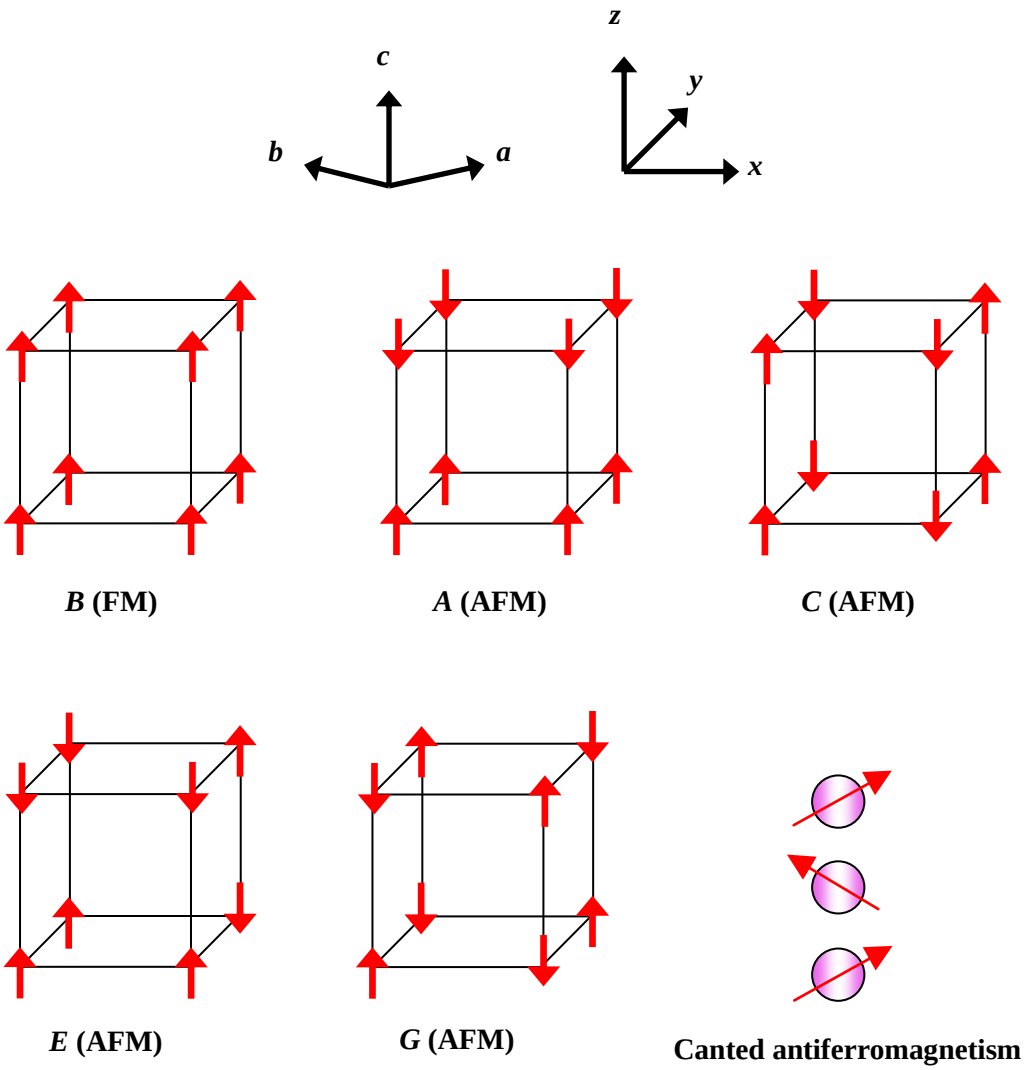

Fig. 1. 8 Different types of magnetic structures or modes found in manganites

The magnetic structure of manganites is determined by the competition between different magnetic interactions present in the system. While the double exchange interaction in manganites favors ferromagnetism, superexchange interaction favors antiferromagnetism. In manganites, superexchange antiferromagnetic interaction competes with ferromagnetic double exchange and this competition plays a major role in various properties. The first evidence for the complex spin structures due to mixed interactions was studied by Wollen and Kohler in $La_{1-x}Ca_xMnO_3$ ($0 \leq x \leq 1$) from neutron diffraction studies. [16] Some of the simplest magnetic ordering/modes exist in the perovskite structure are illustrated in Fig. 1.8. Mode *B* is ferromagnetic (FM), but all the other modes are antiferromagnetic (AFM). While

the modes *A*, *C* and *G* consist of oppositely aligned ferromagnetic planes of the type {001}, {110} and {111}, respectively. The mode *G* where each Mn-site is oriented antiparallel to its six neighbors will be favored by negative Mn-O-Mn superexchange interactions. The mode *A* is called layered antiferromagnet which has four parallel and two antiparallel neighbors, whereas, mode *C* and *E* each have four antiparallel and two parallel neighbors. The other magnetic mode is a composite *CE* mode which is composed of a chequerboard of alternating *C* and *E* blocks. The magnetic axis is indicated by a suffix *x*, *y* or *z* which are shown in Fig. 1.8. The magnetic modes can be combined for example, A_xB_z represents a canted antiferromagnet with the antiferromagnetic axis along *x* (≡ *a*) but with the net ferromagnetic moment along *z* (≡ *c*). The canted antiferromagnetism is also illustrated in Fig. 1.8.

1. 3 Colossal magnetoresistance (CMR) effect

Colossal magnetoresistance (CMR) effect is one of the interesting features of manganites. It refers to a dramatic change in the dc electrical resistance of a material in the presence of a magnetic field. The CMR is defined as,

$$CMR = \frac{\rho(H) - \rho(0)}{\rho(0)} \times 100\%$$

where, $\rho(0)$ and $\rho(H)$ are the resistivity values in zero and specific magnetic field, respectively. In undoped manganites, all the e_g and t_{2g} electrons are subject to electron repulsion interaction or the electron correlation effect and thus, they tend to localize to form so called Mott insulator. [17] The hole doping in manganites creates mobile Mn^{4+} such that e_g electrons become itinerant and play an important role in the electron conduction. Whereas, the t_{2g} electrons are stabilized by the crystal field splitting and become localized with spin (S = 3/2). In the case of strong Hund's coupling between the e_g conduction electron spin (S = 1/2) and t_{2g} localized spin, the effective hopping interaction of the conduction electron is expressed as, [13]

$$t_{ij} = t^0_{ij}\cos(\theta_{ij}/2).$$

According this relation, the ferromagnetic state is stabilized when the kinetic energy of the conduction electron is maximum (θ_{ij} =0). As discussed earlier, the metallic ferromagnetism is achieved due to hopping of e_g electron from Mn^{3+} ion to Mn^{4+} ion via oxygen as proposed by Zener in his double exchange mechanism. [12] However, the spins are dynamically disordered above or near by the ferromagnetic transition (T_C) which effectively reduces the hopping interaction and increases the resistivity. On the application of an external magnetic field, these local spins are relatively aligned and this results in an increase in the effective hopping interaction which in turn gives rise to colossal magnetoresistance around T_C in manganites.

The properties of hole-doped manganites of the general formula $RE_{1-x}AE_xMnO_3$ highly depend on the hole-doping level (x). [1] For instance, let us discuss the detailed magnetic and electronic ground states and transport properties of a canonical example of manganite, $La_{1-x}Sr_xMnO_3$ system. The hole-doping in $La_{1-x}Sr_xMnO_3$ increases the spin canting angle and favors the double exchange interaction in this system thereby transforming the canted antiferromagnetic phase ($x \leq 0.15$) to ferromagnetic phase ($x \geq 0.15$). [18] The ferromagnetic Curie temperature, T_C, of $La_{1-x}Sr_xMnO_3$ system increases dramatically up to x = 0.3 and then saturates. The detailed electrical transport properties of $La_{1-x}Sr_xMnO_3$ ($0 < x < 0.4$) has been studied by Urushibara *et al*. [19] by measuring the temperature dependence of resistivity (ρ).The system shows a semiconductor behavior ($d\rho/dT < 0$) above T_C for $x < 0.3$, but a metallic behavior ($d\rho/dT > 0$) is seen at low temperature below T_C. A scaling of magnetization with CMR effect for a single crystalline $La_{1-x}Sr_xMnO_3$ has been studied by Tokura *et al.*, [20] and the scaling function is given by

$$\Delta\rho/\rho = C(M/M_s)^2$$

where C is the effective coupling between the spins of itinerant e_g-holes and localized t_{2g}-electrons. In addition, it has been proposed by Majumdar and Littlewood in their phenomenological model [21] that the suppression of magnetic fluctuations by an external magnetic field can give rise to a large CMR in the wide bandwidth itinerant ferromagnets

such as $La_{0.7}Sr_{0.3}(Co, Mn)O_3$ and they predicted the occurrence of a large CMR around T_C and a negligible CMR for temperature away from T_C *i.e.*, $T << T_C$ and $T >> T_C$. The magnitude of CMR has a close relation to the magnetization even in polycrystalline samples and it shows a quadratic dependence as observed by Mahendiran *et al.* [22]

1. 4 Complex ordering phenomena and electronic phase separation

In manganites, electrons that localize on specific atomic sites frequently exhibit cooperative electronic ordering phenomena due to the strong correlation effect. These cooperative electronic ordering phenomena include charge order, orbital order and spin order and they are usually accompanied by magnetic, structural and metal-insulator phase transitions etc. Hence, electronic ordering phenomena in manganites play significant roles in controlling the fascinating physical properties and they are briefly explained below.

1. 4. 1 Charge ordering

Charge ordering is a phenomenon observed in solids which refers to the ordering of metal ions in different oxidation states in specific lattice sites of a mixed valent material. In such ordering, the electrons in the material generally localized which makes the material insulating or semiconducting because when the charges are localized, electrons cannot readily hop from one cation site to another. This phenomenon was first proposed by Eugene Wigner in the late 1930s and it was later applied to the transition that occurs in magnetite (Fe_3O_4) at T = 120 K by J. W. Verwey. [23], now known as the Verwey transition. The low-temperature ordered state in Fe_3O_4 is very complex which gives rise to low crystal symmetry (monoclinic or triclinic) and involves the distribution of Fe^{3+} and Fe^{2+} over several sites. Verwey suggested that the electrons belonging to Fe^{2+} and Fe^{3+} ions in Fe_3O_4 order themselves over octahedral sites coordinated by oxygen. It is found that the charge-ordered state below a Verwey transition is less conducting than the disordered state in which electrons can hop or tunnel from one cation site to the next.

Complex charge-ordering is also found in the several perovskite oxides such as $La_{1-x}Sr_xFeO_3$ [24] and quasi-two-dimensional $La_{2-x}Sr_xNiO_4$. [25] Complex charge-ordering in

manganites had been noticed by Wollan Kochler in 1955 and later by Jirak in 1985. [26, 27] The study of charge ordering in these manganites has recently received much attention because of the colossal magnetoresistance (CMR) exhibited by these materials. While the double-exchange interaction in rare earth manganites $RE_{1-x}AE_xMnO_3$ ($x \approx 0.3$) involving Mn^{3+}-O-Mn^{4+} units favors the metallicity and ferromagnetism, charge-ordering of the Mn^{3+} and Mn^{4+} ions favors antiferromagnetism and insulating behavior. Charge ordering competes with double exchange interaction which gives rise to an unusual range of properties that are sensitive to factors such as the size of *A*-site cations. Whereas, the cooperative Jahn-Teller effect induces additional effects such as lattice distortion and electron localization in the charge-ordered state. Chen and Cheong [28] observed the charge ordering in $La_{0.5}Ca_{0.5}MnO_3$ by using electron microscopy for the first time. The $La_{0.5}Ca_{0.5}MnO_3$ compound undergoes two transitions on cooling: first one is the ferromagnetic transition around T = 220 K with conducting state and second one is the antiferromagnetic transition around T = 160 K with insulating state. At this antiferromagnetic transition, the Mn^{3+} and Mn^{4+} ions were thought to adopt the charge ordered chequerboard arrangement [29] as shown in Fig. 1.9(a). A pattern of orbital ordering also exists independent of the charge ordering [30] as shown in the Fig. 1.9(b) and 1.9(c), and it is discussed below.

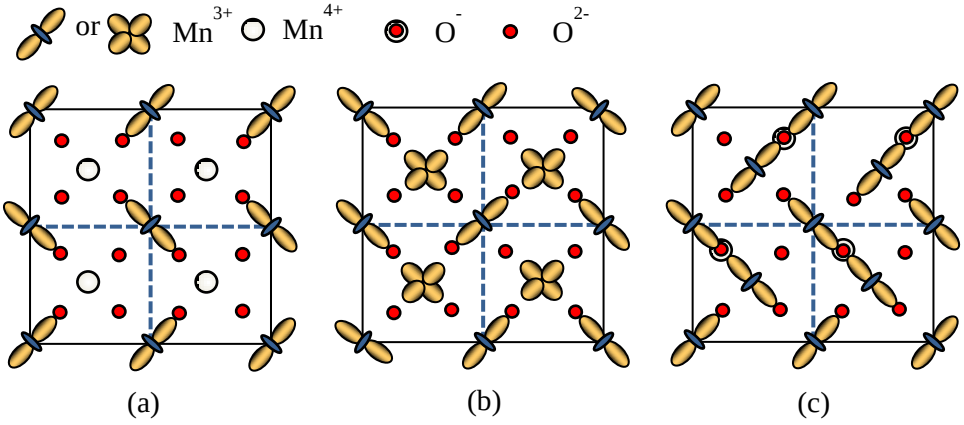

Fig. 1. 9 (a) The chequerboard charge-ordered arrangement of Mn^{3+} and Mn^{4+} ions, originally proposed for $La_{0.5}Ca_{0.5}MnO3$ by Goodenough. [29] (b) A pattern of orbital order for Mn^{3+} ions [31] (c) The ordered arrangement of O^- ions between Mn^{3+} pairs in the Zener polaron model. [32, 33, 34].

1. 4. 2 Orbital ordering

Orbital ordering refers to the development of a long-range ordered pattern of occupied orbitals due to a preferential occupation of specific *d* orbitals on the transition metal. The orbital ordering plays an important role in the CMR effect and it gives rise to anisotropy of the electron-transfer interaction. This favors or disfavors the double-exchange interaction (ferromagnetic) and the superexchange interaction (antiferromagnetic) in an orbital direction dependent manner and thus, it gives a complex spin-orbital coupled state. The orbital ordering phenomenon is usually observed indirectly from the cooperative Jahn-Teller distortions that result as a consequence of the orbital order [35] and vice versa. Many compounds in manganites show this orbital ordering at low temperature. For example, at the antiferromagnetic transition of $La_{0.5}Ca_{0.5}MnO_3$, the single e_g electron of Mn^{3+} can occupy one of the two e_g orbitals due to the Jahn-Teller effect, forming an orbital ordering pattern as shown in Figs. 1.9(b)-(c). In $La_{0.5}Ca_{0.5}MnO_3$ where the ionic radius of Ca is less than that of Sr, it is expected that the doping introduces more distortion into the crystal structure. Thus, instead of a typical double exchange behaviour observed in the Sr doped manganite, both charge and orbital ordering is observed in $La_{0.5}Ca_{0.5}MnO_3$. In half-doped manganites, an important ordering configuration occasionally emerging is the *CE*-type, in which both orbital and charge ordering occur simultaneously for example, $Pr_{0.5}Ca_{0.5}MnO_3$ [36] and it is shown in Fig 1.10. The structural features of these charge/orbital ordering is investigated by transmission electron microscopy for example, in single-layered manganites $Pr_{1-x}Ca_{1+x}MnO_4$. [37]

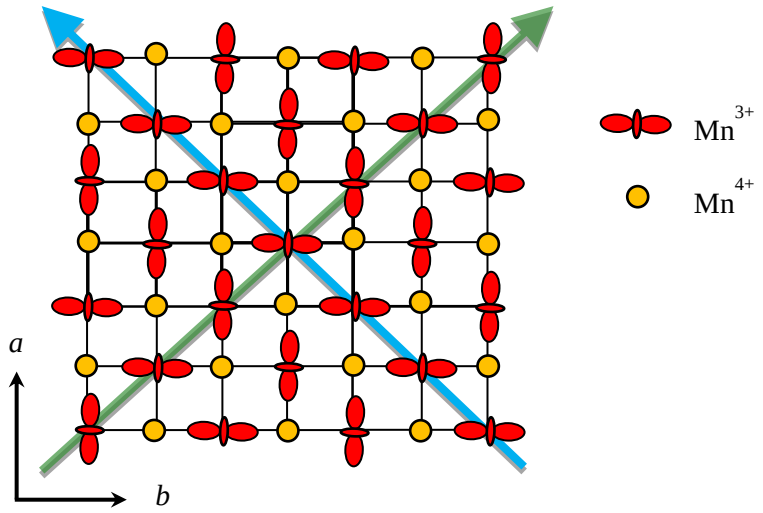

Fig. 1. 10 Schematic picture of the orbital [$(3x^2 - r^2)/(3y^2 - r^2)$] and charge order of the *CE*-type projected on the MnO_2 sheet (*ab* plane). [38]

1. 4. 3 Electronic phase separation

Phase separation in manganites refers to the co-existence of two or more phases such as charge and orbital ordering in a single compound. The most relevant examples of phase separated compounds are the cuprates at the hole- densities in the under-doped region and the manganites in the regime of colossal magnetoresistance (CMR). [39] The phase separation is generally due to the result of competition between charge localization and delocalization, both of which are associated with contrasting electronic and magnetic properties. While the inhomogeneities in cuprates occur due to phase competition between antiferromagnetic insulating and superconducting or metallic phases, in manganites it arises due to phase competition between ferromagnetic metallic and charge-ordered insulating phases. These microscopic and intrinsic inhomogeneities are the driving factors for the phase separation in hole-doped manganites. [40, 41] Nagaev *et al.*, [42] observed the existence of phase separation in an antiferromagnetic semiconductor where the ferromagnetic phase is embedded in the antiferromagnetic matrix. Interestingly, phase separation covers a wide range of length scales from 1 - 200 nm and it can be either static or dynamic in nature. [40]

In manganites, the existence of phase separation leads to interesting electronic and magnetic properties. The double-exchange mechanism of electron hopping between the Mn^{3+}

and Mn^{4+} ions favors the ferromagnetic metallic phase below T_C and the paramagnetic insulating state above T_C. Whereas in the insulating state, the Jahn–Teller distortion associated with the Mn^{3+} ions localizes the electrons and favors the charge ordering of Mn^{3+} and Mn^{4+} ions. In some manganites, the competition between the charge ordering and double exchange interaction promotes the antiferromagnetic insulating behavior, and hence there is a coexistence of both charge order antiferromagnetic and ferromagnetic clusters. [43, 40] The coexistence of ferromagnetic metallic clusters/domains and the insulating antiferromagnetic phase lead to different charge densities and transport properties and it is generally known as the electronic phase separation. These electronic phase separation gives rise to microscopic or mesoscopic inhomogeneous distribution of electrons which results in rich phase diagrams that involves various types of magnetic structures. There are few clear evidences of presence of these electronic phase separation in several rare earth manganites. [40] Neutron diffraction study in $La_{1-x}Ca_xMnO_3$ by Wollan and Koehler [44] has revealed the coexistence of ferromagnetic and *A*-type antiferromagnetic (layered antiferromagnet) reflections. Using the transmission electron microscopy, Uehera *et al.*, [45] found the coexisting domains of charge order insulating and ferromagnetic metallic phases of size 500 nm in $La_{5/8-y}Pr_yCa_{3/8}MnO_3$ for y = 0.375 at T = 20 K. The coexistence of inhomogeneous clusters of metallic and insulating phases has also been investigated by Fath *et al.*, [46] employing scanning tunneling spectroscopy study. Now let us discuss the melting of charge and orbital ordering in manganites by external parameters such as magnetic and electric fields, pressure, photon and electron irradiation. [1, 47] Kuwahara *et al.* [48] observed the magnetic field-induced melting of charge ordered state in $Nd_{0.5}Sr_{0.5}MnO_3$ and hence, a huge magnetoresistance is also observed. The delocalization of charge ordered state due to irradiation by visible light has been observed by Miyano and Fiebig. [49, 50] Fiebig *et al.*, [50] observed the light-induced insulator-metal transition in $Pr_{0.7}Ca_{0.3}MnO_3$ and showed that the resistance of this compound decreases from GΩ value to metallic one. This dramatic change in resistivity of CMR compound due to irradiation of light may be useful in the construction of optical switches.

1. 5 Giant magnetoimpedance (GMI) effect

Giant magnetoimpedance effect refers to a large change in the complex impedance of a soft ferromagnetic conductor carrying a small alternating current (ac) in response to external magnetic field. The complex electrical impedance of a magnetic material is a function of angular frequency (ω) and applied magnetic field (H) and it is expressed as:

$$Z(\omega,H) = R(\omega,H) + iX(\omega,H)$$

where, R is the ac resistance and X is the reactance. The magnetoimpedance (*MI*) is the relative change of impedance with applied magnetic field and it is defined as:

$$MI = \frac{\Delta Z}{Z} = \frac{Z(H) - Z(0)}{Z(0)} \times 100\%$$

where *Z(0)* and *Z(H)* are the values of impedance in zero and external dc magnetic field, respectively. Thus, the magnetoimpedance is nothing but the ac electrical transport measurement under the external magnetic field which we call as 'ac magnetotransport'.

The discovery of giant magnetoimpedance (*GMI*) in metal-based amorphous alloys [51, 52, 53] has attracted particular interest in the scientific community to develop the high-performance magnetic sensors based on GMI effect as it offers several advantages over conventional magnetic sensors such as fluxgate sensors, Hall effect magnetic sensors, giant magnetoresistive (GMR) sensors, and superconducting quantum interference device (SQUID) gradiometers [53]. The decisive factor is the ultra-high sensitivity of GMI sensors which is as high as 500%/Oe compared to a GMR sensor (~1%/Oe). [53] The GMI sensors have wide applications over other magnetic sensors because of its low cost and high flexibility. However, a thorough understanding of the GMI phenomena and the best utilization of GMI effect for technological applications are very much needed in order to design and produce practical GMI sensors. Hence, many efforts have been put, mainly on special thermal treatments and/or on the development of new materials for the improvement of GMI

properties. [54, 55, 56] Table 1.1 compares the different magnetic sensors including the GMI sensor. [53]

Types of sensor	Head length	Detectable field range (Oe)	Response speed	Power consumption
Hall	10-100 μm	$1 - 10^{6}$	1 MHz	10 mW
GMR	10-100 μm	$0.1 - 10^{2}$	1 MHz	10 mW
Flux gate	10-20 mm	$10^{-6} - 10^{2}$	5 kHz	1 W
GMI	1-2 mm	$10^{-8} - 10^{2}$	1-5 MHz	10 mW

Table 1. 1 A comparison of different magnetic sensors

1. 5. 1 Fundamental aspects of GMI

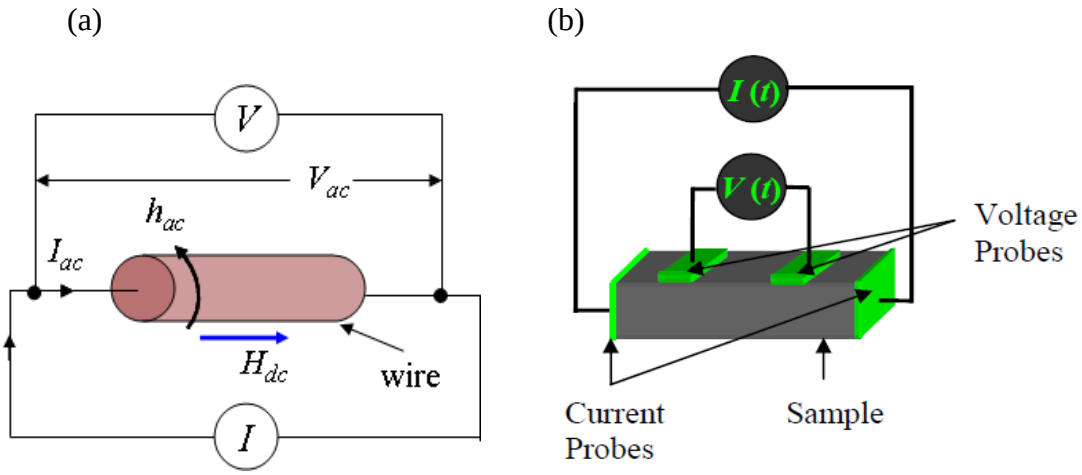

Fig. 1. 11 (a) The definition of the impedance of a current carrying conductor (b) Schematic diagram of the impedance measurement in four probe configuration

The complex impedance of a magnetic conductor carrying a sinusoidal current $I = I_{ac}e^{-i\omega t}$ is given by,

$$Z = R + iX = R + i\omega L = \frac{V_{ac}}{I_{ac}}$$

where, R is the ac impedance, X is the reactance, L is the self-inductance of the sample which reflects in X, I_{ac} is the amplitude of the sinusoidal current and V_{ac} is the voltage measured between the ends of the conductor. Fig. 1.11(a) shows a schematic illustration of the

definition of the electrical impedance and Fig. 1.11(b) shows the schematic diagram of the impedance measurement in four probe configuration. The above definition of impedance is valid only for a uniform magnetic conductor [57] and the expression for the impedance of a magnetic conductor with fixed shape can be given as described below.

Assuming a linear approximation, expression for the impedance of a metallic ferromagnet with length l and cross-sectional area A can be expressed as,

$$Z = \frac{lE_z(S)}{A\langle j_z \rangle_A} = R_{dc}\frac{j_z(S)}{\langle j_z \rangle_A},$$

Where, R_{dc} is the dc electrical resistance, E_z and j_z are the longitudinal components of the electric field and current density respectively, S denotes the value at the surface, and $< >_A$ is the average value over the correctional area A.

From the classical electrodynamics of continuous media, the current density $j(r)$ can be obtained by solving the Maxwell equation,

$$\Delta^2 H - \frac{\mu_0}{\rho}\dot{H} = \frac{\mu_0}{\rho}\dot{M} - \nabla(\nabla.M)$$

where, M is the magnetization of the magnetic conductor.

The ac components of the magnetic field and magnetization can be obtained by separating the vectors H and M into their dc and ac components by writing $H = H_0+h$ and $M = M_0+m$ assuming h, $m \propto e^{i\omega t}$ as follows:

$$\Delta^2 h - \frac{2i}{\delta_0^2}h = \frac{2i}{\delta_0^2}m - \nabla(\nabla.m),$$

where $\delta_0 = \sqrt{\frac{2\rho}{\omega\mu_0}}$ is the nonmagnetic skin depth. The classical skin effect solution of above equations is obtained [58] and the impedance equations for a cylindrical magnetic conductor of diameter $2a$ and an infinite planar film of thickness $2t$ can be written as,

$$\frac{Z}{R_{dc}} = ka\frac{J_0(ka)}{2J_1(ka)}$$

and

$$\frac{Z}{R_{dc}} = ikt\coth(ikt)$$

where J_0 and J_1 are the Bessel functions of the first kind, R_{dc} is the dc electrical resistance and $k = (1 + i)/\delta$ where δ is the skin depth in a magnetic medium and can be defined as below.

Let us suppose j is the alternating current density in a magnetic conductor which decreases exponentially from its value at the surface, j_s, to the depth d from the surface as,

$$j = j_S e^{-d/\delta}$$

where, $\delta = \sqrt{\frac{2\rho}{\omega\mu_0\mu_r}}$ with ρ is the resistivity of the conductor, ω is the angular frequency, μ_0 and μ_r are the magnetic permeabilities of the vacuum and conductor, respectively. Thus, the skin depth is the depth below the surface of a conductor at which the current density has fallen to $1/e$ of j_s. The impedance of a sample is determined by its resistance and reactance both of which are influenced by the skin effect. The application of an external magnetic field decreases the permeability of the sample which increases the skin depth leading to a giant magnetoimpedance in magnetic conductors.

In the later part of this thesis, we have paid much attention to the investigation of electrical impedance of few selected metallic and semiconducting ferromagnetic manganites in response to external magnetic field or in other words, we have investigated the ac magnetotransport in few selected manganites in detail. Since the discovery of colossal magnetoresistance in the manganites a decade ago, numerous studies have been focused on the magnetotransport of these oxides measured with direct current (dc). [59] Although there are some ac electrical transport studies in the frequency range f = 1-100 kHz aimed to investigate dielectric relaxation effect or to probe possible ME coupling in capacitance structure, [60, 61, 62] ac electrical response of the manganites in the radio frequency (*rf*) range (f = 1-30 MHz) using four-probe method has been scarcely studied. [63, 64, 65, 66] Despite the fact that dc magnetoresistance ($\Delta R/R$) of manganites can reach nearly 100% in a field of $\mu_0 H$ = 5-7 T, it is rather small ($\Delta R/R$ < 5%) in a field of few hundred Gauss. Thus, it is

imperative to increase the magnitude of the magnetoresistance at low magnetic fields if at all manganites can be useful for device applications. In this context, a huge low-field microwave magnetoresistance ($\Delta R/R$ = 80% in H = 600 G and f = 9.8 GHz) observed in $R_{0.67}B_{0.33}MnO_3$ (R = La, Nd, B = Sr, Ba) by Lofland and coworkers [67] are very interesting. The origin of microwave magnetoresistance in manganites is believed to be related to decrease of the dynamical complex permeability, $\mu(\omega)$, under an external magnetic field. The dynamical permeability affects the surface impedance ($Z = (1+i)\rho/\delta$) of the sample through change in the electromagnetic penetration depth (δ) and hence it affects the micro wave absorption. [68] In the forthcoming chapters, we present our results on ac magnetotransport in few selected manganites which we have studied in the frequency range f = 100 kHz - 20 MHz by the simultaneous measurements of ac resistance (R) and reactance (X). These results demonstrate that ac magnetotransport is a powerful tool in detecting the magnetic transition as well as the structural transition in doped manganites and also to enhance the ac magnetoresistance.

1. 6 Magnetoabsorption

Magnetoabsorption refers to a large change in electromagnetic absorption by a magnetic material under an external magnetic field. The electromagnetic absorption in magnetic materials is very interesting due to the fact that it is related to the several factors such as hysteresis losses, eddy current losses and the loss due to the flux motion in magnetic and high *Tc* superconductors. [69] The study of *rf* magnetoabsorption related with the power dissipation in magnetic materials is currently attracting much attention from both fundamental and application points of view as many physical phenomena are observable at radio frequencies. The exploration of several effects in *rf* range, which are not accessible at lower frequencies, include nuclear magnetic resonance (NMR), electron paramagnetic resonance (EPR), relaxation processes such as spin-spin and spin-lattice relaxations, domain wall resonance and also the probing of resistivity through the normal state skin effect. The electromagnetic absorption is studied by measuring the skin depth or penetration depth (δ)

using a method originally devised by Schawlow and Devlin. [70] In ferromagnetic metals, the magnetoabsorption is influenced not only by the conductivity, but also by the magnetic permeability (μ) of absorbing media. Thus, the *rf* magnetoabsorption *i.e.*, the attenuation of an oscillating electromagnetic field, is due to the skin effect. On the application of a magnetic field, there is a considerable decrease in the permeability of a magnetic material near the magnetic transition which causes increase in the skin depth, and hence a giant magnetoabsorption occurs around the magnetic transition. The magnetoabsorption is fairly large only for optimal frequency range to assure that δ is smaller than the sample dimensions [71] and the magnitude of μ_r of a magnetic materials in zero magnetic field should be high enough. But it is well known fact that the value of μ_r in ferromagnetic metals decreases with increasing frequency and goes close to unity for $f > 100$ MHz [72] and hence, a ferromagnetic metal behaves like a non-magnetic one at very high frequency. Therefore, the optimal frequency for the observation of a giant magnetoabsorption should be of the order of $f \sim 1$ MHz and it is in the *rf* range. In this context, a self-oscillating LC circuit driven by a tunnel diode (TD) or integrated circuit (IC) which oscillates at $f \sim 1$ MHz should be an ideal choice for the magnetoabsorption studies.

The *rf* magnetoabsorption is considered to be a promising contactless technique to study a wide range of physical properties of Mn-based oxides. There are few reports of magnetoabsorption properties of manganites, which have studied using LC oscillator circuit powered by either tunnel diode or integrated circuit, are listed down here. Frank J. Owen [73] observed that the resonance frequency of a tunnel diode powered *LC* tank circuit with inductor loaded with $La_{0.7}Sr_{0.3}MnO_3$ sample showed a large change of -53% in $\Delta f_r/f_r$ under $\mu_0 H = 0.2$ T at $f_r = 350$ kHz around T_C. Here, $\Delta f_r = f_r(T,H) - f_r(T,0)$ is the difference between the resonance frequency of the tank circuit at a given temperature with and without magnetic field ($\mu_0 H$). Interestingly, a giant *rf* magnetoabsorption of 67% at $f = 2.525$ MHz and $H = 1$ kG around the Curie temperature (T_C) has also been observed in $La_{0.67}Sr_{0.33}MnO_3$ single crystal. [74] From the dynamic experiment employing tunnel diode oscillator (TDO), Woods

et al. [75] showed that the *rf* contactless method is useful in detecting the magnetic anomaly due to polaron ordering below the long range ferromagnetic ordering in $La_{0.85}Sr_{0.15}MnO_3$. The large fractional shift in the resonance frequency was attributed to changes in the magnetic penetration depth ($\Delta\delta / \delta \propto -\Delta f_r / f_r$). Srikanth *et al*. [76] found a small change of 4% in $\Delta f_r/f_r$ at $\mu_0 H$ = 2 T and T = 100 K in $Nd_{0.7}Ba_{0.3}MnO_3$. Apart from the change in the resonance frequency (f_r) of the oscillator, the *rf* current through the resonance circuit powered by integrated circuit (IC) containing inductor loaded with $La_{0.7}Sr_{0.3}MnO_3$ sample also changes with the applied magnetic field and temperature as observed by Sarangi *et al*. [77] In the later part of this thesis, we have presented our results of *rf* magnetoabsorption studies in few selected manganites by measuring both current and resonance frequency of IC oscillator circuit simultaneously as a function of temperature and magnetic field. We demonstrate that IC oscillator circuit is a powerful technique to study the magnetic and structural transitions in manganites as well as to investigate the *rf* magnetization dynamics in manganites.

1. 7 Magnetocaloric effect (MCE)

A MCE refers to the reversible change in the adiabatic temperature (ΔT_{ad}) of a magnetic material when it is exposed to a varying magnetic field (H). The MCE is also known as adiabatic demagnetization due to the application of this process specifically to create a temperature drop. The MCE was discovered in iron in 1881 by E. Warburg. [78] Debye [79] and Giauque [80] have independently explained the origin of MCE and they have also suggested the first practical use of the MCE to achieve temperature lower than the liquid helium temperature. In recent years, magnetic refrigeration (MR) based on MCE is emerging as an alternative technique to conventional vapour-compression refrigeration due to its potential impact on energy savings (20% less) and environmental concerns. [81] Hence, there is a resurgence of interest in magnetic refrigeration following the discovery of a large MCE in $Gd_5(Ge_{1-x}Si_x)_4$ alloys. [81] Magnetic refrigeration makes use of solid refrigerants (magnetic materials) instead of environmentally harmful gases and is considered to be more energy efficient than the conventional vapor compression based refrigeration. The MCE is quantified

by the adiabatic change in temperature of sample (ΔT_{ad}) or isothermal change in the magnetic entropy (ΔS_m) when the sample is subjected to a changing magnetic field (H). While some paramagnetic salts are already being used to obtain temperatures below 1 K, new materials exhibiting large ΔS_m and ΔT_{ad} values are currently in demand for applications at ambient temperature as well as for continuous cooling from 300 K down to 10 K. The MCE is greatly enhanced in first-order magnetic phase transitions that are coupled to structural transitions. A large magnetic entropy change due to field-induced first-order ferromagnetic transition has been reported in $MnFeP_{0.45}As_{0.55}$ [82] and Ni-Ga-Mn [83] alloys.

The physical origin of the MCE is the coupling of the magnetic sublattice to the applied magnetic field, H, which changes the magnetic contribution to the entropy (S) of the solid. The total entropy of a magnetic material at constant pressure (P) is given by:

$$S(T, H) = S_m(T, H) + S_l(T, H) + S_e(T, H)$$

where, S_m is the magnetic entropy, S_l is the lattice entropy and S_e is the electron entropy. Under isothermal condition, the magnetic domains will be aligned in the field direction upon application of the external magnetic field and hence magnetic entropy decreases. The total entropy of a system remains constant in an adiabatic condition *i.e.*, there is no exchange of heat with the environment. Hence, both the lattice and electron entropy will have to increase in order to compensate the decrease in the magnetic entropy and this in turn makes the temperature of a magnetic material to increase.

1. 7. 1 Indirect and direct methods of estimating the MCE

The MCE is quantified by two important parameters: 1. Isothermal magnetic entropy change (ΔS_m) and 2. Adiabatic temperature change (ΔT_{ad}). There are two important methods of estimating the ΔS_m and ΔT_{ad} values: 1. Indirect method in which one makes use of Maxwell's thermodynamical equations to estimate the ΔS_m and ΔT_{ad} values and 2. Direct method in which both ΔS_m and ΔT_{ad} values are estimated experimentally from the differential scanning calorimetry (DSC) and differential thermal analysis (DTA), respectively.

Let us first discuss the indirect way of estimating the ΔS_m and ΔT_{ad} values using the magnetic method. We can derive the expressions for both ΔS_{m} and ΔT_{ad} from the Maxwell thermodynamical relations as follows. The magnetic entropy is related to the magnetic properties of the materials through the Maxwell relation,

$$\left[\frac{\partial S_M(T,H)}{\partial H}\right]_T = \left[\frac{\partial M(T,H)}{\partial T}\right]_H$$

The change in the magnetic entropy, $\Delta S_m(T, H)$, is calculated by

$$\Delta S_m(T,H) = S_m(T,H) - S_m(T,0)$$

$$= \int_0^H \left(\frac{\partial M(T,H)}{\partial T}\right)_H dH$$

From the set of isothermal magnetization versus field data taken, the magnetic entropy change is estimated using the numerical approximation to the above equation as:

$$\Delta S_m = \sum_i \frac{M_i(T_i,H) - M_{i+1}(T_{i+1},H)}{T_i - T_{i+1}} \Delta H$$

where, M_i and M_{i+1} are the magnetization values measured at temperatures T_i and T_{i+1}, respectively for a magnetic field interval of ΔH.

On the other hand, $\Delta S_m(T, H)$ can also be obtained from the calorimetric measurements of field dependence of the specific heat capacity, $C(T, H)$, using the relation,

$$\Delta S_m(T,H) = -\int_0^T \frac{C(T,H) - C(T,0)}{T} dT$$

where, $C(T, H)$ and $C(T, 0)$ are the values of the specific heat measured in a field H and zero field, respectively. From the above equations, the change in adiabatic temperature is given by,

$$\Delta T_{ad} = -\int_0^H \frac{T}{C_{P,H}} \left(\frac{\partial M}{\partial T}\right) dH$$

On the other hand, in direct estimation of ΔS_m using DSC method, the absorption or emission of heat during phase transition in the sample while sweeping the magnetic field at a fixed base temperature leads to a differential voltage across the Peltier cells, which is

measured in the experiment. The field dependence of the heat (dQ/dH) evolved during the magnetic phase transition is then evaluated at different temperatures by using the sensitivity of the Peltier cells and the field sweep rate (dH/dt). The latent heat (L) and the magnetic entropy change (ΔS_m) are obtained from the integration of dQ/dH curves using the following relations,

$$L = \int_{H_i}^{H_f} \frac{dQ}{dH} dH; \quad \Delta S_m = \frac{L}{mT}$$

where, H_i and H_f are the initial and final fields of the transition and m is the mass of the sample. [84] Using DTA measurement, the change in temperature (ΔT) of a sample during the field induced magnetic transition can directly be measured by the temperature sensor placed on the surface of a magnetic material. [85]

For magnetic refrigerator applications, a material which shows a giant MCE is expected. This can be achieved in a material which shows a large $(\delta M/\delta T)_H$ (a large change in magnetization occurs in a narrow temperature change) and small $C(T, H)$ at the same temperature. [86] Besides the large values of ΔS_m and ΔT_{ad}, the temperature span over which ΔS_m spreads is important for practical application and this is measured by the quantity known as the refrigeration capacity (RC). The RC is calculated using the equation,

$$RC = \int_{T_2}^{T_1} \Delta S_m(T) dT$$

where T_1 and T_2 are the temperatures corresponding to extremum values of half-maximum of the $\Delta S_m(T)$ peak around T_C.

1. 7. 2 Normal and inverse MCEs

There are mainly two kinds of MCEs depending upon the materials response to applied magnetic field. The materials which show paramagnetic-to-ferromagnetic transition exhibit the decrease of magnetic entropy *i.e.*, $\Delta S_m = S_m(H) - S_m(0)$ is negative, under the magnetic field and the effect is called 'normal MCE'. Most of the ferromagnetic compounds show normal MCE which cool upon the removal of a magnetic field or upon the adiabatic

demagnetization. In contrast to ferromagnets, the materials which undergo paramagnetic-to-antiferromagnetic transition exhibit the increase of magnetic entropy under the magnetic field *i.e.*, $\Delta S_m = S_m(H) - S_m(0)$ is positive, and the effect is called 'inverse MCE'. Thus, the antiferromagnets cool upon the application of a magnetic field or upon the adiabatic magnetization. The materials which show the coexistence of both normal and inverse MCEs are in high demand as it can be used to enhance refrigerant capacity (RC) as it is cooled by both adiabatic magnetization as well as demagnetization. [87] Generally, inverse MCE is seen in the antiferromagnetic compounds. However, the metallic alloys which undergo a martensitic transition *i.e.*, from austenite-to-martensite phase transition, also show a giant inverse MCE for example, $Ni_{50}Mn_{34}In_{16}$ alloy shows an inverse MCE around the martensitic transition below the ferromagnetic transition temperature. [88]

Let us now give a brief note of MCE observed in manganites. A comprehensive review of the MCE in manganites can be found in a recent review by Phan and Yu. [89] The manganites are considered to be promising candidates for magnetic refrigeration due to several reasons:

1. They can be easily prepared by solid state or wet chemical routes at low cost.
2. The magnetic transition can be easily tuned over a wide temperature range (400-10 K) by controlling the hole-doping (x) or the average ionic radii ($<r_A>$) of the *A* site cations.
3. Apart from the magnetic transitions, they also exhibit structural transition in the vicinity of magnetic transition that could influence the MCE because of unusual strong coupling between lattice and magnetic degrees of freedom. [90, 91]
4. These materials exhibit both normal and inverse MCEs in a single material due to coexistence of both ferromagnetic and antiferromagnetic transitions, respectively thus, it increases the efficiency of the magnetic refrigerator. [92, 93]

In the forthcoming chapters, we present our results of MCE investigated in few selected manganites which reveal the coexistence of both normal and inverse MCEs in a single compound with excellent magnetocaloric properties.

1. 8 Multiferroic materials

1. 8. 1 A brief introduction to multiferroics

Multiferroics are materials in which two or more ferroic orders coexist such as ferromagnetism, ferroelectricity and ferroelasticity. Although the class of multiferroic materials includes compounds with two or more ferroic orders, the current trend has made it to extend to non-primary order parameters, such as antiferromagnetism or ferrimagnetism. [94] In some multiferroics, symmetry consideration allows coupling between the electrical and magnetic dipole moments and these materials are generally termed as magnetoelectric (ME) multiferroics. The ME multiferroic materials which show a strong coupling between ferromagnetic and ferroelectric order parameters are promising for applications in new kind of multistate nonvolatile memories such as magnetically tunable ferroelectric random access memories (FeRAMs), electrically tunable magnetic random access memories (MRAMs) and high frequency filters etc. [94, 95, 96, 97, 98] Fig.1.12 shows the relationship between multiferroic and ME materials. [94] Ferromagnets form a subset of magnetically polarizable materials such as paramagnets and antiferromagnets. In the similar way, ferroelectrics form a subset of electrically polarizable materials such as paraelectrics and antiferroelectrics. The red lines represent multiferroic materials which is a coexistence of both ferromagnets and ferroelectrics. The circle with blue lines represents the ME materials in which ME coupling is an independent phenomenon that can, but need not to arise in any of the materials that are both magnetically and electrically polarizable.

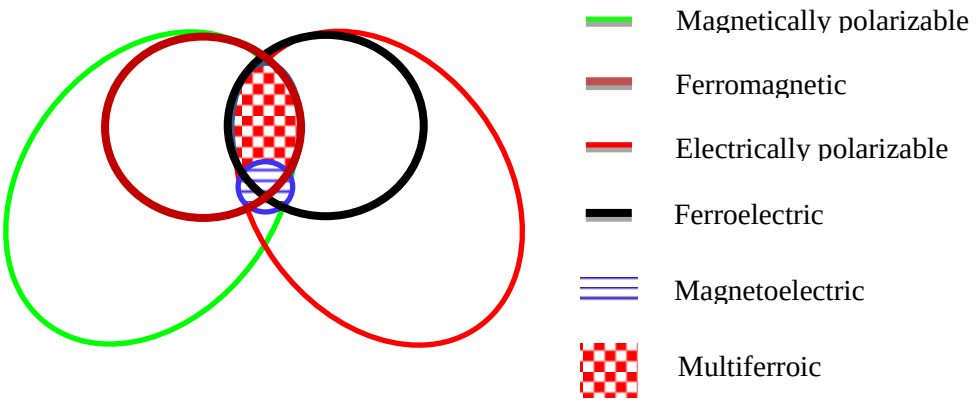

Fig. 1. 12 A schematic diagram which shows the relationship between the multiferroic and ME materials.

1. 8. 2 A bit of history

The field of linear magnetoelectrics and multiferroics research has been "revived" from 2000 onwards after 30 years of limited activity, and it has attracted researchers from both magnetism and ferroelectricity backgrounds, since it involves both ferroelectric and magnetic properties of matter. Such 'ME multiferroics' were studied up to some extent in the 1960s and 1970s [99] and the term *multiferroic* was coined relatively late in 1994 by H. Schmid. [100] However, the study of multiferroics languished because the single-phase materials with both properties could not be widely produced since ferromagnetism requires d-electrons while ferroelectricity generally occurs only in the absence of d-electrons. The field of multiferroics has attracted great interest and opened the door to the design of practical devices based on ME coupling only after the following three main developments:

1. The production of high quality single crystalline samples has led to the identification of new types of multiferroics. [101, 102]

2. The improved first-principle computational techniques have aided in the design of new multiferroics and provided the understanding of factors that promote the coupling between magnetic and ferroelectric order parameters. [103, 104]

3. Advances in the thin film growth techniques have provided routes to structures and phases that are inaccessible by traditional chemical means. [105]

Fig. 1.13 shows a classification of insulating oxides, which display different

properties as discovered by various research groups during the past few years. [106] This classification is based on the schematic diagram shown in Fig. 1.12. The largest circle represents all insulating oxides which includes electrically polarizable materials (red color ellipse) and magnetically polarizable materials (green color ellipse). The circle within each ellipse represents materials with a finite polarization (ferroelectrics) and a finite magnetization (ferromagnets, antiferromagnets and ferrimagnets). The multiferroic materials correspond to the intersection between the ellipses. A small circle in the middle denotes the system of materials, which exhibits ME coupling.

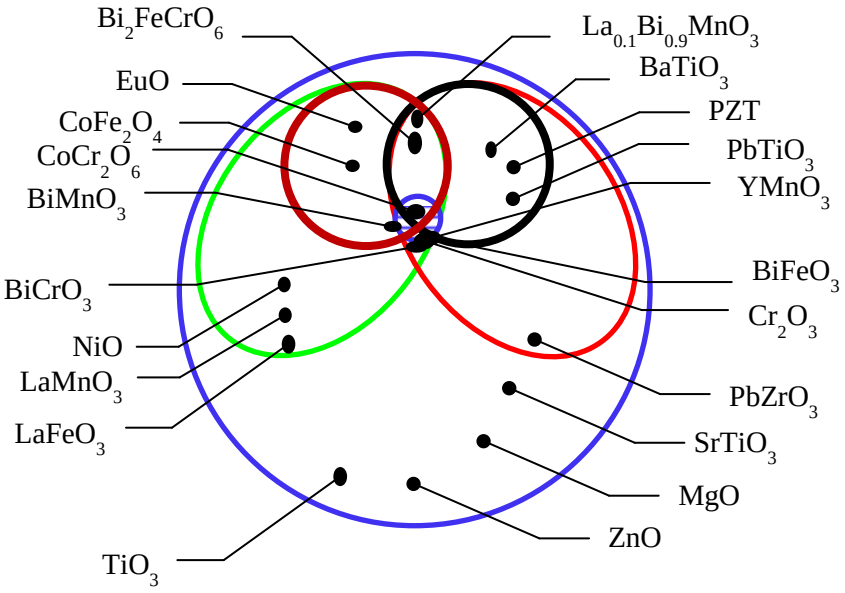

Fig. 1. 13 Classification of insulating oxides

1. 8. 3 Magnetoelectric (ME) effect

The ME effect is the phenomenon in which the magnetic (electric) polarization can be tuned by applying an external electric (magnetic) field. The ME coupling between magnetic and electric dipole moments can be linear or/and non-linear with respect to the external fields. The ME effect in a crystal is described in Landau theory by writing the free energy, *F*, of the system in terms of applied electric $\vec{E}$ and magnetic $\vec{H}$ fields as follows:

$$-F(\vec{E},\vec{H}) = F_0 - P_i^S E_i - M_i^S H_i - \frac{1}{2}\varepsilon_0\varepsilon_{ij}E_iE_j - \frac{1}{2}\mu_0\mu_{ij}H_iH_j$$

$$-\alpha_{ij}E_iH_j - \frac{1}{2}\beta_{ijk}E_iH_jH_k - \frac{1}{2}\gamma_{ijk}H_iE_jE_k - ...$$

where, $\vec{P}^S$ and $\vec{M}^S$ are the spontaneous polarization and magnetization, ε and μ are the electric and magnetic susceptibilities, α is the tensor which corresponds to induction of polarization by a magnetic field or of magnetization by an electric field that refers to the linear ME effect, β and γ are the tensors correspond to higher order ME effects. The majority of research on the ME effect is devoted to linear ME effect and thus, the 'ME effect' generally refers to the linear ME effect. The size of the ME effect depends on the microscopic mechanism involved in the system. Unfortunately, the ME effect is usually small as the term α_{ij} is limited by the relation:

$$\alpha_{ij}^{\ 2} \leq \varepsilon_{ij}\mu_{ij}\,.$$

In an actual ME experiment, the voltage developed across the sample surface is measured in response to a small ac magnetic field. The ME coefficient (α) is expressed as:

$$\alpha = \frac{dE}{dH} = \frac{1}{t}\frac{dV}{dH}$$

where, V is the induced ME voltage appeared across the sample, H is the dc bias field and t is the thickness of the sample. The SI-unit of α is [s/m] which can be expressed in the practical unit: V/(cm Oe). A comprehensive summary of the ME effect in various single phase and composite materials can be found in a recent review by M Fiebig. [107] The ME effect is observed in single phase materials such as Cr_2O_3, [108] $GaFeO_3$, [109, 110] Ti_2O_3, [111] solid solutions like $PbFe_{0.5}Nb_{0.5}O_3$ [112] and several boracites [113] and phosphates [114] etc. A large ME effect is also seen in composite materials which can be prepared by combining the ferroelectric/piezoelectric material and ferromagnetic/piezomagnetic in a eutectic composite by unidirectional solidification, for example: $BaTiO_3$ and $CoFe_2O_4$. [115, 116, 117, 118]

While in single phase magnetoelectrics the effect can be due to the coupling of magnetic and electric orders as observed in some multiferroics, in composite materials the effect originates from the interface coupling effects such as strain. The ME effect has some of the promising applications in detection of very low magnetic fields, advanced logic devices and tunable microwave filters. [107]

1. 8. 4 Mechanisms of multiferroicity and ME effect

There are several mechanisms for electric and magnetic order to occur simultaneously and also to see the coupling between them. Few such mechanisms are described below.

1. **Lone pair multiferroics:** One of the possible mechanisms for the coexistence of magnetism and ferroelectricity (multiferroic) is lone-pair driven, where the *A*-site drives the displacement and partially filled "d" shell on the B-site contributes to the magnetism for example, $BiFeO_3$ [119] and $BiMnO_3$. [120] Here, Bi^{3+} has a stereochemically active $6s^2$ lone-pair that causes Bi-6p (empty) orbital to come closer in energy to the O-2p orbitals which leads to hybridization between the Bi-6p and O-2p orbitals and drives the off-centering of the cation towards the neighboring anion resulting in ferroelectricity.
2. **Charge ordering:** Other possible origin for multiferroicity is the charge ordering which can occur in a compound containing ions of mixed valence and with geometrical or magnetic frustration. Here, ions form a polar arrangement cause improper ferroelectricity without any ionic displacement. If these ions are magnetic, then a coexisting magnetic order can be established and may be coupled to ferroelectricity such as in the case of $LuFe_2O_4$ [102] which shows improper ferroelectricity below 330 K.
3. **Improper geometric ferroelectricity:** Here, a structural phase transition at high temperatures causes the appearance of ferroelectricity for example, family of hexagonal rare earth manganites (h-$RMnO_3$ with R = Ho-Lu, *Y*). In the case $YMnO_3$,

the ferroelectric phase is characterized by a buckling of the layered MnO_5 polyhedra accompanied by displacements of the Y ions, which lead to a net electric polarization. [121]

4. **Spin driven ferroelectricity:** Spin driven ferroelectricity is the breaking of space inversion by magnetic order which generally occurs in frustrated magnets. This kind of induced electric polarization by magnetic order has been confirmed from intensive theoretical and experimental studies. [122] Unlike in the case of proper ferroelectric materials, here the primary order parameter is not the ferroelectric distortion but it is due to magnetic ordering or a structural change, thus these materials exhibit ME effect. There several materials that show such spin driven ferroelectricity such as $R Mn_2O_5$ (R – rare earth elements), $Ni_3V_2O_8$, $CuFeO_2$, $CoCr_2O_4$ and MnO_4 etc.
5. **ME effect in composite multilayers:** The composite multiferroic multilayers which is composed of piezoelectric and magnetostrictive heterostructures are found to show ME effect due to cross interaction between the magnetostrictive effect (mechanical/magnetic effect) in magnetic phase and the piezoelectric effect (electrical/mechanical effect) in piezoelectric phase through a relation, ME effect = $\frac{electrical}{mechanical} \times \frac{mechanical}{magnetic}$. These materials show an induced voltage in presence of a small ac magnetic field which reveals the ME voltage through $\delta E/\delta H$. A comprehensive review of such ME effect in composite multiferroic multilayers can be found in review article by M. Fiebig. [107]

1. 9 Motivation of the present work

In the past few years, a lot of attention has been focused on the CMR properties of Mn-based manganites and its relation to structural and magnetic properties due to exotic physics involved in CMR and its envisaged applications as magnetic field sensors. [123] Although the dc MR can be nearly 100% in higher magnetic fields $\mu_0 H \approx$ 5-6 T around T_C, it is negligible far below and above T_C. Thus, it is imperative to increase the magnitude of

magnetoresistance at low magnetic fields if at all manganites can be useful for device applications. In this context, observation of a huge magnetoimpedance (= -80% in a field of 600 G) in microwave frequency range (f = 9.8 GHz) range by cavity perturbation method is noteworthy. [124] In contrast to numerous reports on dc electrical transport in manganites, ac magnetotransport in manganites are relatively scarce. In dc electrical transport, e_g electron hopes between Mn^{3+} and Mn^{4+} ions along the direction of the dc electric field. The motion of e_g electrons is coupled to ferromagnetic alignment of t_{2g} spins through double exchange interaction. However, little is known about the electrical response of these manganites to alternating current.

Similarly, there is another interesting low-field effect called giant magnetoabsorption, *i.e.*, a large change in *rf* electromagnetic wave absorption under a magnetic field that remains less explored. There are few reports of *rf* magnetoabsorption in Mn-based oxides studied using LC tank circuit powered by tunnel diode and integrated circuits. Here, the sample enclosed in inductor is exposed to the ac magnetic field generated by an inductance coil. The *rf* magnetoabsorption is a very interesting noncontact method to investigate the power absorption and also the *rf* magnetization dynamics. Earlier work showed that *rf* magnetoabsorption is useful in detecting magnetic anomaly due to polaron ordering below the long range ferromagnetic ordering, [75] finding London penetration depth in superconductors, [125] analyzing the critical exponents in some magnetic materials, [126, 127] and also to study the electrical conductivity without making contact to the sample. [128] Recently Sarangi *et al*., [77] noted that *rf* current through the IC oscillator circuit containing $La_{0.7}Sr_{0.3}MnO_3$ sample changes with the applied magnetic field and temperature, and attributed their observation to the magnetoimpedance effect. A measurement of both resonance frequency of IC oscillator and current through it will be helpful to understand the nature of electromagnetic absorption in these materials.

Next, we will consider thermal effects, particularly magnetic entropy change *i.e.*, MCE in manganites. It has been recently demonstrated that the manganites are considered to be promising candidates for magnetic refrigeration applications. Although there is handful of

magnetocaloric studies in ferromagnets which show normal MCE, magnetocaloric studies in antiferromagnetic manganites which show inverse MCE are relatively scarce due to the need for higher magnetic field ($\mu_0 H$ > 5 T) to destroy antiferromagnetic ordering. [129, 130, 131, 132] Compounds in which normal and inverse MCEs coexist can find application over a wide temperature range, since they can be cooled by adiabatic magnetization and demagnetization in antiferromagnetic and ferromagnetic states, respectively so as to increase the efficiency of a magnetic refrigerator. In this context, half-doped manganites, which exhibit both ferromagnetic and antiferromagnetic ordering at different temperatures in a single compound, seem to be good candidates to investigate both normal and inverse MCEs in the viewpoints of fundamental research and practical applications.

Finally, we focus on different system, which magnetic and electrical polarizations are expected to couple. The Fe-based ME multiferroic oxide materials which show coupling between electrical and magnetic dipole moments are finding promising applications in data storage, sensors and also show intriguing physics involved in the coupled phenomena. However, there exist very few single-phase multiferroic oxides due to the fact that the ferroelectricity in ABO_3 type perovskite oxides requires transition metal ions (*B*) with d^0 electronic configuration, whereas ferromagnetism requires transition metal ions with odd number of d electrons. Though the physics of ME coupling in $AMnO_3$ is very exciting, they are not useful for practical applications at room temperature since the magnetic field-induced ferroelectric polarization is rather small and the magnetic transition occurs mostly below the liquid nitrogen temperature. Nevertheless, Fe-based materials such as $BiFeO_3$ and $GaFeO_3$ show coupling between electrical and magnetic dipole moments. [133] The high values of ferroelectric Curie temperature [$T_{C(FE)} \approx$ 836 °C] [134, 135] and antiferromagnetic transition temperature ($T_N \approx$ 370 °C) [136] found in $BiFeO_3$ make this compound more attractive. However, ferro or ferrimagnetism instead of antiferromagnetism along with enhanced polarization is highly preferable for low-field practical applications.

1. 10 Objective of the present work

The main focus of our work is to exploit the multifunctional properties of both Mn and Fe-based oxides, and also to demonstrate the powerfulness of *rf* magnetoabsorption and ac magnetotransport in detecting magnetic as well as the structural transitions and also to understand the magnetization dynamics in manganites. The main objectives of this thesis work are as follows.

1. To investigate the ac magnetotransport properties of two compounds in the $La_{1-x}Ba_{x-y}Ca_yMnO_3$ series with x = 0.33 and y = 0, and x = 0.33, y = 0.1 by monitoring the changes in the resonance frequency and the *rf* current through the ICO circuit simultaneously.
2. The study of ac magnetotransport properties of $La_{1-x}Ba_{x-y}Ca_yMnO_3$ compounds with x = 0.33, 0.25, 0.2 and y = 0 and 0.1 by simultaneous measurements of the ac resistance (*R*) and reactance (*X*) using ac impedance method.
3. Detailed investigations of magnetic, magnetoabsorption, ac magnetotransport and magnetocaloric properties of $Sm_{0.6-x}La_xSr_{0.4}MnO_3$ series of compounds with $0 \leq x \leq 0.6$ whose ground state changes from semiconducting ferromagnetic state (x = 0) to metallic ferromagnetic state (x = 0.6).
4. Investigations of both normal and inverse MCEs in $Pr_{1-x}Sr_xMnO_3$ with x = 0.5 and 0.54 by both magnetic (indirect) and calorimetric (direct) methods.
5. The detailed study of magnetic and ME properties of pure and cation doped $Bi_{1-x}A_xFeO_3$ compounds with *A* = Sr, Ba and $Sr_{0.5}Ba_{0.5}$ and x = 0 and 0.3.

1. 11 Methodology

The samples studied in this thesis work were prepared by standard solid state synthesis route. The work presented in this thesis was studied by using several commercial characterization techniques and automated control measurement setups by constructing electronic circuits and interfacing various instruments using LabVIEW 8.2 software. We have

exploited the impedance spectroscopy technique to investigate the ac magnetotransport in Mn-based oxides by measuring the four-probe ac resistance and reactance as functions of magnetic field, temperature and frequency. A LC oscillator circuit powered by an integrated chip (IC 74LS04 – NOT gate) was constructed to study the *rf* power absorption in Mn-based oxides. MCEs have been investigated in some of the selected ferromagnetic and antiferromagnetic manganites by measuring the ΔS_m by both magnetic (indirect) and homebuilt calorimetric or DSC/DTA (direct) methods. A homebuilt dynamic lock-in technique was used to measure the ME coefficient of Fe-based oxide materials.

1. 12 Novelty of the present work

This thesis work focuses on the investigation of rarely studied ac magnetotransport, *rf* magnetoabsorption, magnetocaloric and multiferroic properties of selected Mn-based (manganites) and Fe-based (ferrites) oxides. Below are the few novel findings in this thesis work.

1. **Ac magnetotransport in manganites:** In this study, we have observed a huge change in the ac magnetoresistance ($\Delta R/R$ = -45%) under a small magnetic field of H = 1 kG in one of the Mn-based oxides, $La_{0.67}Ba_{0.33}MnO_3$. Interestingly, our study shows that four-probe ac magnetotransport is a power tool to detect magnetic as well as hidden structural transitions (not visible in dc resistivity measurement) in manganites. In one of the other interesting studies, we have shown that the conducting ferromagnet like $La_{0.67}Ba_{0.33}MnO_3$ can show a huge magnetoinductance effect ($\Delta X/X = \Delta L/L$ = 60% in H = 1 kG) which may find application in thin film inductor. More importantly, we have shown that ME coupling observed in the Mn-based oxides (reported in several reputed journals) is not necessarily due to change in the capacitance under the external magnetic field, rather it can arise from large change in the magnetoreactance or magnetoinductance of the sample.

2. **Rf magnetoabsorption in manganites:** We have shown here that a simple IC oscillator is a powerful contactless tool to study the magnetization dynamics as well as to investigate the magnetic and structural phase transition in manganites.
3. **MCEs in selected manganites:** In this study, we shown that *A*-type antiferromagnet $Pr_{0.46}Sr_{0.54}MnO_3$ exhibits a large inverse MCE (ΔS_m = +9 $Jkg^{-1}K^{-1}$ for a field change of ΔH = 7 T) among the reported manganites. We have also showed a coexistence of huge inverse (ΔS_m = +7 $Jkg^{-1}K^{-1}$ for ΔH = 7 T) and normal (ΔS_m = -4.5 $Jkg^{-1}K^{-1}$ for ΔH = 7 T) MCEs in a single compound, $Pr_{0.5}Sr_{0.5}MnO_3$. We give a clear experimental evidence for both normal and inverse MCEs from the home-built DSC and DTA techniques. In other related work, we have shown a new possibility of observing inverse MCE in the pure ferromagnetic compound, $Sm_{0.6-x}La_xSr_{0.4}MnO_3$ (x = 0 to 0.6) at low temperatures within the long-range ferromagnetic ordered state due to coupling between Mn-3d and Sm-4f moments. This is the first report of inverse MCE in a purely ferromagnetic manganite because only antiferromagnetic manganites show such effect. An inverse MCE of magnitude ΔS_m = +1.07 $Jkg^{-1}K^{-1}$ at T = 10 K for ΔH = 5 T and a significant normal MCE (ΔS_m = -4 $Jkg^{-1}K^{-1}$) at T_C = 320 K observed in one of the samples ($Sm_{0.2}La_{0.4}Sr_{0.4}MnO_3$) makes this compound very attractive for both low temperature and room temperature magnetic refrigeration technology.
4. **Magnetic and ME studies in Fe-based oxides:** We have investigated the ME effect in one of the famous multiferroic materials $Bi_{0.7-x}A_xFeO_3$ (*A* = Sr, Ba, Ca) and showed that one of the compounds of the series, $Bi_{0.7}Sr_{0.15}Ba_{0.15}FeO_3$ exhibits an enhanced ME effect (2.1 mV/cmOe) compared to other Sr and Ba doped compounds. We have also shown that the compound which has less saturation magnetization can show high ME coefficient, and it is suggested that the changes in the ME coefficient is due to possible modification in the domain structure and ME coupling in the compound.

1. 13 Organization of the thesis

This thesis is organized as follows. In chapter 1, we have presented a brief description of introduction to Mn and Fe-based oxides and various phenomena involved in as well as its few exotic properties. The chapter 2 mainly focuses on the description of various experimental techniques used in this study. In chapter 3, the study of *rf* magnetoabsorption and ac magnetotransport properties of $La_{1-x}Ba_{x-y}Ca_yMnO_3$ compounds have been presented. The chapter 4 gives a detailed study of magnetic, magnetoabsorption, ac magnetotransport and magnetocaloric properties of $Sm_{0.6-x}La_xSr_{0.4}MnO_3$ series of compounds. The chapter 5 focuses on the investigations of normal and inverse MCEs in $Pr_{1-x}Sr_xMnO_3$ compounds using magnetic (indirect) and calorimetric (direct) methods. In chapter 6, we present the detailed magnetic and ME properties of pure and cation doped $Bi_{1-x}A_xFeO_3$ compounds. Finally, the chapter 7 provides the summary of main results obtained in this thesis work and its applications with an outlook of future research and development in this field.

Chapter 2

Experimental methods and instruments

This chapter gives a brief overview of the various experimental methods and techniques used to prepare and characterize the Mn and Fe based oxides. The details of the various commercially available instruments and home-built instruments used in the measurements of *rf* magnetoabsorption, magnetoimpedance, magnetocaloric and ME properties of selected Mn and Fe based oxides are also described.

2. 1 Sample preparation methods

There are several methods have been demonstrated so far to synthesize the perovskite oxide materials. The most widely used methods are ceramic or solid state synthesis, sol-gel, combustion, co-precipitation, etc. [137] While the former method is a high temperature synthesis, the later ones are belonging to the class of soft-chemical routes of synthesis. In the present study, the Mn and Fe based oxides were prepared using the standard solid state synthesis method using the high purity (> 99.9%) raw materials procured from Sigma-Aldrich, U.S.A. The samples were prepared in high purity alumina crucible or boat using a high temperature furnace (Carbolite, U.S.A) which has controlled heating and cooling options with temperature stability of 0.01°C.

2. 1. 1 Solid state synthesis method

Solid state synthesis method is the most conventional synthesis method used to prepare the perovskite oxide materials. This method involves the repeated grinding and heating of mixed raw materials to obtain a single phase material due to the ionic diffusion. The prerequisite for this method is that the particle size of raw materials has to be smaller than the diffusion length which is expressed as: [138]

$$(2Dt)^{1/2} \geq L$$

where, $(2Dt)^{1/2}$ is the diffusion length, D is the diffusion constant which is depending on the reaction temperature and materials, t is the reaction time and L is the typical particle size. As the ionic diffusion generally a slow process and it requires a high temperature and a longer heating duration are required for the solid state synthesis method. In a typical solid state synthesis method, the precursors in the form of metal oxides or carbonates are weighed in the stoichiometric proportions and mixed thoroughly in an agate mortar using a pestle. The well-ground mixtures are initially calcined at 1000°C for 24 hours and further at 1200°C for 24 hours with three intermediate grindings in order to ensure the homogeneity of the mixed powders. The prepared compounds are then characterized for their phase formation after subsequent calcination using powder X-ray diffraction method and accordingly, the processing conditions of the mixed powder are modified to obtain single phase compounds.

2. 2 Characterization techniques

2. 2. 1 X-ray powder diffractometer

The powder X-ray diffraction (XRD) is a widely used technique to identify the crystalline structure, grain size and internal strains of the crystalline materials. [139] The single crystals or polycrystalline powders of substances which have regularly repeating units of ions/atoms are capable of diffracting the X-ray radiation due to the fact that the inter-atomic distances are comparable to the wavelength of the X-ray radiation. This is technique is based on the principle of Bragg's law of diffraction:

$$2d \sin\theta = n\lambda$$

where, d is the spacing between the crystalline lattice planes, θ is the glancing angle between the incident X-ray beam and crystalline plane, n is the order of diffraction and λ is the wavelength of the incident X-ray beam. The main advantage of the XRD technique is that it is a nondestructive method. In the present study, Philips X'PERT MPD powder X-ray diffractometer with Cu-Kα radiation (λ = 1.542 Å) was used for the structural

characterization of the polycrystalline compounds. The Rietveld refinement method was used to fit the observed powder XRD pattern of the compounds with the help of TOPAS software version 2.1 in order to calculate the unit cell parameters. In a typical XRD experiment, the sample was scanned from 2θ = 10° to 90° with a scan rate of 4º/minute and 0.25º/minute for normal (to confirm the phase formation of compounds) and slow-scan (to fit the observed XRD pattern using Rietveld refinement in order to calculate the unit cell parameters) measurements, respectively.

2. 2. 2 Magnetic and magnetotransport measurements

A Physical Property Measurement System (PPMS) equipped with superconducting electromagnet supplied by Quantum Design Inc. (U.S.A) was used to carry out the low temperature dc resistivity measurements in the temperature range of T = 10-400 K under external magnetic field up to $\mu_0 H$ = 7 T. An inbuilt dc resistivity measurement option comes with the PPMS was used to measure the dc resistivity of the sample. A specially made Vibrating Sample Magnetometer (VSM) for PPMS by Quantum Design, which is a fast and sensitive DC magnetometer, was used to measure the magnetic properties of the sample as a function of temperature and magnetic field. In a typical magnetic measurement, sample is placed inside a uniform magnetic field to magnetize the sample and then the sample is physically vibrated sinusoidally near the detection or pickup coil. The induced voltage in the pickup, which is proportional to the sample's magnetic moment, is then measured using the inbuilt lock-in amplifier. By using a compact gradiometer pickup coil configuration, relatively large oscillation amplitude of 1-3 mm peak-to-peak and a frequency of 40 Hz, the VSM is able to resolve magnetization changes of magnitude less than 10^{-6} emu at a data rate of 1 Hz. The photograph of PPMS equipped with VSM module used for the present study is shown in the Fig. 2.1. It consists of VSM linear motor transport (head) for vibrating the sample, pickup coil for detection, electronics for driving the linear motor transport and detecting the response from pickup coil, and it uses a MultiVu software for automation and control.

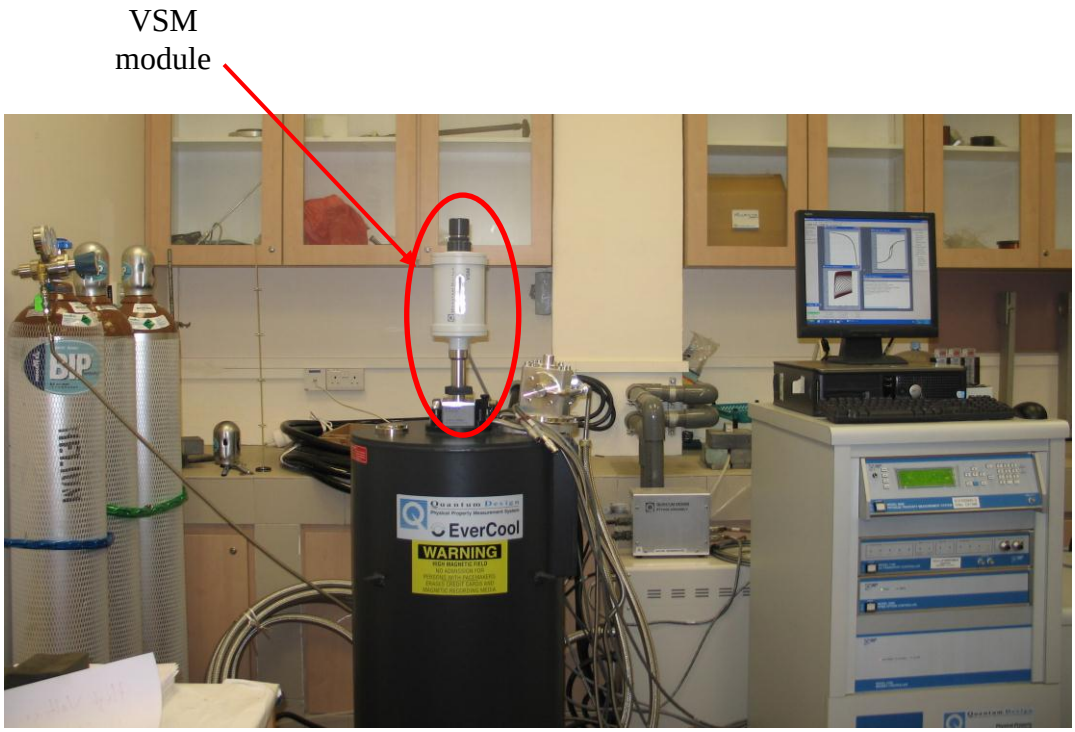

Fig. 2. 1 Physical Property Measurement System (PPMS) equipped with Vibrating Sample Magnetometer (VSM) module.

2. 2. 3 Integrated Chip (IC) oscillator setup

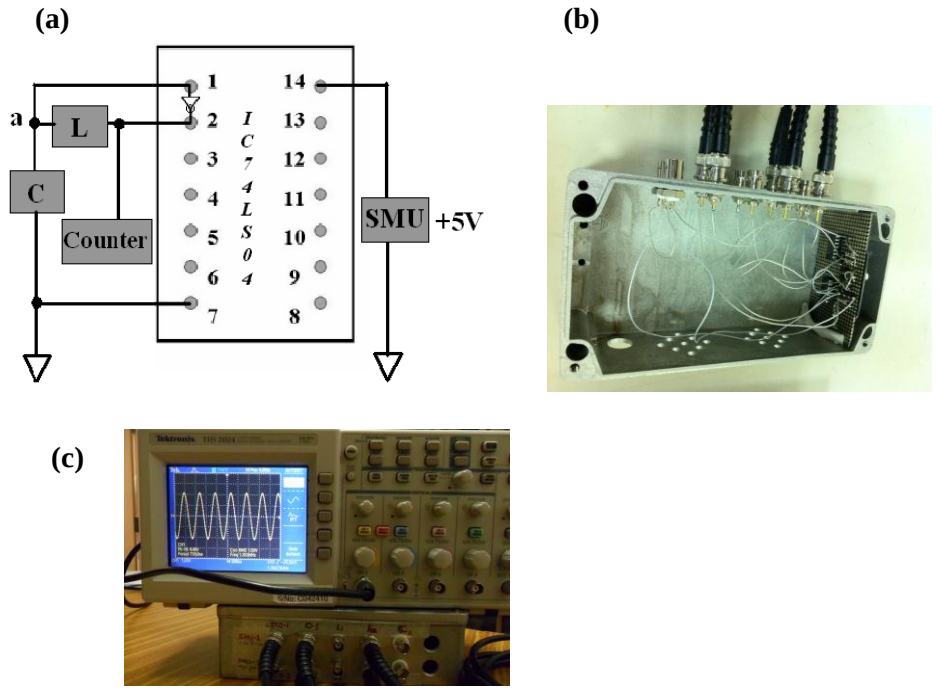

Fig. 2. 2 (a) A schematic diagram of the IC based LC oscillator circuit used for *rf* power absorption studies, where SMU – source measure unit, Counter – frequency counter, *L* – inductor loaded with sample and *C* – standard capacitor, (b) actual wiring inside the IC oscillator set up and (c) sinusoidal signal of the IC oscillator observed in oscilloscope.

The schematic diagram of integrated chip oscillator (IC) set up for the *rf* power absorption measurement is shown in Fig. 2.2(a) which is similar to the LC oscillator designed by others. [140] The IC 74LS04 is a TTL bipolar Hex inverter which can be used in high frequency oscillator circuit since the typical propagation delay of each NOT gate is ~15 ns. A *dc* bias (+5V) is applied to the pin 14 of the IC 74LS04. The pin numbers '1' and '2' are the input and the output of one of the six NOT gates of the IC, respectively. Suppose the voltage at point 'a' is low, then the output at pin '2' is high that builds up the current in the inductor which makes the capacitor to charge; as soon as the voltage at point 'a' is high due the charging of the capacitor, output at pin '2' becomes low and the capacitor starts discharging. This charging and discharging of capacitor (C) driven by the NOT gate of the IC through inductor (L) sets the LC tank circuit into resonance at frequency, $f_r \approx 1.3$ MHz at room

temperature. Fig. 2.2(b) shows the actual wiring inside the ICO circuit and the Fig. 2.2(c) shows sinusoidal signal of the IC oscillator observed in oscilloscope.

The values of inductance and capacitance at room temperature are 6 μH and 2000 pF. The resonance frequency is slightly modified from the theoretical value by cable capacitance and resistance in the circuit. A slight variation in the value of f_r in different experiments is due to the variation in the capacitance values of the different coaxial cables used in the respective ICO experiments. A Yokogawa GS 610 source-measure unit (SMU) was used to supply a stable *dc* bias to the IC as well as to measure the *dc* current (I) through the circuit. The amplitude of the *ac* voltage across the inductor was measured and found to be 2 V (rms). The *ac* current in the LC circuit was determined by measuring *ac* voltage across a 10 Ω resistance connected in series with the coil and found to be 7.2 mA (rms) at room temperature which is lower but close to the *dc* current dawn from the power supply. The ac magnetic field is estimated to be H_{ac} = 0.52 G from the *rf* current measured. The inductance coil loaded with the sample was inserted into a commercial cryostat (PPMS, Quantum Design Inc) using coaxial cables whereas the IC and the capacitor were a part of the room temperature circuit. The shift in resonance frequency (f_r) of the tank circuit was tracked using an Agilent 53131 universal frequency counter. When the sample absorbs power from the *rf* field due to changes in its physical property, the impedance of the coil changes which in turn changes the total current drawn from the dc voltage source. If $I(T_1,H_2)$ and $I_0(T_1,H_1)$ are the currents in the circuit under the magnetic fields H_2 and H_1, and at a temperature T_1, the *rf* power absorbed by the sample at any instant of time can be written as $P = V(I-I_0) = V\Delta I$. In a typical *rf* power absorption experiment, the temperature and magnetic field dependences of the resonance frequency and current through the ICO circuit are measured simultaneously using the PPMS.

2. 2. 4 Dynamic lock-in technique for ME measurements

ME effect refers to the coupling between the electrical and magnetic dipole moments which exists in the certain class of materials called ME materials. Multiferroic materials showing this ME effect is referred as multiferroic magnetoelectrics which are promising for data storage sensor applications. The widely used method to measure the ME coefficient is the dynamic lock-in technique. Fig. 2.3 shows the schematic diagram of the dynamic lock-in technique used to measure the ME coefficient which is similar to the experimental set up used by Duong *et al*. [141] The sine output of the internal function generator of a lock-in amplifier (Stanford Research, model SR850) was given to a power amplifier (PA) and the amplified current fed the Helmholtz coils (HC – 130 turns of AWG 26 copper wire with a diameter of 40 mm) which provided *ac* magnetic fields up to h_0 = 10 G at a frequency of 7 kHz. We restricted our measurements to the optimal frequency, f = 7 kHz due to the limitation of the power amplifier (the gain of the amplifier decreases for frequency above 7 kHz, and hence the magnitude of the *ac* magnetic field decreases). The *ac* magnetic field at the center of the Helmholtz coils was monitored using Hall probe (HP) with Gauss meter (GM). In addition, the strength of the magnetic field was estimated by measuring the *ac* voltage developed across a standard resistor connected in series with the Helmholtz coils using a Keithley 2700 digital multimeter. A Yokogawa GS610 – source measure unit (SMU) was used to ramp *dc* current through the electromagnet (EM) up to ±3 A to provide a maximum field of ± 3 kG with the pole spacing of 20 mm.

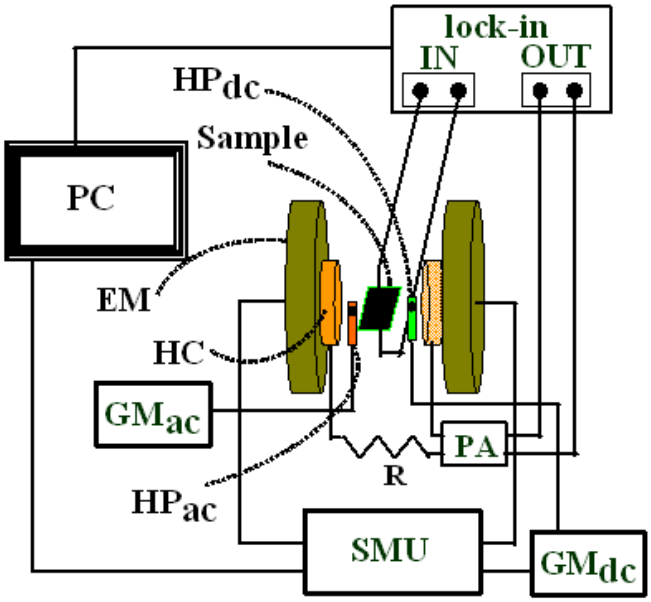

Fig. 2. 3 Schematic diagram of the experimental set up to measure the ME coefficient using dynamic lock-in technique: where, SMU – source measure unit, PA – power amplifier, HC – Helmholtz coil, EM – electromagnet, HP_{ac}, HP_{dc}, and GM_{ac}, GM_{dc} are the Hall probes and Gauss meters for *ac* and *dc* magnetic fields, respectively. Both Hall probes are close to each other unlike it appears in the diagram.

The reorientation of the electrical dipoles in the sample by *ac* magnetic field induces *ac* voltage on the top and bottom surfaces of the sample through ME coupling, which was measured using the lock-in amplifier in the differential mode to eliminate the errors due to induction by Faraday effect. The *ME* coefficient, α_{ME} can be calculated using relation:

$$\alpha_{ME} = \frac{dE}{dH} = \frac{1}{t}\frac{dV}{dH} = \frac{V_{out}}{h_0 t}$$

where, V_{out} is the *ac* ME voltage appeared across the sample surface (measured by the lock-in), h_0 is the amplitude of the *ac* magnetic field, and t is the thickness of the sample. Both longitudinal and transverse ME coefficients were measured. The longitudinal ME coefficient refers to the measurement of ME voltage parallel to the direction of the applied magnetic fields (*ac* and *dc*) *i.e.*, the silver paste coated surfaces of the sample is perpendicular to the magnetic fields. In the transverse case, silver paste coated surfaces of the sample is parallel to the magnetic fields. All the instruments were controlled by the LabVIEW 8.2 software programme. In our typical ME measurement, a dc magnetic field is swept and the ME

coefficient is measured at room temperature in both longitudinal (L-α_{ME}) and transverse (T-α_{ME}) configurations.

2. 2. 5 Magnetoimpedance measurements

We have investigated the magnetoimpedance behavior of polycrystalline rectangular bar shaped samples using Agilent LCR meters (4285A and 4294A) and PPMS by measuring the ac resistance and reactance simultaneously in the frequency range (f = 1 kHz to 20 MHz) with *ac* excitation current of 5 mA.

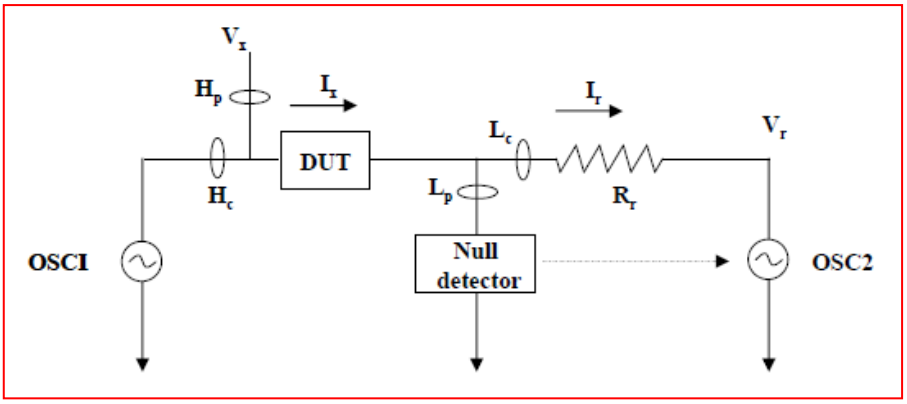

Fig. 2. 4 Schematic diagram of the auto-balancing bridge.

Electrical impedance of the device under test (DUT) is measured using the Agilent LCR meters employing auto balancing bridge method. [142] The schematic diagram of operation of the auto-balancing bridge is shown in Fig. 2.4. For frequencies below 100 kHz, an *I*-*V* converter operational amplifier acts as a null detector and maintains the potential at low point *L* to be zero (virtual ground). The current I_x balances with the current I_r which flows through the range resistor *R*. The impedance *Z* is computed from the voltage measured across the DUT (V_x) and the range resistor (V_r) using the relation:

$$Z = R\frac{V_x}{V_r}$$, where, *R* is the resistance value of a known resistor.

We have used the Agilent LCR meters with standard Agilent 16048D test fixture for the impedance measurements in our samples. Open and short corrections were performed prior to experiment to eliminate the measurement errors arise due to stray parasitic impedance in the

test fixture and the load correction was performed by using a calibrated device as a reference load.

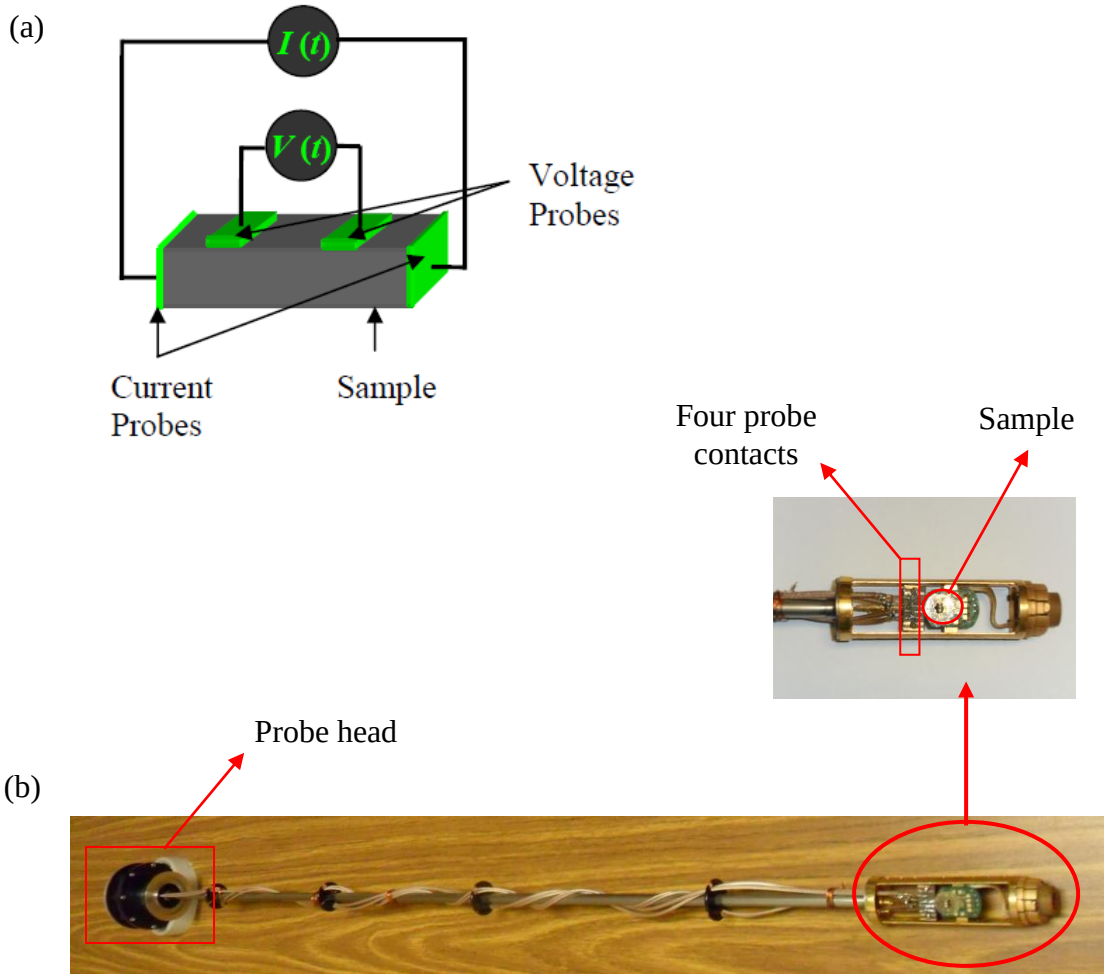

Fig. 2. 5 (a) Schematic diagram of the impedance measurement in four probe configuration and (b) the multifunctional probe wired with high frequency coaxial cables for impedance measurement using PPMS.

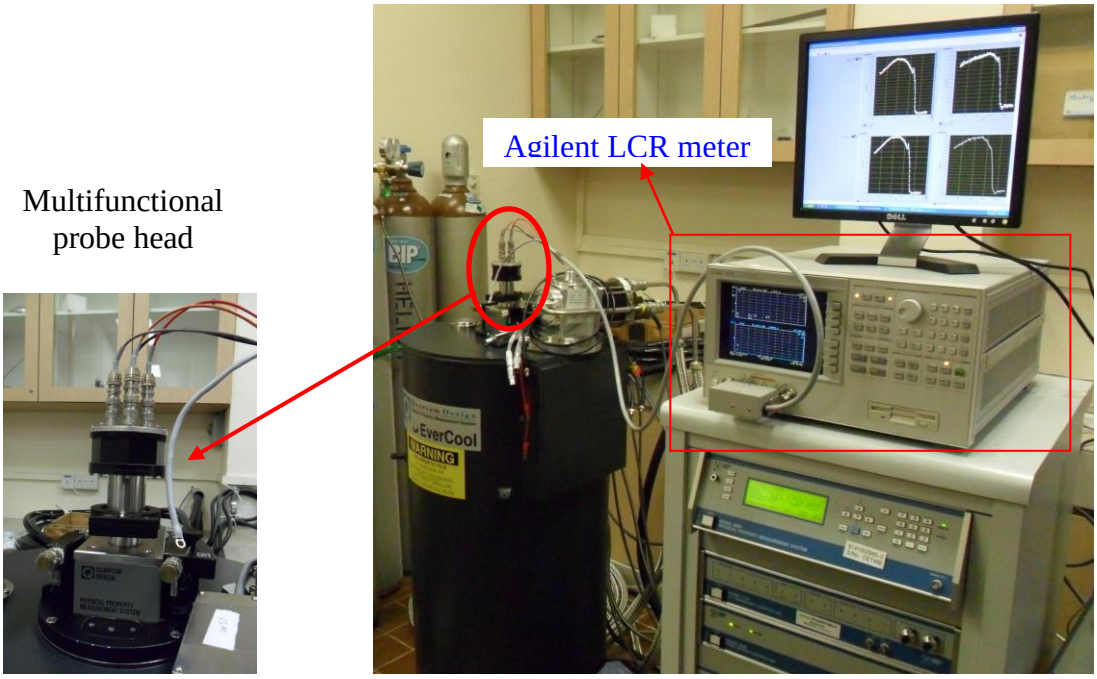

Fig. 2. 6 A photograph of the Magnetoimpedance measurement set up with LCR meter and PPMS

For impedance measurement, the sample was cut into parallopiped shape and the electrical contacts were made with Ag-In alloy. The distance between voltage probes was kept around 2-3 mm. The sample was mounted in a specially designed sample holder wired with high frequency coaxial cables to carryout out the impedance measurement in PPMS at low temperature (T = 400-10 K) and under high magnetic field ($\mu_0 H$ = 0-7 T). Both the resistive (R) and reactive (X) components of the impedance of the sample were measured in four probe configuration using the Agilent 4285A and 4294A LCR meters as shown in Fig. 2.5(a). Fig. 2.5(b) shows the photograph of the multifunctional probe wired with high frequency coaxial cables to carry out the magnetoimpedance measurement in PPMS. In a typical magnetoimpedance experiment, the temperature dependence of both R and X under different dc bias magnetic fields and magnetic field dependence at selected temperatures were measured simultaneously using Agilent LCR meters in PPMS. Fig. 2.6 shows a complete view of the magnetoimpedance measurement set up using Agilent LCR meter and PPMS.

2. 2. 6 Magnetocaloric measurements: magnetic and calorimetric methods

MCE is quantified by the change in magnetic entropy (ΔS_m) and also the change in temperature of a magnetocaloric material. Generally one estimates the magnetic entropy change from the isothermal magnetization versus field data and is called "indirect method". However, a very few researchers estimate the magnetic entropy change using differential scanning calorimeter by measuring the heat flow during the field-induced magnetic transition and is called as "direct method". We have investigated the MCE in selected compounds by estimating ΔS_m using both magnetic (indirect) and calorimetric (direct) methods.

In magnetic method of estimating ΔS_m, we have measured the field dependence of magnetization up to a maximum field of $\mu_0 H$ = 7 T in isothermal condition at close temperature intervals around the magnetic transition using the vibrating sample magnetometer equipped with PPMS. According to the standard Maxwell's thermodynamical relation for reversible process, the expression for ΔS_m is given by,

$$\Delta S_m(T,H) = S_m(T,H) - S_m(T,0) = \int_0^H \frac{dM(T,H)}{dT} dH \,.$$

From the set of isothermal magnetization versus field data taken, the magnetic entropy change is estimated using the numerical approximation,

$$\Delta S_m = \sum_i \frac{M_i(T_i,H) - M_{i+1}(T_{i+1},H)}{T_i - T_{i+1}} \Delta H$$

where, M_i and M_{i+1} are the magnetization values measured at temperatures T_i and T_{i+1}, respectively. Next we describe the direct estimation of ΔS_m using differential scanning calorimetry.

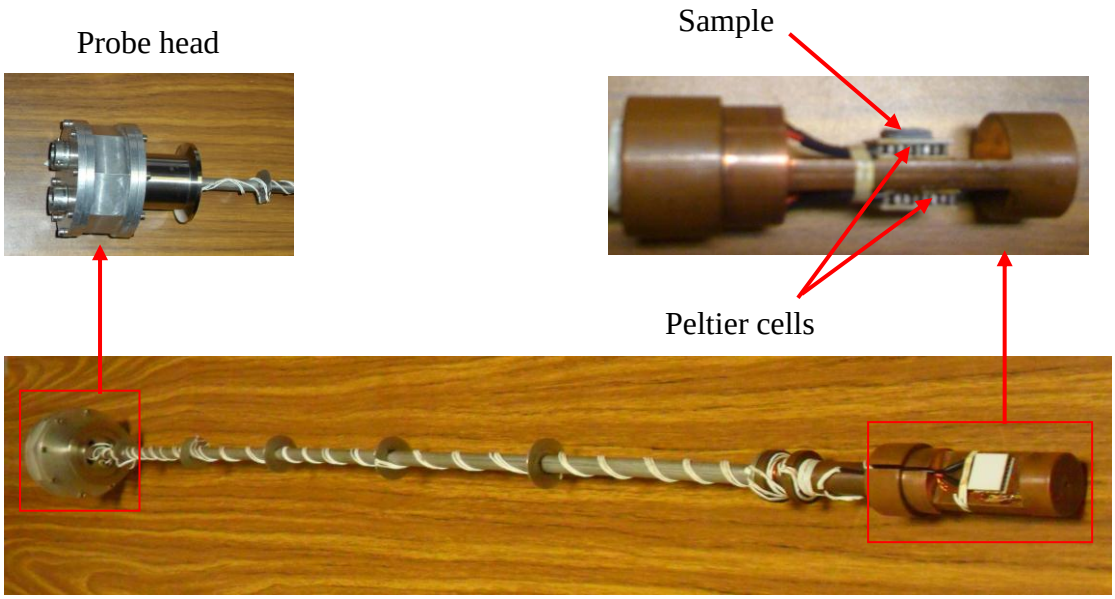

Fig. 2. 7 Differential scanning calorimetry probe designed for PPMS for the direct estimation of magnetic entropy change (ΔS_m)

Fig. 2.7 shows homebuilt DSC set up for the direct estimation of magnetic entropy change (ΔS_m) which makes use of two Peltier cells connected in differential mode to measure the heat transfer during the magnetic transition. Our experimental set up is similar to the design used by J. Marcos *et al*. [143] The absorption or emission of heat (Q) during phase transition in the sample while sweeping the magnetic field at a fixed base temperature leads to a differential voltage across the cells, which is measured in the experiment. By using the sensitivity of the Peltier cell and the field sweep rate (dH/dt), the field dependence of the heat (dQ/dH) is evaluated at different temperatures. The latent heat (L) and the magnetic entropy change (ΔS_m) are obtained from the integration of these curves, using the following relations:

$$L = \int_{H_i}^{H_f} \frac{dQ}{dH} dH; \quad \Delta S_m = \frac{L}{mT}$$

where, H_i and H_f are the initial and final fields of the transition and m is the mass of the sample. [144] In our calorimetric measurements, we have swept the magnetic field at the rate of dH/dt = 40 G/s.

Chapter 3

Magnetically tunable *rf* power absorption and giant magnetoimpedance in $La_{1-x}Ba_{x-y}Ca_yMnO_3$

3. 1 Introduction

In the past few years a lot of attention has been focused on the colossal magnetoresistance (CMR) properties of the hole-doped pseudocubic perovskite $RE_{1-x}AE_xMnO_3$ (*RE* – rare earth element and *AE* – alkaline-earth element) and its relation to structural and magnetic properties due to exotic physics involved in CMR shown by them and envisaged applications as magnetic field sensors. [1, 123] The hole-doping level x, the amount of the substitution of AE^{2+} for RE^{3+}, is the crucial factor in controlling the electronic phase of $RE_{1-x}AE_xMnO_3$. [47] Besides this hole-doping level x, the electronic phase of these doped manganites can also be controlled by creating the disorder in the system by doping different *AE*-site cations with different sizes. [47] For applications as low-magnetic field sensors, a large magnetoresistance, typically $\Delta R/R$ = 10-40% in a relatively low magnetic field strength, H = 10-100 G is preferable. There are two major contributions to the magnetoresistance (MR) in manganites, one is the intrinsic magnetoresistance arising from the change in the magnetization within a grain or a single domain and another is the extrinsic magnetoresistance due to tunneling of spin-polarized electrons between ferromagnetic grains through semiconducting grain boundaries. [145] Although the intrinsic MR can be nearly 100% in higher magnetic fields $\mu_0 H \approx$ 5-6 T around the Curie temperature (T_C), it is negligible far below and above the T_C. On the other hand, the extrinsic MR can reach 20-40% in $\mu_0 H$ = 0.3-0.5 T at T = 10 K, but becomes only a few percent at room temperature. Thus, it is imperative to increase the magnitude of the magnetoresistance at low magnetic fields if at all manganites can be useful for device applications. In this context, observation of a huge magnetoimpedance (= -80% in a field of 600 G) in microwave frequency range (f = 9.8 GHz) range by cavity perturbation method is noteworthy. [124] In the cavity perturbation

experiment, change in the reflected power of microwave in the cavity with and without sample in the presence of magnetic field was measured and the observed changes in power were related to microwave surface resistance of the sample. Since, the cavity perturbation technique is not available in many laboratories, it will be interesting to investigate the magnetoimpedance effect in the *rf* range (f = 0.1-25 MHz) with easily available RF LCR meters. In contrast to numerous reports on dc electrical transport in manganites, ac magnetotransport in manganites are scarce. [146, 147, 148, 149, 150] In this chapter, we report temperature and field dependence of ac impedance in $La_{1-x}Ba_{x-y}Ca_yMnO_3$ compounds with x = 0.33, 0.25, 0.2 and y = 0 and 0.1 in the frequency range f = 1-22 MHz.

There is another interesting low-field effect called giant magnetoabsorption, *i.e.*, a large change in *rf* electromagnetic wave absorption under a magnetic field that remains less explored. Belevtsev *et al*. [74] studied *rf* wave absorption in thin plate of $La_{0.67}Sr_{0.33}MnO_3$ in zero and external magnetic fields using a transmitter–receiver coil technique. Frank J Owen [151] showed that the resonance frequency of tunnel diode powered LC tank circuit with inductor loaded with $La_{0.7}Sr_{0.3}MnO_3$ sample changes as large as $\Delta f_r/f_r$ = -53 % in $\mu_0 H$ = 0.2 T at f_r = 350 kHz around the Curie temperature. Here, $\Delta f_r = f_r(T,H)-f_r(T,0)$ is the difference between the resonance frequency of the tank circuit at a given temperature with and without magnetic field ($\mu_0 H$). The large fractional shift in the resonance frequency was attributed to changes in the magnetic penetration depth ($\Delta\delta/\delta \alpha -\Delta f_r/f_r$). It was also found that $\Delta f_r/f_r$ is large for certain range of frequencies and decreases at higher frequencies. Srikanth *et al*. [152] found a much smaller effect ($\Delta f_r/f_r$ = 4% at $\mu_0 H$ = 2 T and T = 100 K) in $Nd_{0.7}Ba_{0.3}MnO_3$. Woods *et al*. [75] showed that the *rf* contactless method is useful in detecting a magnetic anomaly due to polaron ordering below the long range ferromagnetic ordering in $La_{0.85}Sr_{0.15}MnO_3$. The LC-tank resonance circuit biased by tunnel-diode was exploited to study the London penetration depth in superconductors, [125] to detect the magnetic transition and to analyze the critical exponents in some magnetic materials, [126, 127] and also to study the electrical conductivity without making contact to the sample. [128] Recently

Sarangi *et al*. [77] noted that *rf* current through the resonance circuit containing $La_{0.7}Sr_{0.3}MnO_3$ sample changes with the applied magnetic field and temperature, and attributed their observation to the magnetoimpedance effect. A measurement of both resonance frequency and current in the tank circuit will be helpful to understand the nature of electromagnetic absorption in these materials.

In the first half of this chapter, we report magnetoabsorption properties of $La_{1-x}Ba_{x-y}Ca_yMnO_3$ compounds with x = 0.33, 0.25, 0.2 and y = 0 and 0.1 by monitoring the changes in the resonance frequency and the *rf* current through the ICO circuit simultaneously. We also demonstrate the ability of ICO technique to detect magneto-structural transitions. In the second half of the chapter, we present the results of simultaneous measurements of the ac resistance (*R*) and reactance (*X*) by measuring the four probe impedance of the $La_{1-x}Ba_{x-y}Ca_yMnO_3$ compounds with x = 0.33, 0.25, 0.2 and y = 0 and 0.1. We demonstrate here that the *rf* magnetotransport provides an alternative strategy to enhance magnetoresistance, and to study the structural anomalies and magnetization dynamics in manganites.

3. 2 Experimental details

The polycrystalline $La_{1-x}Ba_{x-y}Ca_yMnO_3$ (LBCMO) compounds with x = 0.33, 0.25, 0.2 and y = 0, 0.1 were synthesized using a conventional solid state route. The solid solution was prepared by mixing the stoichiometric mixtures of La_2O_3, $BaCO_3$, $CaCO_3$ and Mn_2O_3 precursors, and was homogenized in an agate mortar before it was reacted at 1000°C for 24 hours. The calcined powders were reground thrice and final sintering was done at 1200°C for 24 hours. Single phase identification was performed by the powder XRD experiment (Philips X'pert Pro) using Cu Kα radiation. The compounds were pressed into pellets and heat treated at 1200°C for 24 hours to get a relatively dense pellets of LBCMO compounds. The observed room temperature XRD patterns of all the compounds were indexed using TOPAS software version 2.1 and found to be rhombohedral symmetry with $R\bar{3}c$ space group. For resistivity measurement, the samples were cut into parallelepiped and the electrical contacts were made

with Ag-In alloy. The distance between voltage probes was kept at around 3 mm. The temperature dependence of the resistivity under different dc bias magnetic fields was done using the Physical Property Measuring System (PPMS, Quantum Design, U.S.A). The ac susceptibility (f = 30 kHz and ac magnetic field is 0.2 G) at different applied dc bias magnetic fields was studied by measuring the self-inductance (L_{ac}) of a 50 turns single layered solenoid loaded with the sample using the National Instrument PXI 4072 LCR meter plug-in card. For impedance measurement, the sample was mounted in a specially designed sample holder wired with high frequency coaxial cables. Both the resistive (R) and reactive (X) impedance of the sample in four probe configuration were measured using the Agilent 4285A *rf* LCR meter. The temperature dependence of R and X under different dc bias magnetic fields were done using the PPMS and studies were done as described in the experimental section: 2.2.4. For *rf* power absorption study, the inductance coil loaded with sample was mounted in a specially designed sample holder wired with high frequency coaxial cables and the magnetic field was applied along the coil axis. Temperature and magnetic field dependent *rf* electromagnetic absorption have been investigated using a home built *LC* resonant circuit powered by an integrated chip oscillator (ICO) with PPMS as described in the experimental section: 2.2.3.

3. 3 Results and Discussions

3. 3. 1 Structural characterization using XRD

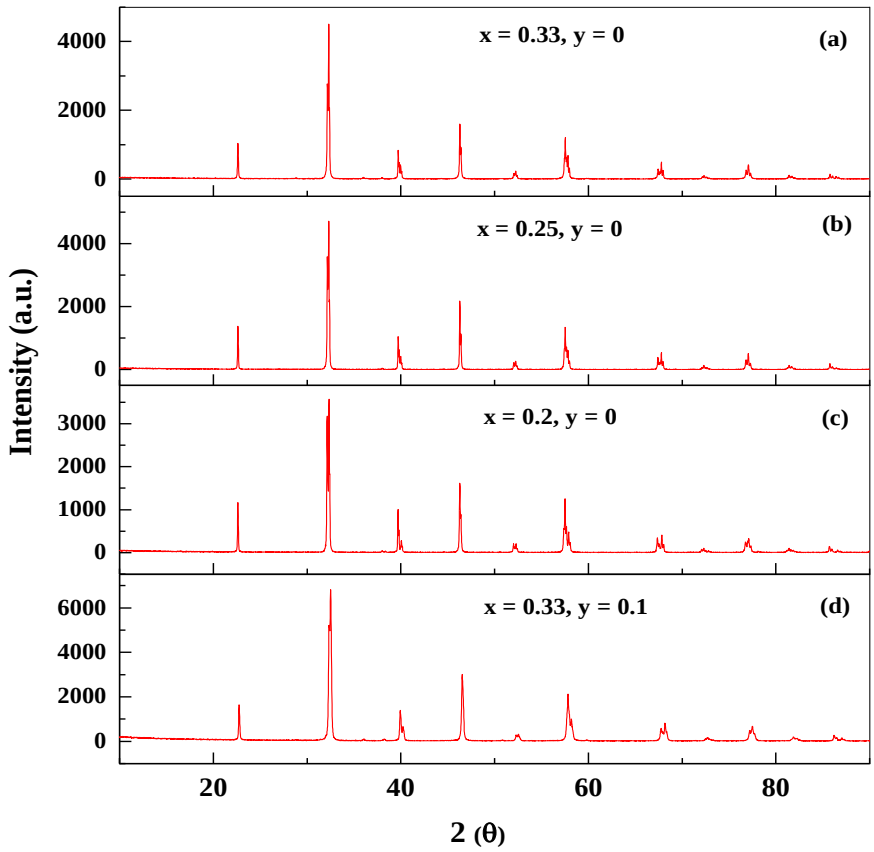

Fig. 3. 1 XRD patterns of $La_{1-x}Ba_{x-y}Ca_yMnO_3$ (x = 0.33, 0.25, 0.2 and y = 0 and 0.1) compounds at room temperature.

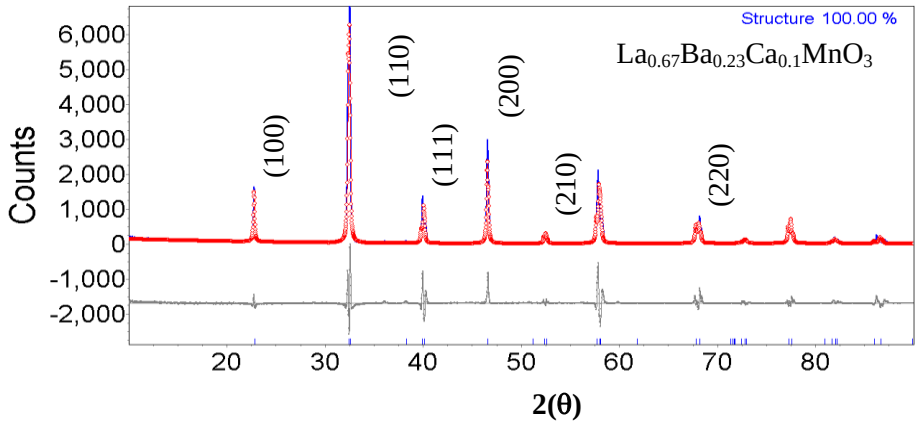

Fig. 3. 2 Observed (blue color) and Rietveld refinement (red color) of the XRD pattern for the $La_{0.67}Ba_{0.23}Ca_{0.1}MnO_3$ with space group $R\bar{3}c$ at room temperature.

Figs. 3.1(a)-(d) show the XRD patterns of the $La_{1-x}Ba_{x-y}Ca_yMnO_3$ compounds (x = 0.33, 0.25, 0.2 and y = 0, 0.1) at room temperature, which confirm the single phase compound formation. Fig. 3.2 shows the XRD pattern of one of the compounds in the series *i.e.*, $La_{0.67}Ba_{0.23}Ca_{0.1}MnO_3$. Observed XRD pattern (blue color) was indexed (red color) to rhombohedral structure of $La_{0.67}Ba_{0.23}Ca_{0.1}MnO_3$ with space group $R\bar{3}c$ using TOPAS software version 2.1. The prominent peaks in the XRD pattern are indexed by its crystallographic planes, which are represented by the miller indices (*hkl*). The lattice parameters of the compound determined by the above Rietveld refinement are found to be a = b = 5.4983 Å, and c = 13.5537 Å.

3.3.2 Results and discussions of *rf* power absorption in $La_{0.67}Ba_{0.33}MnO_3$ and $La_{0.67}Ba_{0.23}Ca_{0.1}MnO_3$

In this section, we show the *rf* power absorption in two compounds of the LBCMO series: $La_{0.67}Ba_{0.33}MnO_3$ compound and Ca doped $La_{0.67}Ba_{0.33}MnO_3$ *i.e.*, $La_{0.67}Ba_{0.23}Ca_{0.1}MnO_3$ compound.

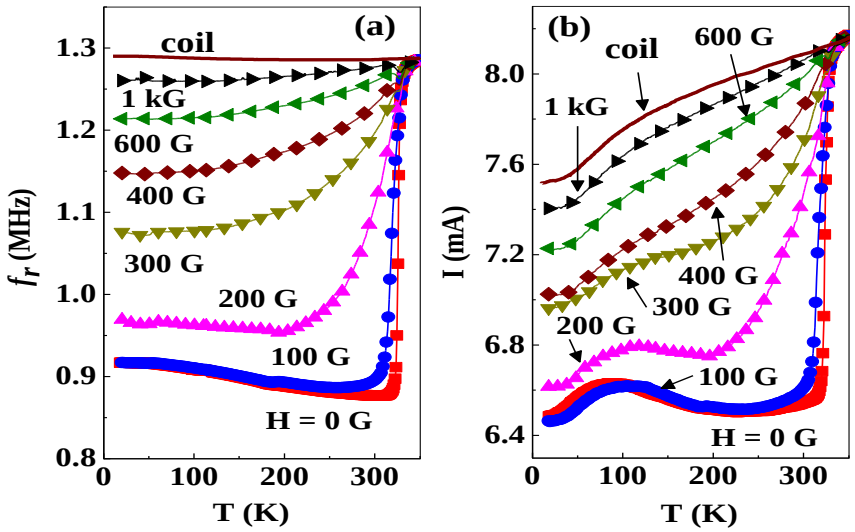

Fig. 3. 3 Temperature dependence of the (a) resonance frequency (f_r) and (b) current (I) through the circuit for different values of external *dc* magnetic fields (H) for $La_{0.67}Ba_{0.33}MnO_3$ compound. The data for empty coil are also included.

Figs. 3.3(a) and 3.3(b) show the temperature dependence of the resonance frequency (f_r) and current (I) through the ICO circuit for various strengths of the external *dc* bias magnetic fields (H = 0-1 kG) applied along the coil axis, respectively for $La_{0.67}Ba_{0.33}MnO_3$ compound. We have also shown the temperature dependence of I and f_r for the empty coil for comparison. In the absence of external magnetic field (H = 0), the f_r of the tank circuit loaded with the sample increases gradually with increasing temperature from 10 K but shows steep increase just below T_C = 321 K and becomes nearly temperature independent above 321 K. It is interesting to note that f_r increases as much as $\Delta f = f_r$ (330 K) - f_r(322 K) = (1.26 - 0.89) MHz = 370 kHz within an interval of ΔT = 8 K around T_C. A small magnetic field of H = 100 G hardly affects f_r below 200 K, but an appreciable change occurs close to T_C. However, f_r is enhanced over a wide temperature range below T_C and a broad minimum occurs around T = 186 K < T_C under H = 200 G. The largest change in f_r occurs just below T_C. The broad minimum is no more visible at higher fields. Instead, f_r smoothly increases from 10 K and changes rapidly as it approaches T_C at higher fields. For $H \geq 1$ kG, f_r appears to approach the value of the empty coil. Whereas, the current I in the circuit as like the resonance frequency increases sharply around T_C in H = 0 G upon warming. Although the abrupt change in the current at T_C is suppressed, the magnitude of the current at the lowest temperature increases with increasing strength of the *dc* magnetic field. A broad maximum appears around 100 K in H = 0 G and 100 G, and it is suppressed with increasing field. We do not have a clear understanding of its origin, but we note that it may be connected with the temperature dependence of resistivity of copper coil used for the inductor. The significant point here is that both I and f_r change appreciably in zero magnetic field at T_C and the applied magnetic field strongly affects the behavior of both, unlike in the case of a highly insulating multiferroic $GaFeO_3$ compound where I showed a very weak anomaly at T_C and the effect of magnetic field is also not very appreciable. [153] Next we show the response of both I and f_r for $La_{0.67}Ba_{0.23}Ca_{0.1}MnO_3$ compound.

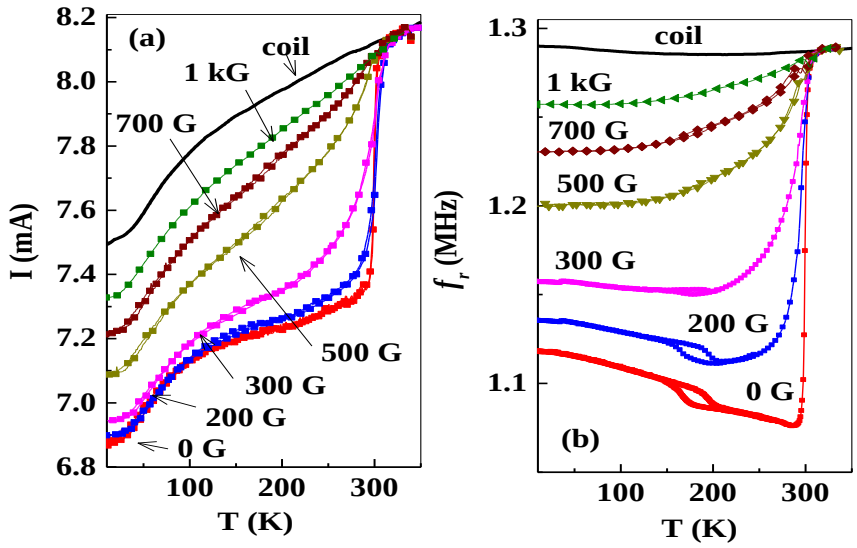

Fig. 3. 4 Temperature dependence of the (a) current (*I*) through the circuit, (b) resonance frequency (f_r) of ICO under different external dc magnetic fields (*H*) for $La_{0.67}Ba_{0.23}Ca_{0.1}MnO_3$ compound.

In Fig. 3.4, we show the temperature dependence of *I* drawn by the ICO circuit [Fig. 3.4(a)] and the f_r of the oscillator [Fig. 3.4(b)] under different *dc* bias magnetic fields (H = 0-1 kG) applied along the coil axis for $La_{0.67}Ba_{0.23}Ca_{0.1}MnO_3$ compound. The data for the empty coil are also shown for comparison. The I (H = 0) initially decreases with lowering temperature from 321 K, but then shows a sudden decrease at the onset of paramagnetic to ferromagnetic transition (T_C = 300 K) followed by a broad hump around 100 K below which it decreases. A small magnetic field of H = 200 G suppresses the minimum in I around T_C, while the low temperature part is unaffected. As H increases, the minimum in I considerably gets suppressed around T_C and the magnitude of I at low temperature also increases. On the other hand, the temperature dependent f_r shows a remarkable feature. The f_r in zero field dramatically decreases as much as Δf_r = (1.288 - 1.074) MHz = 214 kHz at the para-ferromagnetic transition with lowering temperature. Interestingly, the f_r shows a step-like anomaly below the ferromagnetic ordering around T^* = 165 K while cooling which shifts to 195 K while warming, thus leading to a clear thermal hysteresis. On the application of a small magnetic field of 200 G, the abrupt decrease in f_r gets suppressed, but the hysteresis is still visible. As the strength of the applied magnetic field increases, the abrupt decrease in f_r at T_C

transforms into a broad hump with increase in f_r values. In addition, the hysteresis has completely vanished for $H \geq 300$ G.

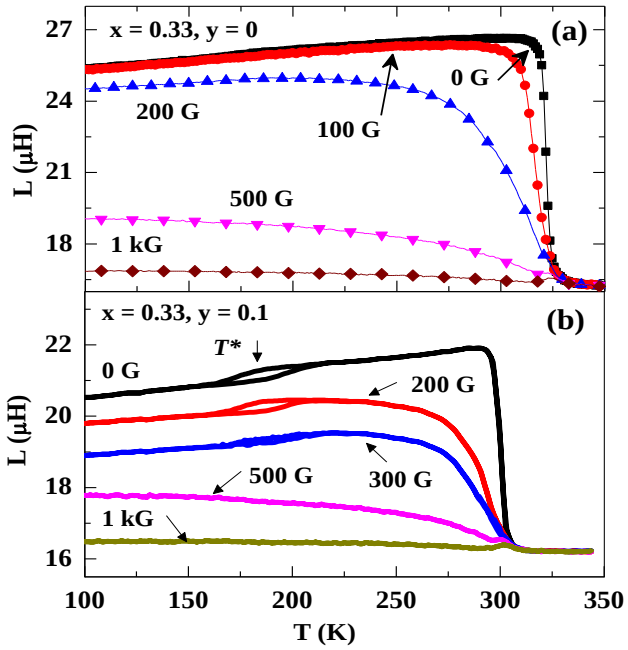

Fig. 3. 5 Temperature dependence of the *ac* inductance (*L*) of a solenoid loaded with sample under different *dc* bias magnetic fields for (a) $La_{0.67}Ba_{0.33}MnO_3$ and (b) $La_{0.67}Ba_{0.23}Ca_{0.1}MnO_3$ compounds.

Fig. 3.5(a) and Fig. 3.5(b) show the temperature dependence of the ac inductance (*L*) of a solenoid loaded with sample measured at f = 30 kHz under different *dc* external magnetic fields applied parallel to the long axis of the coil for $La_{0.67}Ba_{0.33}MnO_3$ and $La_{0.67}Ba_{0.23}Ca_{0.1}MnO_3$ compounds. Let us first discuss the results of $La_{0.67}Ba_{0.33}MnO_3$. The *ac* inductance is small and is independent of temperature above 330 K, but it increases rapidly around T_C and exhibits a peak close to T_C = 321 K in the absence of an external magnetic field. The peak decreases in magnitude, broadens and shifts down in temperature with increasing strength of the magnetic field. On the other hand, the *ac* inductance of a solenoid loaded with $La_{0.67}Ba_{0.23}Ca_{0.1}MnO_3$ sample shows an interesting feature at low temperature. While the behavior of *L* around T_C = 300 K is similar to that of $La_{0.67}Ba_{0.33}MnO_3$, a step-like anomaly occurs around T = 165 K = T^* while cooling and it is shifted to T = 195 K while warming as in Fig. 3.4(b). As a consequence, a clear thermal hysteresis is seen between 165 K

and 195 K. On the application of a dc magnetic field of H = 200 G, the value of L at T_C reduces more significantly than at the low temperature. However, both the low temperature anomaly and the hysteresis completely vanished for H > 300 G. As H increases further, the peak at T_C reduces in magnitude and becomes more broadened. The suppression and broadening of the susceptibility peak is due to the suppression of spin fluctuations and also due to the inability of the small *ac* magnetic field to induce domain wall motion when the direction of domain magnetization is fixed by the larger *dc* magnetic field. As the *dc* magnetic field strength increases, domain rotation and the effect of *ac* magnetic field in reversing the domain magnetization have also to be considered.

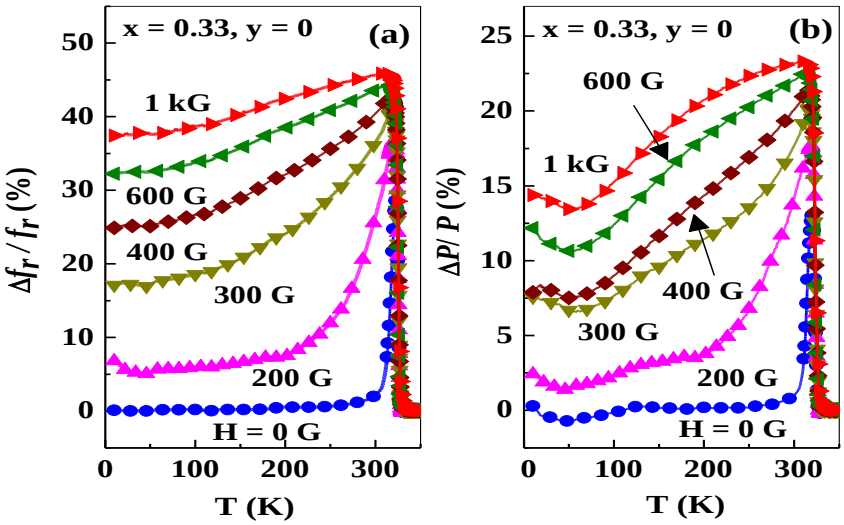

Fig. 3. 6 Temperature dependence of the percentage change in the (a) resonance frequency ($\Delta f_r/f_r$) and (b) power absorption ($\Delta P/P$) for different values of the external magnetic fields (H) for $La_{0.67}Ba_{0.33}MnO_3$ compound.

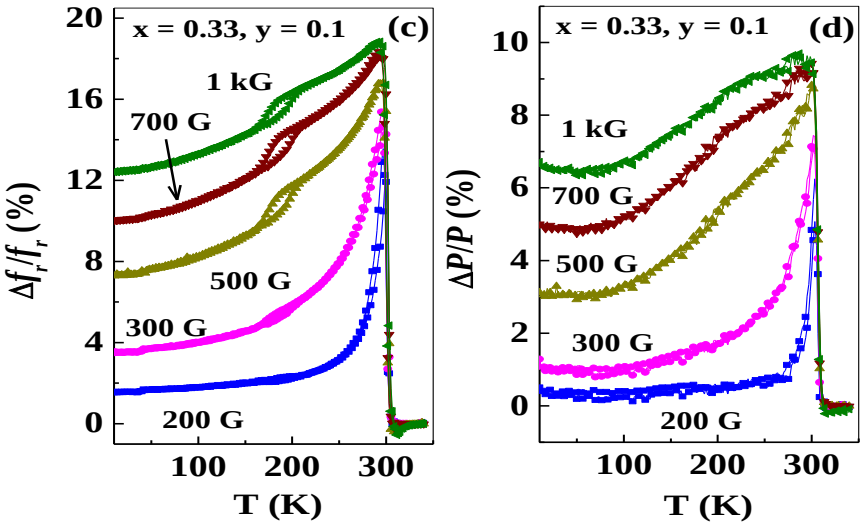

Fig. 3. 7 Temperature dependence of the percentage change in the (a) resonance frequency ($\Delta f_r/f_r$) and (b) power absorption ($\Delta P/P$) for different values of the external magnetic fields (H) for $La_{0.67}Ba_{0.23}Ca_{0.1}MnO_3$ compound.

Next we show the temperature dependence of the fractional changes in the resonance frequency [$\Delta f_r/f_r = [f_r(H)-f_r(0)] / f_r(0)$] and power absorption [$\Delta P/P = \Delta I/I = [I(H)-I(0)] / I(0)$] as a function of temperature at different magnetic fields for $La_{0.67}Ba_{0.33}MnO_3$ sample in Fig. 3.6(a) and 3.6(b), respectively. Here, the power drawn by the ICO circuit from the dc power supply is $P = IV$ (I is the dc current drawn from, and V is the constant dc voltage supplied by the power supply), the change in I implies the power absorption by the sample under magnetic field in the coil. The $\Delta f_r/f_r$ at H = 100 G is nearly zero below 290 K, but it increases and exhibits a sharp peak of magnitude $\Delta f_r/f_r$ = 28% at T_C = 321 K and drops to zero above T = 328 K. As H increases, the magnitude of the peak also increases and it broadens on the low temperature side. The $\Delta f_r/f_r$ reaches a maximum value of ≈ 46% for H = 1 kG at T_C, but its magnitude at T = 10 K is still large (≈37%). A similar trend is also seen in $\Delta P/P$. The magnitude of the peak increase from $\Delta P/P$ ≈13% at H = 100 G to ≈ 23% at H = 1 kG. At the same time, the value of $\Delta P/P$ for $T << T_C$ also increases with the field. As a result, we observe a maximum at T_C instead of a sharp peak at higher fields. Similar results of the fractional changes in f_r and I for $La_{0.67}Ba_{0.23}Ca_{0.1}MnO_3$ sample are shown in Fig. 3.7(a) and 3.7(b),

respectively. Both $\Delta f_r/f_r$ and $\Delta P/P$ show a peak close to T_C = 300 K and its magnitude increases with H. While the magnitude of $\Delta f_r/f_r$ attains a maximum value of 19% at H = 1 kG around T_C, the $\Delta P/P$ showed a maximum value of 9.5%. Interestingly, as H increases above H = 300 G, a clear hysteresis is seen in $\Delta f_r/f_r$ at low temperature (T^*) which is due to the effective suppression of the low temperature anomaly at higher magnetic fields ($H \geq$ 500 G).

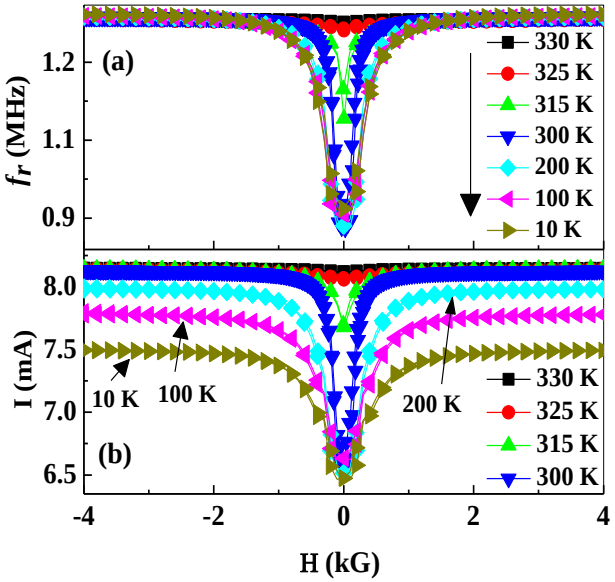

Fig. 3. 8 Magnetic field dependence of the (a) resonance frequency (f_r) and (b) current (I) at selected temperatures for $La_{0.67}Ba_{0.33}MnO_3$ compound.

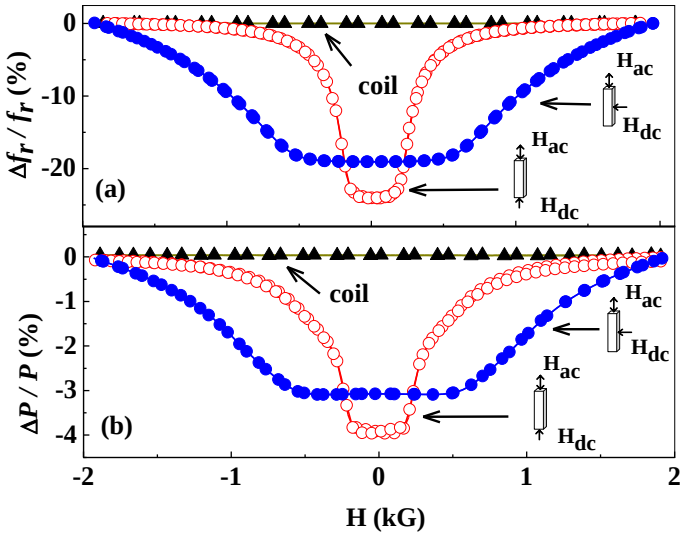

Fig. 3. 9 Magnetic field dependence of (a) $\Delta P/P$ and (b) $\Delta f_r/f_r$ at T = 300 K for $La_{0.67}Ba_{0.33}MnO_3$ compound when the coil axis is parallel and perpendicular to the *dc* magnetic field direction. The relative directions of the *dc* and *ac* magnetic fields are shown in the insets.

We have also studied the field dependences of f_r and I at selected temperatures and the effect of demagnetizing field. The field dependences of f_r and I of $La_{0.67}Ba_{0.33}MnO_3$ and $La_{0.67}Ba_{0.23}Ca_{0.1}MnO_3$ samples are similar, hence we show only the results of $La_{0.67}Ba_{0.33}MnO_3$. Fig. 3.8 shows the magnetic field dependence of (a) f_r and (b) I at selected temperatures as the field is swept through H = +4 kG → -4 kG → +4 kG. As it can be seen in Fig. 3.8(a), the f_r is independent of H above T_C = 321 K. However, f_r changes from almost saturation for $H \geq \pm 3$ kG to a rapid decrease below ±2 kG followed by a minimum at the origin for $T < T_C$. The current I also shows a similar trend with a minimum at the origin and almost saturation at higher fields. On the other hand, the effect of orientation of the sample with applied dc magnetic field, which was studied using a variable field electromagnet at room temperature, revealed interesting features. Fig. 3.9(a) shows a comparison of $\Delta f_r/f_r$ at T = 300 K for $La_{0.67}Ba_{0.33}MnO_3$ compound in a narrow field interval of -2 kG $\leq H \leq$ 2 kG when the *dc* magnetic field (H_{dc}) is parallel and perpendicular to the length of the sample and hence to the coil axis. In the parallel configuration, H_{ac} (ac magnetic field in the inductance coil due to *rf* current supplied by the oscillator) and H_{dc} are parallel to each other, whereas they are transverse to each other in the perpendicular configuration. A similar comparison for $\Delta P/P$ is shown in Fig. 3.9(b). The normalization was done here for f_r and P values at the highest field (H = 2 kG). In the parallel configuration, $\Delta f_r/f_r$ shows a plateau between -200 G $\leq H \leq$ +200 G followed by increase in the intermediate field range and saturation at H = ±2 kG. In the perpendicular configuration, the plateau in $\Delta f_r/f_r$ extends to higher fields (H = ±600 G) and the saturation is not achieved even at H = 2 kG. The overall magnitude of the $\Delta f_r/f_r$ also decreases from 20% for parallel to 25% for perpendicular configuration. The $\Delta P/P$ shown in Fig. 3.9(b) shows a similar non saturation behavior in the perpendicular configuration. The change in $\Delta P/P$ is larger ≈ 4% for the parallel case than ≈ 3% for the perpendicular case. These differences can be attributed to differences in the internal magnetic fields ($H_{int} = H_{dc}+H_{demag}$) felt by the sample as the demagnetizing fields ($H_{demag} = -DM_{sat}$) are different when

the applied *dc* magnetic field is parallel (D = 0) and perpendicular (D = ½) to the length of sample.

The resonance frequency of the parallel LC tank circuit is

$$f_r = \frac{1}{2\pi\sqrt{LC}}$$

where L is the inductance of the empty coil and C is the capacitance in the circuit. The resonance frequency, upon insertion of a metallic sample, changes due to two reasons, one is due to the true magnetic response, *i.e.*, a change in the real part *rf* magnetic permeability μ' of the sample following the magnetic induction

$$B_{ac} = \mu H_{ac}, \text{ [125]}$$

and the other one is the change in the electromagnetic permeability due to the induced eddy currents which screens the alternating magnetic field from the interior of the sample *i.e.*, due to change in magnetic penetration depth (magnetic skin depth). [154] The relative change in the resonance frequency due to a small change in the penetration depth can be written as $\Delta f_r/f_r = -2(\Delta\delta/\delta)$ based on skin depth.

If the inductance of the coil changes by a small value ΔL (<< L), then the fractional change in the resonance frequency can be approximated as

$$\frac{\Delta f_r}{f_r} \approx -\frac{1}{2}\frac{\Delta L}{L} = -\frac{1}{2}(\eta\chi' + 2\eta\frac{\Delta\delta}{\delta})$$

where $\eta = \frac{V_S}{V_C}(1-D)$ is the filling factor, V_S and V_C are the volumes of the sample and the coil, respectively, D is the demagnetization factor, χ' is the real part of the *rf* susceptibility of the sample. In our experiment, η = 0.24. For a highly insulating sample, the dominant contribution to $\Delta f_r/f_r$ comes mainly from χ' whereas incomplete penetration of the *ac* magnetic field due to the induced eddy current causes additional contribution in the metallic samples through the second term $\Delta\delta/\delta$. Thus, the rapid increase in f_r around T_C in zero field can be attributed to the abrupt decrease in the real part of the initial *rf* susceptibility or permeability (μ') upon transition from the ferromagnetic to paramagnetic state while

warming. As our samples are metallic ($d\rho/dT < 0$), the penetration depth (δ) increases with increasing temperature from its lowest value, 10 K and it is expected to show a minimum at T_C and hence f_r shows a minimum at T_C. The application of the external magnetic field decreases the *rf* permeability and increases the penetration depth which leads to increase in f_r. The suppression of spin fluctuations by external magnetic field can further aid a dramatic decrease in μ' leading to a dramatic change in $\Delta f_r/f_r$ at T_C.

On the other hand, the power absorption by the material changes the complex impedance (Z) of the tank circuit. The rapid decrease in I at T_C upon cooling implies the increase in the ac impedance of the coil, $Z = \frac{V_{ac}}{I_{ac}}$, where V_{ac} and I_{ac} are the voltage across and the current in the coil, respectively upon the paramagnetic to the ferromagnetic transition. The power absorption is related to the real part of the impedance, Re(Z), through the relation

$$P = \tfrac{1}{2} H_{ac}^2 \mathrm{Re}(Z)$$

where H_{ac} is the ac magnetic field in the coil. [155] The increase in the *rf* impedance implies increase in the *rf* power absorption by the sample. The impedance of the coil without the sample is $Z = R_0 + i\omega L_0$, where R_0 and L_0 are the resistance and the inductance of the coil, respectively. Upon insertion of the sample in the inductance coil, the inductance of a coil becomes $L = L_0(1+\eta\mu)$, where η is the filling factor and $\mu = 1+\chi' - i\chi''$ is the magnetic permeability of the sample with real (χ') and imaginary (χ'') parts of the susceptibilities. Hence, the ac impedance takes the form: $Z = R_0 + (\Delta R) + i\omega L_0 + (\Delta L)$

where, $\Delta R = \omega L_0 \eta \chi''$ is the change in the resistance and $\Delta L = i\omega L_0 \eta (1+\chi')$ is the change in the inductance of a coil due to the insertion of the sample. Thus, in the weak skin effect regime, the power absorption per unit volume of the sample is given by

$$P_{ac} = I_{ac}^2 \Delta R = I_{ac}^2 \omega L_0 \eta \chi'' .$$

Thus, the effective resistance of the coil increases due to the magnetic loss characterized by χ''. The above relation is true for highly insulating materials for which the

electromagnetic field completely penetrates the sample and it has to be modified for metals, since the eddy current shields the external magnetic field. It was shown earlier [156] that the electrical impedance (Z) of $La_{0.75}Sr_{0.25}MnO_3$ dramatically increases at the T_C even in $\mu_0 H = 0$ T when high frequency current ($f > 1$ MHz) flows through the sample. That was related to increase in the surface impedance of the sample $Z = (1+j)\rho/\delta = \sqrt{(j\omega\mu\rho)}$, where $j = \sqrt{-1}$. A similar situation exists in our study, where the sample is subjected to *rf* magnetic field by the inductor. The real part of the surface impedance given is by,

$$\mathrm{Re}(Z) = \sqrt{\omega\rho\sqrt{(\mu'^2 + \mu''^2)} + \mu''}$$

which depends both on the real and imaginary (μ'') components of the *rf* permeability. The Re(Z) increases from low temperature, shows a sharp peak just below the Curie temperature and decreases to a small value in the paramagnetic state. Hence, a sudden increase in the *rf* current through the circuit is observed at T_C as expected. The suppression of μ' and μ'' by the external magnetic field results in negative magnetoimpedance which leads to magnetically tunable *rf* wave absorption in our sample. It is to be mentioned here that the magnitude of magnetoimpedance in amorphous metallic ribbons and nanocrystalline alloys are much larger than in perovskite manganites in sub-kilo gauss magnetic fields. [157] Nevertheless, the physics of electrical conduction and magnetism in manganites and amorphous metallic alloys are very different and a thorough investigation of low-field magnetoimpedance for different doping level (x) and comparison with amorphous soft ferromagnets will be a well-deserved study. However, it is also to be mentioned that *rf* power absorption may have other contributions in addition to the magnetoimpedance in other materials.

The important point to be addressed is the origin of the low temperature anomaly found in the temperature dependence of both f_r around $T^* = 165$ K for $La_{0.67}Ba_{0.23}Ca_{0.1}MnO_3$ as well as in the inductance L of a solenoid loaded with sample. The anomaly around $T^* = 165$ K with a clear thermal hysteresis in temperature dependence of both f_r and L is possibly caused by the structural transition. A previous work on $La_{0.67}Ba_{0.33}MnO_3$ [158] has revealed that this compound undergoes a structural transition from a high-temperature rhombohedral

($R\bar{3}c$) phase to a low-temperature orthorhombic (*Imma*) phase around T = 178 K while cooling and the reverse transition occurs around 200 K while warming. The temperature driven structural transition seems to be pervasive in $La_{1-x}Ba_xMnO_3$ series. X-ray diffraction study on single crystalline $La_{1-x}Ba_xMnO_3$ ($0.14 < x \leq 0.25$) by Gavikov *et al*. [159] revealed that the low temperature orthorhombic phase is of *Pbnm* symmetry and the high temperature phase is rhombohedral ($R\bar{3}c$ space group). Both the phases coexist over a temperature interval of ΔT = 150 K for x = 0.14 and 0.15, but reduces to ΔT = 20-30 K for x = 0.2 and 0.25. The X-ray diffraction confirmed that the room temperature structure of the compounds is rhombohedral with $R\bar{3}c$ space group. Hence, the observed low temperature anomaly around T^* = 165 K with thermal hysteresis of 8 K in our $La_{0.67}Ba_{0.23}Ca_{0.1}MnO_3$ compound can be ascribed to the modification in the magnetic domain structure caused by the first-order structural transition from rhombohedral to orthorhombic phase. The suppression of this low temperature anomaly in few hundred Gauss suggests that the differences in the magnetic susceptibility of these two phases are small and the magnetic domain configuration can be easily changed in few hundred Gauss. Since χ'' is expected to be much lower than χ' below the characteristic relaxation frequency connected with either the domain wall relaxation or the domain wall resonance, the anomaly in χ'' is not so clearly visible in the current drawn by the circuit unlike in the case of f_r.

3. 3. 3 Results and discussions of giant magnetoimpedance in $La_{1-x}Ba_{x-y}Ca_yMnO_3$

3. 3. 3. 1 A large magnetoinductance effect in $La_{0.67}Ba_{0.33}MnO_3$

In the previous sections, we have studied magnetoabsorption by the sample when the sample is subjected to *rf* magnetic field inside a solenoid. In this section, we study the influence of *rf* current directly passing through the sample. Here, we report four probe impedance of $La_{0.67}Ba_{0.33}MnO_3$ at f = 100 kHz under different dc bias magnetic fields and show that a conducting ferromagnet like $La_{0.67}Ba_{0.33}MnO_3$ can show a huge magnetoinductance effect ($\Delta X/X = \Delta L/L$ = 60% in H = 1 kG) around the ferromagnetic Curie

temperature. The motivation behind this work is the observation of a huge magnetocapacitance effect (which is considered to be the indirect way of confirming the possible coupling between the electric and magnetic dipoles in the field of multiferroics) in certain manganites. In recent years, multiferroic materials which show coupled magnetic and electric dipoles ordering have received a great attention due to the possibility of controlling the ferroelectric polarization with magnetic field and magnetization with electric field. [96] One of the indications of the coupled magnetic and electrical ordering is the appearance of an anomaly in the dielectric constant (ε) at the magnetic phase transition temperature while varying the temperature. [160] The ε can increase or decrease under an external magnetic field. A large magnetodielectric response around the magnetic phase transition has been reported in manganites of the formula $RMnO_3$ where R = Tb, Gd, Dy etc., [161] and perovskites containing Mn and Ni or Fe ions. [162] These oxides are highly insulating and show negligible magnetoresistance. However, a large increase in the dielectric constant ($\Delta\varepsilon/\varepsilon$ = 60% at $\mu_0 H$ = 0.5 T) was also reported in $La_{0.67}Ca_{0.33}MnO_3$ [163] just above the ferromagnetic Curie temperature (T_C) and in the phase separated $Pr_{0.67}Ca_{0.33}MnO_3$ [164] at low temperature. G. Catalan [165] has suggested that the magnetocapacitance in these materials could be an artifact of magnetoresistance and can be understood through the Maxwell-Wagner relaxation model developed for inhomogeneous semiconductors. A recent theoretical prediction suggests possible occurrence of the magnetocapacitance effect even in the nonmagnetic composite media. [166]

In dielectric measurements, one generally measures the real (Z') and imaginary (Z'') components of the total impedance ($Z = Z'+iZ''$). From the measured impedance, the real (ε') and imaginary (ε'') components of the dielectric permittivity (ε) are calculated using the relations $\varepsilon' = Z''/(\omega C_0 Z^2)$ and $\varepsilon'' = Z'/(\omega C_0 Z^2)$, where C_o is the capacitance of the empty cell with dimensions of the sample. However, if a sample is magnetic and has low resistivity, the measured Z' and Z'' have substantial contribution from the magnetic permeability which can exceed that of the dielectric permittivity. In this case, the change in Z' and Z'' under external

magnetic fields is not necessarily due to magnetocapacitance effect but is caused by variation of magnetic permeability under the magnetic field. Although the idea is simple, it had not yet been investigated carefully. Thus, the purpose of this work is to investigate the impedance behavior of the ferromagnetic conductor $La_{0.67}Ba_{0.33}MnO_3$ and to show that the Z'' is dominated by the self-inductance. In this work, we also show a phenomenon called magnetoimpedance effect that occurs even in absence of magnetoresistance in conducting ferromagnets such as $La_{0.67}Ba_{0.33}MnO_3$. The observed magnetoimpedance effect at low frequencies is attributed to changes in the inductance rather than to the capacitance under an external magnetic field. The results of this study are discussed below in detail.

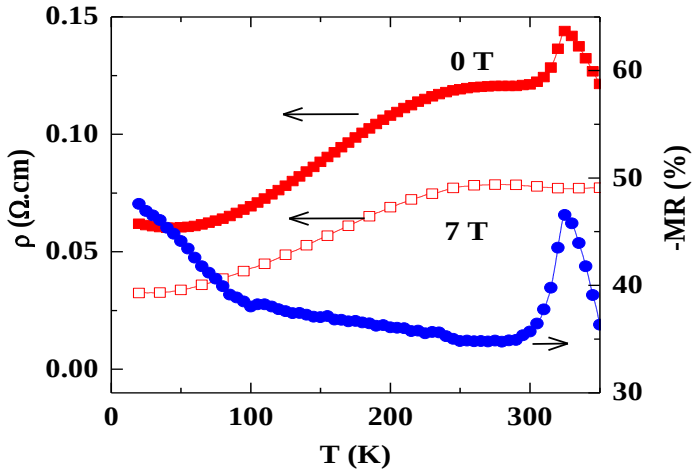

Fig. 3. 10 Temperature of the *dc* resistivity (ρ) of $La_{0.67}Ba_{0.33}MnO_3$ under μ_0H = 0 T and 7 T (left scale) and the magnetoresistance ($\Delta\rho/\rho$) at μ_0H = 7 T (right scale).

Fig. 3.10 shows the temperature dependence of the *dc* resistivity of $La_{0.67}Ba_{0.33}MnO_3$ in zero magnetic field and μ_0H = 7 T (left scale). The sample undergoes a paramagnetic semiconductor to a ferromagnetic metal transition in a zero magnetic field with a peak in $\rho(T)$ at T_P = 325 K. The *dc* magnetoresistance at μ_0H = 7 T shown on the right scale exhibits a peak ($\Delta R/R$ = -47%) close to T = 325 K and it is -50% at T = 10 K. It is known that the *dc* magnetoresistance for $T << T_C$ in ferromagnetic manganites is an extrinsic effect which arises from spin-polarized tunneling of charge carrier between the ferromagnetic grains through spin disordered grain boundaries. [167] Next we show the *ac* resistance (R) and reactance of

$La_{0.67}Ba_{0.33}MnO_3$ at f = 100 kHz under different *dc* magnetic fields applied parallel to the direction of the *ac* current in the sample in Fig. 3.11(a) and 3.11(b), respectively. The R in a zero field exhibits a peak at T_P = 325 K. While the peak is hardly affected as H increases from H = 0 G to H = 1 kG, the *ac* resistance below 300 K decreases slightly. However, the peak decreases in magnitude and shifts to higher temperatures as H increases beyond 1 T as like in the *dc* transport. The X shown in Fig. 3.11(b) shows a spectacular behavior under sub-kilo gauss magnetic fields. The X in a zero field is nearly independent of temperature above T = 330 K, but it steeply increases around T_C = 321 K and shows a peak close to it. The T_C is estimated from the inflection point of the X-T curve. Below the peak, X decreases down to T = 150 K and then shows a tendency to increase with further decrease in T. The X is one order of magnitude lower than R. Very interestingly, the X, unlike R, is very sensitive to sub-kilo gauss magnetic fields as like the inductance L of a solenoid loaded with $La_{0.67}Ba_{0.33}MnO_3$ sample shown in Fig. 3.5(a). The peak decreases in magnitude and broadens as H increases from 0 to 500 G. The peak is no more visible for H = 700 G or above. Instead, we notice only a gradual increase of X with lowering temperature below 325 K. A similar behavior is seen in X up to $\mu_0 H$ = 7 T.

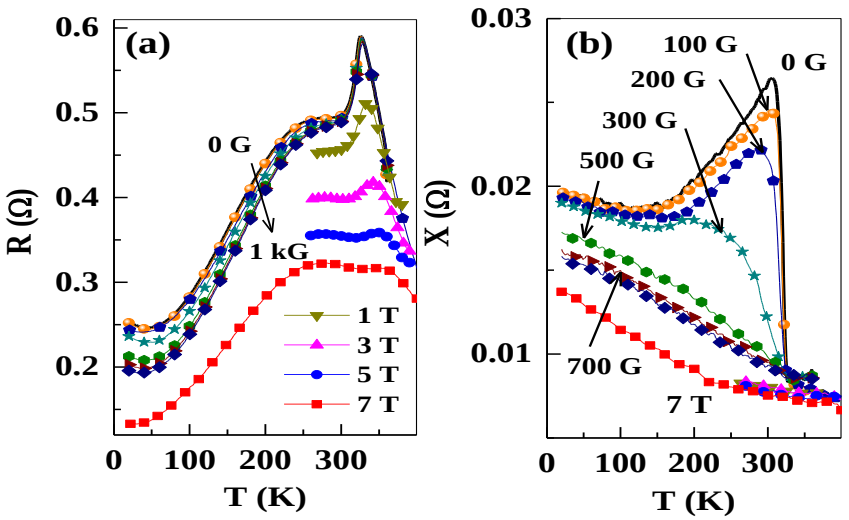

Fig. 3. 11 Temperature dependence of the (a) *ac* resistance (R) and (b) reactance (X) under different *dc* bias fields (H) at f = 100 kHz for $La_{0.67}Ba_{0.33}MnO_3$.

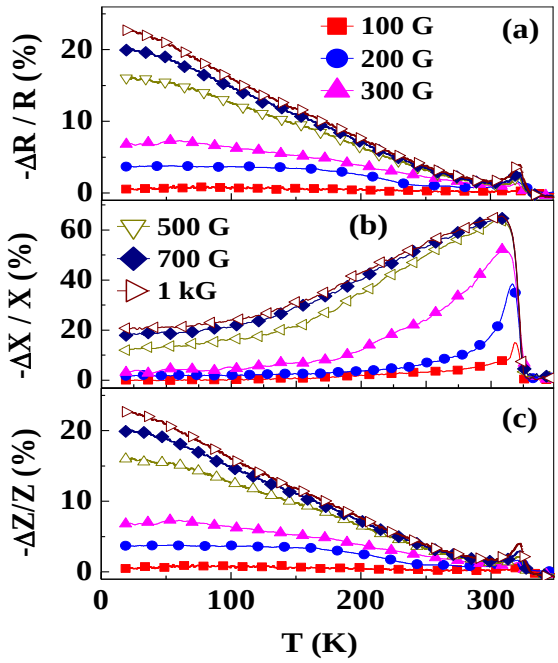

Fig. 3. 12 Temperature dependence of the (a) *ac* magnetoresistance (Δ*R*/*R*), (b) magnetoinductance (Δ*X*/*X*) and (c) magnetoimpedance (Δ*Z*/*Z*) under different *dc* bias magnetic fields at *f* = 100 kHz for $La_{0.67}Ba_{0.33}MnO_3$ compound.

We show the percentage change in the ac magnetoresistance

$$\frac{\Delta R}{R} = \frac{R(H)-R(0)}{R(0)}\times 100\% \quad \text{and the magnetoreactance} \quad \frac{\Delta X}{X} = \frac{X(H)-X(0)}{X(0)}\times 100\%$$

under different *dc* magnetic fields for $H \leq 1$ kG in Fig. 3.12(a) and (b), respectively. The value of $\Delta R/R$ at H = 100 G is very small and does not show a peak around T_C. As H increases, a peak in $\Delta R/R$ emerges at T_C. In addition, the ac magnetoresistance at the lowest temperature also increases in magnitude. For instance, the magnitude of peak at T_C attains a maximum value of 5% at 1 kG, but it increases to ≈ 22% at T = 10 K. On the other hand, $\Delta X/X$ shows a sharp peak at T_C and decreases with lowering temperature. The magnitude of the peak in $\Delta X/X$ increases from ≈ 10% at H = 100 G to a huge value of ≈ 60% at H = 1 kG. Thus, the magnitude of the magnetoreactance far exceeds that of the ac magnetoresistance at the same field strength. The position of the $\Delta X/X$ peak is not much affected by the magnetic field. We find that the value of $\Delta X/X$ at the lowest temperature also increases in magnitude as H increases from 100 G to 1 kG, but it is still lower than its peak value at all values of H

below 1 kG. Fig. 3.12(c) shows the magnetoimpedance ($\Delta Z/Z$) which reaches a maximum value of 5% at the peak at 1 kG and it is dominated by the behavior of the *ac* magnetoresistance. The observed $\Delta Z/Z$ at f = 100 kHz and T = 200 K is slightly lower than 10% reported in a similar composition by Hu *et al*., [168] but their samples showed a semiconductor-metal transition around 200 K which was much below the onset of ferromagnetic transition.

Let us now discuss the origin of the spectacular features seen in *X* under sub-kilo gauss magnetic fields. It is known that low field magnetoresistance in polycrystalline manganites arises from tunneling of the spin polarized e_g-holes between ferromagnetic grains separated by high resistive grain boundaries. The monotonic increase of $\Delta R/R$ below the peak suggests that the tunneling magnetoresistance is still active at f = 100 kHz. We are more concerned with the huge magnetoreactance observed. Generally, the reactance in polycrystalline manganites is attributed to intra- and inter-grain (grain boundary) capacitances. Glazer and Zieze [169] showed that the capacitance of grain boundaries formed at step-edges in $La_{0.7}Ca_{0.3}MnO_3$ film is negligible in the paramagnetic state but increases below the T_C. Their model indicated that the capacitance increases with the second power of the difference between grain and grain-boundary magnetization below T_C. They concluded that the capacitance follows more closely the grain boundary magnetization. Although it is tempting to attribute the observed magnetoreactance to magnetocapacitance effect, we would like to consider other possibility. It is known that if an alternating current,

$$I(t) = I_0 e^{i\omega t}$$

flows through a ferromagnetic metal of resistance R, the *ac* voltage drop across a ferromagnetic conductor is not simply $V(t) = I(t)R$, but

$$V(t) = I(t)R + \frac{L\mathrm{d}I(t)}{\mathrm{dt}}$$

where L is the self-inductance of the sample. Thus, the impedance is

$$Z = \frac{V(t)}{I(t)} = R + j\omega L = R + jX$$

Hence, the reactance is proportional to the self-inductance of the sample, which in turn is proportional to the initial permeability of the sample though the relation,

$$X \propto \mu_t$$

where $X = \omega L = \omega G \mu_t$ (G is the geometrical factor). Thus, X is the dominant factor. Hence, the observed peak in X at T_C and its suppression in a small magnetic field can be understood in terms of magnetoinductance. The similarity between the observed *ac* inductance using coil shown in Fig. 3.5(a) and X under different biased *dc* magnetic fields shown in Fig. 3.11(b) supports the magnetoinductance effect rather than the magnetocapacitance effect. Similar results can be also obtained from the classical theory of electromagnetic wave propagation in solids and it is discussed at the end of this chapter.

3. 3. 3. 2 *rf* detection of structural anomaly and giant magnetoimpedance in $La_{1-x}Ba_{x-y}Ca_yMnO_3$ (x = 0.33, 0.25, 0.2 and y = 0, 0.1)

In this section, we report *rf* magnetotransport in $La_{1-x}Ba_{x-y}Ca_yMnO_3$ compounds (x = 0.33, 0.25, 0.2 with y = 0 and x =0.33 with y = 0.1) by measuring the ac resistance R and reactance X simultaneously as a function of temperature and magnetic field while passing the *rf* current directly through the sample in the frequency range f = 0.1-20 MHz using the impedance spectroscopy. We observe a remarkable feature in X for $f \leq 5$ MHz and in R for $f \geq$ 10 MHz in all the compounds around T^* which is well below the ferromagnetic Curie temperature. We suggested this low temperature anomaly in both X and R at T^* is due to a structural phase transition from the high temperature rhombohedral phase to the low temperature orthorhombic phase as discussed in the section 3.3.3 of this chapter. In this section, we show that that the *rf* electrical transport measurement using impedance spectroscopy is a useful method to enhance magnetoresistance and to investigate the structural and magnetic transition in manganites.

We first show the temperature dependences of the ac resistance $R(T, f)$ and reactance $X(T, f)$ under zero magnetic field for selected frequencies (f = 0.1, 1, 2, 3 and 5 MHz) in Fig. 3.13 for four compositions of LBCMO series. The results of $La_{0.67}Ba_{0.33}MnO_3$ (x = 0.33), $La_{0.75}Ba_{0.25}MnO_3$ (x = 0.25), $La_{0.8}Ba_{0.2}MnO_3$ (x = 0.2) and $La_{0.67}Ba_{0.23}Ca_{0.1}MnO_3$ (y = 0.1) are shown in the figures [(a), (e)], [(b), (f)], [(c), (g)] and [(d), (h)], respectively. While the R of x = 0.33 and 0.25 compounds for $f \leq 2$ MHz show a peak close to their respective T_Cs and a gradual decrease with decreasing T below T_C, a step-like increase around T_C is seen in R for $f \geq 3$ MHz. A similar behavior of R is seen for x = 0.2 and y = 0.1 compounds, except that R shows a broad hump around T = 190 K for x = 0.2 and T = 225 K for y = 0.1. The value of R increases in the entire temperature range with increasing f for all compounds. On the other hand, the X of all four LBCMO samples at all f shows a step-like increase around their respective T_Cs followed by a peak close by and a monotonic decrease with further decrease in T. The inflection point of ac susceptibility versus temperature curve (not shown here) indicates the Curie temperature, which also coincides with inflection point of $X(T)$ for all samples. A remarkable feature in X is the appearance of a low temperature (low-T) peak at a temperature, T^* below T_C for $f \geq 3$ MHz. This low-T peak is clearly visible in X at f = 5 MHz and it is pointed by a downward arrow for all samples. The value of T^* decreases with increasing x *i.e.*, T^* = 190 K for x = 0.33, T^* = 175 K for x = 0.25, T^* = 160 K for x = 0.2 while cooling and it is T^* = 165 K for y = 0.1. Next we show the detailed temperature dependence of both R and X under sub-kilo gauss magnetic fields for selected compounds starting with x = 0.33 compound.

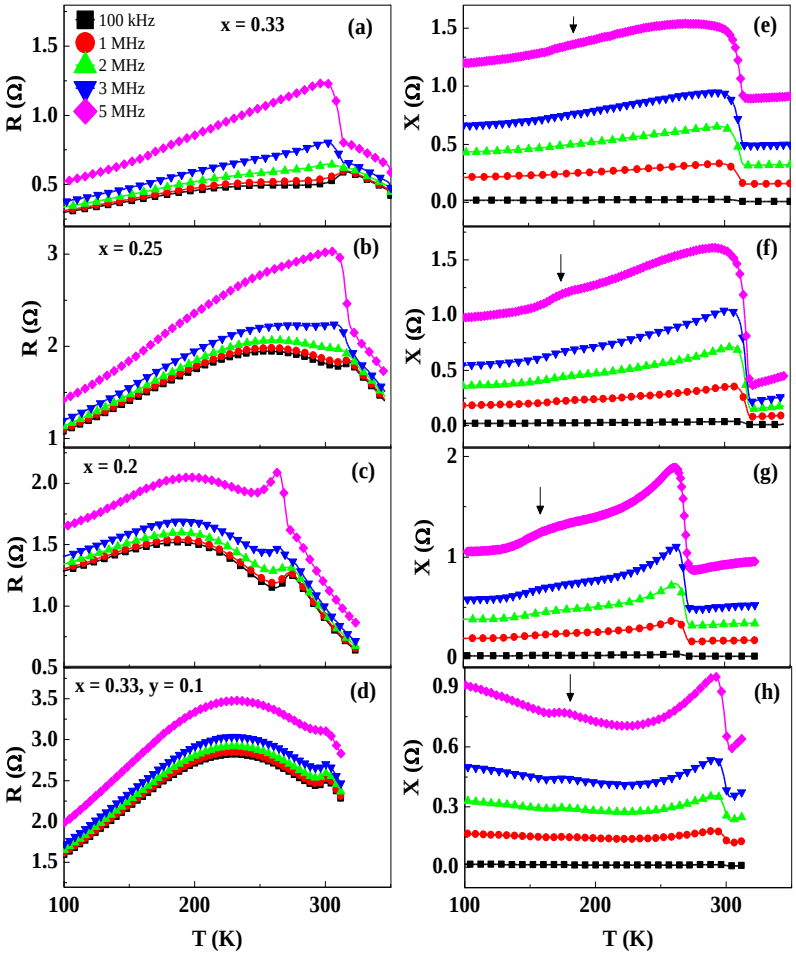

Fig. 3. 13 Temperature dependence of the ac resistance (*R*) and reactance (*X*) under zero field for selected frequencies (*f* = 0.1-5 MHz) for x = 0.33 [(a) and (e)], x = 0.25 [(b) and (f)], x = 0.2 [(c) and (g)] and y = 0.1 with x = 0.33 [(d) and (h)].

Let us first see the response of $R(T, f, H)$ and $X(T, f, H)$ of $La_{0.67}Ba_{0.33}MnO_3$ (x = 0.33) compound. We show the temperature dependence of the ac resistance $R(T, f)$ and the reactance $X(T, f)$ under different dc bias fields (H = 0-1 kG) for f = 1 and 5 MHz in Fig. 3.14(a) and 3.14(c), and Fig. 3.14(b) and 3.14(d), respectively for x = 0.33. The zero-field $R(T, 1\ \text{MHz})$ shows a primary peak (α) at the insulator-metal transition, T_{IM} = 325 K similar to $\rho(T)$ in zero field. While the α-peak is hardly affected under low magnetic fields (H < 1 kG), the magnitude of the peak decreases and shifts to higher temperature as H increases above 1 T. On the other hand, $R(T, 5\ \text{MHz})$ shows an interesting feature. The primary peak (α) seen in $R(T, 1\ \text{MHz})$ at T = 325 K is overshadowed by the appearance of a more pronounced peak (β) at T = 300 K. While the α peak is not affected by low magnetic fields (H

< 1 kG), β peak dramatically decreases in magnitude, becomes smeared and shifts towards low temperature as H increases. Now let us look at the behavior of $X(T, f, H)$. The $X(T,$ 1 MHz) in $H = 0$ rapidly increases around T_C and goes through a peak near T_C. Interestingly, $X(T,$ 1 MHz) shows a spectacular behavior under H. The peak in $X(T,$ 1 MHz) is smeared and decreases in amplitude as H increases from 0 G to 300 G. The peak is completely suppressed under H = 1 kG and $X(T)$ shows a T-independent behavior down to T = 10 K. The most striking feature here is the appearance of a low temperature (low-T) anomaly in $X(T,$ 1 MHz) around T^* = 190 K while cooling which is pointed by a downward arrow (Fig. 3.14c). This low-T anomaly is weakened under H = 300 G and it completely disappears under H = 500 G. The behavior of $X(T,$ 5 MHz) shown in Fig. 3.14(d) is similar to $X(T,$ 1 MHz), except that the low-T anomaly seems to be more pronounced. Next we show the response of $R(T, f, H)$ and $X(T, f, H)$ at higher frequencies (f = 10-20 MHz).

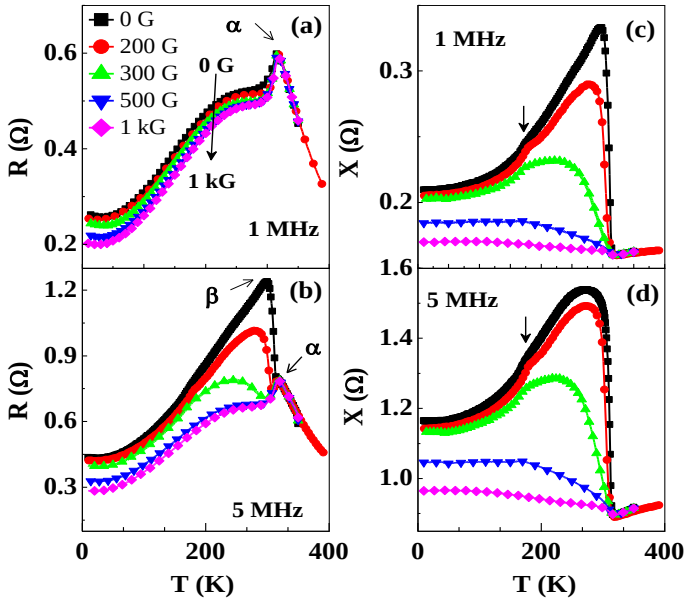

Fig. 3. 14 Temperature dependence of the ac resistance R [(a) and (b)] and reactance X [(c) and (d)] under H = 0-1 kG for f = 1 and 5 MHz for $La_{0.67}Ba_{0.33}MnO_3$.

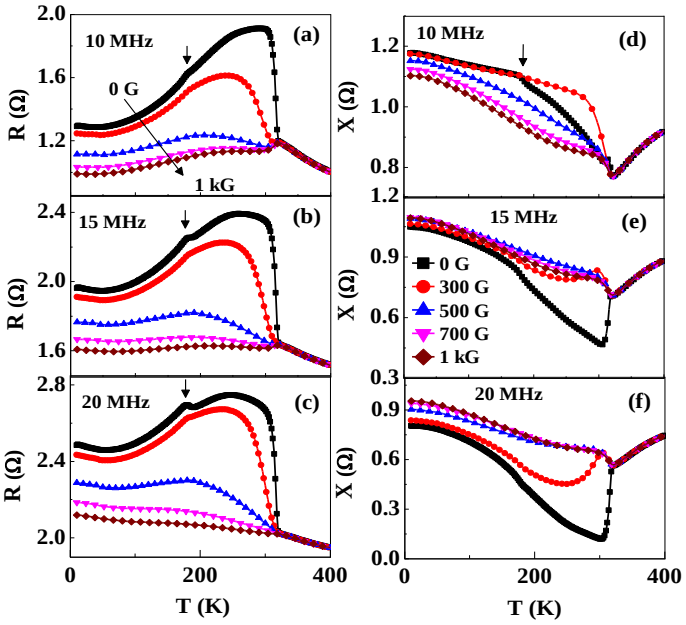

Fig. 3. 15 Temperature dependence of the ac resistance *R* [(a), (b) and (c)] and reactance *X* [(c), (d) and (e)] at different dc bias fields (*H* = 0-1 kG) for *f* = 10, 15 and 20 MHz for $La_{0.67}Ba_{0.33}MnO_3$ (x = 0.33) compound.

The response of *R* and *X* at higher frequencies (*f* = 10, 15 and 20 MHz) as a function of *T* for $H \leq 1$ kG are shown in the Figs. 3.15(a), (b), (c) and (d), (e), (f), respectively. Only β peak is seen in *R*(*T*). The low-*T* anomaly seen in *X*(*T*, 1 MHz) now shows up in *R*(*T*, 10 MHz) around the same temperature (T^* = 190 K) under *H* = 0 G, but it disappears under *H* = 500 G. The β peak decreases in magnitude as *H* increases and shifts towards low-*T*. On the other hand, *X*(*T*, f>5 MHz) shows a completely different behavior as compare to *X*(*T*, $f \leq$5 MHz). In contrast to abrupt increase of *X*(*T*, 5 MHz) at T_C, *X*(*T*, 10 MHz) in zero field shows a sharp decrease at T_C and increases with decreasing *T* below T_C. The low-*T* anomaly is still present around 190 K which is shown by downward arrow. Under sub-kilo gauss *H*, the low-*T* anomaly disappears and the value of *X*(*T*, 10 MHz) decreases below T_C, while the effect of *H* is completely neglected above T_C. Note that *X*(*T*, *H* = 300 G) lies above *X*(*T*, *H* = 0 G) in a narrow temperature range just below T_C. At *f* = 15 and 20 MHz, the *X*(*T*) in zero field shows a sudden decrease below T_C and then increases with further lowering in *T* without showing any low-*T* anomaly. Interestingly, *X*(*T*) at *f* = 15 and 20 MHz increases below T_C with increasing

H. Next we show the similar results of *rf* magnetotransport in $La_{0.8}Ba_{0.2}MnO_3$ (x = 0.2), which showed a more pronounced peak at T^* = 160 K with clear thermal hysteresis while cooling and warming.

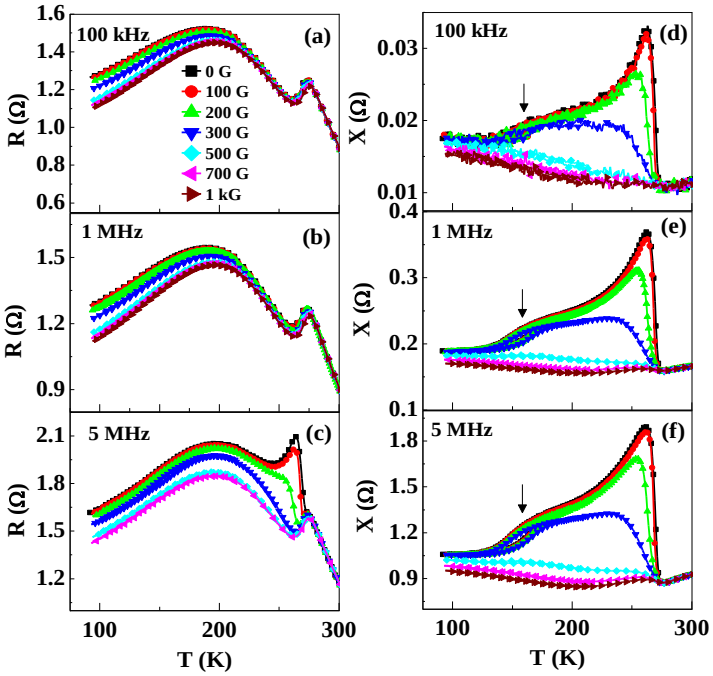

Fig. 3. 16 Temperature dependence of the ac resistance *R* [(a), (b) and (c)] and reactance *X* [(d), (e) and (f)] at different dc bias fields (*H* = 0-1 kG) for *f* = 100 kHz, 1 MHz and 5 MHz for $La_{0.8}Ba_{0.2}MnO_3$ (x = 0.2) compound.

Temperature dependence of the ac resistance $R(T, f)$ and the reactance $X(T, f)$ under different dc bias fields (H = 0-1 kG) for three selected frequencies f = 100 kHz, 1 MHz and 5 MHz are shown in the Figs. 3.16(a), (b), (c) and (d), (e), (f), respectively for $La_{0.8}Ba_{0.2}MnO_3$ (x = 0.2) compound. The zero-field $R(T$, 100 kHz and 1 MHz) shows a peak at the insulator metal transition, T_{IM} = 274 K similar to $\rho(T)$ in zero field and a maximum around T = 190 K. While the sub-kilo gauss magnetic fields (H < 1 kG) hardly affects the peak at T_{IM}, the magnitude of R at low temperature (T < 200 K) decreases with increasing H. Whereas, $R(T$, 5 MHz) shows a rapid increase around T = 265 K *i.e.*, just below the peak. Unlike $R(T$, 100 kHz, 1 MHz), $R(T$, 5 MHz) is sensitive to sub-kilo gauss magnetic fields below T = 265 K. A rapid increase in R dramatically decreases in magnitude, becomes smeared and shifts towards

low temperature as H increases. On the other hand, the $X(T, 100\ kHz)$ in zero field shows a sharp increase around T_C with a peak nearby. The peak in $X(T, 100\ kHz)$ is smeared and decreases in amplitude as H increases from 0 G to 300 G and is completely suppressed under $H > 500$ G. A similar behavior is seen in $X(T)$ at higher frequencies (f = 1 and 5 MHz). The most striking feature here is the appearance of a low temperature (low-T) anomaly in $X(T)$ in the form of a downward step around $T^* = 160$ K while cooling and an upward step around $T^* = 185$ K while warming, which is pointed by a downward arrow (Figs. 3.16d, 3.16e and 3.16f). A clear hysteresis in $X(T)$ occurs between 160 K and 185 K and it is more clear for f = 1 and 5 MHz. The observed hysteresis at low-T is very sensitive to small external dc magnetic fields. The amplitude of the anomaly becomes smaller under $H = 300$ G and is invisible above $H = 300$ G.

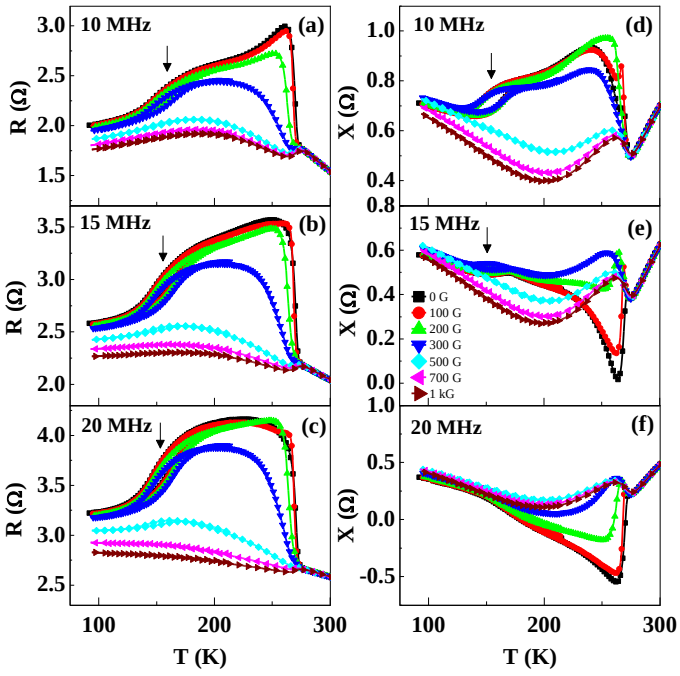

Fig. 3. 17 Temperature dependence of the ac resistance R [(a), (b) and (c)] and reactance X [(c), (d) and (e)] at different dc bias fields (H = 0-1 kG) for f = 10, 15 and 20 MHz for $La_{0.8}Ba_{0.2}MnO_3$ (x = 0.2) compound.

The responses of R and X for $La_{0.8}Ba_{0.2}MnO_3$ at higher frequencies (f = 10, 15 and 20 MHz) as a function of T under H = 0-1 kG while cooling and warming are shown in the Figs. 3.17(a), (b), (c) and 3.17(d), (e), (f), respectively. Unlike the behavior of R at lower

frequencies ($f \leq 5$ MHz), the $R(T, f \geq 10$ MHz, $H = 0$ G) shows a sharp increase around T_C and it is very sensitive to sub-kilo gauss magnetic fields. Interestingly, the low-T anomaly seen in $X(T, f \leq 5$ MHz) at T^* now shows up in R with a clear hysteresis and it is more pronounced at f = 15 and 20 MHz. The applied magnetic field decreases the rapid increase in R and shifts down in T. Both the rapid increase in R and low-T anomaly with hysteresis are completely suppressed for $H \geq 500$ G as like in $X(T, f \leq 5$ MHz). Whereas $X(T$, 10-20 MHz) shows an unusual behavior under sub-kilo gauss magnetic fields. While the $X(T$, 10 MHz) shows a similar behavior as $X(f \leq 5$ MHz), $X(T$, 15 MHz, $H = 0$ G), shows a rapid decrease at T_C followed by a minimum near T_C and then it increases with further decrease in T. The low-T anomaly is still present around T^* with a small hysteresis which is shown by downward arrow. Under sub-kilo gauss H, the low-T hysteresis disappears and the value of $X(T$, 15 MHz) decreases below T_C, while the effect of H is completely neglected above T_C. Note that $X(T, H$ = 300 G) lies above $X(T, H = 0$ G) below T_C, which means there is an increase in the magnitude of X under the magnetic field and is called "positive magnetoreactance effect". However, $X(T$, 20 MHz) in zero field shows a sudden decrease below T_C and then increases with further lowering in T. The low-T anomaly at T^* completely disappeared at f = 20 MHz.

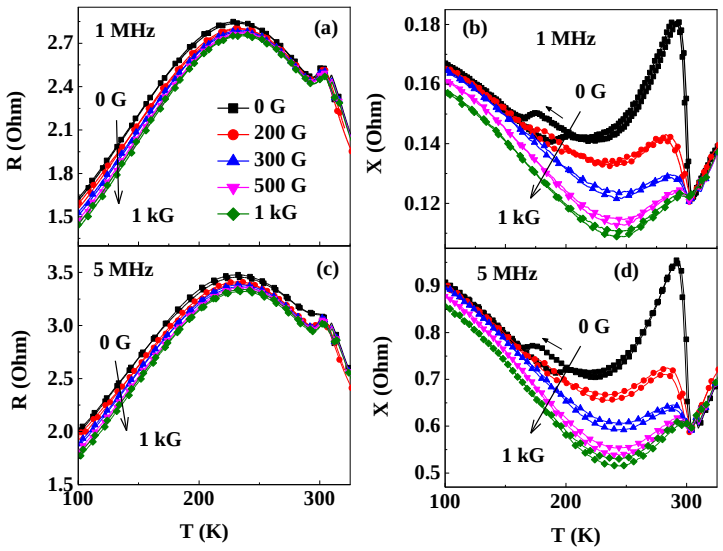

Fig. 3. 18 Temperature dependence of the ac resistance R [(a) and (b)] and reactance X [(c) and (d)] under different dc bias magnetic fields (H = 0-1 kG) for f = 1 and 5 MHz for $La_{0.67}Ba_{0.23}Ca_{0.1}MnO_3$ (y = 0.1 and x = 0.33) compound.

A similar behavior of *R* and *X* also found in Ca doped $La_{0.67}Ba_{0.33}MnO_3$ compound *i.e.*, $La_{0.67}Ba_{0.23}Ca_{0.1}MnO_3$ (x = 0.33 and y = 0.1). Figs. 3.18 shows the responses of *R* and *X* as a function of temperature to applied bias magnetic fields for two frequencies of *f* = 1 MHz and 5 MHz for $La_{0.67}Ba_{0.23}Ca_{0.1}MnO_3$ (y = 0.1 and x = 0.33) compound. The behaviors of both *R* and X are almost similar to $La_{0.8}Ba_{0.2}MnO_3$ compound except that T^* varies from T^* = 165 K while cooling to T^* = 195 K while warming. The two main differences are: 1. the change in *R* at T_C = 300 K for *f* = 5 MHz is not very pronounced compared to $La_{0.8}Ba_{0.2}MnO_3$ compound and 2. *X* continues to increase with lowering *T* below T^*. The behaviors of *R* and *X* at higher frequencies (*f* = 10 MHz, 15 MHz and 20 MHz) for $La_{0.67}Ba_{0.23}Ca_{0.1}MnO_3$ compound shown in Figs. 3.19(a), (b), (c) and 3.19(d), (e), (f), respectively are also almost similar to $La_{0.8}Ba_{0.2}MnO_3$ compound except that the *X* at *f* = 15 and 20 MHz did not show sudden drop just below T_C as like in case of $La_{0.8}Ba_{0.2}MnO_3$. Next we show the fractional changes in both *R* and *X* for selected samples *i.e.*, x = 0.33 and 0.2.

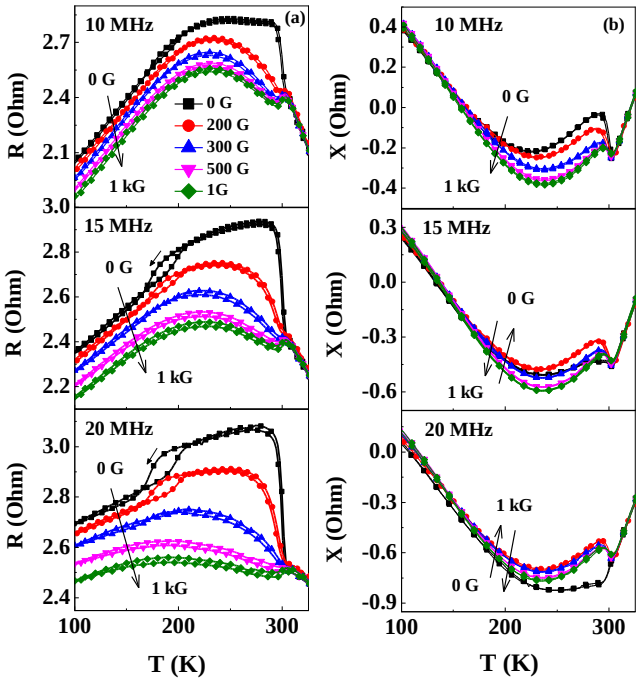

Fig. 3. 19 Temperature dependence of the ac resistance *R* [(a), (b) and (c)] and reactance *X* [(c), (d) and (e)] at different dc bias fields (*H* = 0-1 kG) for *f* = 10, 15 and 20 MHz for $La_{0.67}Ba_{0.33}Ca_{0.1}MnO_3$ (y = 0.1 and x = 0.33) compound.

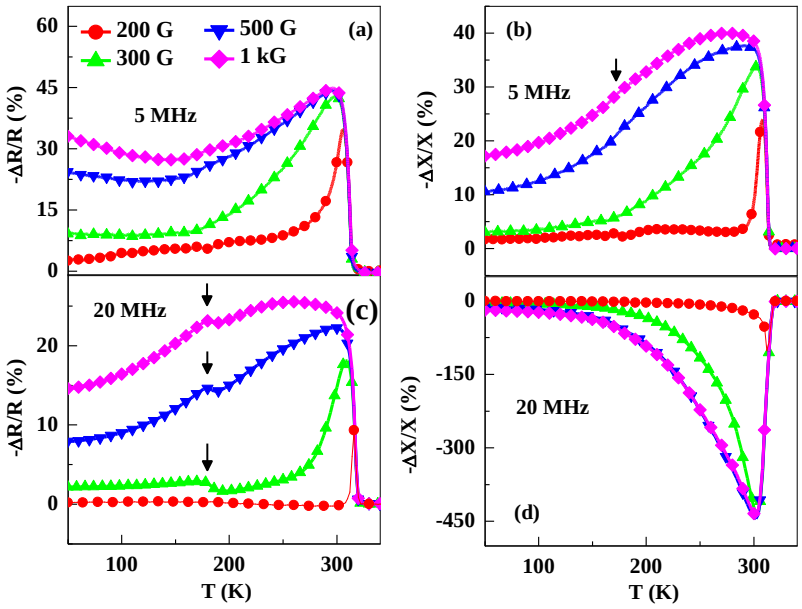

Fig. 3. 20 Temperature dependence of the ac magnetoresistance ($\Delta R/R$) [(a) and (b)] and magnetoreactance ($\Delta X/X$) [(c) and (d)] at H = 200 G - 1 kG for two selected frequencies, f = 5 and 20 MHz for $La_{0.67}Ba_{0.33}MnO_3$ (x = 0.33) compound. The frequency dependence of the ac (e) magnetoresistance ($\Delta R/R$) and (f) magnetoreactance ($\Delta X/X$) at T = 300 K and H = 500 G.

The Figs. 3.20(a), (b) and 3.20(c), (d) show the temperature dependence of the fractional changes in the ac magnetoresistance $\{\Delta R/R = [R(H) - R(0)] / R(0)\}$ and the magnetoreactance $\{\Delta X/X = [X(H) - X(0)] / X(0)\}$ at different dc bias fields ($H \leq 1$ kG) for two selected frequencies, f = 5 and 20 MHz, respectively for $La_{0.67}Ba_{0.33}MnO_3$ (x = 0.33) compound. The $\Delta R/R$ at f = 5 MHz under H = 200 G is zero above T_C, but shows an abrupt increase around T_C and a peak close by. As H increases, the magnitude of the peak at T_C increases from 35% at H = 200 G to 45% at H = 1 kG. In addition, the value of $\Delta R/R$ at low temperature also increases as H increases. The $\Delta R/R$ at f = 20 MHz shows a rapid increase around T_C as like f = 5 MHz, but interestingly it shows a pronounced anomaly at T^* = 190 K under all magnetic fields. While $\Delta X/X$ at f = 5 MHz shows a similar behavior as $\Delta R/R$, $\Delta X/X$ at f = 20 MHz shows an unusual behavior. At f = 20 MHz, $\Delta X/X$ decreases very rapidly around T_C and then increases with further decrease in T. In contrast to $\Delta X/X$ = -40% at f = 5 MHz around T_C, $\Delta X/X$ = +450% at f = 20 MHz for H = 1 kG. Next we show the temperature

dependence of the ac magnetoresistance and magnetoreactance for $La_{0.8}Ba_{0.2}MnO_3$ (x = 0.2) compound which showed clear thermal hysteresis behavior.

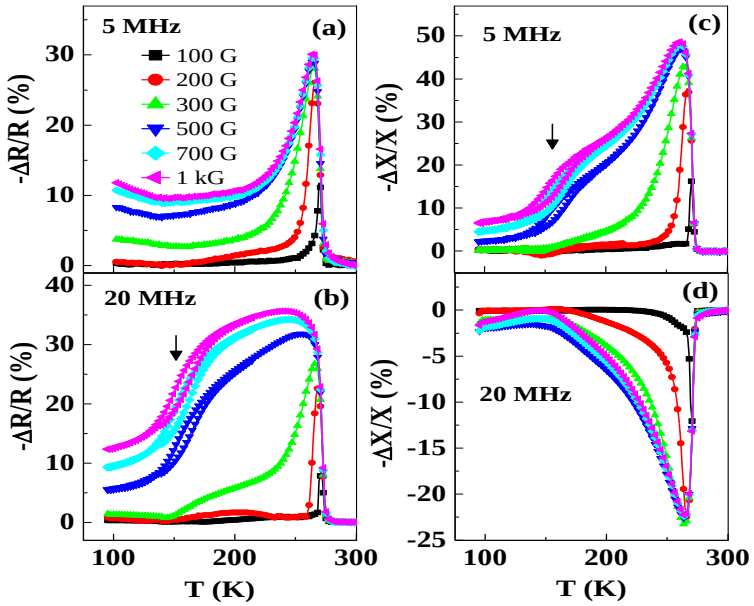

Fig. 3. 21 Temperature dependence of the ac magnetoresistance ($\Delta R/R$) [(a) and (b)] and magnetoreactance ($\Delta X/X$) [(c) and (d)] at H = 100 G - 1 kG for two selected frequencies, f = 5 and 20 MHz $La_{0.8}Ba_{0.2}MnO_3$ (x = 0.2) compound.

The Figs. 3.21(a), (b) and 3.21(c), 5(d) show the behavior of temperature dependence of the ac magnetoresistance and magnetoreactance at different dc bias fields ($H \leq 1$ kG) for f = 5 and 20 MHz, respectively for $La_{0.8}Ba_{0.2}MnO_3$ (x = 0.2) compound which is similar to $La_{0.67}Ba_{0.33}MnO_3$. The magnitude of $\Delta R/R$ at f = 5 MHz around T_C increases from 12% at H = 100 G to 30% at H = 1 kG. Whereas the $\Delta R/R$ at f = 20 MHz shows a rapid increase around T_C and a pronounced low-T anomaly around T^* = 160 K with a hysteresis for H > 300 G. On the other hand, $\Delta X/X$ at f = 5 MHz shows a similar behavior as $\Delta R/R$, but $\Delta X/X$ at f = 20 MHz shows an unusual behavior. The $\Delta X/X$ at f = 20 MHz, decreases and shows a minimum around T_C. In contrast to a negative magnetoreactance of -48% at f = 5 MHz around T_C, a positive magnetoreactance of +23% is observed at f = 20 MHz for H = 1 kG. The behavior of both $\Delta R/R$ and $\Delta X/X$ of $La_{0.67}Ba_{0.23}Ca_{0.1}MnO_3$ compound is almost similar to that of $La_{0.8}Ba_{0.2}MnO_3$ compound and thus it is not shown here.

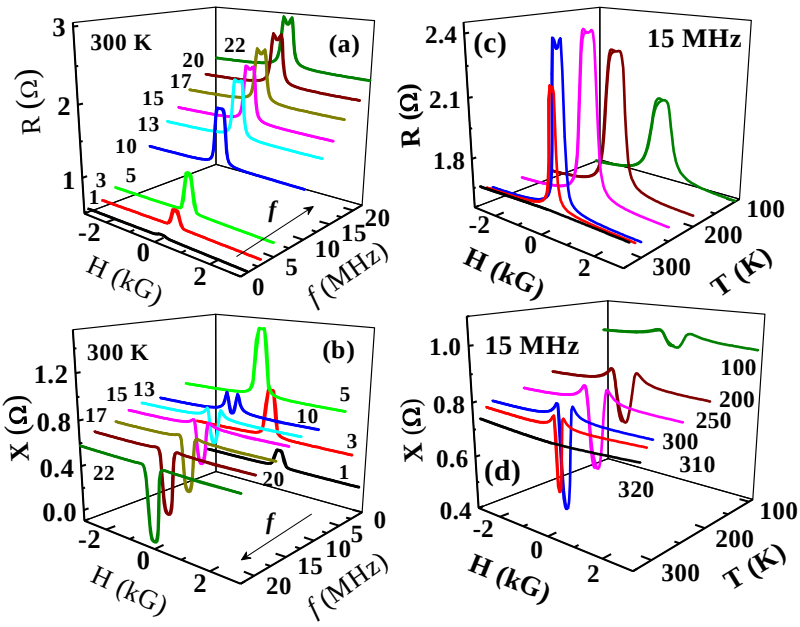

Fig. 3. 22 The field dependence of the ac resistance *R* and reactance *X* for $La_{0.67}Ba_{0.33}MnO_3$. The field dependence of the (a) *R* and (b) *X* at *T* = 300 K for six selected frequencies, *f* = 1, 3, 5, 10, 13, 15, 17, 20 and 22 MHz. Figs. (c) and (d) show the field dependence of the *R* and *X*, respectively at six selected temperatures, *T* = 100, 200, 250, 300, 310 and 320 K for *f* = 15 MHz.

Since the results are almost similar for all samples, we present here the field dependence of one of the samples in the series *i.e.*, $La_{0.67}Ba_{0.33}MnO_3$. The Figs. 3.22(a) and (b) show the three dimensional (3D) plot of field dependence of the ac resistance $R(H, f)$ and the reactance $X(H, f)$, respectively in a narrow field interval of -3 kG ≤ H ≤ 3 kG at room temperature for f = 1, 3, 5, 10, 13, 15, 17, 20 and 22 MHz. The $R(H, 1\text{ MHz})$ shows a peak at the origin (H = 0 G) and decreases rapidly in 0 ≤ H ≤ 500 G, and shows saturation at H = ±1 kG. As f increases further, the value of R increases. Interestingly, the peak moves to a higher field and a valley occurs at the origin for f > 15 MHz. For instance, the R (H, 22 MHz) shows a clear double peak at H = ±170 G on either side of the origin. On the other hand, the X for f ≤ 5 MHz shows a peak at H = 0 G, but changes into a dip for f ≥ 10 MHz. The $R(H, T)$ and $X(H, T)$ for f = 15 MHz at selected temperatures (T = 320, 310, 300, 250, 200 and 100 K) are shown in the Figs. 3.22(c) and (d), respectively. The $R(H)$ at 320 K is hardly affected by the magnetic field. However, there is a dramatic change in $R(H, T)$ just below T_C. The $R(H, 310\text{ K})$ shows a peak

at $H = 0$ and decreases rapidly between $+300G \leq H \leq -300$ G and shows saturation above $H = \pm 1$ kG. The $R(H)$ curve broadens as T decreases with a "flat top" at the origin. As like $R(H, T)$, $X(H, T)$ also shows interesting features developing below T_C. While the $X(H, 320\ K)$ is field independent, $X(H, T<320\ K)$ shows a minimum at $H = 0$ and a peak on either side of the origin and shows saturation behavior for $H \geq 1$ kG. The position of the double peaks in the $X(H)$ shifts to high field as T decreases, from $H = 170$ G for $T = 310$ K to $H = 600$ G for $T = 100$ K, but the value of X also decreases with decreasing T.

The important observations in this section are:

1. A step like increase in R occurs at T_C with increasing f in $H = 0$.
2. Appearance of an anomaly in X at T^* ($<T_C$) for $f \leq 5$ MHz which is transferred to R for $f \geq 10$ MHz.
3. R and X are sensitive to sub-kilo Gauss magnetic fields.
4. Huge low field magnetoresistance and magnetoreactance.

The appearance of a peak in the ac magnetoresistance around T_C in sub-kilo gauss magnetic field seems to be different from the extrinsic magnetoresistance due to tunneling of spin polarized electrons between ferromagnetic grains through grain boundaries, which is negligible near T_C, increases with decreasing temperature and reaches a maximum value at the lowest temperature. [170] The observed trend in the ac magnetoresistance and magnetoreactance can be qualitatively understood from the models of giant magnetoimpedance developed originally for amorphous and nanocrystalline ferromagnetic alloys. [171, 172] As we know, the flow of *rf* current in a ferromagnetic material is confined to a surface layer of thickness known as skin depth ($\delta = \sqrt{(2\rho)/(\omega\mu_t)}$, where μ_t is the effective transverse initial permeability). We consider the transverse permeability instead of the longitudinal permeability, because the flow of *ac* current along the long axis of the sample induces an *ac* magnetic field in the transverse direction to the current. The flow of *rf* current in the sample creates a circular ac magnetic field and magnetization of ferromagnetic domains oscillates in response to changing magnetic flux. From the classical theory of

electromagnetism, electrical impedance of a current carrying conductor of cylindrical geometry with radius 2*a* is obtained as

$$\frac{Z}{R_{dc}} = \frac{(ka)J_0(ka)}{2J_1(ka)}$$

where R_{dc} is the *dc* resistance,

$$k = (1-j)/\delta$$

J_0 and J_1 are zero and first-order Bessel functions. [173]

If the skin effect is weak, then the Bessel functions can be expanded to give the real and imaginary parts of the impedance:

$$Z' = R = R_{dc}[1+1/48(a/d)^4] = R_{dc}[1+(\mu_t\sigma\omega a^2)^2/192]$$

and

$$Z'' = X = ¼R_{dc}(a/\delta)^2 \propto (\mu_t\omega)$$

The second term in the bracket of the expression of *R* is due to the eddy current which shields the interior of the ferromagnetic grains from the alternating magnetic field. Thus, the ac resistance *R* in the ferromagnetic state will rise above the dc resistance if the second term in the bracket dominates the dc resistance. Hence, a step-like behavior occurs in *R* at T_C with increasing *f*. At low frequencies such as *f* = 100 kHz which corresponds to the weak skin effect, the $(a/\delta)^4$ term in *Z'* is smaller than R_{dc} and hence, it has negligible effect on the *ac* resistance. On the other hand,

$$X \propto \mu_t$$

where $X = \omega L = \omega G\mu_t$ (*G* is the geometrical factor and *L* is the self-inductance of sample) and thus, *X* is the dominant factor. Hence, the observed peak in *X* around T_C at *f* = 100 kHz and its suppression in a small magnetic field can be understood in terms of magnetoinductance effect in $La_{0.67}Ba_{0.33}MnO_3$ sample as described in the section 3.3.3.1 of this chapter. Since, *X* monitors the change in the real part of the magnetic permeability (μ'), the appearance of a step-like increase around T_C in *X* (*T*, *f* = 100 kHz) for all the samples

signals the onset of ferromagnetic transition. Moreover, the appearance of an anomaly in $X(T, H = 0\ \text{G})$ around T^* for $f \leq 5$ MHz in our compounds and its disappearance in the sub-kilo gauss magnetic fields ($H \geq 500$ G) is possibly caused by the structural transition as described in the section 3.3.2 of this chapter.

As the frequency increases, the skin depth decreases and the flow of *rf* current becomes confined to the outer shell of thickness δ. The ac impedance in the regime of strong skin depth is

$$Z = R_{dc}\left[(1+i)/\delta\right] \text{ or } Z = R + iX = \sqrt{i\omega\rho\mu(f,T,H)}\,.$$

The abrupt increase of the permeability around T_C leads to decrease of δ below its value in the nonmagnetic state and hence the ac resistance R shows an abrupt increase. This results in the secondary peak in $Z(T, H = 0\ \text{G})$. In addition, the magnetization process is also affected with increasing frequency. While at low frequencies, the magnetization which increases by domain wall motion is damped by micro eddy current, the domain magnetization rotation (DMR) becomes the major contributor to the magnetization with increasing frequency above 10 MHz. Just below the Curie temperature, the magnetic domains form. In zero field, the domain magnetization experience small angle oscillation in response to the circular ac magnetic field. When a small dc magnetic field is applied, domain magnetization rotates by an angle favored by the balance between Zeeman energy and magnetic anisotropy energy. The ac magnetic field becomes less influential in rotating the magnetization far away from that angle and hence the permeability decreases. Hence, the peak in the ac resistance R also decreases. With increasing strength of dc magnetic field, the angle between the easy axis of domain magnetization and the field decreases and the peak in R decreases and moves towards lower temperature. When the domain magnetization rotation is complete in a field of few kG, the primary peak in *R(T)* reappears and moves towards higher temperature with increasing H above 1 T. The decrease in permeability under the dc bias field increases the magnetic penetration depth ($\delta \propto 1/\sqrt{\mu}$) and ac resistance R decreases dramatically in low-dc

magnetic fields. When we consider the complex nature of the permeability, the impedance becomes,

$$Z = \sqrt{\omega\rho(\omega, H)}\left[\sqrt{\mu_R} + j\sqrt{\mu_X}\right]$$

where, $\mu_R = |\mu| + \mu''$, $\mu_X = |\mu| - \mu''$ and $|\mu| = \sqrt{(\mu'^2 + \mu''^2)}$. Thus, the $\mathrm{Re}(Z) = R_{ac}$ will have the significant contribution from $|\mu|$ and μ''. Hence, the low temperature anomaly appears in *R*. However, it is not clear why the low temperature anomaly vanishes in *X* for *f* > 10 MHz. Note that the *X* also changes the sign to negative for *f* > 10 MHz, whereas it is positive for *f* < 10 MHz. It is possible that the change in the sign is related to the changes in the magnetization process from the domain wall motion dominated regime to the domain rotation dominated regime, but further investigations are necessary to understand this behavior.

Now let us comment on the transition from a maximum to minimum observed at the origin in the field dependence of *X* around 10 MHz at 300 K for $La_{0.67}Ba_{0.33}MnO_3$ sample as shown in Fig. 3.22(b). A transition from a maximum to minimum at *H* = 0 in the field dependence of reactance with increasing frequency was also found in amorphous ferromagnetic ribbons and wires. [174] In an amorphous ferromagnetic wire, there is an internal core with axial domains along the wire axis. There are also circular domains at the surface of wire which surround the internal core. As the frequency increases, flow of ac current moves towards the surface and the contribution to the permeability comes from the rotation of magnetic domains. If the magnetic anisotropy is axial, increasing the magnetic field results in decrease of the permeability and only a single peak centered about the origin is observed. If the magnetic anisotropy is circumferential or transverse, then increase in the strength of the dc magnetic field causes the circumferential permeability to increase until the dc magnetic field overcomes the circumferential anisotropy field (H_k). The circumferential susceptibility (transverse anisotropy in case of thin film or ribbon) is expected to diverge at $H = H_k$ in an ideal system, though only a maximum is observed at $H = H_k$ in real system. Hence,

the impedance Z also increases and reaches a maximum in the low-field region at $H = H_k$, followed by a slow decrease up to saturation at large applied fields. Hence, the observed increase of reactance X with the magnetic field (*i.e.*, positive magnetoreactance) indicates the existence of transverse anisotropy in the sample.

3. 4 Conclusions

The main experiments carried out and the important results of this chapter are summarized below.

1. In the first half of the chapter, we have investigated the temperature and magnetic field dependent *rf* electromagnetic absorption in $La_{0.67}Ba_{0.33}MnO_3$ and $La_{0.67}Ba_{0.23}Ca_{0.1}MnO_3$ compounds by monitoring the changes in resonance frequency (f_r) and current (I) through a LC resonant circuit powered by an integrated chip oscillator (ICO). The ferromagnetic to paramagnetic transition at T_C in zero external magnetic field is accompanied by an abrupt increase in f_r and I and they are tunable by small external magnetic field.
2. We have observed fractional changes as much as $\Delta f_r/f_r$ = 46% and $\Delta P/P$ = 23% for $La_{0.67}Ba_{0.33}MnO_3$, and $\Delta f_r/f_r$ = 19% and $\Delta P/P$ = 10% for $La_{0.67}Ba_{0.23}Ca_{0.1}MnO_3$ samples around T_C for H = 1 kG. The magnetically tunable resonance frequency and power absorption demonstrated here can be exploited for magnetic field sensor and other applications.
3. We have detected an anomaly around T^* = 165 K with hysteresis behavior around T = 165-195 K in the temperature dependence of f_r of ICO circuit containing $La_{0.67}Ba_{0.23}Ca_{0.1}MnO_3$ sample as a core of the inductance coil. The observed anomaly was attributed to rhombohedral-orthorhombic structural transition that occurs below the long range ferromagnetic order in the sample. Both the magnetic and structural anomalies are very sensitive to sub-kilo Gauss magnetic fields. Our study suggests that *rf* ICO technique is a versatile contactless experimental tool to study the magnetization dynamics as well as to investigate the magneto-structural phase transition in manganites and possibly also in other compounds.

4. In the second half of the chapter, we have investigated the alternating current electrical transport in $La_{0.67-x}Ba_{x-y}Ca_yMnO_3$ (x = 0.33, 0.25, 0.2 and y = 0 and 0.1) compounds by measuring the ac resistance (*R*) and reactance (*X*) simultaneously in four probe configuration while passing the *rf* current directly through the sample in the frequency range *f* = 0.1-20 MHz.
5. Our investigation of ac electrical transport in $La_{0.67}Ba_{0.33}MnO_3$ compound at *f* = 100 kHz indicates a large low field magnetoreactance ($\Delta X/X$ = 60% at T_C and *H* = 1 kG) which exceeds the ac magnetoresistance ($\Delta R/R$ = 5%). The observed magnetoreactance is attributed to the change in the magnetic permeability ("magnetoinductance effect") of the sample rather than the variation in the dielectric permittivity ("magnetocapacitance effect"). Such a large low field magnetoreactance may find applications in thin film inductor. Further studies over a wide frequency range could be helpful to understand the competition between the magnetocapacitance effect found in phase separated manganites such as bulk Cr doped $Nd_{0.5}Ca_{0.5}MnO_3$ [175] and La-Pr-$CaMnO_3$ thin film [176] and the magnetoinductance effect reported here in this chapter.
6. We have observed a rapid change around the magnetic transition (T_C) and an anomaly at a temperature T^* below T_C in both *R* and *X* for $La_{0.67-x}Ba_{x-y}Ca_yMnO_3$ compounds. We attribute the low-*T* anomaly observed at T^* to the high temperature rhombohedral to low temperature orthorhombic structural phase transition in the compounds.
7. One of the compounds in the series, $La_{0.67}Ba_{0.33}MnO_3$ compound showed large ac magnetoresistance of -45% and magnetoreactance of -40% at *H* = 1 kG and *f* = 5 MHz near T_C. In addition, we have also observed a large positive magnetoreactance of +450% around T_C at *f* = 20 MHz and *H* = 1 kG which we attribute to existence of transverse or circular magnetic anisotropy.
8. Our results reveal that the *rf* magnetotransport using the impedance spectroscopy is a valuable tool to study the magnetization dynamics, to detect the magnetic and structural transitions, and to enhance the low-field magnetoresistance.

Chapter 4

Magnetic, magnetoabsorption, magnetocaloric and ac magnetotransport studies in $Sm_{0.6-x}La_xSr_{0.4}MnO_3$

4. 1 Introduction

One of the most interesting phenomena observed in manganites is the real space ordering of charges (electrons and holes) and e_g-orbitals. While in narrow bandwidth manganites such as $Nd_{0.5}Ca_{0.5}MnO_3$ charge-orbit ordering precedes antiferromagnetic ordering, charge ordering occurs below the ferromagnetic transition in $Nd_{0.5}Sr_{0.5}MnO_3$. [38, 47, 48] However, as the e_g-bandwidth decreases in $RE_{0.6}Sr_{0.4}MnO_3$ due to reduction in the size of RE^{3+} cation, long range charge ordering is also destroyed. [47, 177] For example, $Pr_{0.5}Sr_{0.5}MnO_3$ does not show long-range charge ordering unlike $Nd_{0.5}Sr_{0.5}MnO_3$. [20, 47] The $Sm_{1-x}Sr_xMnO_3$ series has been studied by few groups. [178, 179, 180] Tomioka *et al.*, [180] obtained the phase diagram of $Sm_{1-x}Sr_xMnO_3$. He has reported that while $0.2 \leq x \leq 0.4$ samples are ferromagnetic, $x = 0.5$ is at the bicritical point which separates the ferromagnetic phase ($x < 0.45$) from antiferromagnetic phase ($x > 0.55$) and exhibits short range charge ordering. Our interest in $Sm_{1-x}Sr_xMnO_3$ is motivated by the observation of unusual metamagnetic transition in the paramagnetic state and large MCE. [181] In this work, we change the bandwidth of $Sm_{0.6}Sr_{0.4}MnO_3$ by La doping at Sm site, while keeping electron concentration constant in the system. Our interest here is to investigate how does the change in bandwidth affect the *rf* magnetoabsorption, magnetoimpedance and magnetocaloric properties as compare to ferromagnetic La-Ba-Ca-MnO_3 compounds presented in earlier chapters.

In the previous chapter, we have discussed the behavior of *rf* power absorption and ac magnetotransport properties of double exchange interaction mediated ferromagnetic $La_{0.67-x}Ba_{x-y}Ca_yMnO_3$ (LBCMO) compounds undergoing a temperature driven paramagnetic metal to ferromagnetic metal transition with lowering temperature from 400 K. We have

demonstrated that the *rf* ICO technique is a versatile contactless experimental tool to investigate the magneto-structural phase transition in manganites. In the second half of the previous chapter, we have shown that ac electrical transport is a valuable tool to study the magnetization dynamics, to detect the magnetic and structural transitions, and to enhance the low-field magnetoresistance. The large ac magnetoresistance found in LBCMO samples is attributed to the suppression of the transverse magnetic permeability (μ_t) under dc magnetic fields which enhanced the skin depth for current distribution compared to its zero field value. It is not clear whether ac electrical transport enhances magnetoresistance in other manganites too. Moreover, it is interesting to know the response of ac electrical transport in the compound which undergoes semiconducting paramagnetic to ferromagnetic metal. Hence, in this chapter, we have investigated ac electrical transport in $Sm_{0.6-x}La_xSr_{0.4}MnO_3$. Here, the paramagnetic state in $Sm_{0.6}Sr_{0.4}MnO_3$ is semiconducting in contrast to metallic behavior of LBCMO compounds. Furthermore, investigation of this $Sm_{0.6-x}La_xSr_{0.4}MnO_3$ compound is also interesting because of the following reasons:

1. The pure $Sm_{0.6}Sr_{0.4}MnO_3$ shows a sudden drop in magnetization in the long-range ferromagnetic ordering. The details of which are described in the later part of this chapter. But what it is interesting here to know is that the response of *rf* power absorption of this compound around the semiconducting paramagnetic to ferromagnetic metal transition and also below the temperature at which it shows sudden drop in magnetization.
2. It is also interesting to study the effect of La doping at Sm site on the ac magnetotransport properties in $Sm_{0.6-x}La_xSr_{0.4}MnO_3$ as the La doping is expected to decrease the resistivity of the compound and enhance the double exchange interaction in the system.
3. Since the ionic radius of La^{3+} ion (= 1.216 Å) is larger than that of Sm^{3+} ion (= 1.132Å), the ferromagnetic T_C is expected to increase with varying x in $Sm_{0.6-x}La_xSr_{0.4}MnO_3$. Thus, it is also interesting to study this system from the viewpoints of magnetic refrigeration technology for room temperature applications as it provides the possibility of continuously tuning the T_C and MCE over a wide temperature.

4. Most importantly, the influence of rare earth moment ordering, which we propose to the origin of sudden drop in magnetization observed in our $Sm_{0.6-x}La_xSr_{0.4}MnO_3$ compounds, on magnetocaloric or ac electrical transport has not been investigated so far.

This chapter is divided into four main sections. In the first section, we present the detailed magnetic properties of $Sm_{0.6-x}La_xSr_{0.4}MnO_3$ (SLSMO) compounds with compositions $0 \leq x \leq 0.6$. We show that an anomalous peak occurs in the magnetization at a temperature T^* = 30 K << T_C for x = 0 compound. While T_C of SLSMO series increases with increasing x (T_C = 118 K for x = 0 and T_C = 363 K for x = 0.6), T^* increases from 30 K (x = 0) to 120 K (x = 0.4) and then decreases to 105 K (x = 0.5). In the second section, we present our results on the *rf* magnetoabsorption properties of two compounds: x = 0 which showed low-*T* anomaly and x = 0.6 which didn't show any anomaly at low temperature, by using ICO oscillator technique. Here, we compare the *rf* magnetoabsorption of two compositions: x = 0 and x = 0.6 and show that while the behavior of *rf* magnetoabsorption in x = 0.6 compound is similar to $La_{0.67}Ba_{0.33}MnO_3$ as described in the previous chapter, the compound x = 0 reveals unusual *rf* magnetoabsorption properties by showing interesting features below and above T^* = 30 K. In the third section, we present magnetocaloric properties of $Sm_{0.6-x}La_xSr_{0.4}MnO_3$ (x = 0-0.6) compounds and we show that a rapid increase around T_C and an anomalous peak at a temperature T^* << T_C occur in magnetization which lead to normal and inverse MCEs, respectively. This is the first observation of an inverse MCE in a ferromagnetic compound and is attributed to the antiferromagnetic coupling between Sm-4*f* and Mn-3*d* spin sublattices. In the last section of this chapter, we present a detailed ac magnetotransport study in $Sm_{0.6-x}La_xSr_{0.4}MnO_3$ (x = 0-0.6) compounds and show the unusual temperature dependence of ac magnetoresistance with varying frequency in x = 0 compounds and its disappearance with increasing La content in $Sm_{0.6-x}La_xSr_{0.4}MnO_3$ compounds. We discuss the possible origins of the above observed effects.

4. 2 Experimental details

A series of polycrystalline $Sm_{0.6-x}La_xSr_{0.4}MnO_3$ (SLSMO) compounds with compositions x = 0, 0.05, 0.1, 0.2, 0.3, 0.4, 0.5, 0.55 and 0.6 were prepared by the standard solid state synthesis method. The stoichiometric mixtures of Sm_2O_3, La_2O_3, $SrCO_3$ and Mn_2O_3 precursors were mixed together and were homogenized in an agate mortar. The powders were first reacted at 1000°C for 24 hours and then the calcined powders were reground and final sintering was done at 1200°C for 24 hours. Single phase identification was performed by the powder XRD experiment (Philips X'pert Pro) using Cu Kα radiation. The compounds were pressed into pellets and heat treated at 1200°C for 24 hours to get a relatively dense pellets of SLSMO compounds. The observed room temperature XRD patterns of all the compounds were indexed using TOPAS software version 2.1. The samples of SLSMO are characterized by the standard ac magnetic susceptibility and dc resistivity measurements. Temperature dependence of the magnetization was performed using a vibrating sample magnetometer (VSM) with a superconducting magnet and a commercial cryostat (PPMS, Quantum Design Inc.). Magnetization versus field measurements were done at selected temperatures to estimate the ΔS_m values using the method described in experimental section: 2.2.5. We have measured the temperature and magnetic field dependent *rf* electromagnetic absorption using a home built *LC* resonant circuit powered by an integrated chip oscillator (ICO) with PPMS as described in the experimental section: 2.2.3. For ac impedance measurement, the samples were cut into rectangular shape. While the current leads were attached to the two ends of the sample with Ag-In alloy, the voltage was measured across the two linear electrodes placed on the top surface of the sample. Agilent 4294A LCR meter was used to measure the ac impedance in the frequency range from f = 1 kHz to 5 MHz in series inductance resistance (*L-R*) mode with a current excitation of 5 mA. The temperature dependence of R and X under different dc bias magnetic fields were done using the PPMS and studies were done as described in the experimental section: 2.2.4.

4. 3 Results and Discussions

4. 3. 1 Structural characterization using XRD

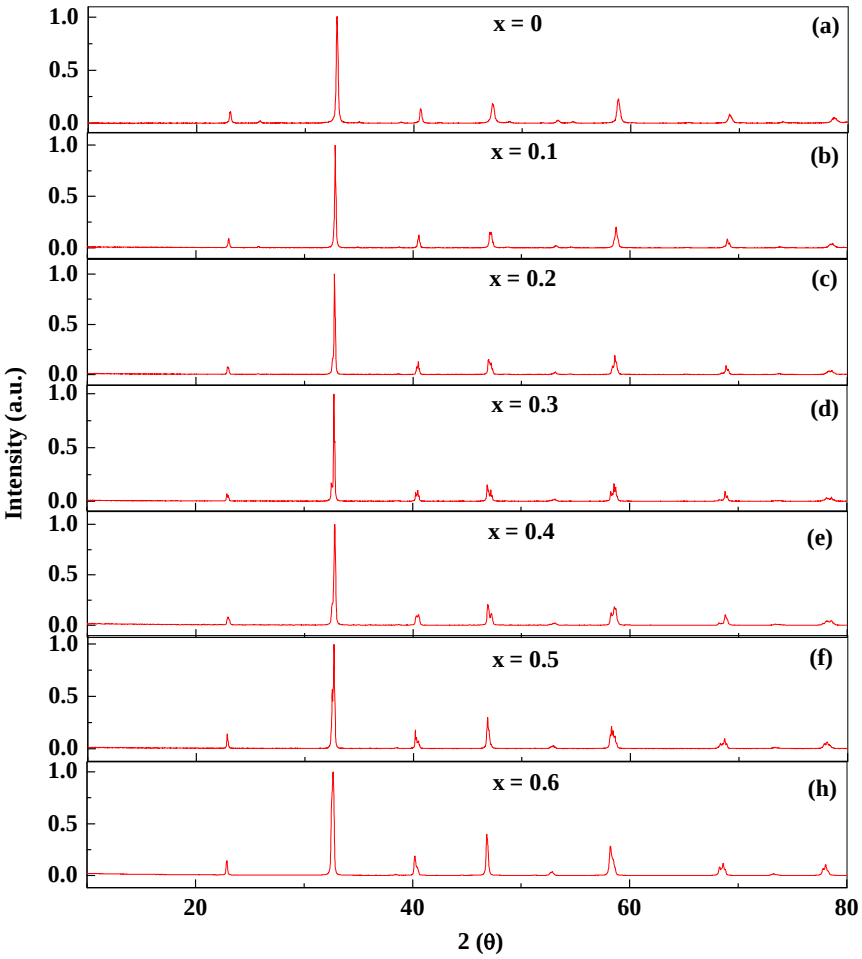

Fig. 4. 1 XRD patterns of $Sm_{0.6-x}La_xSr_{0.4}MnO_3$ (x = 0, 0.1, 0.2, 0.3, 0.4, 0.5 and 0.6) compounds at room temperature.

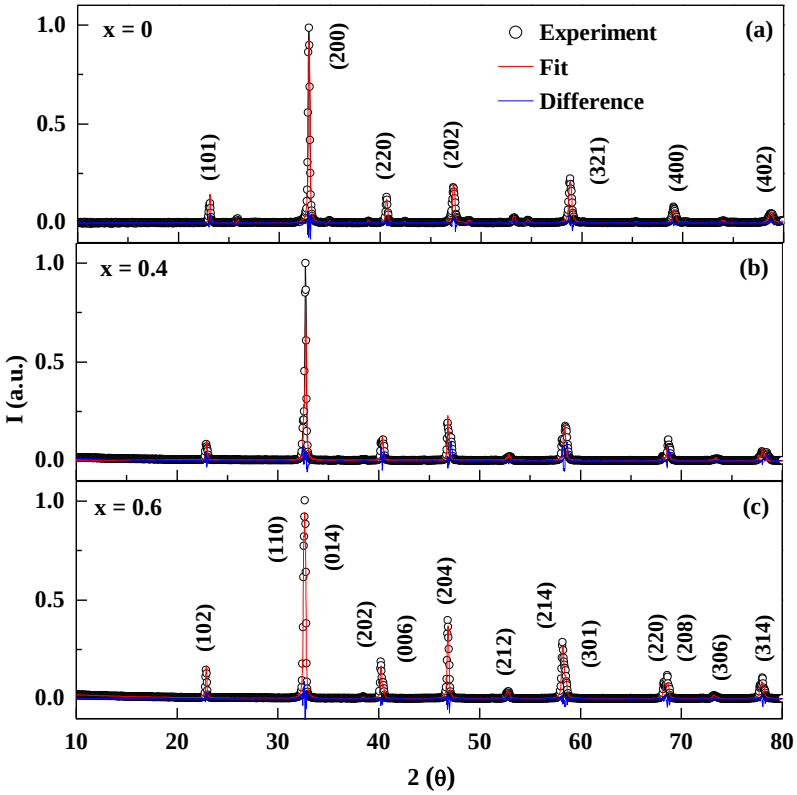

Fig. 4. 2 Rietveld refinement of the XRD pattern for (a) x = 0, (b) x = 0.4 and (c) x = 0.6 compounds.

Fig. 4.1(a)-(h) show the XRD patterns of $Sm_{0.6-x}La_xSr_{0.4}MnO_3$ (x = 0, 0.1, 0.2, 0.3, 0.4, 0.5 and 0.6) compounds at room temperature which reveal the single phase patterns. The Structure refinement by Rietveld method suggests that the compositions $x \leq 0.1$ belong to orthorhombic structure (space group, *Pbnm*) and it changes to rhombohedral (space group, $R\bar{3}c$) for x > 0.3. Figs. 4. 2(a), (b) and (c) show the Rietveld refinement for three selected compounds: x = 0, 0.4 and 0.6, respectively. The prominent peaks in the XRD pattern are indexed by its crystallographic planes and represented by miller indices (*hkl*) in accordance with Ref. [182, 183] The incorporation of La causes a smooth increase in the unit cell volume with increasing x because of the fact that the ionic radius of La^{3+} ($r_{La}{}^{3+}$ = 1.172 Å) ion is slightly higher than that of Sm^{3+} ion ($r_{Sm}{}^{3+}$ = 1.098 Å). The structure of transforms from orthorhombic with space group *Pbnm* for x = 0 to rhombohedral with space group $R\bar{3}c$ for x = 0.6.

4. 3. 2 *dc* resistivity and magnetic properties of $Sm_{0.6-x}La_xSr_{0.4}MnO_3$ compounds

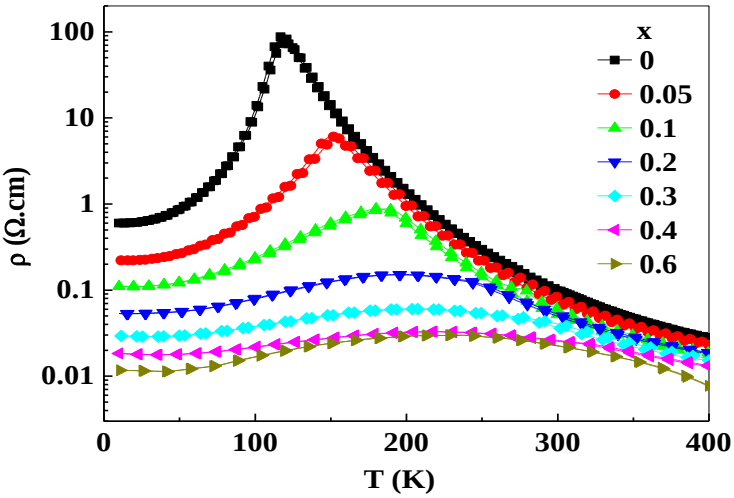

Fig. 4. 3 Temperature dependence of *dc* resistivity behavior in zero field for selected compounds of $Sm_{0.6-x}La_xSr_{0.4}MnO_3$ (x = 0, 0.05, 0.1, 0.2, 0.3, 0.4, and 0.6).

In Fig. 4.3, we show the temperature dependence of the dc resistivity, $\rho(T)$, of selected compositions SLSMO. The $\rho(T)$ of x = 0 in zero field shows a peak at the insulator-metal (*I-M*) transition at T_{IM} = 115 K (just below T_C) while cooling. The peak in $\rho(T)$ shifts to T = 117 K while warming, thus leads to a small hysteresis around T_{IM} (not clearly visible in the plot as the $\rho(T)$ values are given in log scale). The insulator-metal transition in $\rho(T)$ shifts to higher temperature with increasing x. For x > 0.2, the *I-M* transition is broad. The resistivity peak at T_{IM} decreases in magnitude with increasing x. Note that ρ□ peak for x = 0.6 compound is 3 orders of magnitude lower than x = 0.

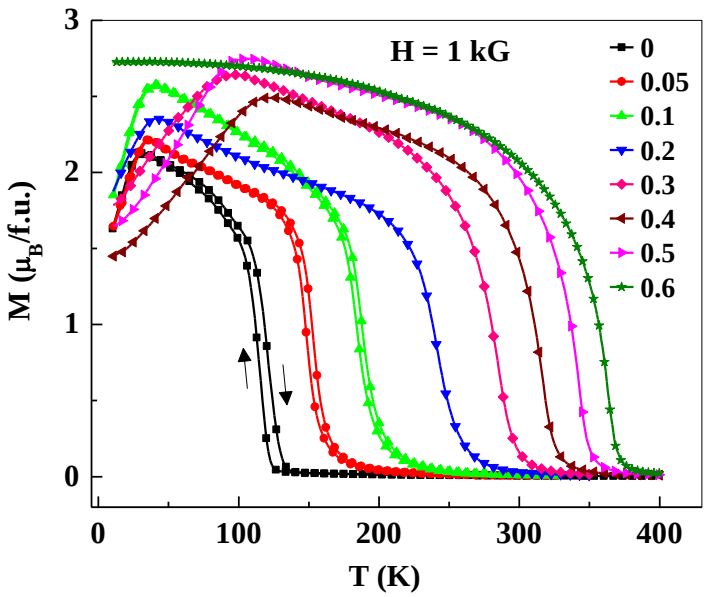

Fig. 4. 4 The field-cooled magnetization *M*(*T*) plots of $Sm_{0.6-x}La_xSr_{0.4}MnO_3$ compounds (x = 0 to 0.6) under *H* = 1 kG.

Fig. 4.4 shows the temperature dependence of the dc magnetization, *M*(*T*) measured while cooling and warming under *H* = 1 kG for SLSMO series with x = 0, 0.05, 0.1, 0.2, 0.3, 0.4, 0.5 and 0.6. The rapid increase of *M*(*T*) around T_C = 118 K for x = 0 is due to the paramagnetic to ferromagnetic (PM→FM) transition and it exhibits hysteretic behavior while warming which indicates that the PM→FM transition is first-order in nature. The substitution of La dramatically increases the T_C and the PM→FM transition becomes second-order for x ≥ 0.2 as indicated by the absence of hysteresis in *M*(*T*). The T_C determined from the minima of *dM*/*dT* curves are 151 K, 185 K, 243 K, 288 K, 320 K, 345 K and 363 K for x = 0.05, 0.1, 0.2, 0.3, 0.4, 0.5 and 0.6, respectively. Interestingly, *M*(*T*) exhibits a peak around T^* = 30 K below the ferromagnetic transition. In Fig. 4.5, we have plotted the variations of both T_C and T^* as a function of composition (x) on left and right scales, respectively. The value of T_C increases monotonically with increasing x from T_C = 118 K for x = 0 to T_C = 363 K for x = 0.6. Whereas the value of T^* initially increases with x from T^* = 30 K for x = 0 to T^* = 120 K for x = 0.4 where it reaches a maximum and then it decreases to T^* = 105 K for x = 0.5, and finally it disappears for the end compound *i.e.*, x = 0.6 (LSMO). Next we show the detailed magnetic properties of x = 0.

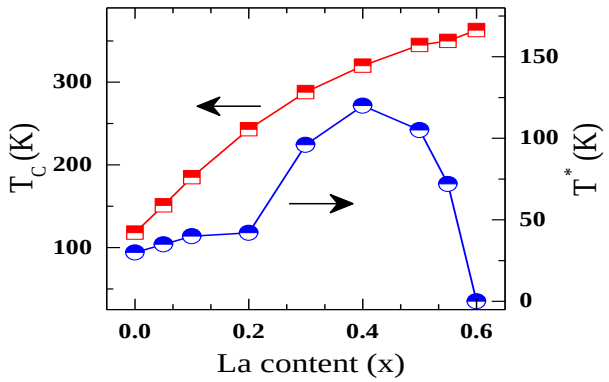

Fig. 4. 5 The variation of T_C and T^* as a function of composition x in $Sm_{0.6-x}La_xSr_{0.4}MnO_3$ compounds.

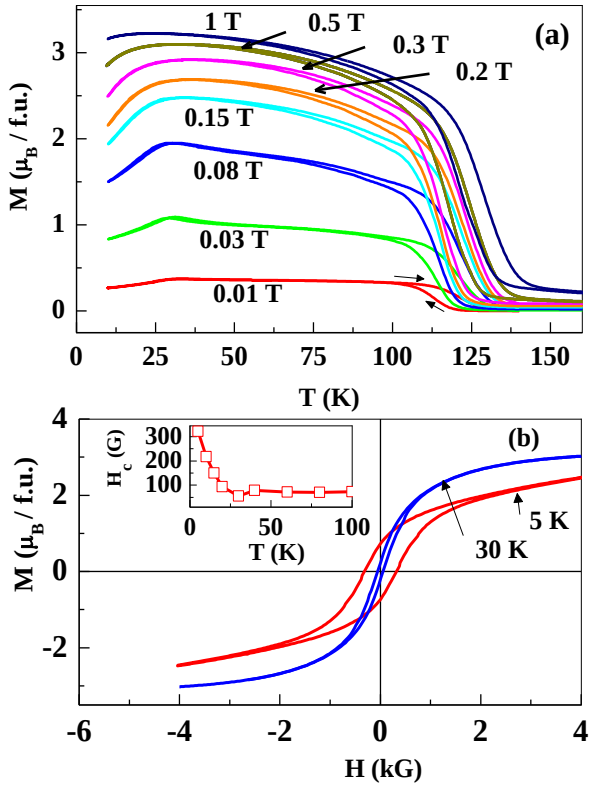

Fig. 4. 6 Temperature dependence of (a) the magnetization under different magnetic fields, (b) *M-H* loops at *T* = 5 K and 30 K and the inset shows the temperature dependence of coercive field (H_C) for x = 0 compound.

Fig. 4.6(a) shows the $M(T)$ plots measured while cooling and warming under different external magnetic fields ($\mu_0 H$ = 0.01-1 T) for x = 0. Application of H causes T_C of x = 0 to shift up rapidly to high temperature, but the position of low temperature (low-T) peak at T^* is not affected with increasing H up to $\mu_0 H$ = 0.15 T. As H increases further, the peak broadens and shifts down in T and it almost disappears under $\mu_0 H$ = 1 T. Such a peak in $M(T)$ was also

observed in $Sm_{1-x}Sr_xMnO_3$ (x = 0.35-0.45) series around the same temperature by other investigators, but its origin was not clearly addressed. Borges *et al.*, [184] attributed the origin of this low-*T* peak to increase in the coercivity with lowering *T*. In order to confirm this point, we have measured the *M*-*H* hysteresis loops at selected temperatures below T = 100 K. The main panel of Fig. 4.6(b) shows the *M*-*H* hysteresis loops at T = 5 K and T^* = 30 K which clearly shows that magnetization at 50 K is lower in magnitude than at 30 K and also widened hysteresis behavior. We show the coercive field (H_C) versus *T* in the inset of Fig. 4.6(b). The H_C is almost zero above 50 K, but it increases rapidly below 40 K and reaches 300 G at 5 K. It is to be noted here that the low-*T* peak in the *M*(*T*) at T^* persists up to $\mu_0 H$ = 0.5 T which is much above H_C. This suggests that the increase in H_C is not the main cause for the observed low-*T* peak in *M*(*T*). The *M*-*H* loop at 5 K is closed only above $\mu_0 H$ = 0.18 T which indicates a strong anisotropy present in the system.

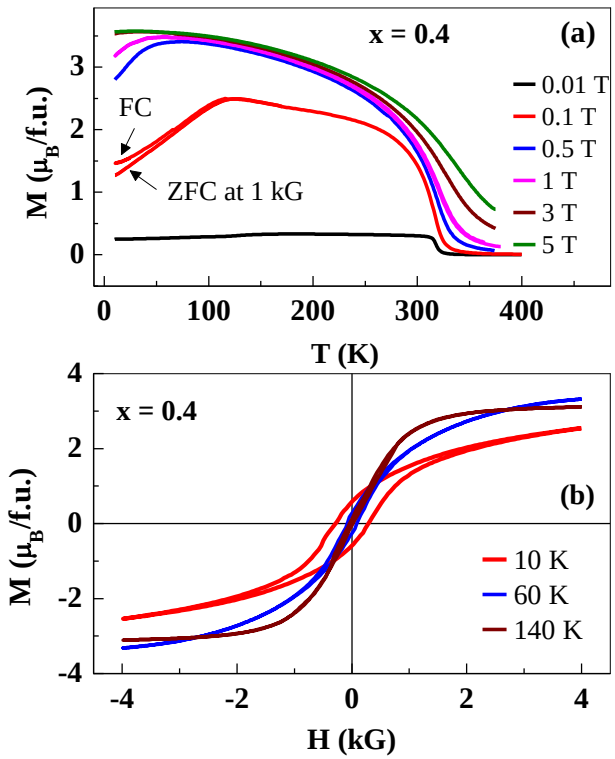

Fig. 4. 7 (a) *M*(*T*) plots under different dc magnetic fields $\mu_0 H$ = 0.01-5 T and ZFC plot at *H* = 1 kG, and (b) *M*-*H* loops at selected temperatures (*T* = 10-140 K) above and below T^* for x = 0.4 compound.

We have also investigated the effect of magnetic field on $M(T)$ for one of the other compounds in the SLSMO series *i.e.*, x = 0.4 which showed the highest value of T^* = 120 K and it is shown in Fig. 4.7(a). While the para-ferromagnetic transition is accompanied by a rapid increase in $M(T)$ under $\mu_0 H$ = 0.01 T, the low-T anomaly is not very clearly visible. However, the low-T anomaly is clearly visible in $M(T)$ under $\mu_0 H$ = 0.1 T at T^* = 120 K. As H increases further, the low-T peak in $M(T)$ broadens and shifts down in T and it almost disappears under a high magnetic field of $\mu_0 H$ = 3 T. The observation of low-T anomaly in SLSMO series and progressive increase of its position towards high temperature with La doping are quite interesting and the possible origin of which will be discussed at the end of this section. The zero-field cooled (ZFC) and field cooled (FC) $M(T)$ measurements have been carried in order to investigate possible existence of cluster-glass or spin-glass behavior in x = 0.4 compound (Fig. 4.7a). Unlike in conventional spin glass or cluster glass behavior, both ZFC and FC $M(T)$ decreases below T^* and the difference between them is small. Fig. 4.7(b) shows the M-H hysteresis loops at selected temperatures above and below T^* (T = 10 K, 60 K and 140 K) which clearly shows the widening of hysteresis loop with lowering T below the low-T peak. We further confirm the nonexistence of cluster-glass or spin-glass state in our SLSMO system by measuring the temperature dependence of ac magnetic susceptibility at different frequencies and under different magnetic fields for x = 0 and 0.4 compounds.

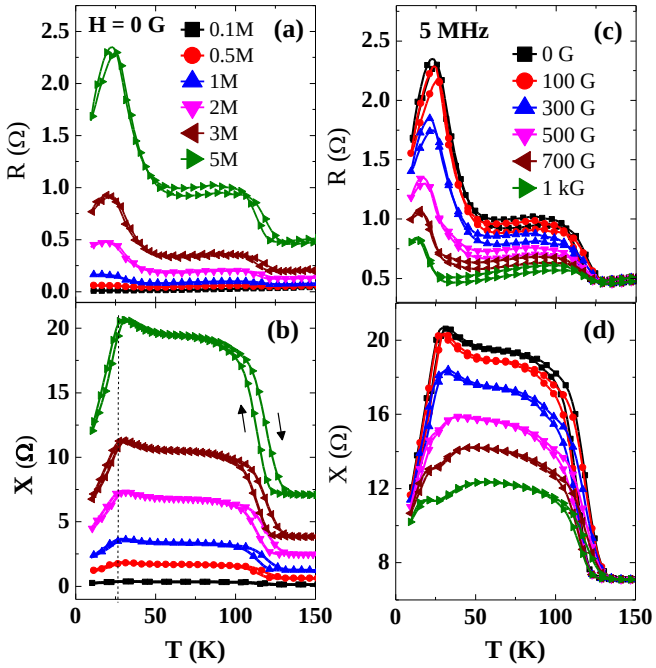

Fig. 4. 8 The ac magnetic susceptibility (μ) behavior of x = 0 compound. Temperature dependence of the (a) ac resistance (*R*) and (b) reactance (*X*) of a 10-turn coil wound on sample at selected frequencies (*f* = 0.1-5 MHz) in zero magnetic field. Figs. (c) and (d) show the temperature dependence of *R* and *X* at *f* = 5 MHz under external dc magnetic fields (*H*), respectively.

In Fig. 4.8, we show the temperature dependence of ac magnetic susceptibility behavior of x = 0. We have measured both the ac resistance (*R*) and reactance (*X*) of a 10-turn coil wound at the centre of 10 mm length of sample using Agilent 4294A LCR meter. Here, *X* is related to the ac magnetic susceptibility (μ) of the sample through the relation,

$$X = \omega L = \omega G \mu$$

where *L* is the self-inductance of the coil and *G* is the geometric factor. Fig. 4.8(a) and 4.8(b) show the temperature dependence of *R* and *X* in zero field at selected frequencies (*f* = 0.1-5 MHz). Both *R* and *X* at all *f* exhibit a rapid increase around T_C while cooling and show a peak at a temperature where *M*(*T*) showed a peak *i.e.*, at T^* = 30 K. The peak in *R* and *X* is more clear at *f* = 5 MHz. The straight line in Fig. 4.8(b) at T^* indicates that the peak in *X* does not shift with *f* which confirms that the origin of the observed peak in *M*(*T*) is not due to spin or cluster glass. In addition, we show temperature dependence of *R* and *X* under sub-kilo gauss magnetic fields for *f* = 5 MHz in Figs. 4.8(c) and 4.8(d), respectively. The applied magnetic

field decreases the magnitude of both *R* and *X* below T_C. The low temperature peak at T^* in both *R* and *X* decreases in magnitude and shifts down in *T* with increasing *H*. We have observed similar ac magnetic susceptibility behavior for x = 0.4 compound but it is not shown here.

The appearance of a low-*T* peak in *M*(*T*) at T^* in our SLSMO compounds for x < 0.6 below the long-range ferromagnetic ordering is puzzling. We can rule of the possibility of antiferromagnetic ordering in the Mn-sublattice because substitution of the large size La^{3+} cation for Sm^{3+} is expected to increase Mn-O-Mn bond angle and widen the e_g-electron bandwidth. The rapid increase of T_C with La-doping and monotonic decrease in low temperature resistivity with increasing x confirms that the ferromagnetic double-exchange interaction among Mn-spins strengthens with increasing x. If the peak at *T** were due to antiferromagnetic ordering in the Mn-sublattice, *T** should have decreased with increasing x, but this is not observed. The peak can neither be due to cluster glass transition nor spin glass transition, since the sample has to become magnetically homogenous with increasing x.

There are two possible origins for the appearance of low-*T* peak in *M*(*T*) at T^* in our samples. One possibility is that a spin-reorientation transition occurs in the Mn-spin lattice due to increase in magnetocrystalline anisotropy driven by e_g-orbital ordering and/or structural phase transition. The metallic ferromagnet $Pr_{0.5}Sr_{0.5}CoO_3$ also showed a magnetic anomaly at T^* = 120 K much below the ferromagnetic transition (T_C = 230 K) and the rotation of magnetic moments from [110] to [100] axis around T^* within the magnetic domain was observed by Lorentz microscopy. [185] Neutron diffraction studies on the same compound revealed changes in the magnetocrystalline anisotropy around T^* = 120 K driven by abrupt shortening of Pr-O bond length. [186, 187] There are no reports available on low temperature study of structural transition in $Sm_{0.6-x}La_xSr_{0.4}MnO_3$ compounds. Even if the spin-reorientation transition is caused by structural transition, the structural transition is most likely to be second-order for $0.2 \leq x \leq 0.5$ as suggested by the absence of hysteresis in *M*(*T*). Another most likely possibility is that 4*f*-3*d* super-exchange interaction is operative in our compounds. The decrease of *M(T)* below T^* can be understood as a result of antiparallel

coupling of 3*d* spins of Mn sublattice and 4*f*-spins of Sm sublattice. Although these sublattices may order ferromagnetically, the coupling between them can be antiferromagnetic. The ordering of Sm-4*f* moments should have been induced by the molecular field of Mn-sublattice. The ordering temperature increases with x and goes through a maximum for x = 0.4 and is absent in the La only compound (x = 0.6). Although relatively less studied, there are some convincing evidences for 4*f*-3*d* interaction in manganites by neutron diffraction experiments. Suard *et al.*' [188] found the ordering of Nd moments below $T \approx 20$ K in $Nd_{0.7}Ba_{0.3-y}Sr_yMnO_3$, but the 4*f*-spins of Nd sublattice align antiparallel to the 3*d*-spins of Mn sublattice for y = 0 and it changes into parallel alignment for $y \geq 0.2$. Dupont *et al.*, [189] suggested the ordering of Nd moments around 50 K in $Nd_{0.7}Ca_{0.3}MnO_3$. Ordering of Pr-4*f* moment around 40 K in antiferromagnetic $Pr_{0.7}Ca_{0.3}MnO_3$ [190] and around 70 K in ferromagnetic $Pr_{0.8}Ca_{0.2}MnO_3$ were suggested from neutron diffraction. [191] Antiferromagnetic coupling between the Dy and Mn spins was suggested to be responsible for a drop of magnetization below 40 K in $Dy_{1-x}Sr_xMnO_3$ (x = 0.2). [192] In our compounds, antiparallel alignment of Sm-$4f^5$ and Mn-3*d* moments can lead to decrease of $M(T)$ below T^*. Surprisingly it occurs around 120 K for x = 0.4. While the ordering of 4*f* moments is appeared to be influenced by the molecular field of Mn-sublattice, the exact mechanism of 4*f*-3*d* coupling is not clearly understood yet. A recent CGA+U calculation on $Nd_{0.67}Sr_{0.33}MnO_3$ by Lin Zhu *et al.*' [193] emphasize on superexchange coupling between Nd-4*f* and Mn-3*d* (t_{2g}) electrons via O-2*p* electrons to understand the drop in magnetization at low temperature.

4. 3. 3 Results and discussions of *rf* power absorption in x = 0 and 0.6

In this section, we compare the *rf* power absorption in two selected compositions: x = 0 compound which showed anomaly at T^* below the long-range ferromagnetic ordering and x = 0.6 compound which did not show any anomaly at low temperature. First, we will show the temperature dependence of both the resonance frequency (f_r) and current (I) through ICO under different magnetic fields.

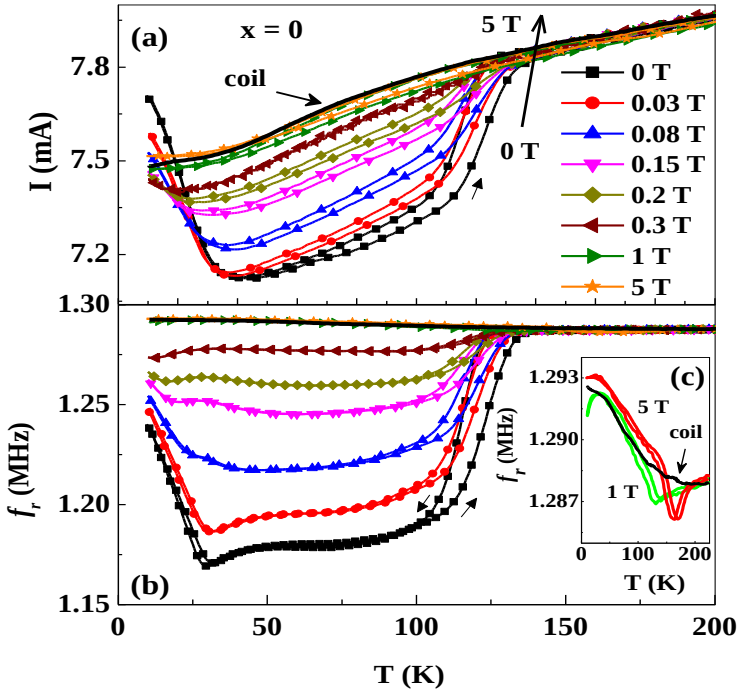

Fig. 4. 9 Temperature dependence of the (a) current (*I*) (b) resonance frequency (f_r) of an ICO under external dc magnetic fields (*H*) for x = 0. (c) Temperature dependence of f_r under $\mu_0 H$ = 0.1 T and 5 T. The data for empty coil are also included (line in black color).

We show the temperature dependence of the current, $I(T)$, through the ICO circuit and resonance frequency, $f_r(T)$, of the ICO under different dc bias magnetic fields in Figs. 4.9(a) and 4.9(b), respectively. The variation of $I(T)$ and $f_r(T)$ for the empty coil, which arise due change in the resistance and self-inductance of the coil, are also shown (continuous line in black color). In the absence of an external magnetic field, the power absorption is large in the paramagnetic (PM) phase and decreases rapidly at the onset of paramagnetic to ferromagnetic (PM→FM) transition, T_C = 118 K upon cooling. The $I(T)$ in zero field continues to decrease gradually with lowering temperature until it reaches a minimum around T^* = 30 K. Interestingly, below T^*, $I(T)$ increases. $I(T)$ shows hysteresis around T_C, which is in consistent with $M(T)$ of x = 0. In the presence of an external magnetic field, $I(T)$ shows a tendency to increase in the ferromagnetic state while it is unaffected in the paramagnetic state. As *H* increases, the low-*T* anomaly becomes weaker and shifts to low temperature. As a result, $I(T)$

curve for $\mu_0 H > 0.08$ T crosses over the $I(T)$ curve in zero field below T^*. At a high magnetic field of $\mu_0 H \geq 1$ T, $I(T)$ approaches the empty coil data. On the other hand, the temperature dependence of f_r *i.e.*, $f_r(T)$ is similar to $I(T)$, but the anomaly at T^* is more sharper than in $f_r(T)$. Both the low-T anomaly and rapid decrease around T_C in $f_r(T)$ are dramatically affected by the external magnetic fields compared to $I(T)$. The inset shows behavior of $f_r(T)$ under $\mu_0 H$ = 1 T and 5 T for clarity. We find that $f_r(T)$ tends to show a minimum followed by a rapid increase below T = 110 K for $\mu_0 H$ = 1 T and the minimum shifts to T = 140 K under 5 T. The observed shift in $f_r(T)$ with the increasing magnetic field is due to field induced shift in the ferromagnetic transition temperature. A clear peak around T^* is seen in $f_r(T)$ under $\mu_0 H$ = 1 T as like the peak seen in $M(T)$. The behavior of $f_r(T)$ under high magnetic fields resembles the behavior of dc magnetization, $M(T)$. Next we show the response of both $I(T)$and $f_r(T)$ for x = 0 compound which didn't show any low temperature peak below T_C. Figs. 4.10(a) and 4.10(b) show the temperature dependence of the current, $I(T)$, and resonance frequency, $f_r(T)$, at different *dc* bias magnetic fields (H = 0-1 kG) for x = 0.6 compound. The behaviors of both $I(T)$ and $f_r(T)$ are similar to that of x = 0 compound, except for a few important differences: 1. Both $I(T)$ and $f_r(T)$ do not exhibit hysteresis around T_C = 363 K. The behaviors of both $I(T)$ and $f_r(T)$ follows the behavior of empty coil under a low magnetic field of H = 1 kG compare to $\mu_0 H$ = 1 T required in case of x = 0 compound. 3. A sudden increase in both $I(T)$ and $f_r(T)$ is absent at low temperature within the ferromagnetic ordered state in contrast to behavior seen in x = 0, instead, both $I(T)$ and $f_r(T)$ continue to show almost temperature independent behavior well below T_C up to T = 10 K.

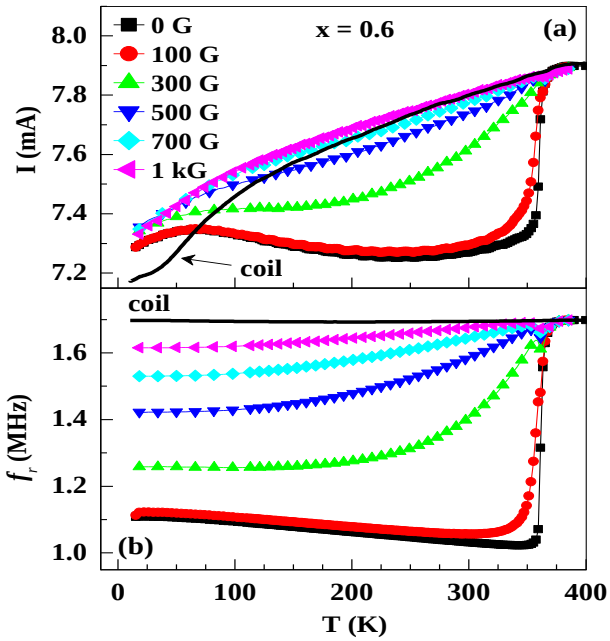

Fig. 4. 10 Temperature dependence of the (a) current (*I*) through ICO circuit, (b) resonance frequency (f_r) of ICO under different external dc magnetic fields (*H*) for x = 0.6 compound.

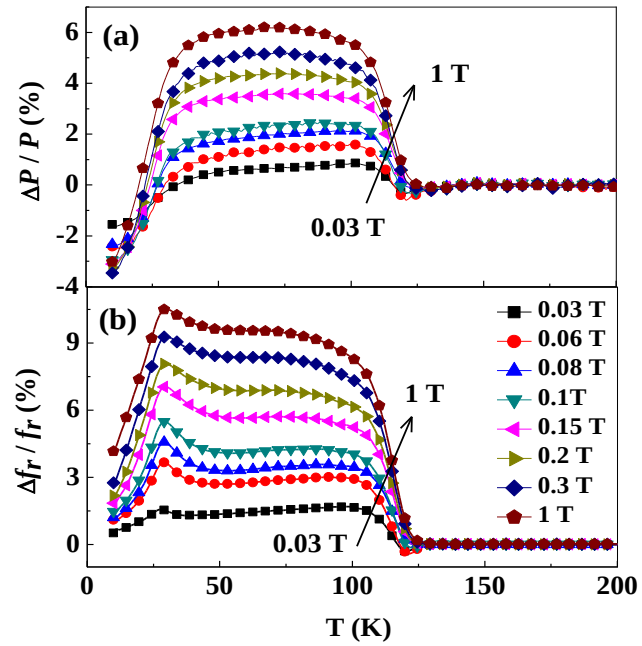

Fig. 4. 11 Temperature dependence of the fractional change in the (a) power absorption ($\Delta P/P$) and (b) resonance frequency ($\Delta f_r/f_r$) for different values of the external magnetic fields (*H*) for x = 0 compound.

We show the temperature dependence of fractional changes in the resonance frequency [$\Delta f_r/f_r = [f_r(H)-f_r(0)] / f_r(0)$] and power absorption [$\Delta P/P = \Delta I/I = [I(H)-I(0)] / I(0)$] as a function of temperature at different magnetic fields ($\mu_0 H$ = 0.03-1 T) for x = 0 in Figs. 4.11(a) and 4.11(b), respectively. The magnetoabsorption ($\Delta P/P$) is negligible above T_C, but it increases just below T_C, shows a plateau between 100 K and 50 K and then it decreases below 40 K. The $\Delta P/P$ in the plateau region increases from 0.6% at $\mu_0 H$ = 0.03 T to a maximum of 6.1% at $\mu_0 H$ = 1 T. The $\Delta P/P$ at $\mu_0 H$ = 0.03 T changes sign to negative below T^*. The $\Delta f_r/f_r$ is also negligible for $T > T_C$ and shows a rapid increase at T_C followed by a gradual increase down to 50 K. It then shows a tendency to increase more rapidly before is shows a peak around T^* below which it decreases rapidly. The maximum value of $\Delta f_r/f_r$ at the peak increases from 1% at $\mu_0 H$ = 0.03 T to 9.5% at $\mu_0 H$ = 1 T. It can be seen that unlike $\Delta P/P$, the magnitude of $\Delta f_r/f_r$ at 10 K increases as H increases. Note that the values of magnetoabsorption and the fractional change in the frequency shift are much larger in $La_{0.67}Ba_{0.33}MnO_3$ ($\Delta P/P$ = 23% and $\Delta f_r/f_r$ = 46% at T_C under $\mu_0 H$ = 0.1 T) as described in the previous chapter. In contrast to x = 0, the fractional changes in $\Delta P/P$ and $\Delta f_r/f_r$ for x = 0.6 sample shown in Figs. 4.12(a) and 4.12(b), respectively is similar to $La_{0.67}Ba_{0.33}MnO_3$ without showing any sudden decrease at low temperature. Both $\Delta P/P$ and $\Delta f_r/f_r$ show rapid increase around T_C and then it decrease monotonically with decreasing temperature. The magnitude of the peak in $\Delta P/P$ and $\Delta f_r/f_r$ increases with increasing magnetic fields. The magnitude of $\Delta P/P$ increased from 3% at H = 100 G to as high as 7.5% at H = 1 kG around T_C. Whereas, the magnitude of $\Delta f_r/f_r$ increased from a high value of 30% at H = 100 G to a large of value of 65% at H = 1 kG around T_C.

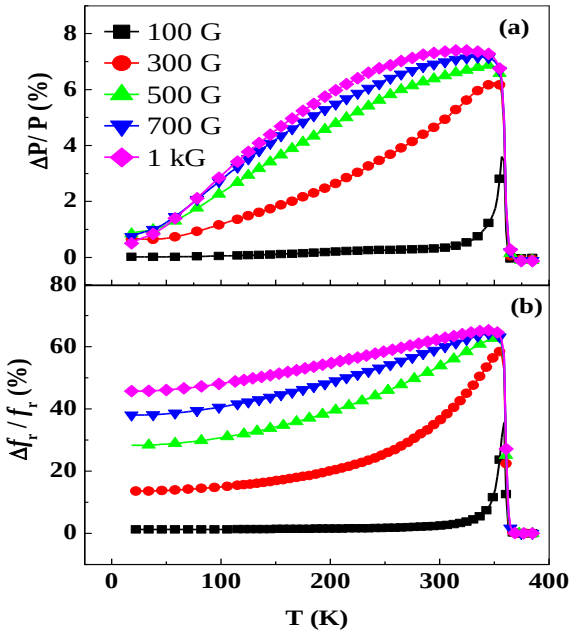

Fig. 4. 12 Temperature dependence of the percentage change in the (a) power absorption ($\Delta P/P$) and (b) resonance frequency ($\Delta f_r/f_r$) for different values of the external magnetic fields (H) for x = 0.6 compound.

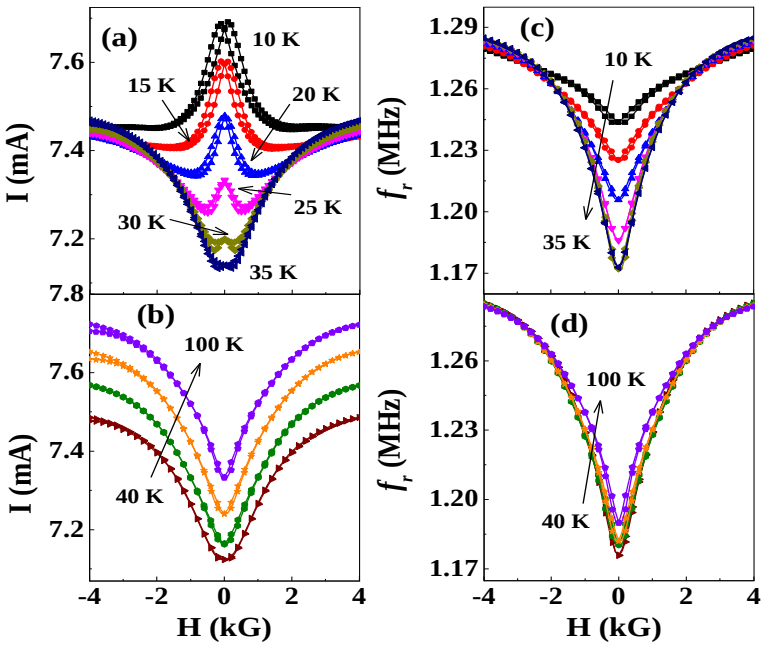

Fig. 4. 13 The magnetic field dependence of the (a) current (I) through ICO (c) resonance frequency (f_r) at selected temperatures for x = 0 compound. The figures (b) and (d) show the same for I and f_r, respectively, from T = 40 K to 100 K in the interval of 20 K.

We show field dependence of the current, $I(H)$, for T = 10-35 K in Fig. 4.13(a) and for T = 40-100 K in Fig. 4.13(b) as the field is swept through H = +4 kG → -4 kG → +4 kG.

We see different behavior of $I(H)$ below and above a temperature T^* = 30 K, where the low temperature peak occurs in the magnetization. The $I(H)$ shows a remarkable feature as the temperature increases from T = 10 K to 35 K in an interval of ΔT = 5 K. The $I(H, T = 10\ K)$ is nearly saturated at H = 4 kG but it quickly rises below H = ±1.4 kG and exhibits a peak at the origin (H = 0 G). Increasing the temperature from 10 K lead to three effects: 1. The magnitude of the peak at the origin decreases. 2. $I(H)$ tends to decrease with lowering field from H = 4 kG to H = 0 G. 3. The peak at the origin (H = 0) is completely suppressed and replaced by a dip at T = 35 K and above *i.e.*, above T^*. On the other hand, the $f_r(H)$ shows only a minimum at all temperatures from T = 10 K to 100 K as can be seen in Fig. 4.13(c) and (d). A similar behavior of $f_r(H)$ is seen for x = 0.6 compound at all temperatures (T = 10-350 K) which is shown in Fig. 4.14(b). Whereas, $I(H)$ of x = 0.6 shown in Fig. 4.14(a) also shows dip at the origin for all temperatures, which is in contrast to the behavior of $I(H)$ seen for x = 0.

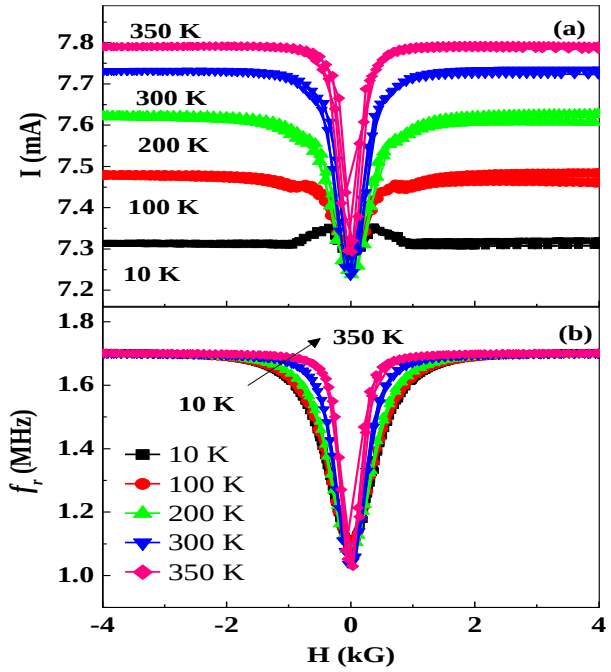

Fig. 4. 14 The magnetic field dependence of the (a) current (I) through ICO (c) resonance frequency (f_r) at selected temperatures (T = 10-350 K) for x = 0.6 compound.

Although the behavior of power absorption in x = 0.6 compound is almost similar to that of $La_{0.67}Ba_{0.33}MnO_3$ as described in the last chapter, remarkable features occur in x = 0 compound. The rapid decrease of $I(T)$ and $f_r(T)$ seen around T_C in both x = 0 and 0.6 compounds and its suppression under the magnetic field is related to the change in real and imaginary parts of the magnetic permeability as described in the previous chapter in case of $La_{0.67}Ba_{0.33}MnO_3$. However, we see new features in x = 0 compound. The important features observed in the power absorption of x = 0 compound are: firstly, the occurrence of a secondary transition in the temperature dependence of both f_r and I below the long-range ferromagnetic ordering and secondly, the transition from a dip seen in $I(H)$ at the origin below T^* = 30 K to a minimum in $I(H)$ for $T > T^*$. A rapid increase in both $I(T)$ and $f_r(T)$ below T^* = 30 K is due to the sudden drop in magnetization below T^* which arises possibly due to the antiparallel coupling of 3*d* spins of Mn sublattice and 4*f*-spins of Sm sublattice as described in the section: 4.3.2. A remarkable transition from a maximum to a minimum in $I(H)$ as T increases above T^* is clearly related to the minimum seen in $I(T, H = 0\ \text{G})$ around T^*. The ferromagnetic ordering of Sm-4*f* moments below T^* induces canting of spins in the Mn sub-lattice which increases the coercive field of the sample. The domain wall oscillates in response to the *rf* field and absorbs power from the *rf* magnetic field. The *rf* power absorption is related to the area of the ac hysteresis loop which is given by,

$$P(H_{ac},T) = 0.5\omega\mu'' {H_{ac}}^2$$

where, μ'' is the imaginary component of the complex permeability $\mu = \mu' - i\mu''$ and H_{ac} is the ac magnetic field in the coil which oscillates with frequency $\omega = 2\pi f$.

When the domains are oriented randomly in zero magnetic field, the *rf* power absorption is maximum. As the dc bias field is increased, the volume of domains oriented favorably parallel to the dc field expands at the expense of antiparallel domains. At higher fields, when the domains are preferentially oriented along the field direction, the ac hysteresis loop traced is small and hence, the power absorption decreases with increasing field. As the temperature increases towards T^*, the domain walls are easily depinned, the coercive field

decreases, and the magnetoabsorption decreases. We have noted that H_C is rather small, less than few Gauss for T = 40-100 K and the dc magnetization mainly proceeds through domain rotation. In this case, $I(H)$ increases with the dc magnetic field. Finally, the magnetoabsorption becomes negligible in the paramagnetic phase in the low field range (-4 kG $\leq H \leq$ +4 kG) investigated. The fractional change in the frequency shift is given by,

$$\frac{\Delta f_r}{f_r} \approx -\frac{1}{2}\frac{\Delta L}{L} = -\frac{1}{2}(\eta\chi' + 2\eta\frac{\Delta\delta}{\delta})$$

is caused by the temperature and field dependence of the real part of the permeability which shows a maximum around T^* and decreases rapidly close to T_C as the spins disorder.

4. 3. 4 Normal and inverse MCEs in ferromagnetic $Sm_{0.6-x}La_xSr_{0.4}MnO_3$

Since the discovery of a giant magnetic entropy change driven by a first-order magnetostructural transition in $Gd_5(Si_{4-x}Ge_x)$ nearly a decade ago, [194] extensive investigations of MCE have been done in ferromagnetic compounds such as doped MnAs [195] and Heusler alloys [196] compounds. The colossal magnetoresistive manganese oxides having the general formula $R_{1-x}A_xMnO_3$ (where R and A are trivalent rare earth ions and divalent alkaline earth ions, respectively), are also considered to be likely candidates for magnetic refrigeration because some of these compounds exhibit ΔS_m values ($-\Delta S_m \approx$ 4-6 $Jkg^{-1}K^{-1}$ for ΔH = 5 T) comparable to intermetallic alloys. [197, 198, 199, 200, 89] Majority of reports on the MCE in manganites are around paramagnetic-to-ferromagnetic (PM→FM) transition which leads to $\Delta S_m = S_m(H) - S_m(0)$ negative *i.e.*, decrease of magnetic entropy under H and the effect is called normal MCE (NMCE). In contrast to ferromagnets which cool upon demagnetization, antiferromagnets cools upon adiabatic magnetization *i.e.*, positive ΔS_m or inverse MCE (IMCE). Composites containing both normal MCE and inverse MCE materials can be used to enhance refrigerant capacity (RC) as it is cooled by both adiabatic magnetization as well as demagnetization. [201] Generally, inverse MCE is observed in a compound which undergoes antiferromagnetic (AFM) transition from the ferromagnetic state,

for example, $La_{0.5}Ca_{0.5}MnO_3$ (ΔS_m = +6.5 $Jkg^{-1}K^{-1}$ for ΔH = 5 T) which is a *CE*-type antiferromagnet in which antiferromagnetic ordering accompanies the long range charge-orbital ordering. [202] Very recently, inverse MCE was reported in $Ni_{50}Mn_{34}In_{16}$ alloy which undergoes austenite→martensite below the FM T_C. [203] The ΔS_m was also found to increase with decreasing rare earth size in $RE_{0.6}Sr_{0.4}MnO_3$ (*RE* = La, Pr. Nd, Sm etc) series. [204] In this section of the chapter, we present the occurrence of a normal MCE around T_C and an unusual inverse MCE at low temperature with increasing rare earth cation size of La in $Sm_{0.6-x}La_xSr_{0.4}MnO_3$.

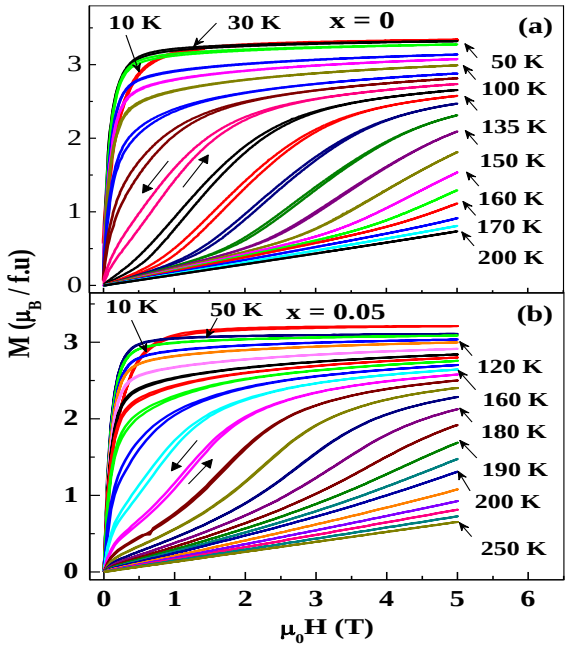

Fig. 4. 15 The *M*(*H*) isotherms at selected temperatures for (a) x = 0 and (b) x = 0.05 compounds.

We have shown the detailed temperature dependence of magnetic properties of $Sm_{0.6-x}La_xSr_{0.4}MnO_3$ compounds in the section 4.3.2 of this chapter. In this section, we present the magnetocaloric properties of $Sm_{0.6-x}La_xSr_{0.4}MnO_3$ compounds with compositions, x = 0, 0.05, 0.1, 0.3, 0.4 and 0.6 by measuring the *M*(*H*) isotherms at selected temperatures with a temperature interval of ΔT = 5 K. We show isothermal *M*(*H*) plots at selected temperatures

for x = 0 and 0.05 in Fig. 4.15(a) and 4.15(b), respectively. Here, we have shown $M(H)$ data only at few selected temperatures for clarity. While the $M(H)$ of x = 0 varies linearly with H above T = 180 K, a field-induced metamagnetic transition *i.e.*, a rapid increase of M above a certain critical field, occurs in the temperature range of 120 K ≤ T ≤ 170 K *i.e.*, above T_C = 118 K. The metamagnetic transition is reversible upon decreasing H with a small hysteresis of width 0.154 T at T = 124 K and the hysteresis in $M(H)$ decreases with lowering T. Such a field-induced metamagnetic behavior with hysteresis is also seen in x = 0.05 which is shown in Fig. 4.15(b). In x = 0.05, a field-induced metamagnetic transition occurs in the temperature range of 150 K ≤ T ≤ 200 K (above T_C) and the width of hysteresis decreases (≈ 0.07 T at T = 160 K). Next, we show the $M(H)$ isotherms for other four samples, x = 0.1, 0.3, 0.4 and 0.6 in Figs. 4.16(a), 4.16(b), 4.17(a) and 4.17(b), respectively. Since $M(T)$ of x = 0.6 compound did not show low-T peak below T_C, we have not measured $M(H)$ curve below T = 290 K. While a similar (as like in x = 0.05) but weak metamagnetic transition is seen in x = 0.1 (Fig. 4.16a) in the temperature range of 180 < T < 225 K without any hysteresis, the metamagnetic transition is absent in all other compositions: x = 0.3, 0.4 and 0.6. The $M(H)$ shows a ferromagnetic behavior in all the compounds below their respective T_Cs. However, we see that $M(H)$ at T = 10 K < T^* shows a cross-over behavior *i.e.*, the $M(H)$ curve at T = 10 K lies below the $M(H)$ curve at T > 10 K in the field range of $\mu_0 H$ < 2 T for all the compositions except x = 0.6 and it is pointed out by an arrow in all the $M(H)$ plots. This behavior is more pronounced in x = 0.4 compared to any other compounds. Next we show the temperature dependence of the ΔS_m values estimated from the isothermal $M(H)$ data

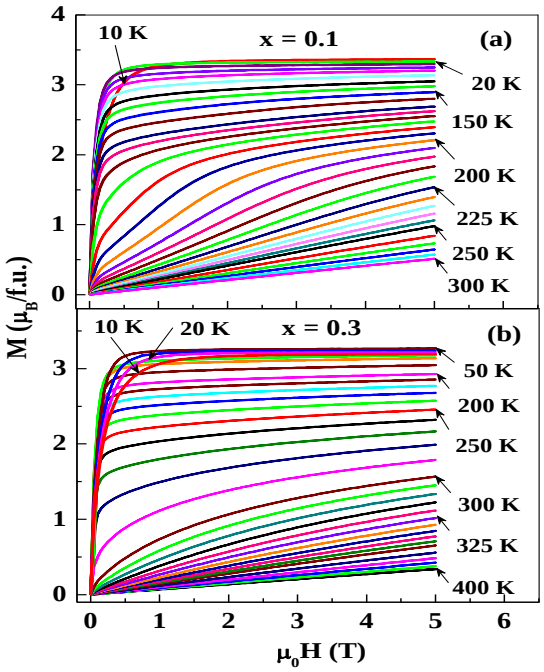

Fig. 4. 16 The *M*(*H*) isotherms at selected temperatures for (a) x = 0.1 and (b) x = 0.3 compounds.

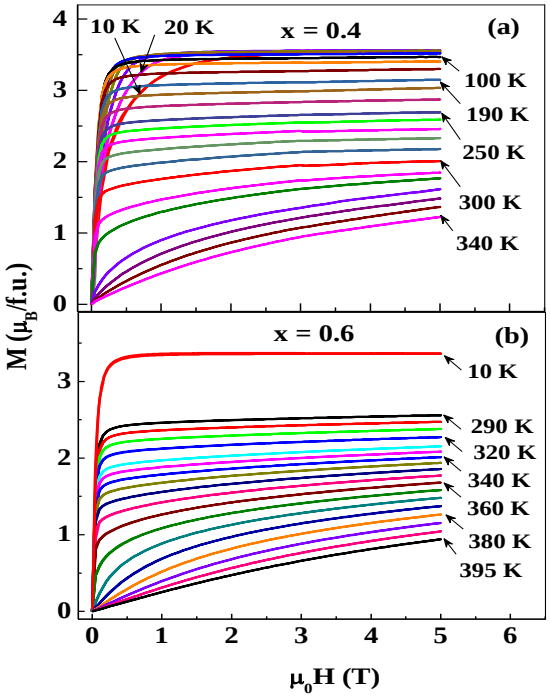

Fig. 4. 17 The *M*(*H*) isotherms at selected temperatures for (a) x = 0.4 and (b) x = 0.6 compounds.

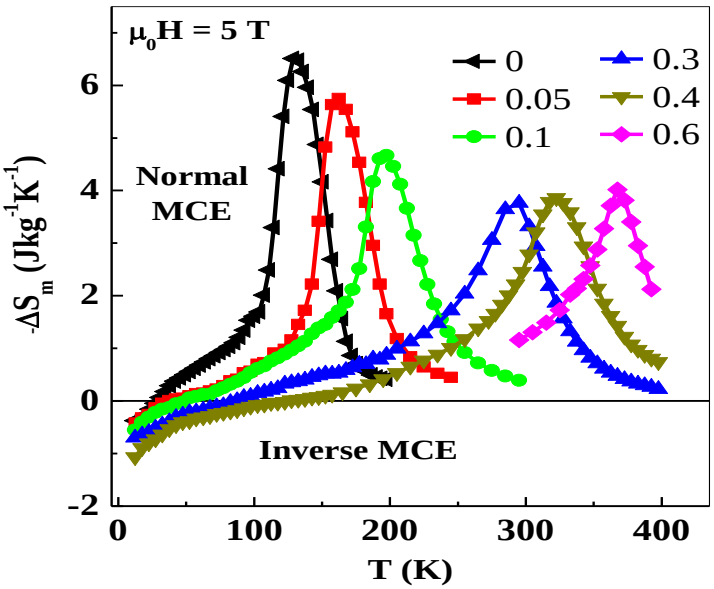

Fig. 4. 18 Temperature dependence of the magnetic entropy (ΔS_m) obtained from $M(H)$ data at ΔH = 5 T for x = 0, 0.05, 0.1, 0.3, 0.4 and 0.6.

A comparison of temperature dependences of ΔS_m estimated from $M(H)$ plots for a field change of ΔH = 5 T for x = 0, 0.05, 0.1, 0.3, 0.4 and 0.6 compounds are shown in Fig. 4.18. All the compounds show normal MCE ($-\Delta S_m$ is positive) at their respective ferromagnetic T_Cs and inverse MCE (except x = 0.6) below their respective T^*s. A horizontal line at $\Delta S_m = 0$ in Fig. 4.18 distinguishes the normal MCE and inverse MCE. Since $M(T)$ of x = 0.6 compound did not show low-T peak, we have not measured $M(H)$ curve below T = 290 K and thus we have $\Delta S_m(T)$ plot is in the temperature range of 290 K < T < 400 K. The peak value of ΔS_m at T_C decreases from -6.5 $Jkg^{-1}K^{-1}$ for x = 0 to -4.7 $Jkg^{-1}K^{-1}$ for x = 0.1 and the ΔS_m spreads over a wider temperature with increasing x as it can be seen in the figure. Below the peak, the magnitude of ΔS_m for x < 0.6 decreases with lowering temperature and changes sign to positive from negative ($-\Delta S_m$ changes from positive to negative) below the respective T^*s. The magnitude of ΔS_m at T_C and T = 10 K (below T^*) are plotted as a function of composition x in Fig. 4.19(a) on left and right scales, respectively. While the magnitude of ΔS_m at 10 K for x < 0.6 increases with increasing x, the magnitude of ΔS_m at T_C initially decreases with increasing x up to x = 0.3 and then increases slightly with further increase in x.

The maximum inverse MCE is observed for x = 0.4 *i.e.*, ΔS_m = +1.07 $Jkg^{-1}K^{-1}$ at T = 10 K for ΔH = 5 T. Besides the large value of ΔS_m, the temperature span over which ΔS_m spreads is important for practical application and this is measured by the quantity known RC and it is shown for a field change of ΔH = 5 T as a function of x in Fig. 4.19(b). A significant value of ΔS_m = -4 $Jkg^{-1}K^{-1}$ at T = 320 K along with a high RC of 214 Jkg^{-1} for x = 0.4 makes it an interesting compound for room temperature magnetic refrigeration technology.

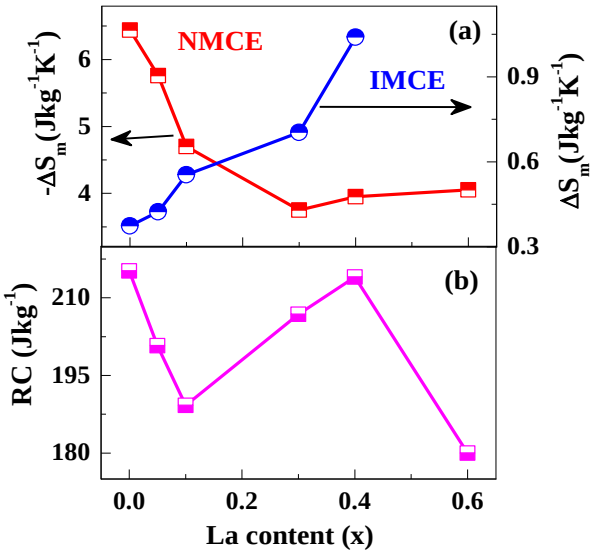

Fig. 4. 19 (a) Values of the RC, and (b) ΔS_m at T_C (left scale) and T = 10 K (right scale) as a function of composition x.

While the normal MCE in our $Sm_{0.6-x}La_xSr_{0.4}MnO_3$ compounds around T_C is due to ferromagnetic exchange-interaction between Mn spins, the appearance of inverse MCE due to well below the long-range ferromagnetic ordering is puzzling. Such a low temperature peak in other manganites is generally attributed to spin or cluster glass like transitions. However we rule out this possibility because the anomaly persists in ac susceptibility even at f = 5 MHz and its position does not shift with frequency. Since a material can show inverse MCE if dM/dT is positive, antiferromagnets are expected to show the inverse MCE over a wide field range as shown recently in $La_{0.5}Ca_{0.5}MnO_3$ (ΔS_m = +6.5 $Jkg^{-1}K^{-1}$ for ΔH = 5 T). [202] However, inverse MCE in ferromagnetic manganites is a rare phenomenon. Very recently, inverse MCE was reported in ($La_{0.7}Sr_{.3}MnO_3/SrRuO_3$) superlattice when a magnetic field was

applied perpendicular to the superlattice surface. [205] A weak antiferromagnetic coupling mediated by the spacer ($SrRuO_3$) layer between adjacent ferromagnetic manganite layers was suggested to the origin of the inverse MCE. An inverse MCE was also found at low temperatures in ferromagnetic $Pr_{0.52}Sr_{0.48}MnO_3$ single crystal, [206] but this composition is close to antiferromagnetic phase boundary in $Pr_{1-x}Sr_xMnO_3$ series (x = 0.5 is a layered *A*-type antiferromagnetic) and a compositional fluctuations can induce antiferromagnetically ordered local regions. We would like to emphasize the point that our samples are not phase segregated into antiferromagnetic and ferromagnetic phases. Manganites with mixed phases generally exhibit pronounced hysteresis in $M(T)$ and field-induced metamagnetic transition at low temperatures. However, we neither found metamagnetic transition nor a pronounced hysteresis in $M(T)$ or in $\rho(T)$ for $x \geq 0.3$. Instead, all the samples are ferromagnetic with small coercive field (H_C < 100 G) at 10 K.

We have discussed all the possibilities of the origin of low temperature anomaly at T^* in our compounds in the section: 4.3.2 including spin reorientation transition, glassy behavior and 4*f*-3*d* super-exchange interaction. We propose that 4*f*-3*d* exchange interaction plays important role for the appearance of low temperature anomaly at T^* in the $Sm_{0.6-x}La_xSr_{0.4}MnO_3$ series. The 3*d* moments of Mn order ferromagnetically within the Mn sublattice. The exchange field created by Mn-moments makes 4*f*-moments of Sm to order. The Sm-4*f* moments most likely orders ferromagnetically within its sublattice but antiparallel to the Mn-sublattice below T^* *i.e.*, there exist a weak antiferromagnetic coupling between Mn and Sm-4*f* sublattice below T^*. The 4*f*-3*d* interaction has not been studied in detail because its influence is weak on transport properties and also the anomaly in magnetization is generally small and masked by the larger contributions from ferromagnetic ordering of Mn spins. As we have already referred few articles in the section: 4.3.2, there are clear evidences for 4*f*-3*d* interaction from neutron diffraction data in various compounds. [188, 189, 190, 191] Thus, we suggest that the inverse MCE in our compounds is due to the antiparallel coupling of 3*d* spins of Mn sublattice and 4*f*-spins of Sm sublattice through the ordering of Sm-4*f* moments which might have induced by the molecular field of Mn-sublattice. Interestingly, the Sm-4*f*

and Mn-3*d* interaction around $T^* = 120$ K in x = 0.4 is very high. What we have to understand is the condition under which rare earth moment can order at such a high temperature. Unfortunately, the effect of 4*f*-3*d* exchange interaction has not been studied theoretically in detail except one recent CGA+U calculation on $Nd_{0.67}Sr_{0.33}MnO_3$ by Lin Zhu *et al.*' [207] which emphasize on superexchange coupling between Nd-4*f* and Mn-3*d* (t_{2g}) electrons via O-2p electrons to understand the drop in magnetization at low temperature.

4. 3. 5 An anomalous ac magnetotransport in $Sm_{0.6-x}La_xSr_{0.4}MnO_3$

In this section, we have investigated the effect of lanthanum (La) substitution on ac magnetotransport properties of $Sm_{0.6-x}La_xSr_{0.4}MnO_3$ series with $0 \leq x \leq 0.6$. Hence, we have measured both the ac resistance (R) and the reactance (X) as a function of temperature (T = 400-10 K), magnetic field ($\mu_0 H$ = 0-7 T) and frequency (f = 1 kHz to 5 MHz). We show that the temperature dependence of R, $R(T)$, of x = 0 shows an anomalous behavior with increasing frequency. The $R(T)$ exhibits a single peak at $f \leq 100$ kHz, but it splits into two peaks which move in opposite directions in temperature with increasing frequency (above f = 100 kHz). While the low temperature peak shifts upward rapidly with increasing strength of the dc magnetic field ($\mu_0 H > 1$ T) for f = 5 MHz, the high temperature peak is insensitive to the magnetic field. Both peaks merge into a single peak for $\mu_0 H = 7$ T. This splitting behavior in $R(T)$ disappears with increasing La content in SLSMO compounds. We report here a detailed ac magnetotransport in SLSMO compounds and we discuss the possible origins of the observed effects.

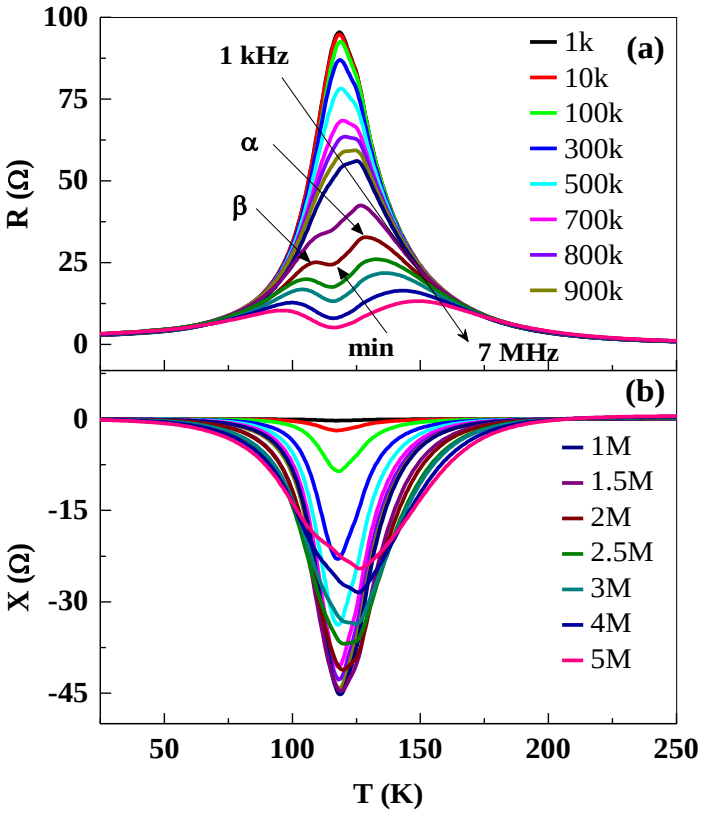

Fig. 4. 20 Temperature dependence of the (a) ac resistance *R* and (b) reactance *X* in zero field at selected frequencies (*f* = 1 kHz - 5 MHz) for x = 0 compound.

Figs. 4.20(a) and 4.20(b) show the temperature dependence of the ac resistance *R* and reactance *X* , respectively, in zero field for selected frequencies (*f* = 1 kHz - 5 MHz) for x = 0 compound. The *R*(*T*) at *f* = 1 kHz shows a single peak at the insulator-metal (*I-M*) transition (T_{IM} = 115 K). The value of resistivity at the *I-M* transition and at room temperature are ρ = 89 Ωcm and $\rho = 90 \times 10^{-3}$ Ωcm, respectively. While the behavior of *R*(*T*) for $f \leq 100$ kHz is similar to that of at *f* = 1 kHz, the magnitude of *R*(*T*) for *f* = 100 kHz is slightly decreased at the peak. Interestingly, a kink appears in *R*(*T*) just above the *I-M* transition for *f* > 100 kHz. This kink in *R*(*T*) is more clear as *f* increases above *f* = 100 kHz and its position shifts up in temperature with increasing frequency. The single peak observed at T_{IM} for *f* = 1 kHz splits into a double peak with a dip occurring around T_{IM} when the frequency is increased to *f* = 1 MHz. A clear double peak behavior is seen in *R*(*T*) for $f \geq 1.5$ MHz. We have designated these peaks and the dip seen in *R*(*T*) as: α – the peak above T_{IM}, β – the peak below T_{IM} and

min – the dip or the minimum in $R(T)$ around T_{IM}. While the position of the β-peak shifts downward in temperature with increasing frequency, the position of the α-peak shifts upward in temperature with increasing frequency. This can be clearly seen in Fig. 4.21 where we have plotted the frequency dependence of the positions of α-peak, β-peak and minimum seen in *R(T)*. While the position of α-peak increases with increasing *f*, the position of β-peak decreases and the position of minimum is frequency independent. Note that the magnitude of *R(T)* below T = 200 K decreases with increasing frequency (Fig. 4.20a). On the other hand, the *I-M* transition is accompanied by a minimum in $X(T)$ for $f \geq 1$ kHz as shown in Fig. 4.20(b). The sign of X is negative, but it is similar to a large capacitance change observed in the tri-layer structure Al-AlO_x-$(La_{1-y}Pr_y)_{0.67}Ca_{0.33}MnO_3$ around T_C by R. P. Rairigh *et al.* [176] The *X(T)* does not exhibit pronounced double peaks unlike *R(T)*. The minimum in the $X(T)$ becomes increasingly negative as the frequency increases to f = 1 MHz and then it decreases again with further increase in *f*. The $X(T)$ curves become broader as *f* increases above f = 1 MHz.

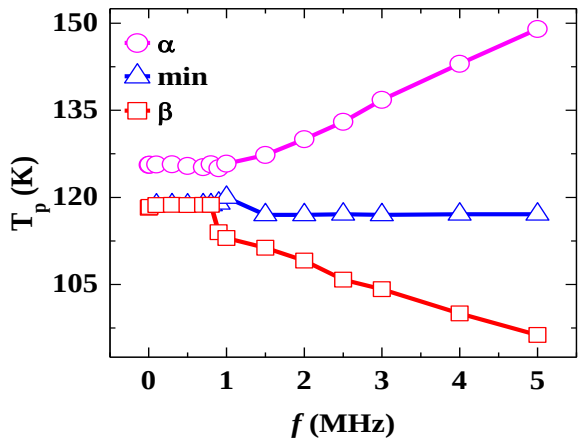

Fig. 4. 21 The peak positions of α, β and minimum seen in the temperature dependence *R* as a function of frequency.

Next we show the effect of La doping on ac electrical transport properties in $Sm_{0.6-x}La_xSr_{0.4}MnO_3$. We have seen that increasing La content in $Sm_{0.6-x}La_xSr_{0.4}MnO_3$ decreases the resistivity of the compounds. Thus, it is interesting to know how the observed double peak get affects with La doping.

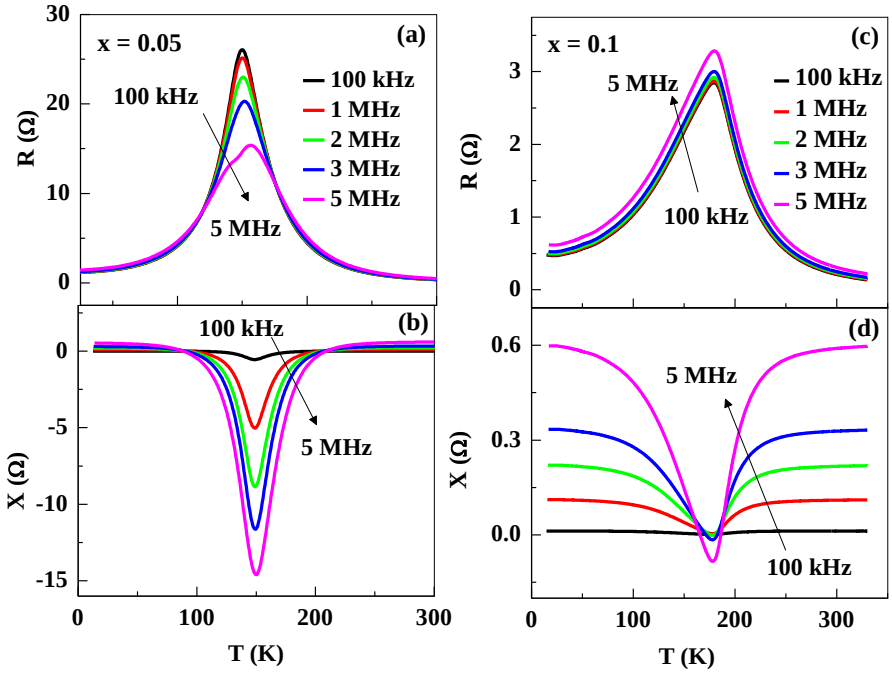

Fig. 4. 22 Temperature dependence of the ac resistance *R* and reactance *X* under zero field for selected frequencies (*f* = 0.1-5 MHz) for x = 0.05 [(a) and (b)] and x = 0.1 [(c) and (d)] compounds.

Figs. 4.22(a) and 4.22(b) show the temperature dependence of the ac resistance *R* and reactance *X*, respectively, in zero field for selected frequencies (*f* = 0.1-5 MHz) for x = 0.05. Figs. 4.22(c) and 4.22(d) show similar results of *R* and *X*, respectively for x = 0.1. The *I-M* transition in x = 0.05 is accompanied by a peak in $R(T)$ at T_{IM} = 150 K at *f* = 100 kHz. The magnitude of $R(T)$ increases around T_{IM} decreases with increasing *f* as like in case of x = 0. In contrast to the behavior of the $R(T)$ in x = 0, the splitting of a single peak into a double peak is almost disappeared in x = 0.05 except there is a weak sign of double peak appearance at *f* = 5 MHz. Whereas, $X(T)$ at all frequencies shows minimum around T_{IM} as like in x = 0, but the magnitude of $X(T)$ increases with increasing *f* unlike in x = 0. On the other hand, both $R(T)$ and $X(T)$ of x = 0.1 show different behavior compared to x = 0 and x = 0.05. The magnitude of $R(T)$ slightly increases with increasing *f* with a maximum around T_{IM} and it does not exhibit the double peak behavior. Whereas, the magnitude of $X(T)$ changes sign from negative to positive just below and above T_{IM}. Let us now discuss the results for x = 0.2 and 0.4 compounds.

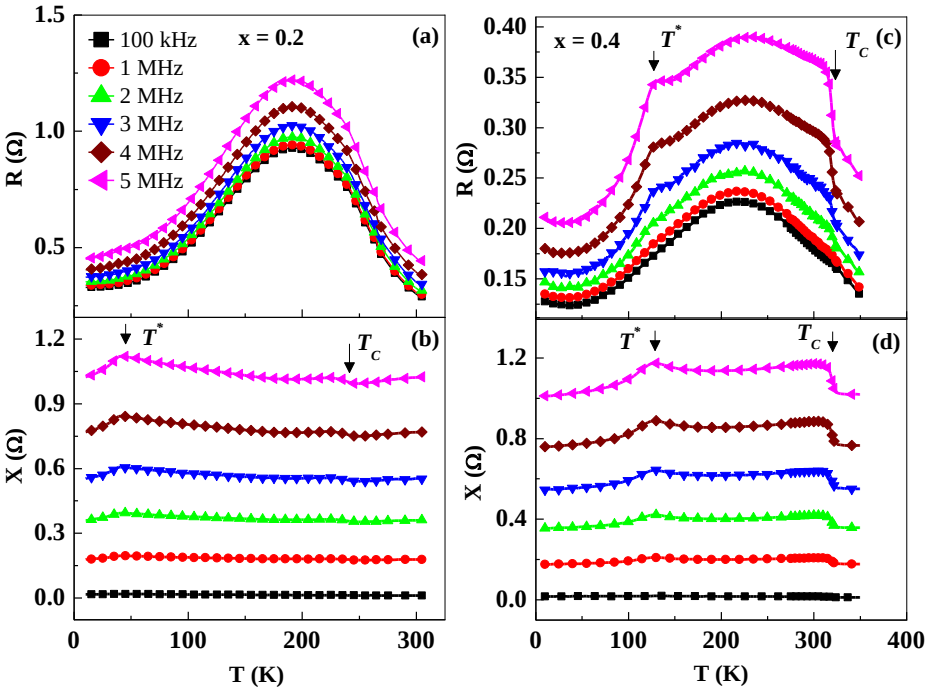

Fig. 4. 23 Temperature dependence of the ac resistance *R* and reactance *X* under zero field for selected frequencies (*f* = 0.1-5 MHz) for x = 0.2 [(a) and (b)] and x = 0.4 [(c) and (d)] compounds.

We show the temperature dependence of the ac resistance R and reactance X, respectively, in zero field for selected frequencies (f = 0.1-5 MHz) for x = 0.2 in Figs. 4.23(a) and 4.23(b), respectively. Figs. 4.22(c) and 4.22(d) show $R(T)$ and $X(T$) for x = 0.4, respectively. While the behavior of $R(T)$ of x = 0.2 is similar to that of x = 0.1 as it shows a broad transition with a maximum around the *I-M* transition, $X(T)$ shows a spectacular behavior. $X(T)$ for f > 100 kHz shows a step like increase around T_C = 243 K and sudden drop at T^* = 42 K. They are marked by the arrows as it is not clearly visible in figure because of the scale used. Unlike $X(T)$ for x ≤ 0.1, the magnitude of $X(T)$ increases with increasing f in the entire temperature range. On the other hand, we see remarkable features in both $R(T)$ and $X(T)$ for x = 0.4 compound. As temperature decreases from 350 K, the $R(T)$ at f = 0.1 MHz increases with a slight change in slope around T_C and goes through a broad maximum around T = 225 K before it decreases at low temperature. The magnitude of $R(T)$ increases in the entire temperature range with increasing f as in the case of x = 0.2. A remarkable feature is

the step-like increase in $R(T)$ around T_C and the appearance of low-T anomaly at $T^* = 120$ K for $f \geq 2$ MHz. While the broad maximum occurs at $T = 225$ K for all f, the amplitude of the step seen in $R(T)$ around T_C increases with increasing f and the low-T anomaly changes to a sudden drop below $T^* = 120$ K. On the other hand, the $X(T)$ at all frequencies ($f \leq 5$ MHz) is nearly temperature independent above 320 K, but it shows a step-like increase around T_C followed by a peak at $T^* = 120$ K and a monotonic decrease with further decrease in T. Next we show the similar behaviors of $R(T)$ and $X(T)$ for x = 0.6 in Figs. 4.24(a) and 4.23(b), respectively. We show the data up to $T = 100$ K, since the x = 0.6 sample did not exhibit any low temperature anomaly. As like x = 0.4, both $R(T)$ and $X(T)$ show a step like increase around T_C except it do not show any sudden drop at low temperature as the low temperature anomaly is absent in x = 0.6.

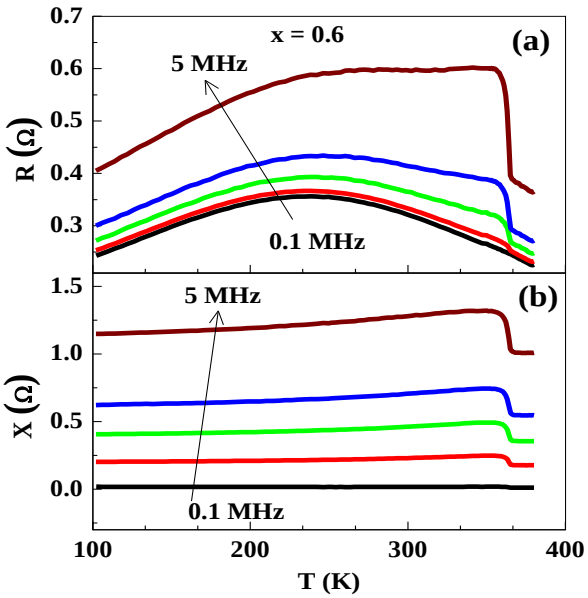

Fig. 4. 24 Temperature dependence of the (a) ac resistance *R* and (b) reactance *X* under zero field for selected frequencies (*f* = 0.1-5 MHz) for x = 0.6 compound.

We have investigated the effect of external magnetic fields on the behavior of $R(T)$ and $X(T)$ for three selected compounds at two selected frequencies ($f = 1$ and 5 MHz):

1. x = 0 which showed a frequency dependent single peak at the *I-M* transition in both $R(T)$ and $X(T)$

2. x = 0.4, an intermediate compound between x = 0 and x = 0.6, which showed a rapid increase around T_C and a sudden drop at T^* in both $R(T)$ and $X(T)$ with increasing frequency, and
3. x = 0.6 which showed only a rapid increase around T_C in both $R(T)$ and $X(T)$ with increasing frequency.

Let us first see the response of both $R(T)$ and $X(T)$ of x = 0 under external magnetic fields.

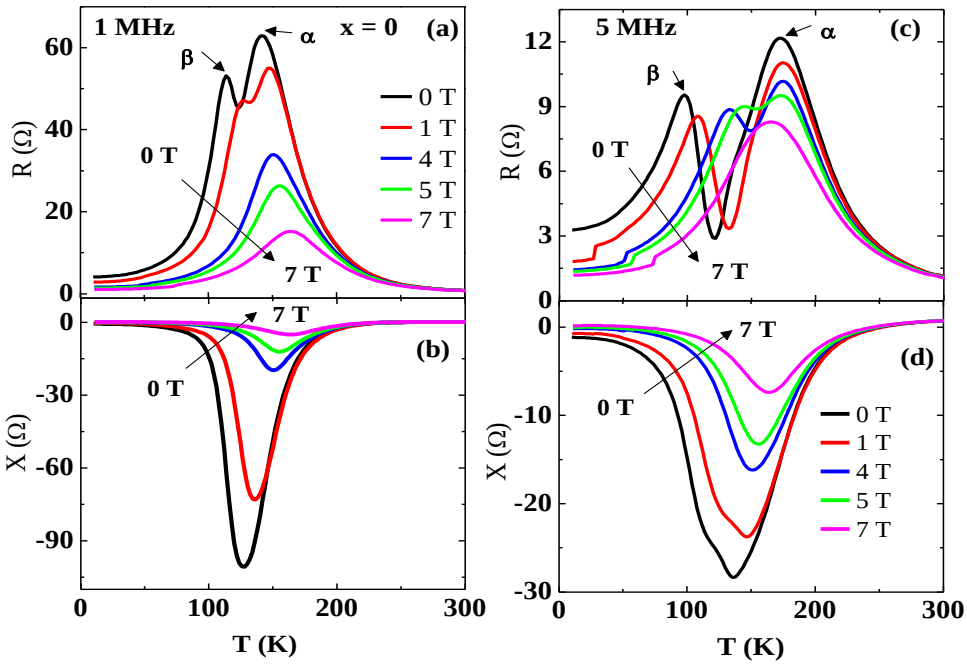

Fig. 4. 25 Temperature dependence of the ac resistance *R* and reactance *X* at *f* = 1 MHz [(a) and (b)] and *f* = 5 MHz [(c) and (d)] under $\mu_0 H$ = 0-7 T for x = 0.

The *R(T)* and *X(T)* of x = 0 were found to be insensitive to sub kilo gauss magnetic fields. Hence, we focus on the behaviors of $R(T)$ and $X(T)$ under high magnetic fields ($\mu_0 H$ = 0, 1, 4, 5, and 7 T) which are shown in Figs. 4.25(a)-(d) for two selected frequencies (f = 1 and 5 MHz). The $R(T)$ at f = 1 MHz exhibits two peaks designated by 'α' (high temperature peak) at T = 141 K and 'β' (low temperature peak) at T = 114 K. While both the peaks are decreased in magnitude under the bias field of $\mu_0 H$ = 1 T, the β-peak is shifted up by ΔT = 13 K compared to ΔT = 3 K for α-peak. The double peak behavior completely disappears for $\mu_0 H \geq 2$ T. The $X(T)$ in zero field shows a sharp minimum around the *I-M* transition. The

sharp minimum decreases in magnitude (becomes less negative), broadens and shifts to high temperature as H increases. Now, let us see the behavior of at f = 5 MHz. The $R(T)$ at f = 5 MHz in zero field exhibits well separated α and β-peaks at T = 173 K and 97 K, respectively. A magnetic field of $\mu_0 H$ = 1 T decreases the magnitude of both the peaks as like in the case of f = 1 MHz. While α-peak does not shift in T under $\mu_0 H$ = 1 T, the β-peak shifts upward in T by ΔT = 12 K with respect to the zero field value. The β-peak shifts upward by ΔT = 35 K (45 K) under $\mu_0 H$ = 4 T (5 T), but the position of the α-peak is unaltered. Interestingly, both the α and β-peaks merge into a single peak at $\mu_0 H$ = 7 T and its position is 15 K below the α-peak in zero field. In addition, we also see a step-like decrease of $R(T)$ around T = 20 K under $\mu_0 H$ =1 T which shifts up in temperature with increasing magnetic field. Its origin is not very clear at the moment and hence, it will not be discussed further. On the other hand, the behavior of $X(T)$ at f = 5 MHz is similar to that of at f = 1 MHz except there is a weak shoulder just below T_{IM}. The sharp minimum decreases in magnitude (becomes less negative), broadens and shifts to high temperature as the magnetic field increases. The weak shoulder observed just below T_{IM} in zero field also disappears with increasing strength of the magnetic field.

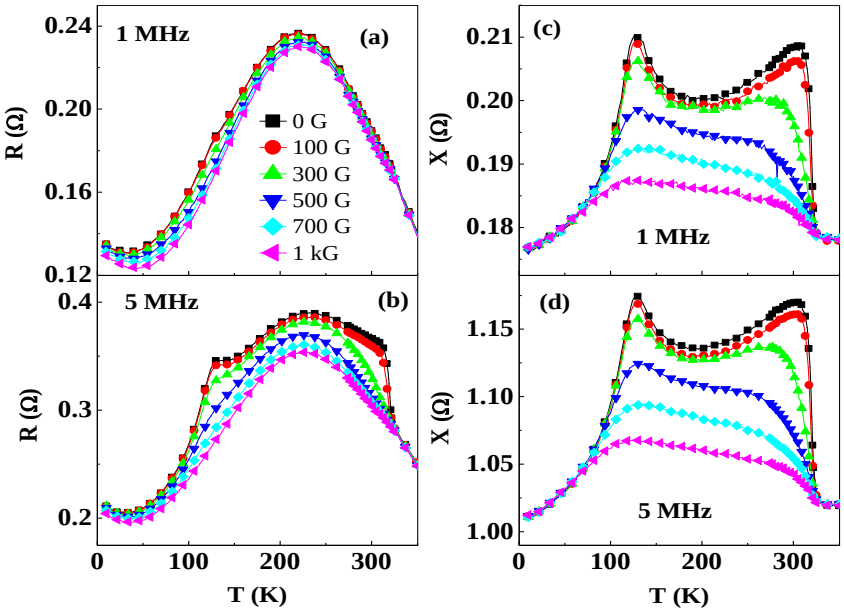

Fig. 4. 26 Temperature dependence of the ac resistance R and reactance X at f = 1 MHz [(a) and (c)] and f = 5 MHz [(b) and (d)] under H = 0-1 kG for x = 0.4.

The effect of sub-kilo gauss magnetic fields (H = 0-1 kG) on the behaviors of $R(T)$ and $X(T)$ at f = 1 and 5 MHz are shown in the Figs. 4.26(a)-(d). Unlike in the case of x = 0, both $R(T)$ and $X(T)$ of x = 0.4 are very sensitive to the sub-kilo gauss magnetic fields and thus we have restricted the field range up to H = 1 kG. The $R(T,$ 1 MHz) under zero field shows a broad hump around T = 225 K with a slight change in slope at T_C. The value of $R(T)$ below T_C decreases by a small value under the sub-kilo gauss magnetic fields. However, the $R(T,$ 5 MHz) in zero field exhibits a step-like increase at T_C followed by a broad hump around 225 K and a sudden drop below T^* = 120 K. While a magnetic field of H = 100 G decreases the magnitude of $R(T)$ by a small value, a slightly higher magnetic field of H = 300 G decreases the amplitudes of both the step-like increase at T_C and sudden drop at T^* = 120 K. Interestingly, both the step-like increase at T_C and the sudden drop at T^* = 120 K disappear under $H \geq$ 500 G. The behavior of $R(T,$ 5 MHz, $H >$ 500 G) resembles the behavior of $R(T,$ 0.1 MHz, 0 G) with just a broad hump around T = 225 K. Whereas, the $X(T)$ at both f = 1 and 5 MHz exhibits a sharp increase at T_C and a sudden decrease at T^* in zero field. A broad minimum around T = 175 K occurs in between T_C and T^*. The extraordinary sensitivity of $X(T)$ to sub-kilo gauss magnetic fields is noteworthy. While the high-T peak decreases in magnitude and shifts down in T with increasing H, the low-T peak just decreases in magnitude without any change in its position. It is also to be noted here that the minimum seen in X around T = 175 K in zero field has disappeared under $H >$ 500 G and both the low and high temperature peaks have become a broad maximum. Next we show the similar results for x = 0.6 in Figs. 4.27(a)-(d). Since x = 0.6 did not show any low-T anomaly in $M(T)$, we have restricted the temperature range up to T = 100 K. The response of both $R(T)$ and $X(T)$ under sub-kilo magnetic fields is almost similar to that of x = 0.4 except that there is no sudden drop at low temperature. Since there is no low-T anomaly in x = 0.6, both $R(T)$ and $X(T)$ show a rapid increase around T_C and then it show monotonic decrease with lowering temperature below T_C down to T = 100 K. Since there is a dramatic change in both $R(T)$ and

$X(T)$ under the magnetic field, we have calculated the fractional changes in them at f = 5 MHz and the results are shown below.

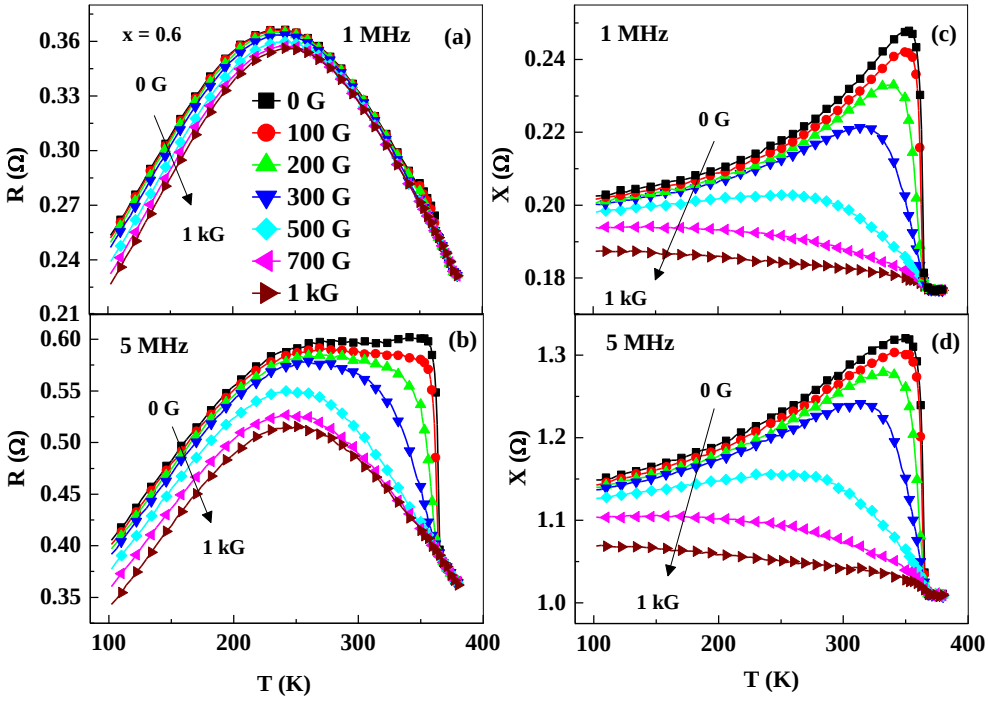

Fig. 4. 27 Temperature dependence of the ac resistance *R* and reactance *X* at *f* = 1 MHz [(a) and (c)] and *f* = 5 MHz [(b) and (d)] under *H* = 0-1 kG for x = 0.6.

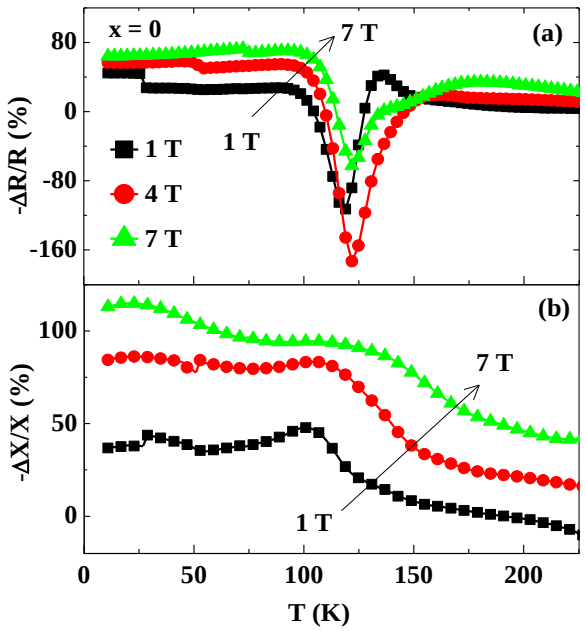

Fig. 4. 28 Temperature dependence of the ac magnetoresistance (Δ*R*/*R*) and magnetoreactance (Δ*X*/*X*) for *f* = 5 MHz at $\mu_0 H$ = 1, 3, 4 and 7 T for x = 0 compound.

First we show the temperature dependence of ac magnetoresistance {$\Delta R/R = [R(H) - R(0)] / R(0)$} and the magnetoreactance {$\Delta X/X = [X(H) - X(0)] / X(0)$ for x = 0 at $\mu_0 H$ = 1 T, 4 T and 7 T for f = 5 MHz in Figs. 4.28(a) and 4.28(b), respectively. The -$\Delta R/R$ is positive at 225 K and it initially increases with lowering temperature but changes sign to negative around 130 K. A deep minimum occurs around 118 K with a magnitude of -115% and the sign of -$\Delta R/R$ changes to positive again below 90 K. The magnitude of the minimum increases to -170% at T = 122 K under $\mu_0 H$ = 4 T but it reduces to -60% at T = 122 K under $\mu_0 H$ = 7 T. It is to be noted here that the magnitude of -$\Delta R/R$ at low temperature increases with increasing magnetic field and the same result is seen at high temperature. On the other hand, -$\Delta X/X$ at $\mu_0 H$ = 1 T, increases slowly with decreasing temperature from 225 K and exhibits a peak of magnitude 48% around T = 103 K and then decreases with further decrease in T. The magnitude of the -$\Delta X/X$ peak increases to 83% at $\mu_0 H$ = 4 T. While the -$\Delta X/X$ at $\mu_0 H$ = 7 T shows a broad peak close to T = 114 K with a magnitude of 94%, it increases with further decrease in T and attains a huge value of 113% at T = 10 K.

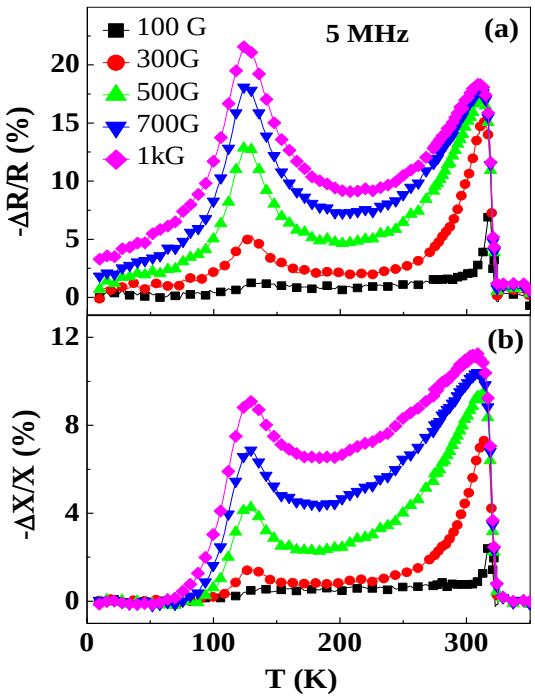

Fig. 4. 29 Temperature dependence of the ac magnetoresistance ($\Delta R/R$) and magnetoreactance ($\Delta X/X$) for f = 5 MHz at H = 100 G – 1 kG for x = 0.4 compound.

Temperature dependence of the -Δ*R*/*R* and -Δ*X*/*X* for x = 0.4 at different dc bias fields ($H \leq 1$ kG) for f = 5 MHz are shown in Figs. 4.29(a) and 4.29(b), respectively. The -Δ*R*/*R* at H = 100 G for f = 5 MHz shows a rapid increase at T_C and exhibits a sharp peak of magnitude 7%. Another peak occurs around T^* = 120 K. As H increases further, the magnitude of both the high-T and low-T peaks increase but the high-T curves broaden on the low temperature side, while the low-T peak position is unaltered. Interestingly, the magnitude of peak in -Δ*R*/*R* at T^* (-Δ*R*/*R* = 22%) exceeds the peak value at T_C (-Δ*R*/*R* = 18%) for f = 5 MHz and H = 1 kG. A similar trend is also seen in -Δ*X*/*X* for f = 5 MHz and the magnitudes of the peaks at H = 1 kG are 9% at T_C and 11% at T^*. Similar results of -Δ*R*/*R* and -Δ*X*/*X* at f = 5 MHz for x = 0.6 are shown in Figs. 4.30(a) and 4.29(b), respectively. In contrast to x = 0.4, x = 0.6 shows only one peak at T_C. While the magnitude of -Δ*R*/*R* around T_C increases from 15% at H = 100 G to 32% at H = 700 G, magnitude of -Δ*X*/*X* around T_C increases from 4% at H = 100 G to 21% at H = 700 G.

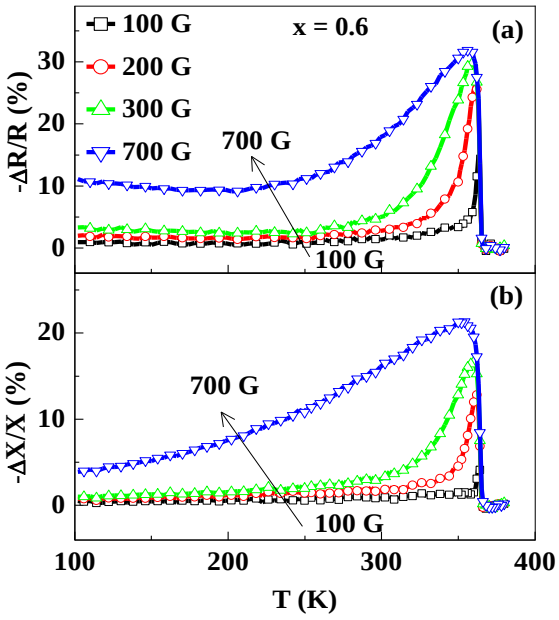

Fig. 4. 30 Temperature dependence of the ac magnetoresistance (Δ*R*/*R*) and magnetoreactance (Δ*X*/*X*) for f = 5 MHz at H = 100-700 G for x = 0.6 compound.

We now focus on the compound x = 0 which showed an unusual behavior in temperature dependence of ac resistance with varying frequency. We have measured the

frequency dependence of both R and X in the frequency range f = 1 kHz to 5 MHz at selected temperatures from T = 108 K to 138 K in a narrow temperature interval of ΔT = 2 K around T_C. From the frequency sweep data of R and X, we have plotted R versus $-X$ at different temperatures in Fig. 4.31. All the plots in the temperature range T = 108-138 K show semicircle behavior as like one obtains in the case of cole-cole plot of Z' versus $-Z''$ of dielectric materials, where Z' and Z'' are the real and imaginary parts of the electrical impedance measured in two probe configurations. The semicircle in our sample is not complete as the measurement frequency is limited to f = 5 MHz. All the curves exhibit a clear maximum. The position of maximum increases with increasing temperature and shows a highest value at T = 122 K and then it decreases with further decreasing temperature. The maximum in R versus $-X$ plot occurs at a characteristic frequency called as f_{max}. We see a systematic change in f_{max} in R versus $-X$ plots with varying temperature just below and above the I-M transition. We define a relaxation time $\tau = 1 / f_{max}$. We compare the temperature dependence of the dc resistivity (left scale) and τ (right scale) in Fig. 4.32. Interestingly, we see a close agreement between the temperature dependences of the dc resistivity and τ.

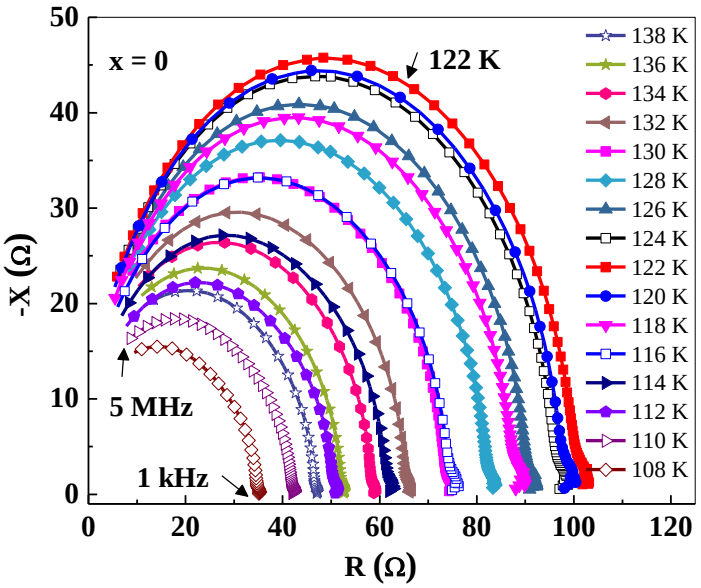

Fig. 4. 31 Plot of R versus $-X$ at selected temperatures (T = 108-138 K) for x = 0 compound derived from the frequency sweep data.

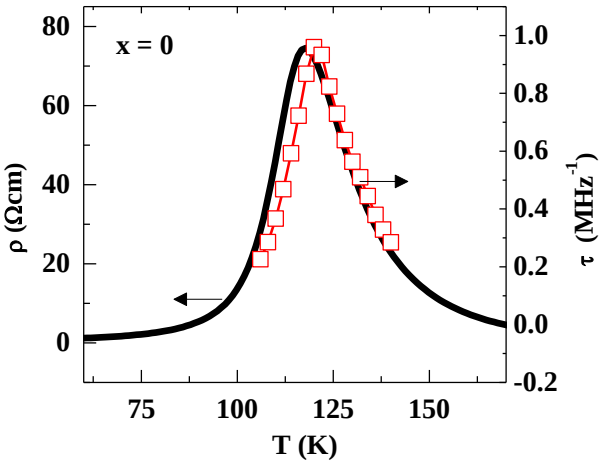

Fig. 4. 32 Temperature dependence of the dc resistivity (ρ) (light scale) and relaxation time (τ) (right scale) estimated from the peak position appeared in $-X$ versus R plot.

The important results obtained in this section are:

1. Splitting of single peak appeared in $R(T)$ around T_{IM} in x = 0 for $f \leq 100$ kHz into double peak (α and β – high and low temperature peaks, respectively) with increasing frequency.

2. Shifting up of β-peak position in temperature with increasing strength of the magnetic field and the insensitiveness of the α-peak position to external magnetic field.

3. Disappearance of a double peak behavior in compounds with x > 0.

4. Observations of step-like increase at T_C and sudden drop at T^* in $X(T)$ of x ≥ 0.2 for $f > 100$ kHz and also $R(T)$ of x > 0.2 for $f \geq 2$ MHz.

5. Sensitiveness of both R and X to external magnetic fields.

Let us first discuss the origin of the splitting of single peak appeared in $R(T)$ in zero-field into double peak with increasing frequency in x = 0 sample. The insensitivity of the position of the high temperature α-peak and the rapid upward shift of the low temperature β-peak with increasing magnetic field suggest that two different mechanisms are involved. The observed frequency-induced single to double peak behavior in zero field has certain resemblance to critical slowing down of fluctuations observed in some ferroelectric and magnetic systems. [208] In these systems, the relaxation time (τ) associated with electrical dipoles (or magnetic dipoles in ferromagnets) increases abruptly very close but above T_C.

Hence, the electrical (magnetic) dipoles are unable to follow the ac electric (ac magnetic) field which results in dispersion in the real part of the dielectric permittivity (magnetic permeability). A similar behavior of increase in relaxation time as temperature approaches to T_C is found in our x = 0 sample too (Fig. 4.32). Thus, the splitting behavior observed in $R(T)$ in x = 0 is possibly due to the dispersion in the real part of the dielectric (magnetic) permeability. It was already recognized that short-range ferromagnetic clusters coexist with fluctuating short-range charge-orbital clusters in the paramagnetic state of the x = 0 sample. [209] While the charge carriers are itinerant within the ferromagnetic clusters, they are scattered by fluctuating charge-orbital ordered clusters. While the correlation length and relaxation time associated with the ferromagnetic clusters can increase dramatically very close to T_C and can show dispersion in magnetic susceptibility, the insensitivity of the α-peak to the applied magnetic field suggests that the observed dispersion in *R(T)* is not necessarily due to freezing of ferromagnetic clusters. We suspect that it is caused by dynamical freezing of the charge-orbital clusters which will cause less scattering of charges. Hence, the ac resistance decreases below the freezing temperature which increases with the frequency of the ac current. As temperature decreases just below T_C, the charge carriers experience additional scattering due to ferromagnetic spin fluctuations and hence the ac resistance increases again and goes through a maximum. The applied magnetic field increases ferromagnetic interaction between the clusters and suppresses the charge-orbital fluctuations. As a result, the β-peak shifts upward and a positive magnetoresistance is observed in a narrow temperature range above T_C.

Let us now discuss the disappearance of double peak behavior with La doping (x > 0). The substitution of bigger size La atom (ionic radius = 1.216 Å) for a smaller size Sm^{3+} atom (ionic radius = 1.132Å) is expected to increase the ferromagnetic T_C with increasing x in $Sm_{0.6-x}La_xSr_{0.4}MnO_3$. In contrast to the metamagnetic transition seen in x = 0 due to field-induced growth and coalescence of ferromagnetic nanoclusters present in the paramagnetic state, we do not see any such field-induced metamagnetic transition in La-rich (x > 0.1) doped

compounds. Thus, it is suggested that the La doping destroys the charge/orbital ordering present in the x = 0 compound due to the fact that La doping favors the double-exchange interaction which induces ferromagnetism at higher temperature. It is also observed that La doping reduces the dc resistivity of the compound. The magnitude of dc resistivity of x = 0 at T_{IM} is ρ = 89 Ωcm which decreases by one order of magnitude in x = 0.05 (ρ = 6 Ωcm) and two orders of magnitude in x = 0.1 (ρ = 0.89 Ωcm). The decrease in dc resistivity hinders the dielectric response of the sample and the resistive part plays the major role in the ac electrical transport. Hence, the splitting behavior which originates from the dispersion in the real part of permeability is weakened with increasing La doping and disappeared in La-rich (x > 0.05) compounds.

Next, we discuss the origin of the observed effects in ac magnetotransport properties of x = 0.4 and 0.6. The ac magnetotransport measurements in x = 0.4 and x = 0.6 compound reveal three important features: firstly, the occurrence of a peak in both $R(T)$ and $X(T)$ at T_C and secondly, the extra sensitiveness of both the peaks to sub-kilo gauss magnetic fields in contrast to x = 0, and thirdly, the occurrence of an extra peak in both $R(T)$ and $X(T)$ at T^* for x = 0.4. It is well known fact that low field dc magnetoresistance in manganites is due to spin polarized tunneling of e_g-holes between the ferromagnetic grains through spin disordered grain boundaries. [210] However, our ac magnetotransport in x = 0.4 and 0.6 compounds under sub-kilo gauss magnetic fields suggests that the intra-grain magnetization process dominates over the intra-grain tunneling of e_g-holes.

The flow of the ac current through the low resistive x = 0.4 and 0.6 samples creates a transverse ac magnetic field perpendicular to the direction of current. The ac magnetic response of the sample to the transverse ac magnetic field is characterized by the transverse ac permeability (μ_t). The reactance can be inductive or capacitive. The positive sign of reactance in both x = 0.4 and 0.6 indicates inductive nature of the reactance is dominating in the samples. The step-like increase in $X(H = 0\ \text{G})$ found around T_C can be understood as a result of the rapid increase of μ_t due to the onset of ferromagnetic ordering in the sample. The

abrupt increase in μ_t at T_C has little impact on the ac resistance at f = 0.1 MHz but the step-like increase becomes pronounced at T_C with increasing frequency above 1 MHz. The anomaly at the T_C can be understood as the effect of the decrease in the magnetic skin depth as a consequence of the rapid increase of μ_t at the T_C. The sudden decrease in the δ for $f \geq 1$ MHz causes a step-like increase in the ac impedance ($Z = (1+i)\rho_{dc} / \delta = (1+i)\sqrt{\pi f \rho \mu_0 \mu_t}$ where $Z = R + iX$) at T_C in the absence of magnetic field. The μ_t decreases dramatically in small dc magnetic fields, which increases δ and hence decreases the excess resistance observed around T_C in zero field. This is similar to the giant magnetoimpedance effect observed in Co-rich amorphous and nanocrystalline ferromagnets with large initial transverse permeabilities. [211] On the other hand, the observation of a low temperature peak in both $R(T)$ and $X(T)$ at T^* in x = 0.4 can also be understood in similar way. When the magnetization of x = 0.4 sample shows a sudden drop at T^* due to antiferromagnetic coupling between Sm-4*f* and Mn-3*d* moments, the dependent parameter μ_t also changes. Hence, both $R(T)$ and $X(T)$ in zero field decrease as T decreases below T^*. In addition, the applied magnetic field also decreases the antiferromagnetic coupling between Sm-4*f* and Mn-3*d* moments below T^*, this will in turn decrease the value of μ_t leading to a rapid decrease in both $R(T)$ and $X(T)$ around T^*. Interestingly, the value of ac magnetoresistance at T^* for x = 0.4 is more than that of T_C and we suggest that which is possibly due to the change in magnetization process due to antiferromagnetic coupling between Sm-4*f* and Mn-3*d* magnetic moments under the applied magnetic fields.

4. 4 Conclusions

The important results of this chapter are summarized below.

1. In the first section (4.3.2) of the chapter, we have investigated the detail magnetic properties of $Sm_{0.6-x}La_xSr_{0.4}MnO_3$ compounds. We have shown that the ferromagnetic T_C increases monotonically with increasing La content from T_C = 118 K for x = 0 to T_C = 363 K for x = 0.6). We observe an anomalous peak in the temperature dependence of

magnetization around T^* = 30 K in x = 0 which initially shifts up with increasing x, reaches a maximum value of T^* = 120 K in x = 0.4 and then decreases to T^* = 105 K for x = 0.5, and finally it disappears for the end compound (x = 0.6). Our results suggest that the anomalous peak in $M(T)$ around T^* is not due to transition into cluster-glass or spin-glass state. Instead, we attribute it to ordering of 4*f* moments of Sm that couples antiferromagnetically to Mn-sub lattice.

2. In the second section (4.3.3) of the chapter, we have compared the temperature and magnetic field dependent *rf* electromagnetic absorption in two compounds x = 0 and 0.6 by monitoring the changes in resonance frequency (f_r) and current (I) through IC oscillator. While both f_r and I showed a rapid decrease around T_C and a sudden increase below T^* for x = 0, both f_r and I showed only a rapid decrease around T_C for x = 0.6. The *rf* magnetoabsorption showed a distinct field dependence below and above T^* for x = 0. Our results show that a simple *LC*-resonance circuit powered by an IC oscillator is a useful technique to investigate the *rf* magnetization dynamics due to domain wall displacement and domain rotation in manganites. While we have observed fractional changes as much as $\Delta f_r/f_r$ = 9.8% and $\Delta P/P$ = 6.1% for x = 0 around T_C at H = 10 kG, we observed a large value of $\Delta f_r/f_r$ = 65% and a small value of $\Delta P/P$ = 7.5% for x = 0.6 around T_C at a smaller filed of H = 1 kG.
3. In the third section (4.3.4) of the chapter, we have investigated the magnetocaloric properties of $Sm_{0.6-x}La_xSr_{0.4}MnO_3$ series with x = 0, 0.05, 0.1, 0.3, 0.4 and 0.6 by estimating the change in magnetic entropy (ΔS_m) from the isothermal $M(H)$ data. The ΔS_m is negative around T_C and it decreases from ΔS_m = -6.2 $Jkg^{-1}K^{-1}$ for x = 0 to -4.2 $Jkg^{-1}K^{-1}$ for x = 0.6 for a field change of ΔH = 5 T. We have observed an inverse MCE within the long-range ferromagnetic ordered state (below $T^* < T_C$) for the first time and ΔS_m showed a maximum value of ΔS_m = +1.07 $Jkg^{-1}K^{-1}$ at T = 10 K for ΔH = 5 T in x = 0.4 compound which also showed a significant normal MCE (ΔS_m = -4 $Jkg^{-1}K^{-1}$) at T_C with a high RC of 214 Jkg^{-1}. The inverse MCE has been suggested to be caused by antiferromagnetic

coupling between Sm-4*f* and Mn-3*d* magnetic moments. The coexistence of normal MCE due to ferromagnetic exchange-interaction between Mn spins and inverse MCE due to 4*f*-3*d* coupling in a single material is interesting since the sample can be cooled by adiabatic magnetization and demagnetization in different temperature regions which will enhance the RC so as to increase the efficiency of the magnetic refrigerator.

4. In the final section (4.3.5) of the chapter, we have investigated the ac magnetotransport in $Sm_{0.6-x}La_xSr_{0.4}MnO_3$ series with $0 \leq x \leq 0.6$ by measuring the ac resistance (R) and reactance (X) simultaneously in four probe configuration using Agilent 4294A LCR meter. We found a frequency-induced transition from a single peak to double peak (α and β – high and low temperature peaks, respectively) in $R(T)$ in zero magnetic field with a dip at T_C for x = 0. We observed the shifting up of β-peak position in temperature with increasing strength of the magnetic field, while the α-peak position is unaltered with increasing external magnetic field. We suggest that although the frequency-induced splitting behavior in $R(T)$ is possibly originated from the dispersion in the real part of permeability, the dynamics of critical fluctuations around T_C and freezing of charge-orbital ordered clusters seem to be essential to understand the ac transport in x = 0. Furthermore, we observed the disappearance of double peak behavior with La doping (x > 0.05) and we attributed it to the decrease in the dc resistivity of the compounds, where resistive part dominates more than the capacitive part. The higher La-doping compounds showed an interesting features in both $R(T)$ and $X(T)$. A step-like increase at T_C and a sudden drop at T^* in $X(T)$ for $x \geq 0.2$ at $f > 100$ kHz and also in $R(T)$ for x > 0.2 at $f \geq 2$ MHz are observed. We also found that both $R(T)$ and $X(T)$ are very sensitive to external magnetic fields. We have explained the observed results qualitatively in terms of changes in the skin depth and transverse permeability of the sample around T_C and T^*.

Chapter 5

Normal and inverse magnetocaloric effects in $Pr_{1-x}Sr_xMnO_3$

5. 1 Introduction

In the section: 4.3.4 of previous chapter, we have demonstrated the coexistence of a large normal MCE around T_C (change in magnetic entropy $\Delta S_m = S_m(H) - S_m(0)$ is negative) and a weak (rather unusual) inverse MCE (ΔS_m is positive) at low temperature (below T_C) in $Sm_{0.6-x}La_xSr_{0.4}MnO_3$ compounds. As stated in the section: 4.3.4, majority of the existing studies have focused on the MCE around the paramagnetic to ferromagnetic transition upon cooling which lead to the normal MCE. [89] In contrast to ferromagnets which cool upon removal of magnetic field adiabatically, antiferromagnets will cool upon adiabatic application of magnetic field [212] but the MCE studies on antiferromagnetic manganites are relatively scarce due to the need for higher magnetic field ($\mu_0 H$ > 5 T) to destroy antiferromagnetic ordering. [129, 130, 131, 132] Compounds in which normal MCE and inverse MCE coexist can find application over a wide temperature range, since they can be cooled by adiabatic magnetization and also by adiabatic demagnetization in antiferromagnetic and ferromagnetic states, respectively so as to increase the efficiency of a magnetic refrigerator. In this context, half-doped manganites, which exhibit both ferromagnetic and antiferromagnetic ordering at different temperatures in a single compound, seem to be good candidates to investigate both normal and inverse MCEs.

There are few recent reports of observation of both normal and inverse MCEs in manganites. Majority of these published studies were done by estimating the ΔS_m from magnetization isotherms which is an indirect method of investigating ΔS_m. Krishnamoorthi *et al.*, found that $La_{0.5}Ca_{0.5}MnO_3$ compound exhibits an inverse MCE (ΔS_m = +6.5 $Jkg^{-1}K^{-1}$ for ΔH = 5 T) at the Neel temperature, which is twice larger than the normal MCE (ΔS_m = -3 $Jkg^{-1}K^{-1}$ for ΔH = 5 T) at the ferromagnetic transition. [213] Recently, Zhang *et al.*, [214] reported

the coexistence of inverse MCE (ΔS_m = +1.4 $Jkg^{-1}K^{-1}$ for ΔH = 5 T) and normal MCE (ΔS_m = -2.5 $Jkg^{-1}K^{-1}$ for ΔH = 5) in *A*-site ordered $NdBaMn_2O_6$ around T_N = 210 K and T_C = 290 K, respectively by magnetic method. Bingham *et al.* [215] also investigated both the inverse MCE and normal MCE in $Pr_{0.5}Sr_{0.5}MnO_3$ by magnetic method and found ΔS_m = +6.8 $Jkg^{-1}K^{-1}$ at T_N = 165 K and ΔS_m = -3.2 $Jkg^{-1}K^{-1}$ at T_C = 260 K for ΔH = 5 T, respectively which are comparable to the values found in $La_{0.5}Ca_{0.5}MnO_3$. However, Liu *et al.* [216] reported a smaller inverse MCE (ΔS_m = +4.8 $Jkg^{-1}K^{-1}$ for ΔH = 8 T) around T_N in $Pr_{0.5}Sr_{0.5}MnO_3$. The discrepancy in the values of ΔS_m reported in $Pr_{0.5}Sr_{0.5}MnO_3$ compound by the above two groups, suggests a difference in the quality of the samples due to sample processing conditions. In this chapter, our focus is on the detailed magnetocaloric properties of $Pr_{1-x}Sr_xMnO_3$ system. Long range charge-order is absent in $Pr_{1-x}Sr_xMnO_3$ system, but increasing the Sr content increases the T_N and reduces the T_C, and both transitions nearly coincide for x = 0.54 ($T_N \approx$ 210 K). [217] The *A*-type antiferromagnetic ordering in this compound, in which two dimensional ferromagnetic planes are coupled antiferromagnetically along the c-axis, is driven by in-plane ordering of the d_{x2-y2} orbitals. While in the majority of existing studies, ΔS_m is estimated from magnetization isotherms, a very few reports are available on the estimation of ΔS_m by calorimetry method [218, 219, 220] or measurement of ΔT_{ad} directly. [85] There is no previous study of MCE in $Pr_{1-x}Sr_xMnO_3$ system by both magnetic and calorimetric methods.

In this chapter, we have investigated the magnetic entropy change, ΔS_m, in $Pr_{1-x}Sr_xMnO_3$ with x = 0.5 and 0.54 by both magnetic (indirect) and DSC (direct) methods. We present the coexistence of a significant normal MCE of magnitude ΔS_m = -4.5 $Jkg^{-1}K^{-1}$ around T_C = 264 K and a large inverse MCE of magnitude ΔS_m = +7 $Jkg^{-1}K^{-1}$ at T_N = 132.5 K for ΔH = 7 T in x = 0.5. The latent heat involved in the field-induced antiferro-ferromagnetic transition is measured with a differential scanning calorimeter which yielded ΔS_m = +6.2 $Jkg^{-1}K^{-1}$ around T_N for x = 0.5. On the other hand, we found only a field-induced antiferromagnetic to ferromagnetic transition in x = 0.54 compound and is accompanied by a

large change in the latent heat as evidenced by the DSC data. We also present the occurrence of a large inverse MCE around T_N = 210.5 K of magnitude ΔS_m = +9 $Jkg^{-1}K^{-1}$ for ΔH = 7 T in x = 0.54 measured by magnetic measurement, which closely agrees with the calorimetric results. We discuss the possible origins of the observed normal and inverse MCEs. In addition, we have also measured the field-induced change in temperature (ΔT) of a sample using home-built DTA setup and we correlate the observed results with calorimetric data.

5. 2 Experimental details

The $Pr_{1-x}Sr_xMnO_3$ compounds with x = 0.5 and 0.54 were prepared by one of our collaborators [221, 222] using the standard solid-state reaction method by mixing Pr_6O_{11}, $SrCO_3$ and MnO_2 precursors intimately in adequate proportions. The mixture was first heated at 950°C for 12 h two times with intermediate grinding and then the powder was pressed in the form of bar shaped pellets. The pellet was sintered at 1500°C for 12 h in air and cooled at a rate of 5°C/min down to 800°C and finally quenched to room temperature. The Rietveld structural analyses of the powder neutron diffraction patterns were already reported by our collaborators and found that the room temperature structure of this compounds to be tetragonal with space group symmetry *I4/mcm*. [221, 222] While the structural parameters do not undergo significant changes at the ferromagnetic transition, the structural symmetry changes to low temperature orthorhombic phase around the antiferromagnetic transition with space group symmetry *Fmmm*. We calculated the change in the magnetic entropy (ΔS_m) using magnetic and calorimetric method as described in the experimental section: 2.2.5. In this work, the calorimetric measurement was performed on a thin piece (~1.5 mm) of sample of mass $m \approx 0.15$ g at selected temperatures by sweeping the field at a rate of dH/dt = 40 G/s. We have also estimated the value of ΔS_m using Clausius-Clapeyron (*C-C*) equation: $\Delta T_N/\Delta H = \Delta M/\Delta S_m$, where ΔT_N is the shift in the Neel temperature for an external magnetic field change of ΔH, ΔM is the difference between the high-field and low-field magnetization, and ΔS_m is the difference between the entropies of the two phases. [223] In addition, we have measured

the change in temperature (ΔT) of a sample during the field induced magnetic transition using home-built DTA setup with PPMS, which is similar to the design used by Quintero *et al.*, [85]. The field induced ΔT measurements were performed in PPMS at selected temperatures by sweeping the magnetic field.

5. 3 Results and Discussions

5. 3. 1 Magnetic and magnetocaloric properties of $Pr_{1-x}Sr_xMnO_3$ (x = 0.5 and 0.54)

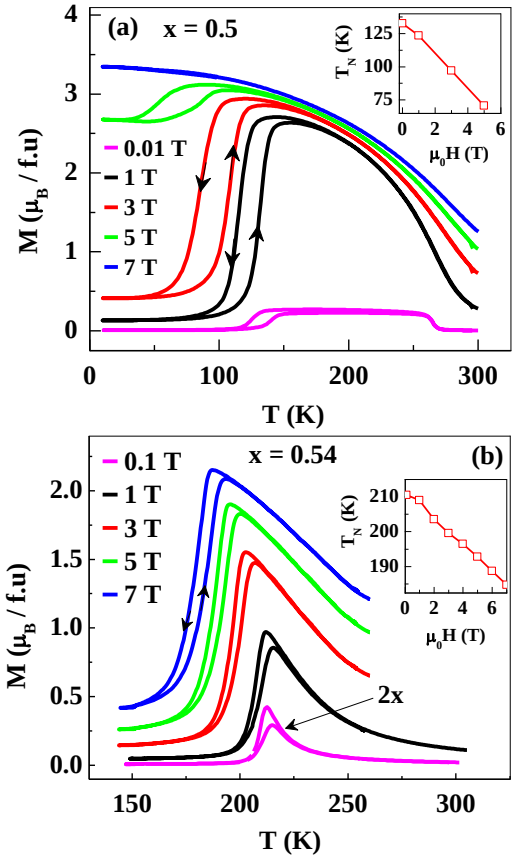

Fig. 5. 1 Temperature dependence of magnetization, $M(T)$ for (a) x = 0.5 and (b) x = 0.54 at selected magnetic fields ($\mu_0 H$ = 0.01, 0.1, 1, 3, 5 and 7 T). The arrows show the cooling and warning processes. The insets in the figure show the average Neel temperature (T_N) as a function of magnetic field.

Figs. 5.1(a) and 5.1(b) show the temperature dependence of the dc magnetization, $M(T)$ for x = 0.5 and x = 0.54 compounds at selected magnetic fields ($\mu_0 H$ = 0.01, 1, 3, 5 and 7 T), respectively. The x = 0.5 sample undergoes a second-order paramagnetic to ferromagnetic (PM→FM) transition around T_C = 264 K, as suggested by the rapid increase of

$M(T)$ under $\mu_0 H$ = 0.01 T. The abrupt decrease of $M(T)$ around T = 125 K while cooling indicates a ferromagnetic to antiferromagnetic (FM→AFM) transition. The reverse transition occurs around T = 140 K while warming. The observed hysteresis indicates that the transition is first-order in nature. We define T_N as the average temperature corresponding to the inflection point of the rapidly decreasing (increasing) part of the curve while cooling (warming) and it is found to be T_N = 132.5 K. In the inset of Fig. 5.1(a), we show the variation of T_N as a function of external of magnetic field. As the strength of H increases, T_N shifts down and the magnitude of M increases. The sample has completely transformed into ferromagnetic state when it is cooled in the presence of $\mu_0 H$ = 7 T. The magnetic moment at T = 10 K under $\mu_0 H$ = 7 T is 3.4 μ_B/f.u., which is slightly lower than the expected magnetic moment of 3.5 μ_B/f.u. for a homogeneous ferromagnetic state. On the other hand, the $M(T)$ of x = 0.54 showed only an antiferromagnetic transition as can be seen in Fig. 5.1(b). It is to be noted here is that the value of M for $M(T)$ plot recorded at $\mu_0 H$ = 0.1 T has been multiplied by a factor 2 for better visibility. The x = 0.54 sample is paramagnetic at room temperature. The $M(T)$ increases with lowering temperature and shows a sharp peak around T = 210 K for $\mu_0 H$ = 0.1 T which indicates the onset of antiferromagnetic transition. The $M(T)$ shows hysteresis around the phase transition while warming as like in x = 0.5. The magnitude of $M(T)$ increases with increasing H and the peak shifts towards lower temperature. The inflection point in $M(T)$ occurs at 209.6 K while cooling and 211.4 K on warming for $\mu_0 H$ = 0.1 T. The T_N, the average temperature corresponding to the inflection point in $M(T)$, for $\mu_0 H$ = 0.1 T is T_N = 210.5 K and it decreases nearly linearly with increasing H above 1 T at a rate of dT_N/dH = -3.78 K/T as shown in the inset of Fig. 5.1(b). Next we show the field dependence of M measured at selected temperature for the estimation of magnetic entropy change (ΔS_m).

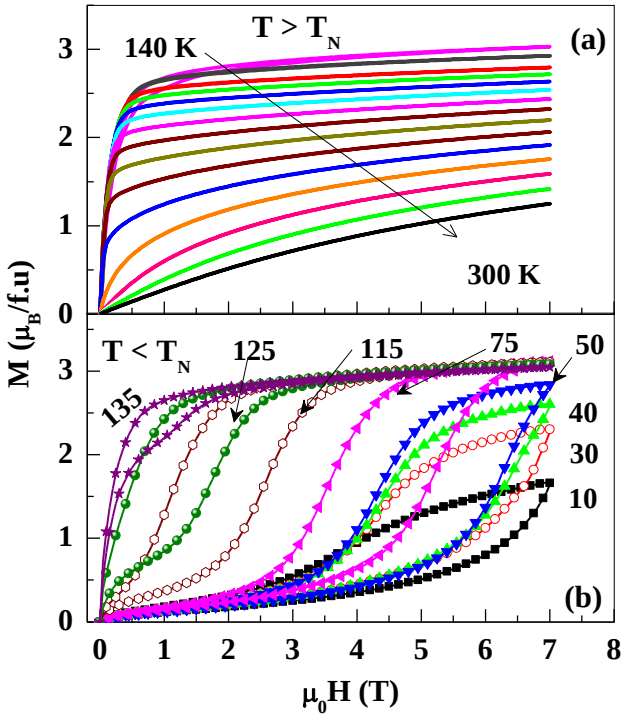

Fig. 5. 2 The magnetic field dependence of magnetization, *M*(*H*) isotherms for x = 0.5 at (a) $T > T_N$ and (b) $T < T_N$.

Fig. 5.2(a) shows the isothermal field dependence of the magnetization, *M*(*H*) for *T* = 140-300 K > T_N, which covers the PM→FM transition and Fig. 5.2(b) shows *M*(*H*) isotherms in the antiferromagnetic state for x = 0.5. Prior to each measurement, the sample was cooled from *T* = 300 K to a selected temperature in zero magnetic field. The *M*(*H*) at *T* = 140 K increases non-linearly with *H* which depicts the long-range ferromagnetism exists in the sample. The magnitude of *M*(*H*) decreases with increase in temperature and shows almost linear behavior at *T* = 300 K which reveals the paramagnetic nature of the sample at room temperature. Whereas, the *M*(*H*) at *T* = 10 K increases linearly with *H* up to 5 T and then shows a rapid increase which indicates a partial transformation of the antiferromagnetic phase into the ferromagnetic phase *i.e.*, a field-induced metamagnetic transition occurs. A clear hysteresis is seen in the field range $\mu_0 H$ = 7-1.5 T while reducing *H* from 7 T to a zero value. The hysteresis is due to the coexistence of both the ferromagnetic and antiferromagnetic phases. The change of *H* to the negative direction resulted in a symmetrical loop (data not

shown here). Interestingly the observed magnetic moment at $\mu_0 H$ = 7 T in $M(H)$ measured at 10 K is only 1.7 μ_B/f.u. which is much smaller than M = 3.4 μ_B/f.u. found when the sample was cooled under $\mu_0 H$ = 7 T from 300 K. This result suggests that the interfacial energy associated with the magnetization process in the isothermal case is larger than in the temperature driven case, while cooling in presence of the magnetic field. As T increases, the metamagnetic transition shifts to lower magnetic fields and the magnitude of the jump in M increases. The critical field (H_t) associated with the field-induced antiferromagnetic→ferromagnetic transition, which is defined as the inflection point of the rapidly varying portion of the increasing branch of $M(H)$ curve, decreases from $\mu_0 H_t$ = 6.2 T at 50 K to $\mu_0 H_t$ = 1 T at 135 K, while sweeping H from 0→7 T. This behavior of decreasing critical field of a metamagnetic transition as T approaches T_N from low temperature is generally expected for an antiferromagnet. Next we show the $M(H)$ isotherms for x = 0.54 sample.

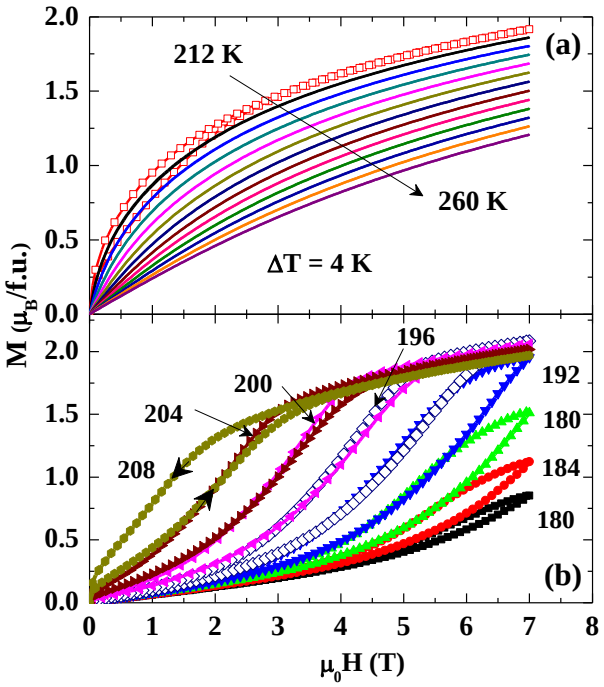

Fig. 5. 3 Field dependence of magnetization, $M(H)$ isotherms for x = 0.54 at (a) $T > T_N$ and (b) $T < T_N$.

We show $M(H)$ isotherms from T = 212 K to 260 K for a temperature interval of ΔT = 4 K for x = 0.54 sample in Fig. 5.3(a). The magnetization increases non-linearly with H even at T = 260 K (> T_N) and the magnitude of M throughout the field range increases progressively with decreasing temperature. It is to be mentioned that the ferromagnetic transition temperature in the $Pr_{1-x}Sr_xMnO_3$ series shifts down from T_C = 260 K for x = 0.5 to 210 K for x = 0.52. [217] In x = 0.54, the long range ferromagnetism has not developed in the investigated temperature range, but the observed non-linear M-H behavior above T_N indicates the existence of ferromagnetic spin correlations above T_N. We find a pronounced hysteresis between $\mu_0 H$ = 0 and 3 T at T = 212 K. The hysteresis behavior is reproducible in the negative field cycles (not shown here). Fig. 5.3(b) shows the M-H isotherms below T_N. At T = 208 K, M increases gradually as the field is increased from 0 T, but shows a rapid increase above 1.2 T and then a gradual increase between 3.5 T and 7 T. A pronounced hysteresis is visible between 3 T and 0 T while reducing the field. The rapid increase of M with increasing H indicates a field-induced metamagnetic transition as like in x = 0.5 and it is caused by the partial conversion of the antiferromagnetic phase into ferromagnetic phase. The phase fraction of the ferromagnetic phase increases and that of the antiferromagnetic phase decreases with increasing H. Above $\mu_0 H$ = 4 T, the ferromagnetic matrix has fully transformed into a ferromagnetic phase. While reducing the field, a reverse process takes place, in which antiferromagnetic nuclei form in the ferromagnetic matrix and grow in size. The critical field for the metamagnetic transition, H_t increases rapidly with lowering temperature. The metamagnetic transition is not completed within the available field range below T = 190 K. We have estimated the change in magnetic entropy (ΔS_m) from these $M(H)$ isotherms and we will next show the temperature dependence of ΔS_m for x = 0.5 and 0.54 samples.

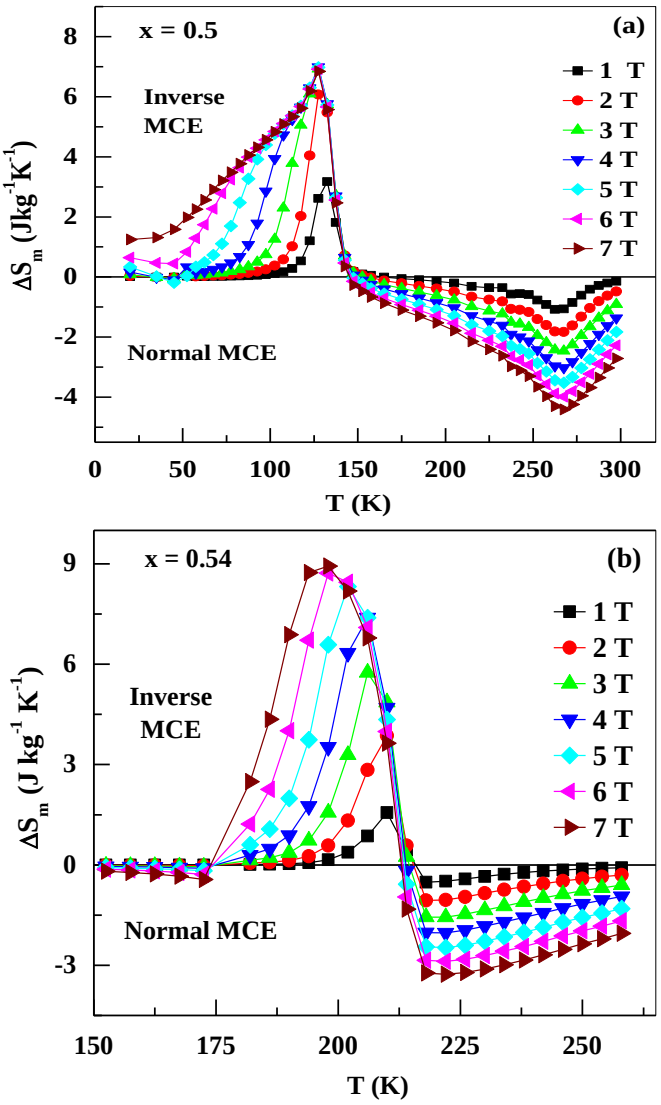

Fig. 5. 4 Temperature dependence of the magnetic entropy change (ΔS_m) obtained from $M(H)$ data for different field intervals (ΔH = 1, 2, 3, 4, 5, 6 and 7 T) while sweeping the magnetic field from $\mu_0 H$ = 0→7 T for (a) x = 0.5 and (b) x = 0.54.

In Fig. 5.4(a) and 5.4(b), we show the temperature dependence of ΔS_m obtained from the $M(H)$ isotherms for different values of field intervals ΔH, as the field is increased from H = 0 to a specified field value for x = 0.5 and 0.54 samples, respectively. We have drawn a straight line at ΔS_m = 0 which distinguishes the normal MCE (ΔS_m is negative) and inverse MCE (ΔS_m is positive) exist in the sample. We will first see the behavior of ΔS_m versus T for x = 0.5. The ΔS_m for ΔH = 1 T shows a negative peak (ΔS_m = -1.09 $Jkg^{-1}K^{-1}$) around T_C = 264 K and a positive peak (ΔS_m = +3.18 $Jkg^{-1}K^{-1}$) around T_N = 132.5 K. The magnitudes of both

peaks increase with increasing values of ΔH. While the position of the peak around T_C is nearly unaltered for different values of ΔH and ΔS_m reaches a maximum value of -4.5 $Jkg^{-1}K^{-1}$ for ΔH = 7 T around T_C, position of the positive peak around T_N shifts down with increasing ΔH and ΔS_m reaches +7 $Jkg^{-1}K^{-1}$ around T_N. On the other hand, ΔS_m of x = 0.54 is negative and small in magnitude in the paramagnetic state ($T > T_N$). The negative sign of ΔS_m in the paramagnetic state indicates the normal MCE due to the existence of ferromagnetic spin correlations above T_N and it is supported by the non-linear *M-H* behavior seen in Fig. 5.3(b) above T_N for x = 0.54. The magnitude of ΔS_m increases with decreasing temperature and increasing ΔH values. The sample shows an inverse MCE below T_N. ΔS_m changes sign to positive below T = 212 K and reaches a peak around 210 K and then decreases rapidly below T_N. The magnitude of ΔS_m at its peak value increases with increasing ΔH and reaches a value of +8 $Jkg^{-1}K^{-1}$ for ΔH = 5 T and a huge value of +9 $Jkg^{-1}K^{-1}$ for ΔH = 7 T. The obtained value of ΔS_m = +8 $Jkg^{-1}K^{-1}$ for ΔH = 5 T is higher than ΔS_m = +6.5 $Jkg^{-1}K^{-1}$ obtained at T_N = 140 K (= T_{CO}) in $La_{0.5}Ca_{0.5}MnO_3$ [213] and +3.5 $Jkg^{-1}K^{-1}$ around T_{CO} in $Nd_{0.5}Ca_{0.5}MnO_3$. [130] In addition to a large value of ΔS_m observed around T_N in our compounds, the spanning of ΔS_m over a wide temperature range with an appreciable value at temperature away from the peak position, for instance, ΔS_m = +1.3 $Jkg^{-1}K^{-1}$ at T = 20 K for x = 0.5, is very interesting and important from a viewpoint of technological applications. While the RC value estimated using the formula given in the section: 1.7.1 for a field change of ΔH = 7 T is found to be RC = 168.42 Jkg^{-1} around T_N for x = 0.54, it is large for x = 0.5 around T_N (RC = 298.8 Jkg^{-1}) and T_C (RC = 288.8 Jkg^{-1}).

5. 3. 2 Calorimetric investigations of MCE in $Pr_{1-x}Sr_xMnO_3$ compounds

In this section, we present our calorimetric results obtained from DSC data for x = 0.5 and 0.54 samples and we correlate these results with the field-induced change in temperature of the sample measured from the DTA. Let us first see the DSC data on the samples starting from x = 0.5.

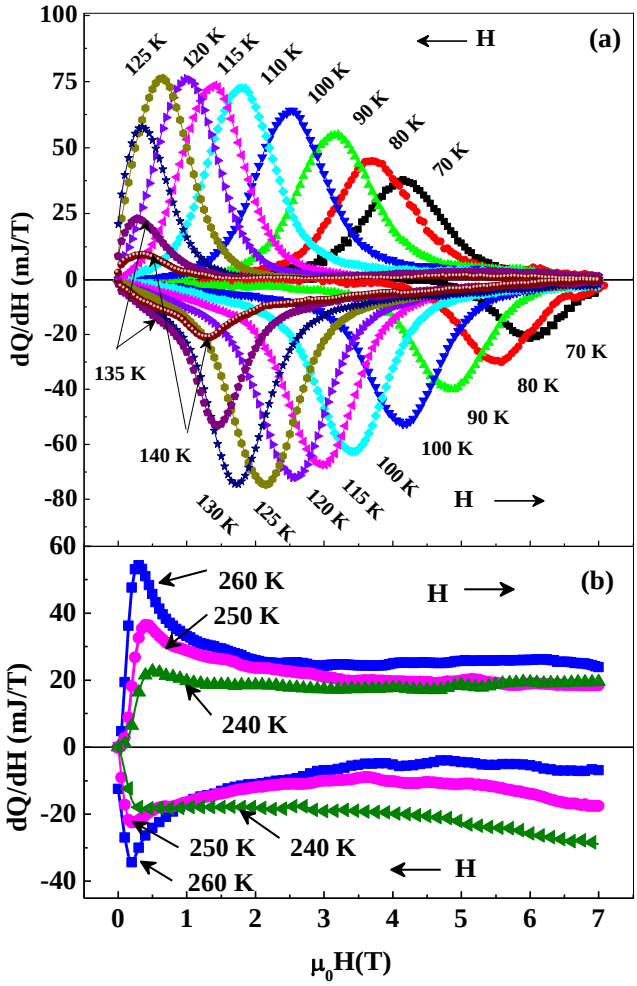

Fig. 5. 5 Differential scanning calorimeter signal (*dQ*/*dH*) as a function of magnetic field (*H*) at selected temperatures for (a) $T \leq 140$ K and (b) $T \geq T_N$ for x = 0.5.

Fig. 5.5(a) shows the rate of heat flow with the magnetic field (*dQ*/*dH*) measured using DSC when the magnetic field is swept from $\mu_0 H$ = 0 T→ +7 T→ 0 T at selected temperatures from T = 70-140 K in the antiferromagnetic state. As H is increased from 0 T→ +7 T, *dQ*/*dH* decreases (*dQ*/*dH* is negative), goes through a minimum around $H = H_p$ and reaches a small value at the highest field. This value of H_p closely agrees with H_t of the metamagnetic transition. When H is decreased from 7 T, *dQ*/*dH* changes sign, increases with decreasing H, goes through a maximum at a field $H = H_p$ and becomes small close to H = 0. The difference between the positions of the maximum and minimum seen in *dQ*/*dH* plot confirms the first-order nature of the metamagnetic transition. The negative sign of *dQ*/*dH*

while increasing H indicates that the sample cools during the field-induced antiferromagnetic→ferromagnetic transition (endothermic process) and the positive sign of dQ/dH indicates the release of heat, *i.e.*, the sample heats up during the reverse transition (exothermic process). It is to be noted here that while the magnitude of the peak (H_P) in dQ/dH decreases as T decreases below T_N, the position of H_P shifts upwards in H as temperature decreases. However, in contrast to the behavior of dQ/dH in the antiferromagnetic state, dQ/dH around the ferromagnetic transition (240 K ≤ T ≤ 260 K) shown in Fig. 5.5(b) is positive while increasing H and negative while decreasing H, which is opposite to the behavior of dQ/dH seen the in antiferromagnetic state. It is to be noted that the DSC data in the ferromagnetic state is rather weak compare to in the antiferromagnetic state. In Fig. 5.6, we show a similar DSC data (dQ/dH) at selected temperatures between T = 190 K and 212 K for x = 0.54. Since the DSC data in the paramagnetic state (above T_N) is very noisy due to the insensitiveness of the DSC set up, we show DSC data only in the antiferromagnetic state (T ≤ 212 K). While sweeping H from 0 to 7 T, the dQ/dH at T = 212 K initially decreases and goes through a negative peak and then decreases towards zero. This negative peak implies the maximum heat absorption by the sample during the metamagnetic transition. When reducing the field, dQ/dH shows a positive peak at a magnetic field which is lower than the position of the negative peak observed while increasing H. This confirms the first-order nature of the field-induced antiferromagnetic→ferromagnetic transition as like in x = 0.5. As the temperature decreases, both negative and positive peaks shift rapidly towards a higher magnetic field value. The value of the negative peak initially increases with decreasing temperature, attains a maximum value around T = 200 K and then decreases. Next we show the similar behavior seen in the field-induced change in temperature in x = 0.5 and 0.54 samples measured by DTA setup.

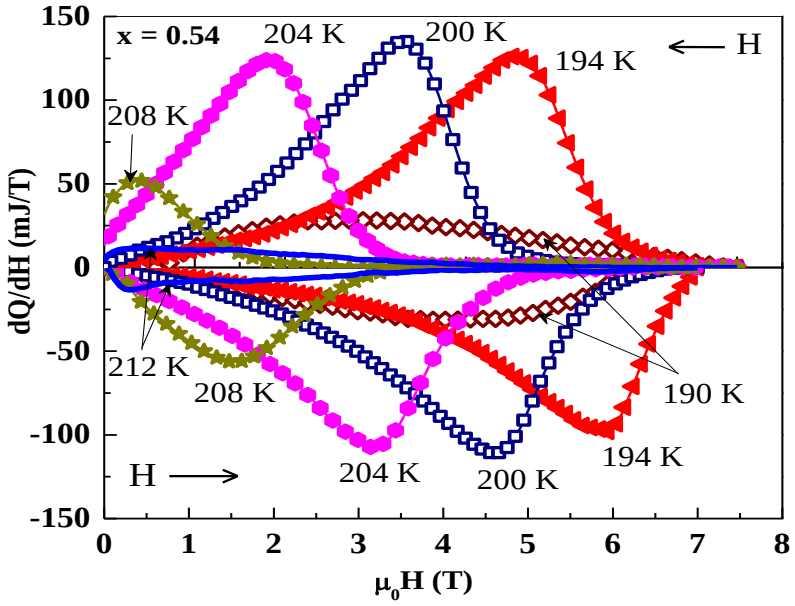

Fig. 5. 6 Differential scanning calorimeter signal (*dQ*/*dH*) as a function of magnetic field (*H*) at selected temperatures in the antiferromagnetic state (*T* < 212 K) for x = 0.54.

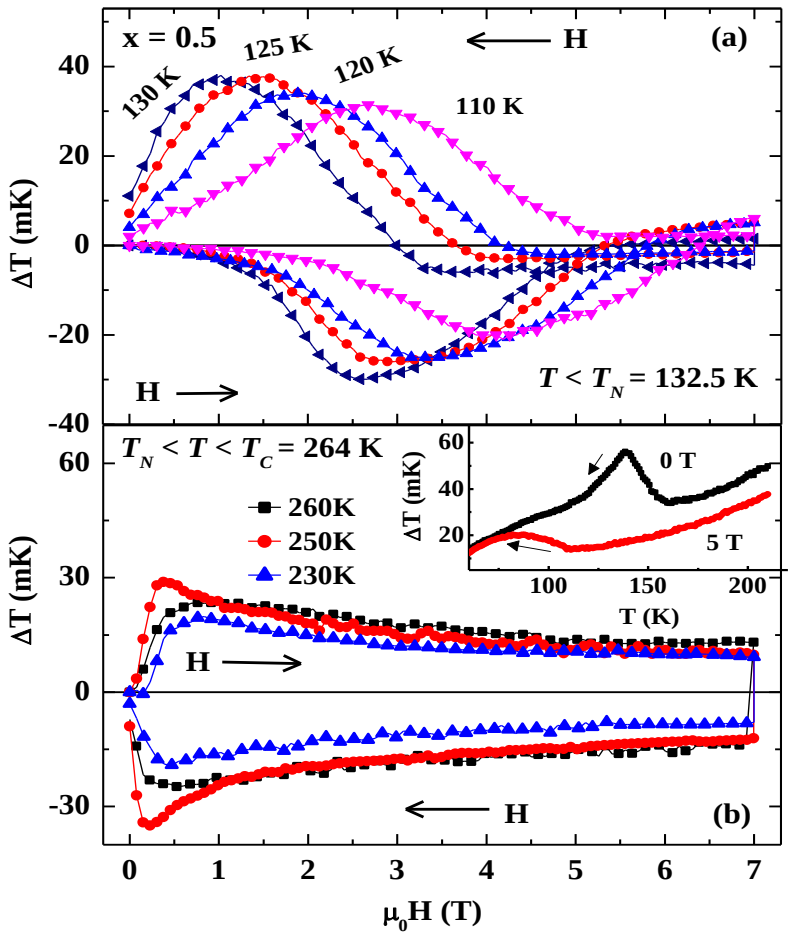

Fig. 5. 7 Field-induced change in temperature (Δ*T*) of x = 0.5 sample as a function of magnetic field at selected temperatures for (a) $T < T_N$ and (b) $T > T_N$.

Fig. 5.7(a) and 5.7(b) show the field-induced change in temperature (ΔT) of x = 0.5 sample measured using DTA when the magnetic field is swept from $\mu_0 H$ = 0 T→ +7 T→ 0 T at selected temperatures in the antiferromagnetic ($T < T_N$) and ferromagnetic ($T_N < T < T_C$) states, respectively. The behavior of ΔT versus H is similar to DSC data *i.e.*, dQ/dH versus H. As H is increased from 0 T→ +7 T, ΔT at T = 130 K ($< T_N$) decreases *i.e.*, ΔT is negative and goes through a minimum around the metamagnetic transition ($H = H_p \approx H_t$) and reaches a small value at the highest field. There is a change of sign in ΔT when H is decreased from 7 T. The magnitude of ΔT increases with decreasing H, goes through a maximum at a field $H = H_p$ and becomes small at H = 0. The cooling of sample or decrease in the temperature of a sample during the field-induced antiferromagnetic→ferromagnetic transition is detected by the direct measurement of ΔT by DTA setup. This decrease in temperature of a sample leads to the absorption of the heat (dQ/dH is negative) as detected by the DSC measurement. The positive sign of ΔT indicates the rise in temperature of a sample *i.e.*, the release of heat as evidenced by DSC (dQ/dH is positive) during the reverse transition. As like in DSC data, the magnitude of the peak (H_P) in ΔT decreases as T decreases below T_N and the position of H_P shifts upwards in H as T decreases. Whereas, the behavior of ΔT in the ferromagnetic state shown in Fig. 5.7(b) is opposite to that of in the antiferromagnetic state. The rise in the sample temperature due to the parallel alignment of spins in the ferromagnetic state which is evidenced by the direct measurement of rise in temperature (ΔT is positive) using DTA. The sign of ΔT is negative when H approaches to zero from high value. The DTA data in the ferromagnetic state is rather weak compare to that of in the antiferromagnetic state as like in the case of DSC data due to the absence of field-induced metamagnetic transition in the ferromagnetic state. The inset in Fig. 5.7(b) shows the temperature dependence of ΔT around T_N in a narrow temperature interval under $\mu_0 H$ = 0 and 5 T while cooling. The antiferromagnetic transition is accompanied by a peak in ΔT in zero field. The shift in the position of a peak in ΔT under $\mu_0 H$ = 5 T indicates the field-induced shift in the

antiferromagnetic transition. We will next show a similar temperature dependence of ΔT for x = 0.54 sample.

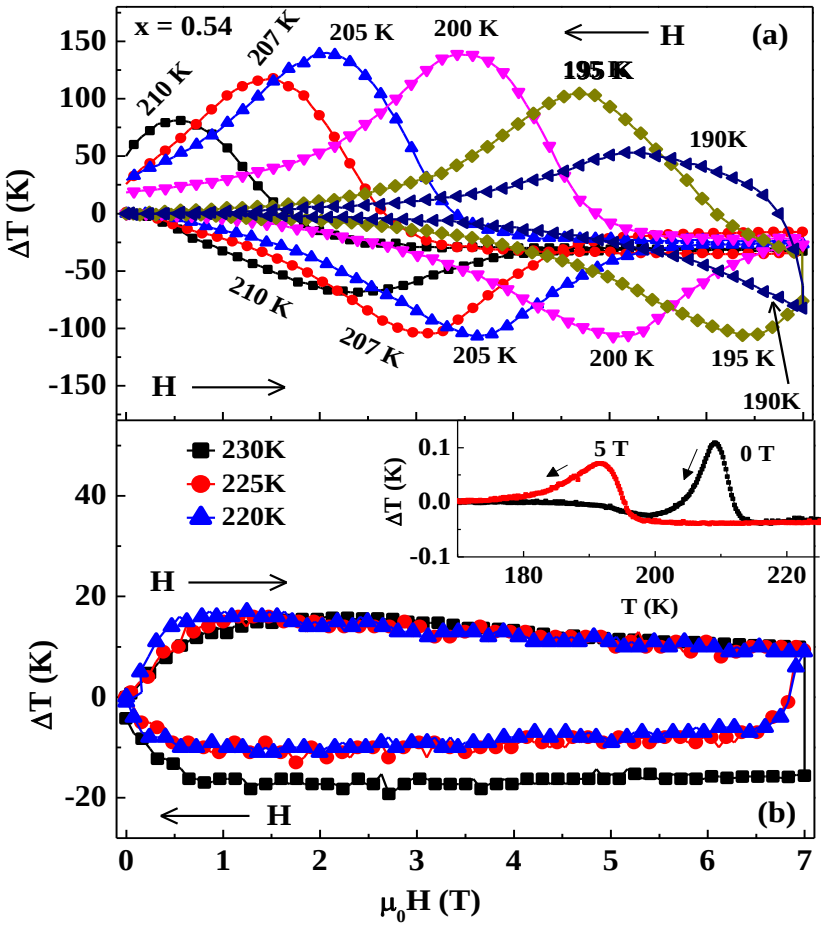

Fig. 5. 8 Field-induced change in temperature (ΔT) of x = 0.54 sample as a function of magnetic field at selected temperatures for (a) $T < T_N$ and (b) $T > T_N$.

Temperature dependence of ΔT for x = 0.54 sample is shown in Figs. 5.8(a) and 5.8(b) in the antiferromagnetic state (T = 190-210 K < T_N) and paramagnetic state (T = 220-230 K > T_N), respectively. As like in case of x = 0.5, while sweeping the field up, the ΔT is negative, shows a peak at $H = H_P$ which is close to H_t and its sign changes to positive while H decreases from a high field value to zero. The position of H_P in ΔT versus H decreases rapidly with lowering T as like in DSC data. While there is a change in temperature of x = 0.54 sample in the antiferromagnetic state due to field-induced metamagnetic transition, the sample temperature changes even in the paramagnetic state as it can be seen in Fig. 5.8(b) where ΔT

is positive while H is increasing and negative while H is decreasing. The change in temperature of x = 0.54 sample in the paramagnetic state is attributed to the ferromagnetic clusters present in the paramagnetic state and it is supported by the nonlinear behavior of $M(H)$ plots observed in the paramagnetic state for x = 0.54. This result reveals that our DTA setup is more sensitive compare to DSC setup in measuring a small change in temperature of sample during the magnetic phase transition. The inset in the Fig. 5.8(b) shows the temperature dependence ΔT of x = 0.54 sample around T_N in a narrow temperature interval under $\mu_0 H$ = 0 and 5 T while cooling, which indicates the field-induced antiferromagnetic phase transition in the compound as like in x = 0.5. Next we show the temperature dependence of ΔS_m estimated from the DSC data and we compare the results with ΔS_m values estimated from the $M(H)$ isotherms as well as Clausius-Clapeyron equation.

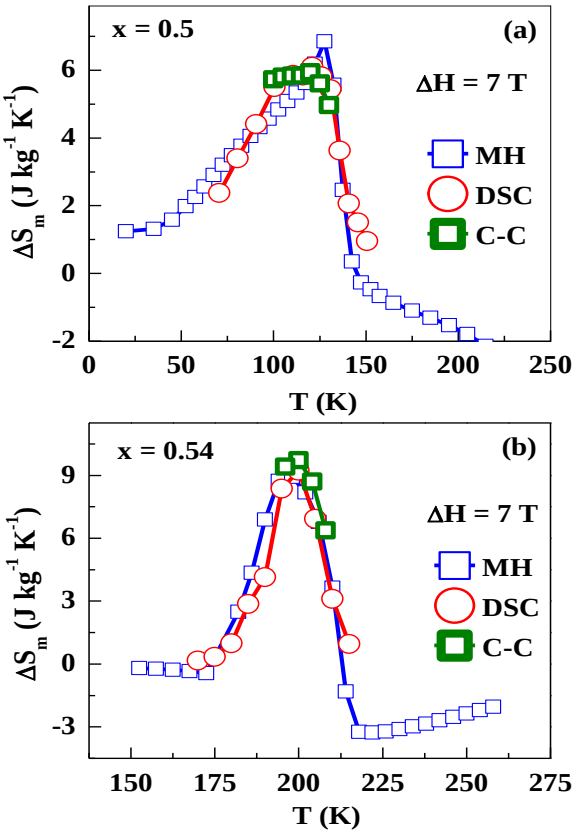

Fig. 5. 9 A comparison of the temperature dependence of magnetic entropy change (ΔS_m) obtained from the $M(H)$ data, DSC data and Clausius-Clapeyron equation (C-C) for a field change of ΔH = 7 T for (a) x = 0.5 and (b) x = 0.54.

In Figs. 5.9(a) and 5.9(b), we compare the ΔS_m values estimated from the DSC data in the antiferromagnetic state with the ΔS_m values estimated from the $M(H)$ data and Clausius-Clapeyron (*C*-*C*) equation for a field change of ΔH = 7 T, respectively. As it can be seen in the Fig. 5.9(a), the peak value of ΔS_m = +6.1 $Jkg^{-1}K^{-1}$ obtained from DSC data for ΔH = 7 T for x = 0.5 is slightly lower than the maximum value (ΔS_m = +7 $Jkg^{-1}K^{-1}$) obtained from the $M(H)$ data. While the ΔS_m values estimated from the *C*-*C* equation agrees with DSC data, it is slightly small compare to that of calculated from the $M(H)$ data. On the other hand, ΔS_m values of x = 0.54 estimated from $M(H)$ data exhibit a peak value of +9 $Jkg^{-1}K^{-1}$ at T = 210 K and it agrees very well with the ΔS_m values estimated from the *C*-*C* equation and DSC data.

The closeness in the peak value of ΔS_m obtained from the magnetization data and calorimetric data suggests the validity of the Maxwell's relation for the first-order transition in this sample. However, we have also noted in some other compounds (for example, Co-doped $Pr_{0.6}Ca_{0.4}MnO_3$) that the application of the Maxwell's equation leads to a higher value of ΔS_m than obtained from calorimetric data or *C*-*C* equation. [224] The large magnetic entropy change in the present $Pr_{1-x}Sr_xMnO_3$ (x = 0.5 and 0.54) system is caused by the abrupt increase of the magnetization triggered by the destruction of the antiferromagnetic state. The $d_{x^2-y^2}$ orbital ordering associated with the *A*-type antiferromagnetic ordering is also expected to be destroyed. An earlier magnetovolume study by some of us [225] indicated that the field-induced antiferromagnetic to ferromagnetic transition was also accompanied by an abrupt increase (≈ 0.14%) in the volume. The positive magnetovolume effect was ascribed to the field-induced structural transition from a low volume orthorhombic (*Fmmm*) to a high volume tetragonal (*I4/mcm*) phase. The field-induced magnetostructural transition enhances the observed MCE as like in the intermetallic alloys. Interestingly, $Pr_{1-x}Sr_xMnO_3$ system also shows a giant anisotropic magnetostriction for example, x = 0.5 compound showed λ_t = $1.5x10^{-3}$ at $\mu_0 H$ = 14.2 T at low temperature (T = 25 K) and a small volume magnetostriction ($\Delta L/L \approx 0.2x10^{-3}$) around the antiferromagnetic transition. [226] A large inverse MCE observed in this study (ΔS_m = +7 $Jkg^{-1}K^{-1}$ for x = 0.5 and ΔS_m = +9 $Jkg^{-1}K^{-1}$ for x = 0.54 for

ΔH = 7 T) with significantly large value of RC (RC = 298.8 Jkg^{-1} for x = 0.5 and RC = 168.42 Jkg^{-1} for x = 0.54) around the antiferromagnetic transition can significantly improve the global efficiency of the magnetic refrigeration technology when it is utilized in composite with the conventional magnetic refrigerants. However, inverse MCE is not necessarily connected with the antiferromagnetic state alone and it can also be observed due to change in magnetic anisotropic energy that accompanies austenite–martensite phase transition below the ferromagnetic Curie temperature as found in $Ni_{50}Mn_{50-x}Sn_x$. [227] A possible application of the inverse MCE, other than magnetic cooling would be to use it as a heat-sink for the heat generated when a conventional MCE material (para or ferromagnet) is magnetized.

5. 4 Conclusions

In this chapter, we have investigated the MCE by estimating the magnetic entropy change ΔS_m, in $Pr_{1-x}Sr_xMnO_3$ system with x = 0.5 and 0.54 by both magnetic (indirect) and home-built DSC (direct) methods. In magnetic method, we have estimated ΔS_m from the isothermal $M(H)$ data taken at selected temperatures. Whereas, in direct method, we have estimated the ΔS_m values from the latent heat evolved in the field-induced antiferromagnetic→ferromagnetic transition using DSC setup. While x = 0.5 compound showed two transitions: high temperature paramagnetic→ferromagnetic transition at T_C = 264 K and low temperature ferromagnetic→antiferromagnetic transition at T_N = 132.5 K, x = 0.54 compound showed a single paramagnetic→antiferromagnetic transition at T_N = 210.5 K. Our magnetic method revealed a large inverse MCE (ΔS_m = +7 $Jkg^{-1}K^{-1}$) around the antiferromagnetic Neel temperature (T_N = 132.5 K) and an appreciable normal MCE (ΔS_m = -4.5 $Jkg^{-1}K^{-1}$) around the ferromagnetic Curie temperature (T_C = 264 K) in x = 0.5 for a field change of ΔH = 7 T. But our DSC data yielded a slightly lower value of ΔS_m of magnitude ΔS_m = +6.2 $Jkg^{-1}K^{-1}$ around T_N for x = 0.5, although it closely agrees with value estimated from the Clausius-Clapeyron equation. On the other hand, we found a large inverse MCE around T_N = 210.5 K of magnitude ΔS_m = +9 $Jkg^{-1}K^{-1}$ for ΔH = 7 T in x = 0.54 estimated by

magnetic method and this ΔS_m value closely agrees with the calorimetric results as well as with the value estimated using Clausius-Clapeyron equation. While the normal MCE is due to paramagnetic→ferroamgnetic transition, we suggest that a large positive ΔS_m (inverse MCE) observed in $Pr_{1-x}Sr_xMnO_3$ system is due to a field-induced structural transition that accompanies the destruction of antiferromagnetism under the magnetic field. In addition, we have measured the field-induced change in temperature (ΔT) of a sample using home-built DTA setup and we showed that there is a close correlation exists between DSC and DTA results. From DTA measurement on $Pr_{1-x}Sr_xMnO_3$ system, we have given a clear experimental evidence that antiferromagnetic compounds cool down (ΔT is negative) upon application of magnetic field and the ferromagnets cool down upon removal of magnetic field. The observation of a large inverse MCE (ΔS_m = +9 $Jkg^{-1}K^{-1}$ for ΔH = 7 T around T_N) in x = 0.54 with RC = 168.42 Jkg^{-1}, and the coexistence of both normal (ΔS_m = -4.5 $Jkg^{-1}K^{-1}$ for ΔH = 7 T around T_C) and inverse (ΔS_m = +7 $Jkg^{-1}K^{-1}$ for ΔH = 7 T around T_N) MCEs in x = 0.5 with significantly large RC of 298.8 Jkg^{-1} and 288.8 Jkg^{-1}, respectively makes our $Pr_{1-x}Sr_xMnO_3$ system very attractive from the viewpoints of magnetic refrigeration technology.

Chapter 6

Magnetic and magnetoelectric studies in pure and cation doped $BiFeO_3$

6. 1 Introduction

In the previous chapters, we showed the multifunctional properties of few selected Mn-based oxide materials such as giant *rf* magnetoabsorption, magnetoimpedance and magnetocaloric properties which may find applications in magnetic sensor and magnetic refrigeration applications. In this chapter, we focus on Fe-based ME multiferroics oxide materials in which symmetry consideration allows coupling between electrical and magnetic dipole moments that finds promising applications in data storage, sensors and also show intriguing physics involved in the coupled phenomena. [96, 94] In this context, recent observations of magnetic field induced ferroelectric polarization in $TbMnO_3$ [228] and $DyFeO_3$ [229] and ME memory effect in $MnWO_4$ [230] are quite interesting from the viewpoints of basic physics and applications. However, there exist very few single-phase multiferroic oxides due to the fact that the ferroelectricity in ABO_3 type perovskite oxides requires transition metal ions (*B*) with d^0 electronic configuration, whereas ferromagnetism requires transition metal ions with odd number of d electrons. [103] Nevertheless, materials such as $BiFeO_3$, $GaFeO_3$ and rare earth manganites of $AMnO_3$ (*A* = Y, Tb, Gd, Ho) [133] in which *A* and Mn are the sources of ferroelectricity and magnetism, respectively show coupling between electrical and magnetic dipole moments. Though the physics of ME coupling in $AMnO_3$ is very exciting, they are not useful for practical applications at room temperature since the magnetic field-induced ferroelectric polarization is rather small and the magnetic transition occurs mostly below the liquid nitrogen temperature. The magnetic transition of $PbFe_{0.5}Nb_{0.5}O_3$ multiferroic compound, which shows spin lattice coupling, is also below 300 K. [231]

The high values of ferroelectric Curie temperature [$T_{C(FE)} \approx 836$ °C] [134, 135] and antiferromagnetic transition temperature ($T_N \approx 370$ °C) [136] found in $BiFeO_3$ make this compound more attractive. Ferroelectricity in $BiFeO_3$ is driven by the sterochemical activity of $6s^2$ lone pair of Bi^{3+} ions, whereas the Fe ions order antiferromagnetically. It is a G-type antiferromagnet with a long-range cycloidal spin arrangement of wavelength 62 nm incommensurate with the lattice. [232] The saturation polarization in this material can reach as much as 90 $\mu C/cm^2$ in suitably prepared thin films, [233] though it is generally small in bulk sample. [134, 234] However, ferro or ferrimagnetism instead of antiferromagnetism along with enhanced polarization is highly preferable for low-field practical applications. Enhancements in magnetization and ferroelectric polarization were reported in the *A*-site doped system of $Bi_{0.9-x}Tb_xLa_{0.1}FeO_3$ where Tb and La are isovalent to Bi^{3+} ions, [235] and also in $Bi_{1-x}Nd_xFeO_3$. [236] Interestingly, divalent cation (*A*) substituted $Bi_{0.7}A_{0.3}FeO_3$ (*A* = Ca, Sr, Pb, and Ba) also exhibits enhanced magnetization [237] and the recent observation of magnetic-field induced ferroelectric hysteresis loop in $Bi_{0.75}Sr_{0.25}FeO_{3-\delta}$ makes it more attractive for practical applications. [238] Although the temperature dependence of structural and magnetic order parameters of $BiFeO_3$ has been studied by Fischer *et al.*, [239] long ago, magnetization over a wide range of temperature (T = 10-700 K) as well as ME coupling in $Bi_{0.7}A_{0.3}FeO_3$ have not been reported and these are the driving factors for the present work.

In this chapter, we have investigated the effect of divalent cation (*A*) substitution on magnetic and ME properties in $Bi_{1-x}A_xFeO_3$ with *A* = Sr, Ba and $Sr_{0.5}Ba_{0.5}$ and x = 0 and 0.3. We show here that all the divalent cation doped samples show enhanced magnetization with a well-defined hysteresis loop compared to the antiferromagnetic nature of the parent compound. We have measured both the longitudinal (L-α_{ME}) and the transverse (T-α_{ME}) ME coefficients with *dc* magnetic field parallel and perpendicular to the direction of induced voltage, respectively, using a home-built ME coefficient measurement setup employing a dynamic lock-in technique. It is found that the T-α_{ME} increases in magnitude and exceeds the L-α_{ME} with increasing size of the *A* cation. We have observed a maximum value of T-α_{ME} =

2.1 mV/cmOe for $A = Sr_{0.5}Ba_{0.5}$ compound, although it is not the compound with the highest saturation magnetization. The observed changes in the ME coefficient are suggested to possible modification in the domain structure and ME coupling in these compounds.

6. 2 Experimental details

We have synthesized the polycrystalline samples of $BiFeO_3$ and $Bi_{0.7}A_{0.3}FeO_3$ with *A* = Sr, Ba and $Sr_{0.5}Ba_{0.5}$ by the conventional solid state reaction. The solid solutions were prepared by mixing and grinding stoichiometric mixtures of Bi_2O_3, $SrCO_3$, $BaCO_3$ and Fe_2O_3 in agate mortar and preheating the powder in the temperature range from 800 °C (x = 0) - 850 °C (x = 0.3) for 5-6 hours. Structural and phase characterizations were done with X-ray diffraction (XRD) experiment (Philips X' pert Pro) using Cu-Kα radiation. All the compounds were pressed into pellets and final heat treatment was done in the temperature range from 850 °C (pure $BiFeO_3$) to 925 °C (Sr) for 5 hours to get relatively dense pellets. The ferroelectric properties (*P-E* loop) were measured using a Precision LC ferroelectric tester (Radiant Technologies). The temperature and field dependence of magnetization were measured using a vibrating sample magnetometer (VSM) with a superconducting magnet (Quantum Design, USA) in the temperature range *T* = 10-400 K, and the high temperature (*T* = 300-700 K) dependence of magnetization under a fixed magnetic field (*H* = 5 kOe) was done using a VSM with an electromagnet (Lakeshore – model: 74034). We have investigated the ME effect using a home-built dynamic lock-in technique as described in the experimental section: 2.2.4. For ME measurements, all the samples were cut into a rectangular shape of similar dimensions, polished and made into parallel plate capacitor structure by applying silver paint on opposite faces of the sample and heat treated. Here, the ME coefficient, α_{ME} is calculated using the relation,

$$\alpha_{ME} = \frac{dE}{dH} = \frac{1}{t}\frac{dV}{dH} = \frac{V_{out}}{h_0 t}$$

where, V_{out} is the *ac* ME voltage appeared across the sample surface (measured by the lock-in), h_0 is the amplitude of the *ac* magnetic field, and *t* is the thickness of the sample. We have

measured both longitudinal (direction of ME voltage is parallel to the direction of the applied magnetic field) and transverse (direction of ME voltage is perpendicular to the direction of the applied magnetic field) ME coefficients.

6. 3 Results and Discussions

6. 3. 1 Structural characterization using XRD

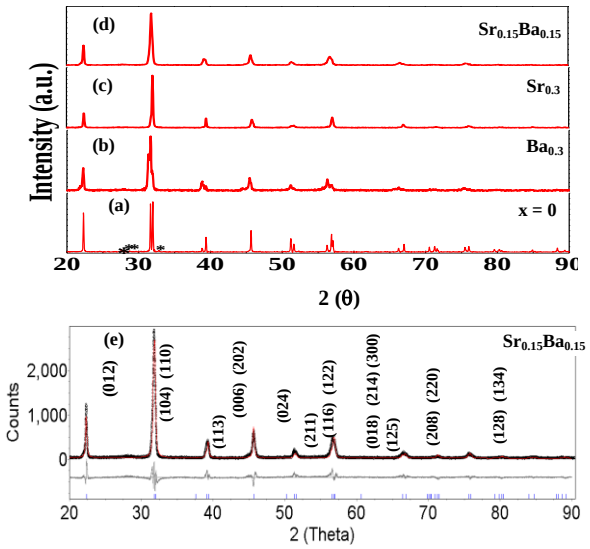

Fig. 6. 1 XRD patterns of (a) $BiFeO_3$, (b) *A* = Ba (c) *A* = Sr (d) *A* = $Sr_{0.5}Ba_{0.5}$ compounds at room temperature. (e) Rietveld refinement of the room temperature XRD pattern for the $Bi_{0.7}Sr_{0.15}Ba_{0.15}FeO_3$ compound with space group *R*3c.

Figs. 6.1(a)-(d) show the XRD pattern of all the samples at room temperature. The XRD pattern of $BiFeO_3$ reveals a small fraction of impurity phases such as $Bi_2Fe_4O_9$, $Bi_{25}FeO_{40}$ [marked by * in Fig. 6.1(a)] in addition to the main rhombohedral phase as reported earlier. [240] It is known that a single phase $BiFeO_3$ is very difficult to prepare by the standard solid state chemistry route. However, impurity phases almost disappear in the Sr and Ba doped $BiFeO_3$ compounds and the XRD patterns of which confirm the compound formation as it can be seen in Figs. 6.1(b)-6.1(d). The observed XRD pattern of one of the doped compounds *i.e.*, Sr and Ba co-doped was indexed to rhombohedral structure of $BiFeO_3$ with space group R3c using TOPAS software version 2.1 and it is shown in Fig. 6.1(e). The lattice parameters of the Sr and Ba co-doped compound are a = 5.592 Å and c = 13.809 Å.

6. 3. 2 Magnetic properties of $Bi_{1-x}A_xFeO_3$ compounds

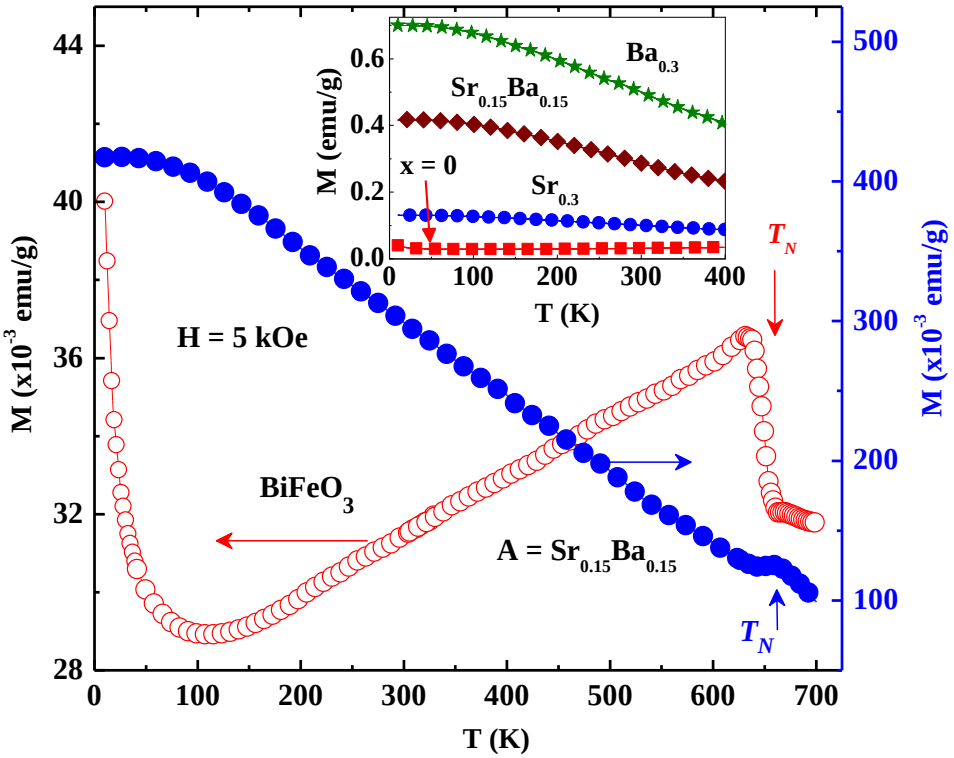

Fig. 6. 2 The temperature dependences (T = 10-700 K) of magnetization at H = 5 kOe for $BiFeO_3$ and $Bi_{0.7}Sr_{0.15}Ba_{0.15}FeO_3$ compounds. The inset shows the temperature dependences (T = 10-400 K) of magnetization at H = 5 kOe for all the compounds.

The main panel of Fig. 6.2 shows $M(T)$ measured at H = 5 kOe for the two selected samples, $BiFeO_3$ and $Bi_{0.7}Sr_{0.15}Ba_{0.15}FeO_3$ over a wide temperature range from T = 700 K to 10 K. The rapid increase of magnetization at T_N = 644±2 K signals the onset of antiferromagnetic transition in $BiFeO_3$. [241] The T_N is determined from the inflection point of the $M(T)$ curve around the transition. Furthermore, $M(T)$ decreases monotonically below T_N and then raises rapidly below T = 100 K. This complex magnetization behavior is possibly due to the development of incommensurate sinusoidal spin structure in $BiFeO_3$. On the other hand, $M(T)$ for $Bi_{0.7}Sr_{0.15}Ba_{0.15}FeO_3$ shows only a weak anomaly around T_N = 642±2 K and increases gradually with lowering in temperature. The magnitude of M at T = 10 K of the latter compound is an order of magnitude higher than the $BiFeO_3$. The inset compares the M versus T under H = 5 kOe for all four compounds in the temperature range from T = 400 K to

10 K. We see that the magnetization increases with lowering temperature for all the doped samples which indicates increase in ferromagnetic component. The Ba (30%) doped compound shows the highest magnetization value.

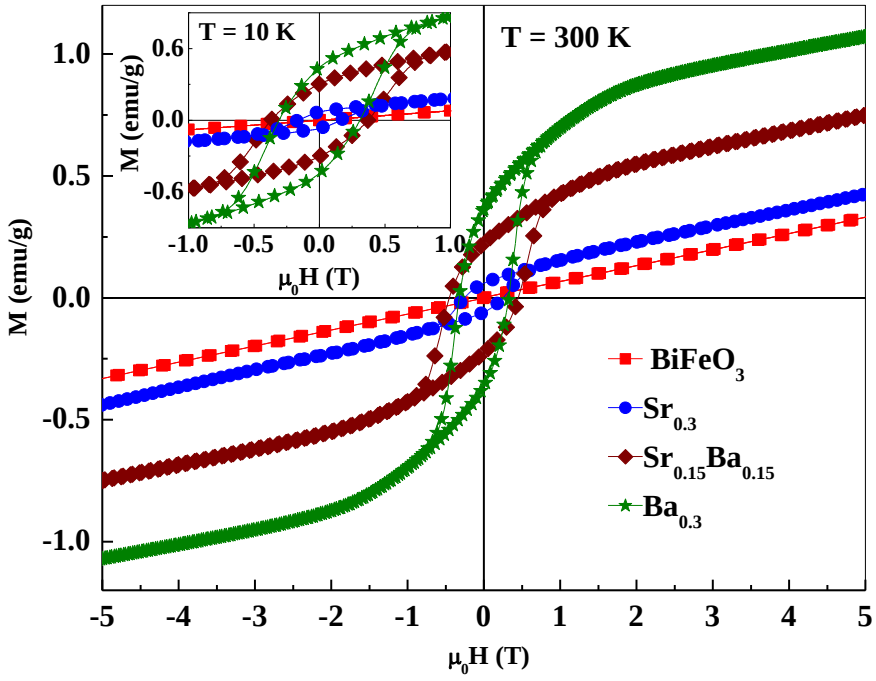

Fig. 6. 3 Field dependences of magnetization for $Bi_{0.7}(Sr, Ba)_{0.3}FeO_3$ compounds at room temperature. The inset shows the field dependences of magnetization at *T* = 10 K.

We show the field dependence of magnetization for $BiFeO_3$ and $Bi_{0.7}A_{0.3}FeO_3$ compounds with *A* = Sr, Ba and $Sr_{0.5}Ba_{0.5}$ at room temperature in the main panel of Fig. 6.3. The magnetization of pure $BiFeO_3$ increases linearly without saturation even at the maximum field ($\mu_0 H$ = 5 T) which confirms that the sample is in the antiferromagnetic state even at the highest field. However, the divalent doped compounds show a weak ferromagnetic like behavior with well-developed hysteresis loop and enhanced magnetization. The spontaneous magnetization (M_s) obtained from extrapolation of the high field *M* to *H* = 0 increases with increasing size of the divalent cation (M_s = 0.098 emu/g for *A* = Sr, and 0.75 emu/g for *A* = Ba). While the coercive field (H_C) initially increases from $\mu_0 H_C$ = 0.27 T for *A* = Sr to $\mu_0 H_C$ = 0.46 T for *A* = $Sr_{0.5}Ba_{0.5}$, it decreases to $\mu_0 H_C$ = 0.32 T for *A* = Ba. The *M-H* loops at *T* = 10 K shown in the inset indicates a slight decrease in the coercive field ($\mu_0 H_C$ = 0.15 T for *A* = Sr

and $\mu_0 H_C$ = 0.37 T for $A = Sr_{0.5}Ba_{0.5}$) compare to the room temperature values. Our $M(H)$ data of A = Ba, Sr compounds are in close agreement with data reported by V. A. Khomchenko *et al*. [237]

The divalent substitution for the trivalent Bi is expected to convert a fraction of Fe^{3+} to Fe^{4+}. However, Fe^{4+} is difficult to form at ambient pressure and the presence of Fe^{4+} ions is not supported by the Mossbauer spectroscopy. [238] Hence, the charge imbalance introduced by divalent cations has to be compensated by oxygen deficiency ($O_{3-\delta}$ instead O_3 with $\delta \approx$ 0.15). We note that the ionic radii of Bi^{3+}, Sr^{2+} and Ba^{2+} are 1.03 Å, 1.18 Å and 1.36 Å, respectively. [242] The systematic increase in the spontaneous magnetization with increasing average ionic radii of the divalent cation possibly indicates that the oxygen deficiency alone may not cause of the enhanced magnetization, but it may be related to the progressive suppression of the spiral spin structure and/or increase in the canting angle of antiferromagnetically coupled layers due to tilting of $FeO_{6-\delta}$ octahedra. However, it is difficult to draw a clear conclusion without magnetic neutron diffraction or other structural studies on these divalent doped compounds. It is interesting to note that the magnetic moment obtained with divalent cation substitution is comparable to the rare earth substituted $BiFeO_3$. [134, 243]

6. 3. 3 Ferroelectric and ME properties of $Bi_{1-x}A_xFeO_3$ compounds

In this section, we present the ferroelectric and ME properties of $Bi_{1-x}A_xFeO_3$ compounds. First we show the *P-E* hysteresis loops measured at room temperature by the Radiant ferroelectric tester. Later, we show the detailed ME properties of $Bi_{1-x}A_xFeO_3$ compounds measured by homebuilt ME coefficient measurement setup employing dynamic lock-in technique.

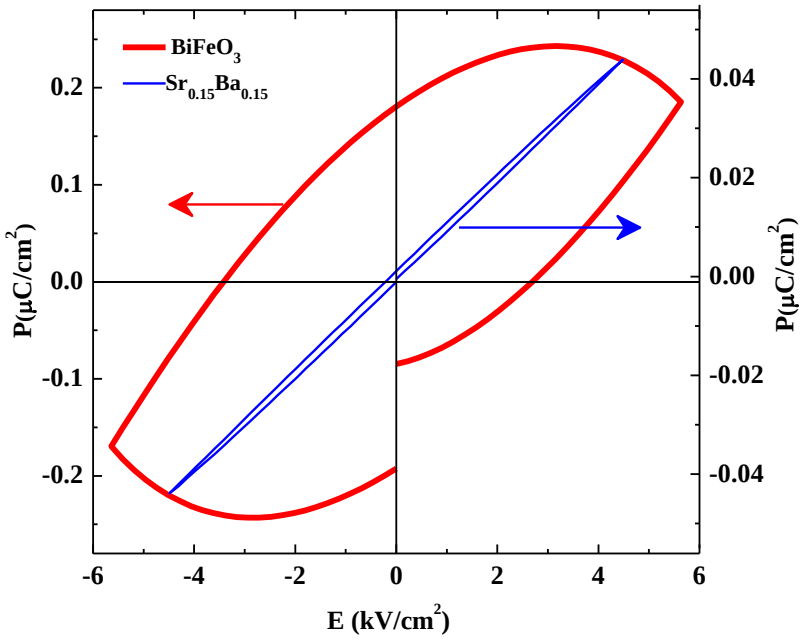

Fig. 6. 4 *P-E* loops for $BiFeO_3$ and $Bi_{0.7}Sr_{0.15}Ba_{0.15}FeO_3$ compounds at room temperature (hysteresis period = 1 ms).

We have measured the polarization versus electric field (*P-E*) loops at f = 1 kHz (frequency of the hysteresis cycle or measurement frequency) at room temperature for two selected samples: $BiFeO_3$ and $Bi_{0.7}Sr_{0.15}Ba_{0.15}FeO_3$ and they are shown in Fig. 6.4. The pure $BiFeO_3$ exhibits an unsaturated hysteresis loop and it is rounded at the highest field, which reveals the leakage current contribution that overshadows true polarization due to the orientation of the electric dipoles. Because, for an insulating ferroelectric material, the switched charge Q due to applied electric field E depends only on the remanent polarization P_r through the relation $Q = 2P_rA$ where A is the surface area of the capacitor, whereas for a lossy dielectric material, extra contribution comes from the conductivity σ of a sample through the relation $Q = 2P_rA + \sigma EAt$, where t is the time for hysteresis measurement. [244] On the other hand, the co-doped compound exhibits an unsaturated *P-E* loop even at the higher limit of electric field of 5.5 kV/cm in our experiment, but it elucidates the considerable suppression of leaky behavior of the compound compared to the parent one. Further, electrical polarization study at higher electric field is necessary to confirm the ferroelectricity in our bulk sample. Next, we show the results of ME properties of $Bi_{0.7}(Sr, Ba)_{0.3}FeO_3$ compounds.

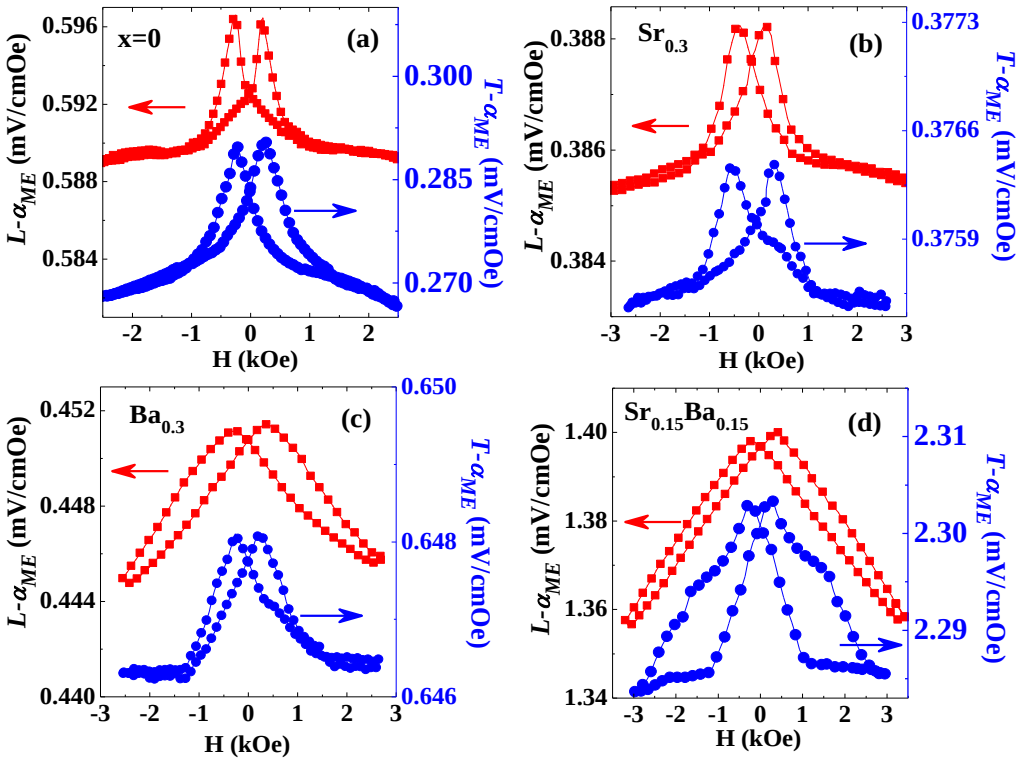

Fig. 6. 5 Room temperature *dc* bias magnetic field dependence of longitudinal (left scale) and transverse (right scale) ME coefficients for $Bi_{0.7}(Sr, Ba)_{0.3}FeO_3$ compounds at 7 kHz *ac* field frequency.

Figs. 6.5(a)-(d) show the magnetic field dependence of the ME coefficient (α_{ME}) at room temperature for (a) $BiFeO_3$ (x = 0), (b) $Sr_{0.3}$, (c) $Ba_{0.3}$ and (d) $Sr_{0.15}Ba_{0.15}$. The longitudinal (L-α_{ME}) and the transverse (T-α_{ME}) ME coefficients are plotted on the left and right scales, respectively. The measurements reported here are at a fixed frequency f = 7 kHz of the *ac* signal. This is the optimum frequency for the maximum gain of the power amplifier we used. All the samples exhibit hysteresis over a certain field range. For $BiFeO_3$ compound (Fig. 6.5a), as the field increases from zero, the L-α_{ME} increases rapidly and exhibits a sharp maximum around H = 0.15 kOe, where L-α_{ME} = 0.6 mV/cmOe. Above H = 0.9 kOe, L-α_{ME} varies little with the magnetic field. Upon reducing the field from the maximum value, hysteresis appears in the field range H = +0.9 kOe to H = -0.9 kOe and a peak at H = -0.15 kOe. The T-α_{ME} shows a similar behavior, but the hysteresis region is widened and the maximum T-α_{ME} = 0.28 mV/cmOe occurs at H = 0.19 kOe. The maximum L-α_{ME} observed in our sample is an order of magnitude smaller than earlier report on the same composition by

Caicedo *et al.* [245] This discrepancy is possibly due to the different sample preparation conditions. The α_{ME} of the Sr (30%) doped $BiFeO_3$ (Fig. 6.5b) shows a similar behavior as $BiFeO_3$. The maximum α_{ME} is 0.34 mV/cmOe observed in this compounds is slightly lower than that of $BiFeO_3$, and we note that L-α_{ME} and T-α_{ME} are comparable in values. However, L-α_{ME} of $Bi_{0.7}Ba_{0.3}FeO_3$ (Fig. 6.5c) shows a completely different behavior: it shows a less pronounced peak at low fields compared to the parent compound and decreases almost linearly with the field above H = 0.45 kOe without saturation. Hysteresis occurs over a wide-field range compared to the undoped and Sr (30%) doped compounds. The field dependence of T-α_{ME} is similar to the parent compound but the magnitude of its peak is nearly twice that of the parent compound. The L-α_{ME} of the co-doped compound, $Bi_{0.7}Ba_{0.15}Sr_{0.15}FeO_3$ is larger than that of parent compound. The T-α_{ME} of the co-doped sample exhibits a complex hysteresis loop and showed the highest value (≈ 2.3 mV/cmOe at H_{dc} = 0.25 kOe) in the series even though this is not the compound with the highest saturation magnetization.

Our ME results on $Bi_{0.7}(Sr, Ba)_{0.3}FeO_3$ compounds suggest that the transverse ME coefficient is comparable or exceeds the longitudinal ME effect in the divalent doped compounds, and the highest ME coefficient is obtained for the co-doped compound. The peak in ME coefficient does not coincide with the coercive field, instead it occurred below the coercive field. The peak is possibly related to the inflection point of the $d\lambda/dH$ curve, where λ is the magnetostriction. [246] The observed variations in the longitudinal and transverse ME effects with increasing size of the *A*-cation is possibly related to the changes in magnetic domain structure and magnetostriction in these compounds. However, further investigations such as magnetostriction as a function of magnetic field is needed to elucidate the origin of the observed effects. The present work is followed by several recent reports focusing on magnetic, electrical and ferroelectric properties of pure and doped $BiFeO_3$ compounds in bulk, nano-material and thin film forms. [247, 248, 249, 250, 251, 252] The Co-doped $BiFeO_3$, $BiFe_{0.95}Co_{0.05}O_3$ bulk ceramic prepared using sol-gel method by Xu *et al.*, [247] showed enhanced magnetic properties with saturate magnetization of 1.6 emu/g and remnant

magnetization of 0.7 emu/g at 300 K. Enhanced room temperature ferromagnetism with a large saturation magnetization of 3 emu/g at $\mu_0 H$ = 1 T was observed in porous $BiFeO_3$ prepared by Xu *et al.* [249] Thin-films of $Bi_{0.75}Sr_{0.25}FeO_{3-\delta}$ prepared by Singh *et al.*, [252] showed a room temperature ferroelectric hysteresis loop with remnant polarization of $2P_r$ = 86.13 μC/cm^2 and coercive field of $2E_C$ = 75.5 kV/cm. The polycrystalline $BiFeO_3$ compound synthesized using high-pressure technique by Zhai *et al.*, [251] showed a well saturated ferroelectric hysteresis loop. It will be worth to study the ferroelectric properties of Sr and Ba doped $BiFeO_3$ in thin film form.

6. 4 Conclusions

In this chapter, we have investigated the magnetic and ME properties of divalent cation (*A*) doped $Bi_{1-x}A_xFeO_3$ compounds with *A* = Sr, Ba and $Sr_{0.5}Ba_{0.5}$ and x = 0 and 0.3. While we used the commercial vibrating sample magnetometer (VSM) equipped with PPMS for temperature and magnetic field dependence magnetization measurements, we have made use of the home-built dynamic lock-in setup for the room temperature magnetic field dependence of ME coefficient measurements employing dynamic lock-in technique. We found that the divalent cation doping in the antiferromagnetic $BiFeO_3$ enhances the magnetization with a well-developed hysteresis loop due to the effective suppression of spiral spin structure and the magnitude of the spontaneous magnetization increases with the size of the dopants. A peak at the Neel temperature T_N = 642±2 K found in $BiFeO_3$ is suppressed in the co-doped sample (*A* = $Sr_{0.5}Ba_{0.5}$). It is found that the transverse α_{ME} increases in magnitude and exceeds the longitudinal α_{ME} with increasing size of the *A*-cation. The *A* = $Sr_{0.5}Ba_{0.5}$ compound showed the maximum transverse ME coefficient, T-α_{ME} = 2.1 mV/cmOe in the series, though it is not the compound with the highest saturation magnetization. The observed changes in the ME coefficient is suggested to possible modification in the domain structure and ME coupling. The co-doped compound, *A* = $Sr_{0.5}Ba_{0.5}$ exhibited lesser leakage current than the parent compound.

Chapter 7

Conclusions and Future scope

In this thesis, the *rf* magnetoabsorption, ac magnetotransport, magnetocaloric and multiferroic properties of selected Mn and Fe-based oxides have been investigated in detail. It is demonstrated that a simple IC oscillator circuit is a versatile contactless experimental tool to study magnetization dynamics as well as to investigate magnetostructural phase transition in manganites. Studies on ac magnetotransport in manganites using impedance spectroscopy reveal that ac magnetotransport is an alternative strategy to enhance the ac magnetoresistance in manganites and also a valuable tool to study the magnetization dynamics, and to detect the magnetic and structural transitions. Studies of MCE in selected manganites showed coexistence of both normal and inverse MCEs in a single compound with excellent magnetocaloric properties which may be very promising for the magnetic refrigeration applications. Detailed magnetic and ME studies on pure and cation doped $Bi_{1-x}A_xFeO_3$ compounds reveal an important observation that the compound need not have high saturation magnetization to show high ME coefficient. The other important observations obtained in this thesis work have already been given in the conclusion part of each chapter. In this chapter, overall view of the present work is summarized and also the future scope of this thesis work is presented.

7. 1 Conclusions

7. 1. 1 *rf* magnetoabsorption studies in manganites using IC oscillator

The *rf* magnetoabsorption in $La_{0.67}Ba_{0.33}MnO_3$ compound was investigated by a homebuilt LC resonant circuit powered by an integrated chip oscillator (ICO) resonating at $f \approx$ 1.5 MHz by monitoring the changes in resonance frequency (f_r) and current (I) through ICO. [253] The *rf* magnetoabsorption in Ca doped $La_{0.67}Ba_{0.33}MnO_3$ compound *i.e.*, $La_{0.67}Ba_{0.23}Ca_{0.1}MnO_3$ which showed a low temperature anomaly below the long range

ferromagnetic ordered state, is studied as a function of both temperature and magnetic field using ICO technique. [254] A comparative study of *rf* magnetoabsorption is done in two compounds (x = 0 and 0.6) of $Sm_{0.6-x}La_xSr_{0.4}MnO_3$ series. The chosen compounds, x = 0 and x = 0.6, are ferromagnetic below T_C = 118 K and 363 K, respectively, but the former exhibits a drop in magnetization at low temperature, T^* = 30 K below T_C. The major results of *rf* magnetoabsorption study are summarized below.

1. It is observed that the ferromagnetic to paramagnetic transition in $La_{0.67}Ba_{0.33}MnO_3$ compound in zero external magnetic field is accompanied by an abrupt increase in f_r and I and they are tunable by small external magnetic field.
2. An anomaly with a small hysteresis around T = 165-195 K (below T_C) is observed in the temperature dependence of f_r for $La_{0.67}Ba_{0.23}Ca_{0.1}MnO_3$ sample. It is suggested that the observed anomaly at low temperature is due to rhombohedral-to-orthorhombic structural transition that occurs below the long range ferromagnetic order in the sample. The observed anomalies at both the magnetic and structural transitions are very sensitive to sub-kilo Gauss magnetic fields. This study demonstrated that the simple ICO technique is a valuable contactless tool to investigate the magnetic as well as structural phase transitions in manganites.
3. The fractional changes as much as $\Delta f_r/f_r$ = 46% and $\Delta P/P$ = 23% in $La_{0.67}Ba_{0.33}MnO_3$ sample, and $\Delta f_r/f_r$ = 19% and $\Delta P/P$ = 10% in $La_{0.67}Ba_{0.23}Ca_{0.1}MnO_3$ sample are observed around T_C for H = 1 kG. It is suggested that the magnetically tunable resonance frequency and power absorption obtained in present study can be exploited for magnetic field sensor and other applications.
4. A comparative study of *rf* magnetoabsorption in two compounds (x = 0 and 0.6) of $Sm_{0.6-x}La_xSr_{0.4}MnO_3$ revealed distinctive features. While a rapid decrease around T_C and a sudden increase below T^* are observed in both f_r and I for x = 0, only a rapid decrease around T_C is observed in both f_r and I for x = 0.6. A distinct field dependence of *rf* magnetoabsorption is observed in x = 0 below and above T^*. This peculiar result revealed

that a simple *LC*-resonance circuit powered by an IC oscillator is a powerful technique to investigate the *rf* magnetization dynamics in manganites. In addition, it is found that x = 0 compound exhibited a small fractional change as much as $\Delta f_r/f_r$ = 9.8% and $\Delta P/P$ = 6.1% around T_C at H = 10 kG, whereas a giant effect was observed in x = 0.6 compound at a smaller field of H = 1 kG ($\Delta f_r/f_r$ = 65% and $\Delta P/P$ = 7.5% around T_C).

7. 1. 2 Ac magnetotransport studies in manganites

The ac magnetotransport properties of a metallic ferromagnet $La_{0.67}Ba_{0.33}MnO_3$ are investigated at low frequency (f = 100 kHz) by measuring the ac resistance (R) and reactance (X) using the impedance spectroscopy in four probe configuration from the viewpoints of fundamental origin of magnetocapacitance effect showed by certain manganites. [255] The ac magnetotransport properties of $La_{0.67-x}Ba_{x-y}Ca_yMnO_3$ compounds is investigated in detail by measuring R and X as a function of magnetic field ($\mu_0 H$ = 0-7 T) and temperature (T = 400-10 K) in a wide frequency range, f = 100 kHz – 22 MHz. [256, 257] A comparative ac magnetotransport study has been carried out in $Sm_{0.6-x}La_xSr_{0.4}MnO_3$ series of compounds with $0 \leq x \leq 0.6$ which showed unusual composition dependent frequency-induced effects. [258] The main findings in this study are given below.

1. A large low field magnetoreactance of magnitude $\Delta X/X$ = 60% at T_C and f = 100 kHz under H = 1 kG is observed in $La_{0.67}Ba_{0.33}MnO_3$ compared to a small ac magnetoresistance ($\Delta R/R$ = 5%). This large magnetoreactance is attributed to the change in the magnetic permeability *i.e.*, magnetoinductance effect of the sample rather than the variation in the dielectric permittivity *i.e.*, magnetocapacitance effect. This study suggests that a large magnetocapacitance observed in other manganites [176] can have the contribution from the magnetoinductance of the sample along with intrinsic coupling between the electrical and magnetic dipole moments. Such a large magnetoinductance effect at low field may find applications in thin film inductor.

2. It is observed that both R and X show a rapid change around T_C in $La_{0.67-x}Ba_{x-y}Ca_yMnO_3$ compounds and are very sensitive to the external sub-kilo Gauss magnetic fields. An anomaly in temperature dependence of both R and X is observed at T^*, a temperature below T_C in $La_{0.67-x}Ba_{x-y}Ca_yMnO_3$ compounds which has been attributed to the high temperature rhombohedral to low temperature orthorhombic structural phase transition in the compounds. Thus, it is demonstrated that the ac magnetotransport using impedance spectroscopy is an alternative strategy to enhance low-field magnetoresistance and to study the magnetization dynamics as well as to detect the magnetic and structural transitions in manganites.
3. $La_{0.67}Ba_{0.33}MnO_3$ compound showed large ac magnetoresistance of -45% and magnetoreactance of -40% at H = 1 kG and f = 5 MHz near T_C and it also showed a large positive magnetoreactance of +450% around T_C at f = 20 MHz. This large change in both magnetoresistance and magnetoreactance is attributed to the change in transverse or circular magnetic anisotropy under the external magnetic field.
4. Unusual ac magnetotransport behaviors are observed in $Sm_{0.6-x}La_xSr_{0.4}MnO_3$ compounds with $0 \leq x \leq 0.6$, particularly in x = 0 compound which showed an insulator-metal transition with a peak around T_C. It is found that an insulator-to-metal transition in x = 0 is accompanied by a frequency-induced splitting of single peak to double peaks in $R(T)$ in zero magnetic field with a dip at T_C. These double peaks are α and β, which correspond to temperatures above and below the insulator-metal transition, respectively. It is observed that the position of β-peak shifts up in temperature with increasing strength of the magnetic field, while that of α-peak is unaltered with increasing external magnetic field. It is suggested that the frequency-induced splitting behavior in $R(T)$ is possibly originated from the dispersion in real part of permeability. The double peak behavior disappeared in La doped compounds (x > 0.05) and it is attributed it to decrease in the dc resistivity of compounds, where the resistive part dominates the capacitive part. A low field magnetoimpedance behavior is observed in higher La-doped compounds around

both T_C and T^*, and the observed results are understood qualitatively in terms of changes in the skin depth and transverse permeability of the sample around T_C and T^*.

7. 1. 3 Normal and inverse MCEs in selected manganites

A detailed investigation of magnetic and magnetocaloric properties has been carried out in $Sm_{0.6-x}La_xSr_{0.4}MnO_3$ compounds with $0 \leq x \leq 0.6$. [259] A comprehensive study of both normal and inverse MCEs was conducted in $Pr_{1-x}Sr_xMnO_3$ compounds with x = 0.5 and 0.54 using both magnetic (indirect) and calorimetric (direct) methods. [260, 261] In indirect method, the magnetic entropy change, ΔS_m is estimated from the isothermal $M(H)$ data taken at selected temperatures. In direct method, ΔS_m value is estimated from the latent heat evolved in the field-induced antiferromagnetic-to-ferromagnetic transition using homebuilt DSC setup, which is rarely investigated by other researchers. The major results obtained in these studies are summarized below.

1. A detailed investigation of magnetic properties of $Sm_{0.6-x}La_xSr_{0.4}MnO_3$ compounds revealed that while the ferromagnetic T_C increases monotonically with increasing La content from T_C = 118 K for x = 0 to T_C = 363 K for x = 0.6, an anomalous peak in the temperature dependence of magnetization is observed at low temperature (T^*) for x < 0.6. The temperature T^*, at which anomalous peak occurs increased from 30 K for x = 0 to a maximum value of 120 K for x = 0.4 and then decreased to 105 K for x = 0.5, and finally it disappeared for the end compound (x = 0.6). It is found that the anomalous peak that appeared in *M(T)* around T^* is not due to occurrence of cluster-glass or spin-glass state existing in the system, but it is due to antiparallel coupling of 3*d* spins of Mn sublattice and 4*f* spins of Sm sublattice.
2. The change in magnetic entropy (ΔS_m) is estimated from the isothermal $M(H)$ data for $Sm_{0.6-x}La_xSr_{0.4}MnO_3$ compounds with x = 0, 0.05, 0.1, 0.3, 0.4 and 0.6. It is found that ΔS_m is negative around T_C and it decreased from ΔS_m = -6.2 $Jkg^{-1}K^{-1}$ for x = 0 to -4.2 $Jkg^{-1}K^{-1}$ for x = 0.6 for a field change of ΔH = 5 T. An unusual inverse MCE is observed

within the long-range ferromagnetic ordered state (below $T^* < T_C$) for x < 0.6. The ΔS_m showed a maximum value of +1.07 $Jkg^{-1}K^{-1}$ at T = 10 K for ΔH = 5 T in x = 0.4 compound. This x = 0.4 compound also showed a significant normal MCE (ΔS_m = -4 $Jkg^{-1}K^{-1}$) at T_C with a high RC of 214 Jkg^{-1}. While the normal MCE is due to ferromagnetic exchange-interaction between Mn spins, it is suggested that the inverse MCE appears to be caused by antiferromagnetic coupling between Sm-4*f* and Mn-3*d* magnetic moments. The unusual inverse MCE observed in this study is the first observation of inverse MCE in a ferromagnetic compound. Coexistence of normal and inverse MCEs in a single material is very interesting from the viewpoints of magnetic refrigeration applications because of the fact that the sample can be cooled by adiabatic magnetization and demagnetization in different temperature regions which would enhance the efficiency of magnetic refrigerator.

3. A detailed study of magnetic and magnetocaloric properties of $Pr_{1-x}Sr_xMnO_3$ compounds showed interesting features. The x = 0.5 compound showed a para-ferromagnetic transition at T_C = 264 K and a ferro-antiferromagnetic transition at T_N = 132.5 K, but x = 0.54 showed a single para-antiferromagnetic transition at T_N = 210.5 K. The magnetic method revealed a large inverse MCE (ΔS_m = +7 $Jkg^{-1}K^{-1}$) around T_N = 132.5 K and an appreciable normal MCE (ΔS_m = -4.5 $Jkg^{-1}K^{-1}$) around T_C = 264 K in x = 0.5 for a field change of ΔH = 7 T. The x = 0.54 showed much larger inverse MCE (ΔS_m = +9 $Jkg^{-1}K^{-1}$ for ΔH = 7 T) around T_N = 210.5 K and the ΔS_m values estimated by magnetic method closely agrees with the calorimetric results as well as Clausius-Clapeyron equation. It is suggested that the normal MCE is due to ferromagnetic exchange-interaction between Mn spins and the inverse MCE is due to a field-induced structural transition that accompanies the destruction of antiferromagnetism under the magnetic field.
4. A clear experimental evidence for both normal and inverse MCE is obtained from the home-built DTA by measuring the field-induced change in temperature (ΔT) of $Pr_{1-x}Sr_xMnO_3$ system. It is observed that ΔT of a sample in the antiferromagnetic state is

negative upon application of magnetic field, whereas in the ferromagnetic state, ΔT is negative upon removal of magnetic field.

5. A large inverse MCE (ΔS_m = +9 $Jkg^{-1}K^{-1}$ for ΔH = 7 T around T_N) observed in x = 0.54 with RC = 168.42 Jkg^{-1}, and the coexistence of both normal (ΔS_m = -4.5 $Jkg^{-1}K^{-1}$ for ΔH = 7 T around T_C) and inverse (ΔS_m = +7 $Jkg^{-1}K^{-1}$ for ΔH = 7 T around T_N) MCEs observed in x = 0.5 with significantly large RC of 298.8 Jkg^{-1} and 288.8 Jkg^{-1}, respectively makes $Pr_{1-x}Sr_xMnO_3$ system very attractive from the viewpoints of magnetic refrigeration technology.

7. 1. 4 Magnetic and ME studies in pure and doped $BiFeO_3$

A detailed study on magnetic and ME properties of divalent cation (*A*) doped $Bi_{1-x}A_xFeO_3$ compounds with *A* = Sr, Ba and $Sr_{0.5}Ba_{0.5}$ and x = 0 and 0.3 is conducted. [262] The ME properties are measured using a home-built setup employing the dynamic lock-in technique. The major results obtained are summarized below.

1. A peak in the temperature dependence of magnetization is observed in $BiFeO_3$ at the Neel temperature, T_N = 642±2 K and it is suppressed in the cation doped $BiFeO_3$ compounds.
2. It is observed that the divalent cation doping in $BiFeO_3$ enhances the magnetization with a well-developed hysteresis loop due to the effective suppression of spiral spin structure and the magnitude of spontaneous magnetization increases with size of the cation dopants.
3. It is found that the transverse ME coefficient, T-α_{ME} increases in magnitude and exceeds the longitudinal ME coefficient, L-α_{ME} with increasing size of the *A*-cation. The *A* = $Sr_{0.5}Ba_{0.5}$ compound showed maximum transverse ME coefficient T-α_{ME} = 2.1 mV/cmOe in the series, although it is not the compound with highest saturation magnetization. Thus, the important finding in this study is that the compounds need not to have high saturation magnetization to show high ME coefficient.

4. It is also found that the co-doped compound, A = $Sr_{0.5}Ba_{0.5}$ exhibits a lesser leakage current than the parent $BiFeO_3$ compound.
5. It is suggested that the observed changes in ME coefficient is due to possible modification in the domain structure and ME coupling.

7. 2 Future scope

Various exotic properties of Mn and Fe-based oxides have been obtained in this thesis work through a detailed investigation of chosen systems using various techniques, however, there are still avenues wherein the systems as well as the results obtained can be probed further.

1. From our *rf* magnetoabsorption measurements, we have shown that electromagnetic absorption in manganites is very sensitive to sub kilo Gauss magnetic fields leading to a giant *rf* magnetoabsorption in ferromagnetic metallic state. However, investigation of *rf* magnetoabsorption in compounds which show charge ordered insulating phase, metallic spin glasses, as well as in some rare earth intermetallic alloys will be a well-deserved study. The *rf* magnetoabsorption investigated in one of the Fe-based oxide families for example, bulk and nanoparticles of insulating $GaFeO_3$ showed completely different behavior as compared to conducting ferromagnetic manganites. [263, 264] It is observed that *rf* magnetoabsorption in these insulating $GaFeO_3$ compounds is very small compare to a giant change observed in low resistive manganites. In this context, it is worth pointing out here about the powerfulness of resonator circuit in measuring the microwave resistance of superconducting compounds governed by power absorption in the sample which has been studied in 1989. [265] Thus, it would be interesting to extend the *rf* magnetoabsorption study in order to utilize the IC oscillator circuit in a contactless measurement of resistivity of certain compounds. The connection between *rf* magnetoabsorption and domain wall dynamics has to be clearly understood. Further, measurements of *rf* magnetoabsorption as a function of frequency will be interesting.

2. The ac magnetotransport investigated in selected manganites showed interesting features including low field giant magnetoimpedance effect, a large magnetoinductance effect at low frequencies (f = 100 kHz) etc. These results are qualitatively understood on the basis of suppression of magnetic fluctuations near T_C, which causes an increase in the magnetic penetration depth and a decrease in the impedance. This large low field magnetoimpedance observed in manganites can be exploited for various sensor applications. However, there are more challenging questions to be addressed from both theoretical and practical application points of view which are mainly: 1. Can we observe the low field magnetoimpedance in single crystalline materials or epitaxial thin films? 2. How does tunneling magnetoresistance respond to higher frequencies (f > 20 MHz)? 3. How do the microstructure and magnetic clusters influence the magnetoimpedance effect? In addition to this, we believe that a detailed study of magnetoimpedance as a function of temperature in manganites having different ground states in the frequency range from a few mHz to a few MHz could be helpful to understand the competition between the magnetocapacitance effect found in phase separated manganites such as bulk Cr doped $Nd_{0.5}Ca_{0.5}MnO_3$ [266] and La-Pr-$CaMnO_3$ thin film [176] and the magnetoinductance effect reported in the present study. Further, the dynamics of critical fluctuations around T_C and freezing of charge-orbital ordered clusters seem to be essential to understand the frequency-induced splitting behavior observed in ac resistance of $Sm_{0.6-x}La_xSr_{0.4}MnO_3$ compounds.
3. The observation of inverse MCE in $Sm_{0.6-x}La_xSr_{0.4}MnO_3$ compounds is the first report of inverse MCE in ferromagnetic compounds because of the fact that inverse MCE is generally seen in antiferromagnets and/or in compounds which show martensitic transition. The increasing value of ΔS_m associated with inverse MCE with decreasing temperature is very promising for low temperature magnetic refrigeration applications and it can encourage other researchers, who are working on MCE, to look for compounds which show such behavior. We have suggested that the observed inverse MCE is due to the antiferromagnetic coupling between the magnetic moments of Sm-4*f* and Mn-3*d*

spins. A clear evidence of 4*f*-3*d* interactions occurred in other manganites, which have been confirmed by neutron diffraction experiments, is given. The proposed Sm-4*f* and Mn-3*d* interaction in the present study occurs around T = 120 K (for x = 0.4 compound) which is very high compared to earlier reported data on other systems. Thus, from the viewpoints of both fundamental and practical applications, it is interesting to understand the condition under which rare earth moments can order at such a high temperature. Further investigation of neutron diffraction in $Sm_{0.6-x}La_xSr_{0.4}MnO_3$ series and theoretical modeling will be very much needed to understand the exact nature of 4*f*-3*d* exchange interaction.

4. A giant MCE due to the destruction of antiferromagnetism under magnetic field is observed in $Pr_{1-x}Sr_xMnO_3$ systems, and these compounds showed excellent magnetocaloric properties. The critical field for destroying the antiferromagnetic ordering can further be reduced by partial replacement of Sr^{2+} by the larger Ba^{2+} cation or by replacement of Pr^{3+} by La^{3+} ion. Hence, by suitable combination of *A*-site ions one can try to get higher magnetic entropy change at lower magnetic fields. The ΔS_m and RC values can further be improved by partial replacement of Sr by Ca which will increase the value of T_N and decrease the value of T_C as seen in the case of $Pr_{0.5}Sr_{0.5-x}Ca_xMnO_3$ compounds. [267] Thus, by a proper combination of Sr and Ca, one can to tune the value of T_N and T_C close to each other in such a way that the magnetic transition becomes strongly first-order so as to achieve enhanced magnetocaloric properties.
5. Although we have presented the detailed magnetic and ME properties of pure and cation doped $BiFeO_3$ compounds, further investigations, particularly magnetostriction and electrical polarization at higher electric field studies will be helpful to understand the origin of enhanced ME coefficient in the divalent doped $BiFeO_3$.

Bibliography

[1] Y. Tokura (Ed.), *Colossal Magnetoresistive Oxides* (Gordon & Breach Science Publishers, Singapore, 2000); C. N. R. Rao, and B. Raveau (Eds.), *Colossal Magnetoresistance, Charge Ordering and Related Properties of Manganese Oxides* (World Scientific, Singapore, 1998).

[2] G. H. Jonker and J. van Santen, Physica **16**, 337 (1950).

[3] J. van Santen and G. H. Jonker, Physica **16**, 599 (1950).

[4] G. H. Jonker, Physica **22**, 707 (1956).

[5] V. M. Goldschmidt, *Geochemistry* (Oxford University Press, Oxford, 1958); J. B. Goodenough, J. A. Kafalas, and J. M. Longon, *Preparation Methods in Solid State Chemistry* P. Hagenmuller (Ed.) (Academic, New York, 1972); A. Manthiram and J. B. Goodenough, J. Solid State Chem. **92** 231, (1991).

[6] S. Blundell, *Magnetism in Condensed Matter* (Oxford University Press, New York, 2001)

[7] H. A. Jahn and E. Teller, Proc. Roy. Soc. A **161**, 220 (1937).

[8] R. Orbach and H. J. E. Stapleton, *Spin-Lattice Relaxation Electron Paramagnetic Resonance*, S Geschwind (Ed.) (Plenum, New York, 1972), Chapter 2.

[9] K. I. Kugel and D. I. Khomskii, Uspekhi Fizicheskikh Nauk **136**, 621 (1982); Y. Murakami, J. Hill, D. Gibbs, M. Blume, I. Koyama, M. Tanaka, H. Kawata, T. Arima, Y. Tokura, K. Hirota, and Y. Endoh, Phys. Rev. Lett. **81**, 582 (1998).

[10] K. I. Kugel and D. I. Khomskii, Uspekhi Fizicheskikh Nauk **136**, 621 (1982); Y. Murakami, J. Hill, D. Gibbs, M. Blume, I. Koyama, M. Tanaka, H. Kawata, T. Arima, Y. Tokura, K. Hirota, and Y. Endoh, Phys. Rev. Lett. **81**, 582 (1998).

[11] J. Kanamori, J. Appl. Phys. **31** 14S (1960).

[12] C. Zener, Phys. Rev. **82**, 403 (1951).

[13] P.W. Anderson and H. Hasegawa, Phys. Rev. **100**, 67 (1955).

[14] H. Kramers, Physica **1**, 182 (1934).

[15] P. W. Anderson, Phys. Rev. **79**, 350 (1950).

[16] E. O. Wollan and W. C. Koehler, Phys. Rev. **100**, 545 (1955).

[17] F. Duan and J. Guojun, *Introduction to Condensed Matter Physics* (World Scientific, Singapore, 2005), Chapter 13.

[18] P.-G. de Gennes, Phys. Rev. **118**, 141 (1960).

[19] A. Urushibara, Y. Moritomo, T. Arima, A. Asamitsu, G. Kido, and Y. Tokura, Phys. Rev. B **51**, 14103 (1995).

[20] Y. Tokura and Y. Tomioka, J. Magn. Magn. Mater. **200,** 1 (1999).

[21] P. Majumdar and P. B. Littlewood, Nature (London) **395**, 479 (1998).

[22] R. Mahendiran, S. K. Tiwary, A. K. Raychaudhuri, T. V. Ramakrishnan, R. Mahesh, N. Rangavittal, and C.N. R. Rao, Phys. Rev. B **53,** 3348 (1996); R. Mahendiran, A. K. Raychaudhuri, A. Chainani, D. D. Sarma, and S. B. Roy, Appl. Phys. Lett. **66,** 233 (1995).

[23] J. W. Verwey, Nature **144**, 327 (1939).

[24] J. Q. Li, Y. Matsui, S. K. Park, and Y. Tokura, Phys. Rev. Lett. **79**, 297 (1997).

[25] G. Blumberg, V. M. Klein, and S. W. Cheong, Phys. Rev. Lett. **80**, 564 (1998); T. Katsufuji, T. Tanabe, T. Ishikawa, Y. Fukuda, T. Arima, and Y. Tokura, Phys. Rev. **B 54**, 14230 (1996).

[26] E. O. Wollan and W. C. Koehler, Phys. Rev. **100**, 545 (1955); Z. Jirák, S. Krupicka, Z. Simsa, M. Dlouha, and S. Vratislav, J. Magn. Magn. Mater. **53**, 153 (1985).

[27] C. N. R. Rao, A. K. Cheetham, and R. Mahesh, Chem. Mater. **8**, 2421 (1996); C. N. R. Rao and A. K. Cheetham, Adv. Mater. **9**, 1009 (1997) and the references therein.

[28] C. H. Chen and S. W. Cheong, Phys. Rev. Lett. **76**, 4042 (1996); C. H. Chen, S. W. Cheong, and H. Y. Hwang, J. Appl. Phys. **81** 4326 (1997).

[29] J. B. Goodenough, Phys. Rev. **100,** 564 (1955).

[30] D. Khomski, in *Spin Electronics* (eds Ziese, M. & Thornton, M. J.) 89–116 (Springer, Berlin, 2001).

[31] S. Grenier, J. P. Hill, Doon Gibbs, K. J. Thomas, M. v. Zimmermann, C. S. Nelson, V. Kiryukhin, Y. Tokura, Y. Tomioka, D. Casa, T. Gog, and C. Venkataraman, Phys. Rev. B **69**, 134419 (2004).

[32] A. Daoud-Aladine, J. Rodríguez-Carvajal, L. Pinsard-Gaudart, M. T. Fernandez-Diaz, and A. Revcolevschi, Phys. Rev. Lett. **89**, 097205 (2002).

[33] G. Zheng and C. H. Patterson, Phys. Rev. B **67**, 220404 (2003).

[34] M. Coey, Nature **430**, 155 (2004).

[35] M. W. Lufaso and P. M. Woodward, Acta Cryst. B **60**, 10 (2004).

[36] M. v. Zimmermann, J. P. Hill, Doon. Gibbs, M. Blume, D. Casa, B. Keimer, Y. Murakami, Y. Tomioka, and Y. Tokura, Phys. Rev. Lett. **83**, 4872 (1999).

[37] X. Z. Yu, R. Mathieu, T. Arima, Y. Kaneko, J. P. He, M. Uchida, T. Asaka, T. Nagai, K. Kimoto, A. Asamitsu, Y. Matsui, and Y. Tokura, Phys. Rev. B **75**, 174441 (2007).

[38] Y. Tokura and N. Nagaosa, Science **288**, 462 (2000).

[39] C. N. R. Rao, and B. Raveau, *Transition Metal Oxides: Structure, Properties and Synthesis of Ceramic Oxides*, 2nd Ed. (Wiley, New York, 1998); E. Sigmund and A. K. Müller (Eds.) *Phase Separation in Cuprate Superconductors* (Springer, Heidelberg, 1994).

[40] E. Dagotto (Ed.), *Nanoscale Phase separation and Colossal Magnetoresistance* (Springer, Berlin, 2002); E. Dagotto, T. Hotta, and A. Moreo, Phys. Rep. **344**, 1 (2001); A. Moreo, S. Yunoki, and E. Dagotto, Science **283**, 2034 (1999).

[41] R. Mathieu and Y. Tokura, J. Phys. Soc. Jpn. **76**, 124706 (2007).

[42] E. L. Nagaev, JETP Lett. **6**, 18 (1967); E. L. Nagaev, Sov. Phys. Lett. **27**, 122 (1968); E. L. Nagaev, JETP Lett. **16**, 3948 (1972); E. L. Nagaev, *Physics of Magnetic Semiconductors* (Mir Publisher, Moscow, 1986); E. L. Nagaev, Phys. Rep. **346**, 387 (2001).

[43] C. N. R. Rao, A. Arulraj, A. K. Cheetham, and B. Raveau, J. Phys.: Condens. Matter **12**, R83, 2000.

[44] E. O. Wollan, and W. C. Koehler, Phys. Rev. **100**, 545 (1955).

[45] M. Uehara, S. Mori, C. H. Chen, and S. W. Cheong, Nature **399**, 560 (1999).

[46] F. Fath, S. Freisem, A. A. Menovsky, Y. Tomioka, J. Aarts, and J. A. Mydosh, Science **285**, 1540 (1999).

[47] Y. Tokura, Rep. Prog. Phys. **69**, 797 (2006).

[48] H. Kuwahara, Y. Tomioka, A. Asamitsu, Y. Moritomo, and Y. Tokura, Science **270**, 961 (1995).

[49] K. Miyano, T. Tanaka, Y. Tomioka, and Y. Tokura, Phys. Rev. Lett. **78**, 4257 (1997).

[50] M. Fiebig, K. Miyano, Y. Tomioka, and Y. Tokura, Science **280**, 1925 (1998).

[51] L. V. Panina and K.Mohri, Appl Phys Lett. **65**, 1189 (1994).

[52] J. E. Lenz, *A Review of Magnetic Sensors*. Proc IEEE **78**, 973 (1990); T. Meydan, J. Magn. Magn. Mater **133**, 525 (1994).

[53] P. Ripka (Ed.), *Magnetic Sensors and Magnetometers* (Artech House Publishers, London, 2001).

[54] M. Vazquez and A. Hernando, J Phys D: Appl Phys **29**, 939 (1996); H. Chiriac and T. A. Ovari, Prog. Mater. Sci. **40**, 333 (1996).

[55] M. Vazquez, J Magn. Magn. Mater, **226**, 693 (2001); M. Knobel and K. R. Pirota, J Magn. Magn. Mater, **242** 33 (2002).

[56] M. Knobel, M. Vazquez, L. Kraus, *Giant magnetoimpedance in Handbook of magnetic materials*, K. H. Buschow (Ed.), vol. **15**. (Elsevier Science, Amsterdam, 2003); L. Kraus, Sens Acta A **106**, 187 (2003); C. Tannous, and J. Gieraltowski, J Mater. Sci. Mater for Elec., **15**, 125 (2004).

[57] L. Kraus, Sens Acta A **106**, 187 (2003).

[58] L. D. Landau, E. M. Lifshitz, and L. P. Pitaevskii, *Electrodynamics of Continuous Media*, 2nd ed. (Butterworth-Heinemann, Oxford, 2004).

[59] J. M. D Coey, M. Viret, and S. von Molnar, Adv. Phys. **58**, 571 (2009).

[60] J. A. Souza, R. F. Jardim, R. Muccillo, E.N.S. Muccillo, M. S. Torikachvili. and J. J. Neumeier, J. Appl. Phys. **89**, 6636 (2001).

[61] J. Rivas, J. Mira, B. Rivas-Murias, A. Fondado, J. Dec, W. Kleemann and M. A. Senaris-Rodriguez, Appl. Phys. Lett. **88**, 242906 (2002);

[62] S. Mercone, A. Wahl, A. Pautrat, M. Pollet, and C. Simon, Phys. Rev. B **69**, 174433 (2004).

[63] J. Hu and H. Qin, J. Magn. Magn. Mater. **234**, 419 (2001); H. Qin, J. Hu, J. Chen, Y. Wang and Z. Wang, J. Appl. Phys. **91**, 10003 (2002).

[64] G. M. B. Castro, A. R. Rodrigues, F. L. A. Machado, and R. F. Jardim, J. Magn. Magn. Mater. **272**, 1848 (2004).

[65] C. Y. Hsu, H. Chou, B. Y. Liao, and J. C. A. Huang, Appl. Phys. Lett. **89**, 262510 (2006).

[66] D. Stanescu, P. Xavier, J. Richard, and C. Dubourdieu, J. Appl. Phys. **99**, 073707 (2006).

[67] S. E. Lofland, S. M. Bhagat, S. D. Tyagi, Y. M. Mukovskii, S. G. Karabashev, and A. M. Balbashov, J. Appl. Phys. **80**, 3592 (1996); V. V. Srinivasu, S. E. Lofland, S. M. Bhagat, K, Ghosh, and S. Tyagi, *ibid* **86**, 1067 (1999).

[68] J. Wosik, L. -M. Xie, M. Strikovski, J. H. Miller, Jr. and P. Przyslupski, Appl. Phys. Lett. **74**, 750 (1999).

[69] W. J. Carr, Jr., *AC Loss and Macroscopic Theory of Superconductivity* Gordon and Breach, New York (1983).

[70] A. L. Schawlow and G. E. Devlin, Phys. Rev. **113**, 120 (1959).

[71] M. Knobel and K.R. Pirota, J. Magn. Magn. Mater. **33**, 242 (2002).

[72] S.V. Vonsovsky, *Magnetism*, Nauka, Moscow (1971).

[73] F. J. Owens, J. Appl. Phys. **82**, 3054 (1997).

[74] B. I. Belevtsev, A. Ya. Kirichenko, N. T. Cherpak, G. V. Golubnichaya, I. G. Maximchuk, E. Yu. Beliayev, A. S. Panfilov, J. Fink-Finowicki, J. Magn. Magn. Mater. **281**, 97 (2004).

[75] G. T. Woods, P. Poddar, H. Srikanth and Ya. M. Mukovskii, J. Appl. Phys. **97**, 10C104 (2009).

[76] H. Srikanth, J. Wiggins, and H. Rees, Rev. Sci. Instrum. **70**, 3097 (1999).

[77] S. Sarangi and S. V. Bhat, Rev. Sci. Instrum. **76**, 023905 (2005).

[78] E. Warburg, Ann. Phys. **13**, 1 (1881).

[79] P. Debye, Ann. Phys. **81**, 1154 (1926).

[80] W. F. Giauque, J. Amer. Chem. Soc. **49**, 1864 (1927).

[81] K. A. Gschneidner, Jr., V. K. Pecharsky, and A. O. Tsokol, Rep. Prog. Phys. **68**, 1479 (2005), and references therein.

[82] O. Tegus, E. Brück, K. H. J. Buschow, and F. R. de Boer, Nature **415**, 150 (2002).

[83] A. Planes, L. Mañosa, and M. Acet J. Phys: Condens. Matter **21**, 233201 (2009).

[84] F. Casanova, A. Labarta, X. Batlle, F. J. Perez-Reche, E. Vives, L. Manosa, and A. Planes, Appl. Phys. Lett. **86**, 262504 (2005).

[85] M. Quintero, J. Sacanell, L. Ghivelder, A. M. Gomes, A. G. Leyva, and F. Parisi1, Appl. Phys. Lett. **97**, 121916 (2010).

[86] E. Bruck, J. Phys. D: Appl. Phys. **38**, R381 (2005).

[87] T. Krenke, E. Duman, M. Acet, E. F. Wassermann, X. Moya, L. Manosa, and A. Planes, Nature Mater. **4**, 450 (2005).

[88] X. Moya, L. Mañosa, A. Planes, S. Aksoy, M. Acet, E. F. Wassermann, and T. Krenke Phys. Rev. B **75**, 184412 (2007).

[89] M. H. Phan and S. C. Yu, J. Magn. Magn. Mater. **308**, 325 (2007) and references therein.

[90] A. Asamitsu, Y. Moritomo, Y. Tomioka, T. Arima, and Y. Tokura, Nature (London) **373**, 407 (1995).

[91] H. Terashita, B. Myer, and J. J. Neumeier, Phys. Rev. B **72**, 132415 (2005); G. F. Dionne, J. Appl. Phys. **101,** 09C509 (2007).

[92] C. Krishnamoorthi, S. K. Barik, Z. Siu and R. Mahendiran, Solid State Commun. **150**, 1670 (2010)

[93] Q. Zhang, F. Guillou, A. Wahl, Y. Breard, and V. Hardy, Appl. Phys. Lett. **96**, 242506 (2010).

[94] W. Eerenstein, N. D. Mathur, and J. F. Scott, Nature (London) **442**, 759 (2006).

[95] S. W. Cheong and M. Mostovoy, Nat. Mater. **6**, 13 (2007).

[96] R. Ramesh and N. A. Spaldin, Nat. Mater. **6**, 21 (2007) and references therein.

[97] J. F. Scott, Nat. Mater. **6**, 256 **(**2007).

[98] M. Gajek, M. Bibes, S. Fusil, K. Bouzehouane, J. Fontcuberta, A. Barthelemy, and A. Fert, Nat. Mater. **6,** 296 (2007).

[99] Freeman, A. J. & Schmid, H. (eds.) *Magnetoelectric Interaction Phenomena in Crystals* (Gordon and Breach, London, 1995)

[100] H. Schmid, Ferroelectrics, **162**, 317, (1994).

[101] T. Kimura, T. Goto, H. Shintani, K. Ishizaka, T. Arima, and Y. Tokura, Nature **426,** 55 (2003).

[102] N. Ikeda, H. Ohsumi, K. Ohwada, K. Ishii, T. Inami, K. Kakurai, Y. Murakami, K. Yoshii, S. Mori, Y. Horibe, and H. Kitô, Nature **436,** 1136 (2005).

[103] N. A. Hill, J. Phys. Chem. B **104,** 6694 (2000).

[104] C. Ederer, N. A. Spaldin, Curr. Opin. Solid State Mater. Sci. **9,** 128 (2005).

[105] D. G. Schlom, J. H. Haeni, J. Lettieri, C. D. Theis, W. Tian, J. C. Jiang, and X. Q. Pan, Mater. Sci. Eng. B **87,** 282 (2001).

[106] H Béa, M Gajek, M Bibes, and A Barthélémy, J. Phys.: Condens. Matter **20,** 434221 (2008).

[107] M. Fiebig, J. Phys. D: Appl. Phys. **38**, R123 (2005).

[108] D. N. Astrov, J. Exptl. Theoret. Phys. (U.S.S.R.) **38**, 984 (1960) [translation: Soviet Phys. JETP **11**, 708 (1960)]; V. J. Folen, G. T. Rado and E. W. Stalder, Phys. Rev. Lett. **6**, 607 (1961).

[109] G. T. Rado, Phys. Rev. Lett. **13**, 335 (1964).

[110] T. Arima, D. Higashiyama, Y. Kaneko, J. P. He, T. Goto, S. Miyasaka, T. Kimura, K. Oikawa, T. Kamiyama, R. Kumai, and Y. Tokura, Phys. Rev. B **70**, 064426 (2004).

[111] B. I. Al shin and D. N. Astrov, Sov. Phys. JETP **17**, 809 (1963).

[112] T. Watanabe and K. Kohn, Phase Transit. **15**, 57 (1989).

[113] E. Ascher, H. Rieder, H. Schmid, and H. Stossel, J. Appl. Phys. **37**, 1404 (1966).

[114] R.P. Santoro, D.J. Segal, and R.E. Newnham, J. Phys. Chem. Solids **27**, 1192 (1966).

[115] J. Van den Boomgaard, D. R. Terrel, R. A. J. Born, and H. F. J. I. Giller, J. Mater. Sci. **9**, 1705 (1974).

[116] A. M. J. G. Van Run, D. R. Terrell, and J. H. Scholing J. Mater. Sci. **9**, 1710 (1974).

[117] J. van den Boomgaard, A. M. J. G. Van Run, and J. Van Suchtelen, Ferroelectrics **10**, 295 (1976).

[118] J. van den Boomgaard and R. A. J. Born, J. Mater. Sci. **13**,1538 (1978).

[119] J. B. Neaton, C. Ederer, U. V. Waghmare, N. A. Spaldin, K. M. Rabe, Phys. Rev. B **71**, 014113 (2005).

[120] R. Seshadri, N. A. Hill, Chem. Mater. **13**, 2892 (2001).

[121] B. B. V. Aken, T. T. M. Palstra, A. Filippetti and N. Spaldin, Nat. Mat. **3**, 164 (2004).

[122] T. Arima, J. Phys. Soc. Jpn, **80**, 052001 (2011)

[123] M. B. Salamon, and Jaime, Rev. Mod. Phys. **73**, 583 (2001) and references therein.

[124] S. D. Tyagi, S. E. Lofland, M. Dominguez, S. M. Bhagat, C. Kwon, M. C. Robson, R. Ramesh, and T. Venkatesan, Appl. Phys. Lett. **68**, 2893 (1996).

[125] R. B. Clover and W. P. Wolf, Rev. Sci. Instrum. **41**, 617 (1970).

[126] J. N. Fox and J. U. Trefny, Am. J. Phys. **43**, 622 (1975).

[127] M. D. Vannette, A. S. Sefat, S. Jia, S. A. Law, G. Lapertot, S. L. Bud'ko, P. C. Canfield, J. Schmalian, and R. Prozorov, J. Magn. Magn. Mater. **320**, 354 (2008); M. D. Vannette and R. Prozorov, J. Phys. : Condens. Matter. **20**, 475208 (2008).

[128] T. Coffey, Z. Bayindir, J. F. DeCarolis, M. Bennett, G. Esper, and C. C. Agosta, Rev. Sci. Instrum. **71**, 4600 (2000).

[129] M. S. Reis, V. S. Amaral, J. P. Araújo, P. B. Tavares, A. M. Gomes, and I. S. Oliveira, Phys. Rev. B, **71,** 144413 (2005).

[130] P. Sande, L. E. Hueso, D. R. Miguens, J. Rivas, F. Rivadulla, and M. A. Lopez-Quintela, Appl. Phys. Lett. **79**, 2040 (2001).

[131] S. Karmakar, E. Bose, S. Taran, B. K. Chaudhuri, C. P. Sun, and H. D. Yang, J. Appl. Phys. **103,** 023901 (2008).

[132] A. Biswas, T. Samanta, S. Banerjee, and I. Das, Appl. Phys. Lett. **92**, 012502 (2008).

[133] P. A. Sharma, J. S. Ahn, N. Hur, S. Park, S. B. Kim, S. Lee, J-G Park, S. Guha, and S. W. Cheong, Phys. Rev. Lett. **93**, 177202 (2004); B. Lorenz, A. P. Litvinchuk, M. M. Gospodinov, and C. W. Chu, Phys. Rev. Lett. **92**, 087204 (2004); T. Goto, T. Kimura, G. Lawes, A. P. Ramirez, and Y. Tokura, Phys. Rev. Lett. **92**, 257201 (2004).

[134] M. M. Kumar, V. R. Palkar, K. Srinivas, and S. V. Suryanarayana, Appl. Phys. Lett. **76**, 2764 (2000).

[135] J. R. Teague, R. Gerson, and W. J. James, Sol. Stat. Comm. **8**, 1073 (1970).

[136] V. G. Bhide and M. S. Multani, Solid State Comm. **3**, 271 (1965).

[137] C. N. R. Rao, *Chemical Approaches to the Synthesis of Inorganic Materials* (Wiley Eastern Ltd., New Delhi, 1994).

[138] R. Valenzuela, *Magnetic ceramics* (Cambridge University Press, New York, 1994).

[139] B. D. Cullity, *Elements of X-ray Diffraction* (Addison-Wesley, Massachusetts, 1972); H. P. Klug, and L. E. Alexander, *X-ray Diffraction Procedures* (John Wiley & Sons, New York, 1954).

[140] S. Patnaik, Kanwaljeet Singh, and R. C. Budhani, Rev. Sci. Instr. **70**, 1494 (1999); S. Sarangi and S. V. Bhat, Rev. Sci. Instr. **76**, 023905 (2005).

[141] G. V. Duong, R. Groessinger, M. Schoenhart, and D. Bueno-Basques, J. Magn. Magn. Mater. **316**, 390 (2007).

[142] *Agilent Impedance Measurement Handbook* (4th edition, Agilent Technologies), downloaded from web: *http://www.home.agilent.com/agilent/home.jspx?cc=US&lc=eng*

[143] J. Marcos, F. Casanova, X. Batlle, A. Labarta, A. Planes and L. Manosa, Rev. Sci. Instrum. **74**, 4768 (2003).

[144] F. Casanova, A. Labarta, X. Batlle, F. J. Perez-Reche, E. Vives, L. Manosa and A. Planes, Appl. Phys. Lett. **86**, 262504 (2005).

[145] H. Y. Hwang, S. W. Cheong, N. P. Ong, and B. Batllogg, Phys. Rev. Lett. **77**, 2041 (1996); R. Mahesh, R. Mahendiran, A. K. Raychaudhuri, and C. N. R. Rao, Appl. Phys. Lett. **68**, 2291 (1996); R. D. Sanchez, J. Rivas, C. Vasquez-Vazquez, A. Lopez-Quintela, M. T. Causa, M. Tovar, and S. Osheroff, Appl. Phys. Lett. **68**, 134 (1996).

[146] J. A. Souza, R. F. Jardim, R. Muccillo, E. N. S. Muccillo, M. S. Torikachvili, and J. J. Neumeier, J. Appl. Phys. **89**, 6636 (2001).

[147] J. Hu H. Qin, Y. F. Wang, and B. Li , J. Magn. Magn. Mater. **322**, 3245 (2010).

[148] D. Stanescu, P. Xavier, J. Richard, and C. Dubourdieu, J. Appl. Phys. **99**, 073707 (2006).

[149] C. Y. Hsu, Hsiung Chou, B. Y. Liao, and J. C. A. Huang, Appl. Phys. Lett. **89**, 262510 (2006).

[150] K. A. Yates, C. Kapusta, P. C. Riedi, L. Ghivelder, and L. F. Cohen, J. Magn. Magn. Mater. **260**, 105 (2003).

[151] F. J. Owens, J. Appl. Phys. **82**, 3054 (1997).

[152] H. Srikanth, J. Wiggins, and H. Rees. Rev. Sci. Instr. **70**, 3097 (1999).

[153] V. B. Naik and R. Mahendiran, J. Appl. Phys. **106**, 123910 (2009).

[154] J. N. Fox, N. Gaggini, and J. K. Eddy, Am. J. Phys. **54**, 723 (1986).

[155] A. H. Morish, 'The Physical Principles of Magnetism', John Wiley & Sons, Inc, New York, page 557 (1965).

[156] S. K. Barik, A. Rebello, C. L. Tan, and R. Mahendiran, J. Phys. D: Appl. Phys. **41,** 022001 (2008).

[157] L.V. Panina, K. Mohri, K. Bushida, and M. Noda, J. Appl. Phys. **76**, 6204 (1994); M. Knobel, M. Vázquez, L. Kraus, Handbook of Magnetic Materials, edited by K. H. J. Buschow (Elsevier, Amsterdam, 2003),Vol. 15, p. 497.

[158] A. B. Beznosov, V. A. Desnenko, E. L. Fertman, C. Ritter, and D. D. Khalyavin, Phys. Rev. B **68**, 054109 (2003).

[159] V. S. Gaviko, N. G. Bebenin, and Ya. M. Mukovskii, Phys. Rev. B **77,** 224105 (2008).

[160] T. Kimura, S. Kawamoto, I. Yamada, M. Azuma, M. Takano, and Y. Tokura, Phys. Rev. B **67**, 180401 (2003); Y. Yang, J.-M. Liu, H. B. Huang, W. Q. Zou, P. Bao, and Z. G. Liu, Phys. Rev. B **70**, 132101 (2004).

[161] N. Hur, S. Park, P. A. Sharma, J. S. Ahn, S. Guha, and S.-W. Cheong, Nature (London) **429**, 392 (2004) and references therein.

[162] M. P. Singh, K. D. Truong, and P. Fournier, Appl. Phys. Lett. **91**, 042504 (2007); N. S. Rogado, J. Li, A. W. Sleight, and M. A. Subramanian, Adv. Mater. **17**, 2225 (2005); P. Padhan, H. Z. Guo, P. LeClair, and A. Gupta, Appl. Phys. Lett. **92**, 022909 (2008); A. K. Kundu, R. Ranjith, B. Kundys, N. Nguyen, V Caignaért, V Pralong, W. Prellier, and B. Raveau, Appl. Phys. Lett. **93**, 052906 (2008).

[163] J. Rivas, J. Mira, B. Rivas-Murias, A. Fondado, J. Dec, W. Kleemann, and M. A. Señaris-Rodríguez, Appl. Phys. Lett. **88**, 242906 (2006).

[164] S. Mercone, A. Wahl. A. Pautrat, M. Pollet, and C. Simon, Phys. Rev. B **69**, 174433 (2004); R. S. Freitas, J. F. Mitchell, and P. Schiffer, Phys. Rev. B **72**, 144429 (2005).

[165] G. Catalan, Appl. Phys. Lett. **88**, 102902 (2006).

[166] M. M. Parish and P. B. Littlewood, Phys. Rev. Lett. **101**, 166602 (2008).

[167] H. Y. Hwang, S. W. Cheong, N. P. Ong, and B. Batlogg, Phys. Rev. Lett. **77**, 2041 (1996).

[168] J. Hu, H. Qin, H. Niu, L. Zhu, J. Chen, W. Xiao, and Y. Pei, J. Magn. Magn. Mater. **261**, 105 (2003).

[169] A. Glaser and M. Ziese, Phys. Rev. B **66**, 094422 (2002).

[170] R. Mahesh, R. Mahendiran, S. K. Raychaudhuri, and C. N. R. Rao, Appl. Phys. Lett. **68**, 2291 (1996); H. Y. Hwang, S.-W. Cheong , N. P. Ong, and B. Batlogg, Phys. Rev. Lett. **77**, 2041 (1996).

[171] K. Mohri, T. Kohzaw, K. Kawashimha, H. Yoshida, and L. V. Paniana, IEEE. Trans. Magn. **31**, 1249 (1995).

[172] D-X. Chen, J. L. Muñoz, A. Hernando, and M. Vázquez, Phys. Rev. B **57**, 10699 (1998).

[173] L. V. Panina, K. Mohri, K. Bushida, and M. Noda, J. Appl. Phys. **76,** 6198 (1994); K. R. Pirota, M. Knobel, and C. Gomez-Polo, Physica B **320**, 127 (2002).

[174] R. B. da Silva, A. M. H. de Andrade, A. M. Severino, A. D. C. Viegas, and R. L. Sommer, J. Magn. Magn. Mater. **249**, 288 (2002); M. Vazquez, J. Magn. Magn. Mater. **226**, 693 (2001).

[175] A. S. Carneiro, F. C. Fonseca, R. F. Jardim, and T. Kimura, J. Appl. Phys. **93**, 8074 (2003).

[176] R. P. Rairigh, G. S. Bhalla, S. Tongay, T. Dhakal, A. Biswas, and A. F. Hebard, Nature Physics **3**, 551 (2007).

[177] H. Sakai, Y. Taguchi and Y. Tokura, J. Phys. Soc. Jpn. **78**, 113708 (2009).

[178] C. Martin, A. Maignan, M. Hervieu, and B. Raveau, Phys. Rev. B **60**, 12191 (1999).

[179] X. Z. Yu, Y. Tomioka, T. Asaka, K. Kimoto, T. Arima, Y. Tokura, and Y. Matsui, Appl. Phys. Lett. **94**, 082509 (2009).

[180] Y. Tomioka, H. Hiraka, Y. Endoh, and Y. Tokura, Phys. Rev. B **74**, 104420 (2006).

[181] A. Rebello and R. Mahendiran, Appl. Phys. Lett. **93**, 232501 (2008).

[182] P. M. Woodward, T. Vogt, D. E. Cox, A. Arulraj, C. N. R. Rao, P. Karen, and A. K. Cheetham, Chem. Mater. **10**, 3652 (1998).

[183] T. Shimura, T. Hayashi, Y. Inaguma, and M. Itoh, J. Solid State Chem. **124,** 250 (1996); R. N. Singh, C. Shivakumara, N. Y. Vasanthacharya, S. Subramanian, M. S. Hegde, H. Rajagopal, and A. Sequeira, J. Solid State Chem. **137,** 19 (1998).

[184] R. P. Borges, F. Ott, R. M. Thomas, V. Skumryev, J. M. D. Coey, J. I. Arnaudas, and L. Ranno, Phys. Rev. B **60**, 12847 (1999); E. M. Levin and P. M. Shand, J. Magn. Magn. Mater. **311**, 675 (2007).

[185] M. Uchida, R. Mahendiran, Y. Tomioka, Y. Matsui, K. Ishizuka, and Y. Tokura, Appl. Phys. Lett. **86**, 131913 (2005).

[186] C. Leighton, D. D. Stauffer, Q. Huang, Y. Ren, S. El-Khatib, M. A. Torija, J. Wu, J. W. Lynn, L. Wang, N. A. Frey, H. Srikanth, J. E. Davies, Kai Liu, and J. F. Mitchell, Phys. Rev. B **79**, 214420 (2009).

[187] A. M. Balagurov, I. A. Bobrikov, D. V. Karpinsky, I. O. Troyanchuk, V. Yu. Pomjakushin, and D. V. Sheptyakov, JETP Letters. **88**, 531 (2008).

[188] E. Suard, F. Fauth, C. Martin, A. Maignan, F. Millange, and L. Keller, J. Magn. Magn. Mater. **264**, 221 (2007).

[189] F. Dupont, F. Millange, S. de Brion, A. Janossy, and G. Chouteau, Phys. Rev. B **64**, 220403 (2001).

[190] D. E. Cox, P. G. Radaelli, M. Marezio, and S-W. Cheong, Phys. Rev. B **57**, 3305 (1998).

[191] J. Dho, E.O. Chi, N.H. Hur, K.W. Lee, H.S. Oh, and Y.N. Choi, Solid State Commun. **123**, 441 (2002).

[192] S Rößler, S Harikrishnan, U. K Rößler, Suja Elizabeth, H L Bhat, F Steglich, and S Wirth, J. Phys.: Conf. Series **200**, 012168 (2010).

[193] L. Zhu, L. Li, T. Cheng, and G. Wei, Phys. Lett. A **374**, 2972 (2010).

[194] K. A. Gschneidner, Jr., V. K. Pecharsky, A. O. Tsokol Rep. Prog. Phys. **68**, 1479 (2005) and references therein.

[195] O. Tegus, E. Brück, K. H. J. Buschow, and F. R. de Boer, Nature **415**, 150 (2002).

[196] A. Planes, L. Mañosa, and M. Acet J. Phys: Condens. Matter **21**, 233201 (2009).

[197] E. Brück, O. Tegus, D. T. H. Thanh, and K. H. J. Buschow J. Magn. Magn. Mater. **310**, 2793 (2007).

[198] Z. B. Guo, Y. W. Du, J. S. Zhu, H. Huang, W. P. Ding, and D. Feng Phys. Rev. Lett. **78**, 1142 (1997).

[199] X. Bohigas, J. Tejada, E. del. Barco, X. Zhang, and M. Sales Appl. Phys. Lett. **73**, 390 (1998).

[200] H. Terashita, J. J. Garbe, and J. J. Neumeier, Phys. Rev. B **70**, 094403 (2004).

[201] T. Krenke, E. Duman, M. Acet, E. F. Wassermann, X. Moya, L. Manosa, and A. Planes, Nature Mater. **4**, 450 (2005).

[202] C. Krishnamoorthy, S. K. Barik, S. Ziu, and R. Mahendiran, Solid State Commun. **150**, 1670 (2010).

[203] X. Moya, L. Mañosa, A. Planes, S. Aksoy, M. Acet, E. F. Wassermann, and T. Krenke Phys. Rev. B **75**, 184412 (2007).

[204] H. Sakai, Y. Taguchi, and Y. Tokura, J. Phys. Soc. Jpn. **78**, 113708 (2009).

[205] S. Thota, Q. Zhang, F. Guillou, U. Luders, N. Barrier, W. Prellier, A. Wahl, and P. Padhan, Appl. Phys. Lett. **97**, 112506 (2010).

[206] M. Patra, S. Majumdar, S. Giri, G. N. Iles, and T. Chatterji, J. Appl. Phys. **107**, 076101 (2010).

[207] L. Zhu, L. Li, T. Cheng, and G. Wei, Phys. Lett. A **374**, 2972 (2010).

[208] Y. Okuda, M. Matsusa, and T. Haseda, J. Magn. Magn. Mater. **15**, 1027 (1980); E. Nakamura and M. Hosoya, J. Phys. Soc. Jpn. **23**, 844 (1967).

[209] A. Rebello and R. Mahendiran, Appl. Phys. Lett.**93**, 232501 (2008) and references therein.

[210] H. Y. Hwang, S. -W. Cheong, N. P. Ong, and B. Batlogg, Phys. Rev. Lett. **77**, 2041 (1996); R. Mahesh, R. Mahendiran, A. K. Raychaudhuri, and C. N. R. Rao, Appl. Phys. Lett. **68**, 2291 (1996).

[211] M. H. Phan and H. X Peng, Prog. Mater. Sci. **53**, 323 (2008) and references therein.

[212] R. J. Joenk, J. Appl. Phys. **30**, 1097 (1963).

[213] C. Krishnamoorthi, S. K. Barik, Z. Siu, and R. Mahendiran, Solid State Commun. **150**, 1670 (2010).

[214] Q. Zhang, F. Guillou, A. Wahl, Y. Breard and V. Hardy, Appl. Phys. Lett. **96**, 242506 (2010).

[215] N. S. Bingam, M. H. Phan, H. Srikanth, M. A. Torija, and C. Leighton, J. Appl. Phys. **106**, 023909 (2009).

[216] G. J. Liu, J. R. Sun, and B. G. Shen, Solid State Commun. **149**, 722 (2009).

[217] C. Martin, A. Maignan, M. Hervieu, and B. Raveau, Phys. Rev. B **60**, 12191 (1999).

[218] A. R. Dinesen, S. Linderoth, and S. Morup, J. Magn. Magn. Mater. **253**, 28 (2002); J. Phys. Condens. Matter. **17**, 6257 (2005).

[219] S. Jeppesen, S. Linderoth, N. Pryds, L. Theil Kuhn, and J. Buch Jensen, Rev. Sci. Instrum. **79**, 083901 (2008).

[220] A. Szewczyk, M. Gutowska, B. Dabrowski, T. Plackowski, N. P. Danilova, and Yu. P. Gaidukov, Phys. Rev. B **71**, 224432 (2005).

[221] F. Damay, C. Martin, M. Hervieu, A. Maignan, B. Raveau, G. Andre, and F. Bouree, J. Magn. Magn. Mater. **184**, 71 (1998).

[222] Z. Jirak, J. Hejtmanek, E. Pollert, C. Martin, A. Maignan, B. Raveau, M. M. Savosta, Y. Tomioka, and Y. Tokura, J. Appl. Phys. **89**, 7404 (2001).

[223] A. Giguère, M. Földeaki, B. Ravi Gopal, R. Chahine, T. K. Bose, A. Frydman, and J. A. Barclay, Phys. Rev. Lett. **83**, 2262 (1999).

[224] V. Suresh Kumar and R. Mahendiran, J. Appl. Phys. **109**, 023903 (2011).

[225] R. Mahendiran, B. G. Ueland, P. Schiffer, A. Maignan, C. Martin, M. Hervieu, B. Raveau, M. R. Ibarra, and L. Morellon, 2003. *http://arxiv.org/abs/cond-mat/0306223* (unpublished).

[226] R. Mahendiran, M. R. Ibarra, C. Marquina, B. Garcia-Landa, L. Morellon, A. Maignan, B. Raveau, A. Arulraj, and C. N. R. Rao, Appl. Phys. Lett. **82**, 242 (2003).

[227] T. Krenke, E. Duman, M. Acet, E. F. Wassermann, X. Moya, L.Mañosa and A. Planes, Nature Mater. **4**, 450 (2005).

[228] T. Kimura, T. Goto, H. Shintani, K. Ishizaka, T. Arima, and Y. Tokura, Nature **426**, 55 (2003).

[229] Y. Tokunaga, S. Iguchi, T. Arima, and Y. Tokura, Phys. Rev. Lett. **101**, 097205 (2008).

[230] K. Taniguchi, N. Abe, S. Ohtani, and T. Arima, Phys. Rev. Lett. **102**, 147201 (2009).

[231] W. Peng, N. Lemée, M. Karkut, B. Dkhil, V. V. Shvartsman, P. Borisov, W. Kleemann, J. Holc, M. Kosec, and R. Blinc. Appl. Phys. Lett. **94**, 012509 (2009).

[232] J. P. Rivera and H. Schmid, Ferroelectrics, **204**, 23 (1997).

[233] J. Wang, J. B. Neaton, H. Zheng, V. Nagarajan, S. B. Ogale, B. Liu, D.Viehland, V. Vaithyanathan, D. G. Schlom, U. V. Waghmare, N. A. Spaldin, K. M. Rabe, M. Wuttig, and R. Ramesh, Science **299**, 1719 (2003).

[234] Y. P. Wang, L. Zhou, M. F. Zhang, X. Y. Chen, J.-M. Liu, and Z. G. Liu, Appl. Phys. Lett. **84**, 1731 (2004).

[235] V. R. Palkar, Darshan C. Kundaliya,S. K. Malik, and S. Bhattacharya, Phys. Rev. B **69**, 212102 (2004).

[236] R.K. Mishra, D. K. Pradhan, R.N.P. Choudhary, and A. Banerjee, J. Magn. Magn. Mater. **320**, 2602 (2008).

[237] V. A. Khomchenko, D. A. Kiselev, J. M. Vieira, L. Jian, A. L. Kholkin, A. M. L. Lopes, Y. G. Pogorelov, J. P. Araujo, and M. Maglione, J. Appl. Phys. **103**, 024105 (2008).

[238] B. Kundys, A. Maignan, C. Martin, N. Nguyen, and C. Simon, Appl. Phys. Lett. **92**, 112905 (2008).

[239] P. Fischer, M. Polomska, I. Sosnowska, and M. Szymanski, J. Phys. C: Solid St. Phys., **13**, 1931 (1980).

[240] M. Valat, A. K. Axelsson, and N. Alford, Chem. Mater. **19**, 5431 (2007).

[241] F. Söffge and W.v. HÖrsten, J. Magn. Magn. Mater, **59**, 135 (1986).

[242] R.D. Shannon, Acta Cryst. A **32** 751 (1976).

[243] Y. H. Lee, J. M. Wu, and C. H. Lai, Appl. Phys. Lett. **88**, 042903 (2006); Z. X. Cheng, X. L. Wang, S. X. Dou, H. Kimura, and K. Ozawa, J. Appl. Phys. **104**, 116109 (2008); R. K. Mishra, D. K. Pradhan, R.N.P. Choudhary, and A. Banerjee, J. Magn. Magn. Mater. **320**, 2602 (2008).

[244] M. Dawber, K. M. Rabe, and J. F. Scott, Rev. Mod. Phys. **77**, 1083 (2005).

[245] J. M. Caicedo, J. A. Zapata, M. E. Gómez, and P. Prieto, J. Appl. Phys. **103**, 07E306 (2008).

[246] G.V. Duong, R. Groessinger, and R. S. Turtelli, IEEE Trans. Magn., **42**, 3611 (2006).

[247] Q. Y. Xu, H. F. Zai, D. Wu, T. Qiu, and M. X. Xu, Appl. Phys. Lett. **95**, 112510 (2009).

[248] C. Yang, J. S. Jiang, F. Z. Qian, D. M. Jiang, C. M. Wang, W. G. Zhang, J. Alloy. Compd. **507**, 29 (2010).

[249] Q. Y. Xu, X. H. Zheng, Z. Wen, Y. Yang, D. Wu, and M. X. Xu, Solid State Comm. **151**, 624 (2011).

[250] Q. Y. Xu, Z. Wen, J. L. Gao, X. Liu, D. Wu, S. L. Tang, and B. Yang, J. Supercond. Nov. Magn. **24**, 1497 (2011).

[251] L. Zhai, Y. G. Shib, J. L. Gaoa, S. L. Tanga, and Y. W. Du, J. Alloy. Compd. **509**, 7591 (2011).

[252] P. Singh**,** Y. A. Park**,** K. D. Sung**,** N. Hur**,** J. H. Jung**,** W. S. Noh**,** J. Y. Kim**,** J. Yoon, and Y. Jo**,** Solid State Comm. **150**, 431 (2010).

[253] V. B. Naik and R. Mahendiran, Appl. Phys. Lett. **94**, 142505 (2009).

[254] V. B. Naik, M. C. Lam, and R. Mahendiran, J. Magn. Magn. Mater. **322**, 2754 (2010).

[255] V. B. Naik, A. Rebello, and R. Mahendiran, Appl. Phys. Lett. **95**, 082503 (2009).

[256] V. B. Naik, M. C. Lam, and R. Mahendiran, J. Appl. Phys. **107**, 09D720 (2010).

[257] V. B. Naik and R. Mahendiran, IEEE transactions on Magnetics, **47**, 2712 (2011).

[258] V. B. Naik, A. Rebello, and R. Mahendiran, J. Appl. Phys. **109**, 07C728 (2011).

[259] V. B. Naik and R. Mahendiran, J. Appl. Phys. **110**, 053915 (2011).

[260] V. B. Naik, S. K. Barik, R. Mahendiran, and B. Raveau, Appl. Phys. Lett. **98**, 112506 (2011).

[261] V. B. Naik and R. Mahendiran, "*Direct and indirect measurements of magnetocaloric effect in* $Pr_{0.5}Sr_{0.5}MnO_3$" (submitted to Solid State Communications).

[262] V. B. Naik and R. Mahendiran, Solid State Commun. **149**, 754 (2009)

[263] V. B. Naik and R. Mahendiran, J. Appl. Phys. **106**, 123910 (2009).

[264] V. B. Naik and R. Mahendiran, IEEE transactions on Magnetics **47**, 3776 (2011).

[265] V. F. Gantmakher, V. I. Kulakov, G. I. Leviev, R. K. Nikolaev, A. V. Polisskii, N. S. Sidorov, and M. R. Trunin, Sov. Phys. JETP **68**, 833 (1989).

[266] A. S. Carneiro, F. C. Fonseca, R. F. Jardim, and T. Kimura J. Appl. Phys. **93**, 8074 (2003).

[267] J. Wolfman, C. Simon, M. Hervieu, A. Maignan, and B. Raveau, J. Solid State Chem. **123**, 413 (1996).